UNIVERSITAT DE BARCELONA

Nanostructured transition metal carbides as potential catalysts for greenhouse gases conversion

Marc Figueras Valls

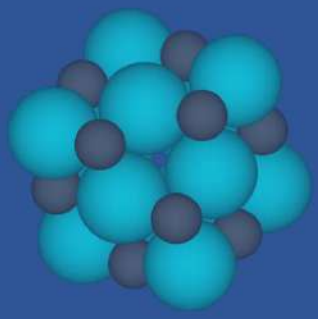


Nanostructured transition metal carbides as potential catalysts for greenhouse gases conversion

Doctoral Thesis by

Marc Figueras Valls

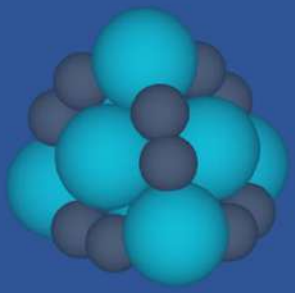

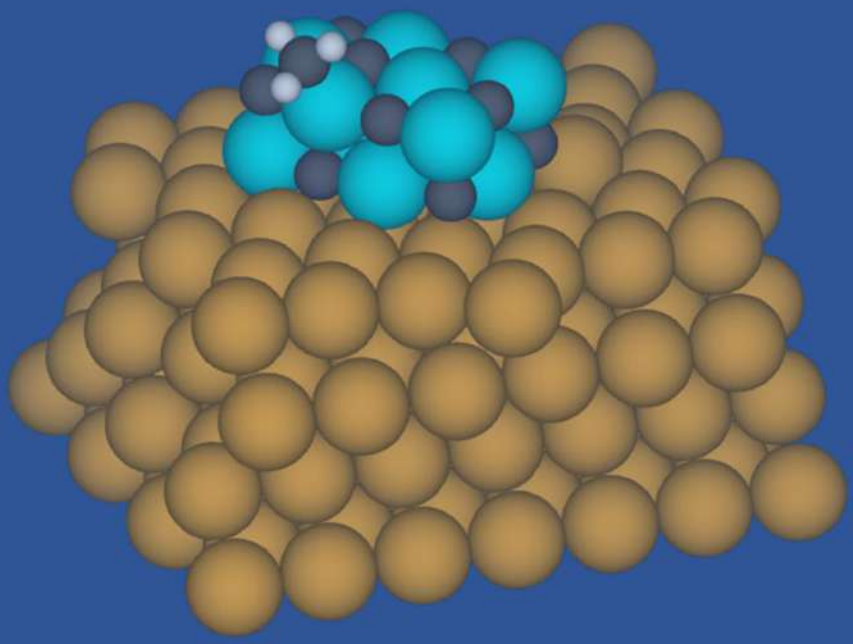


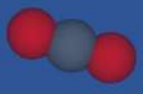

UNIVERSITAT DE BARCELONA

A Thesis submitted in partial fulfilment for the degree of

Doctor of Philosophy in

Theoretical Chemistry and Computational Modelling

entitled

Nanostructured transition metal carbides as potential catalysts for greenhouse gases conversion.

September 2021

Signed:

Author: Marc Figueras Valls

Directors: Francesc Illas Riera and Francesc Viñes Solana

Tutor: Carme Sousa Romero

Abstract

Over the recent decades, several studies revealed the precarious climate situation which is threatening all Life forms on earth, including mankind, even if sometimes we tend to ignore the actual fragility of our situation. Ironically, the human species is at the origin of the rapid change on climate, mostly by practicing unsustainable activities, such as the unregulated consumption of fossil fuels, excessive deforestation, extensive agriculture, and intensive livestock. All these practices have increased the concentration of greenhouse gases in the atmosphere, producing a rapid increase in the average Earth temperature with noticeable consequences in our lifetime. Nevertheless, several efforts have been conducted by the scientific community in order to revert the actual climate situation, even if society acts delayed.

One of the actual work routes implies the use of catalysts to capture and convert greenhouse gases into less harmful and more useful chemicals. This route has found in transition metal carbides (TMCs) proficient candidates that could have an important impact in the aforementioned matter. An interesting aspect of TMCs is their capacity to catalyse such transformation reactions at low temperatures and to withstand several reaction cycles without degrading. Precisely, the present Thesis unveils and discusses several reaction mechanisms involved in the greenhouse gases transformation reactions held by TMCs, particularly, focusing on MoC_y nanoparticles, a largely unexplored field. This Thesis combines experimental and theoretical approaches to explain the observed experimental evidences, where custom synthetized MoC nanoparticle supported on Au(111) are able to activate methane at room temperature, hydrogenate CO_2, and act as superior H_2 sponges with respect to clean MoC extended surfaces. Moreover, other important findings are revealed, such as the reconstruction held by some transition metal carbides and nitrides surfaces and the intrinsic nature of clean MoC nanoparticles towards hydrogenation reactions. Overall, the present dissertation intends to encourage further efforts on developing TMC based catalyst able to be used at industrial levels.

The experimental section of this thesis has been carried out at the Brookhaven National Laboratory by the group of Prof. J. A. Rodriguez, while the computational part and results analysis has been carried out in the present institution, the *Universitat de Barcelona*. The results obtained have led to several joint publications.

Resum

En els darreres dècades, diversos estudis han revelat la precària situació climàtica que està amenaçant totes les formes de vida a la terra, inclosa la humanitat, encara que de vegades tendim a ignorar la fragilitat de la nostra situació. Irònicament, l'espècie humana és l'origen del ràpid canvi climàtic, principalment per practicar activitats insostenibles, com el consum no regulat de combustibles fòssils, la desforestació excessiva, l'agricultura extensiva i la ramaderia intensiva. Totes aquestes pràctiques han augmentat la concentració de gasos d'efecte hivernacle a l'atmosfera, produint un ràpid augment de la temperatura mitjana de la Terra amb conseqüències notables fins i tot durant la nostra vida. No obstant això, la comunitat científica està realitzant diversos esforços per revertir la alarmant situació climàtica, fins i tot si la societat actua amb retard.

Una de les rutes de treball implica l'ús de catalitzadors per capturar i convertir els gasos d'efecte hivernacle en productes químics menys nocius i més útils. Aquesta ruta ha trobat en els carburs de metalls de transició (TMC) candidats competents que podrien tenir un impacte important en la reactivitat esmentada. L'aspecte més interessant dels TMCs és la seva capacitat per catalitzar aquestes reaccions de transformació a baixes temperatures i per suportar diversos cicles de reacció sense degradar-se. Precisament, aquesta Tesi revela i analitza diversos mecanismes de reacció implicats en les reaccions de transformació dels gasos d'efecte hivernacle catalitzades pels TMC, concretament, centrant-se en les nanopartícules de MoC_y, que encara romanen inexplorades. Aquesta tesi combina enfocaments experimentals i teòrics per explicar les evidències experimentals observades, on les nanopartícules de MoC sintetitzades suportades sobre Au (111) són capaces d'activar el metà a temperatura ambient, hidrogenar CO_2 i actuar com a esponges H_2 superiors respecte a les superfícies netes de MoC. A més, altres descobriments importants han estat revelats, com ara la reconstrucció d'algunes superfícies de TMC/TMN i la naturalesa química intrínseca de les nanopartícules de MoC netes pel que fa a les reaccions d'hidrogenació. En general, la present dissertació té la intenció de fomentar nous esforços en el desenvolupament de catalitzadors basats en TMCs que puguin ser utilitzats a nivell industrial.

La secció experimental d'aquesta tesi s'ha dut a terme al *Brookhaven National Laboratory* pel grup del professor J. A. Rodriguez, mentre que la part computacional i

l’anàlisi de resultats s’ha dut a terme a la present institució, la Universitat de Barcelona. Els resultats obtinguts han donat lloc a diverses publicacions conjuntes.

Acknowledgements

Primer de tot, vull agrair als meus dos directors, el Francesc Illas i el Francesc Viñes, per ajudar-me a fer realitat aquest doctorat. La seva incansable dedicació m'ha permès créixer tant en l'àmbit professional com personal. Ambdós han estat allà sempre que els he necessitat, ja sigui en llargues discussions filosòfiques o en la llibertat i compressió mostrada en els moments més difícils. Per tot això, moltes gràcies jefes! Us trobaré a faltar allà on vagi.

Parlant de discussions filosòfiques, no puc marxar sense donar les gràcies a tots els professors que s'han pres la molèstia d'escoltar-me i rebatre els dubtes teòrics que m'han anat sorgint durant el doctorat. En aquest sentit vull donar les gràcies especialment a la Carme Sousa, el Juan Carlos Paniagua i el Iberio Moreira, moltes gràcies per aguantar les meves "chapas". En aquest grup també vull afegir l'Hèctor Prats, mestre de les NEBs i gran company que em va ajudar en els inicis del doctorat.

També vull donar les gràcies a tots els membres del IQTC i del departament que en algun moment han contribuït al meu creixement professional al llarg d'aquests tres anys. Moltes gràcies en especial a l'Ángel, Stefan, Konstantin, Mercè, Jordi, Oriol, Anabel, Martí, Joan M., Raul, Pablo B., Pablo G., Pablo L., Ramon i molts altres que de segur m'estic deixant.

Els del despatx! Tranquils que no m'oblido de vosaltres. Raul, moltes gràcies per les llargues discussions, he aprés molt de tu, sobretot a programar. Toni, que mai has estat del despatx però tot i així t'has fet un lloc en la meva memòria. Genís! Última incorporació... i quina incorporació! Tant de bo ens quedin molts més sopars per celebrar. I per últim, les dues perles, Lorens i Cristina, quin fart de riure m'he fet amb vosaltres! Gràcies per la vostre companyia i escalf, crec que serà difícil trobar un altre lloc amb tant bon ambient. A la memòria em quedaran gravats els divendres a la tarda de música Disney, les discussions acalorades i les sessions de fotos pelo Pantene.

En l'àmbit no acadèmic vull agrair a tots els meus amics que m'han ajudat activa o passivament a tirar endavant en aquests darrers anys. En especial al Julen i la Ivet, el Consejo, Varea, Jennifer, Cucala i Natalia. Gràcies per el vostre suport.

Per últim, dono les gràcies a la meva família. Cosines, cosins, tiets i tietes, sempre atents i estimant, no es pot demanar més. Núria i Maria, no sé què faria sense vosaltres, ja sabeu

com en sou d'importants per mi. Miriam, gràcies pel que m'has ajudat en l'últim any i pel que ens queda per davant, t'estimo petita.

Ara sí, només em queda una persona a la llista. Mare, tan de bo haguessis pogut estar present en aquest moment. Mai et vaig agrair suficient tot el que has fet per mi. Ens vas donar tot el que tenies i, si avui estic a les portes d'acabar aquesta etapa, és gràcies a tu. Siguis on siguis, et portem al cor.

Most used abbreviations

APW - **A**ugmented-**P**lane-**W**ave

BEP - **B**rønsted-**E**vans-**P**olanyi

CDD - **C**harge **D**ensity **D**ifference

CI-NEB - **C**limbing-**I**mage **N**udged **E**lastic **B**and

DAFC - **D**irect **A**lcohol **F**uel **C**ells

DFT - **D**ensity **F**unctional **T**heory

EH - **E**lectronic **H**amiltonian

ELF - **E**lectronic **L**ocalization **F**unction

GGA - **G**eneralized **G**radient **A**pproximation

GTO – **G**aussian-**T**ype **O**rbitals

HEG - **H**omogeneous **E**lectron **G**as

HER - **H**ydrogen **E**volution **R**eaction

HK - **H**ohenberg and **K**ohn

ISS - **I**on-**S**cattering **S**pectroscopy

KS - **K**ohn and **S**ham

LDA - **L**ocal **D**ensity **A**pproximation

ML - **M**ono**L**ayers

NEB - **N**udged **E**lastic **B**and

NEXAFS- **N**ear **E**dge **X**-ray **A**dsorption **F**ine **S**tructure

NP - **N**ano**P**article

PAW - **P**rojector **A**ugmented **W**ave

PBE – **P**erdew-**B**urke-**E**rnzerhof

PES - **P**otential **E**nergy **S**urface

PW - **P**lane **W**ave

STM - **S**canning **T**unnelling **M**icroscopy

TDS - **T**hermal **D**esorption mass **S**pectroscopy

TM - **T**ransition **M**etal

TMC - **T**ransition **M**etal **C**arbide

TPD - **T**emperature-**P**rogrammed **D**esorption

TS - **T**ransition **S**tate

VASP - **V**ienna ***A****b innitio* **S**imulation **P**ackage

WGS - **W**ater-**G**as **S**hift

XPS - **X**-ray **P**hotoelectron **S**pectroscopy

Table of Contents

Chapter 1

Introduction

1.1 Transition Metal Carbides

Since quite long ago, transition metal carbides (TMCs), have been appraised by their ultra-hardness, refractory nature, and relatively low cost, a series of properties which have been a great motivation for their use on a wide-ranging of applications like cutting tools and thermal isolators.[1] However, it was not till almost 50 years ago that some early reports disclosed their catalytic capabilities. Levy and Boudart[2] were among the first to report a TMC catalytic activity. They reported that WC had the capacity to adsorb hydrogen and oxygen in a significantly different way from that of W, reflecting features usually associated with noble metals such as Pt. Furthermore, WC demonstrated its capability to isomerize 2.2-dimethylpropane, a process previously known to be catalysed just by noble, scarce and expensive metals such as Pt, Pd, and Ir. Nevertheless, even if transition metal carbides had an unsuspected catalytic capability, their general performance was still far from comparable to that of the above mentioned noble metals, sometimes displaying rates with several orders of magnitude lower.[1] During the last decades, important efforts have been done aimed at improving the methodology used to synthetize TMCs, mainly by creating stable high surface area catalysts which can endure several catalytic cycles. This constant effort has disclosed other catalytic and electrocatalytic applications plus a deep understanding of the features involved on their performance. In the present work, we will focus on the early TMCs, *i.e.*, groups 4 to 6 on the periodic table.

1.2 Physical and Electronic Properties of TMCs

In general, TMCs can be described as compounds characterized by the presence of small interstitial atoms (carbon in this case) within a metal lattice. The stoichiometry strongly depends on the synthesis conditions and can vary from those naturally encountered or predominantly encountered.[3] As commented above, most carbides have extremely high melting points (2000-4000 ºC), therefore TMCs are usually employed as refractory materials. It is interesting to note that there is a shift on their melting point compared to pure transition metal compounds. While group VI pure transition metal (TM) compounds display the higher melting points among TMs, for TMCs the highest melting points lie on group V. [4] Along with the refractory capacity, TMCs have a great corrosion resistance, which has promoted its use on high-temperature structural materials.[4] Moreover, the most important property of TMC is their high hardness, since these compounds are among the

hardest known. Some of them have microhardness values of 2000 up to 3000 kg/mm^2, which set them just below diamond.[4] Furthermore, TMCs are typically metallic in their electrical, magnetic, and optical properties. In most of these properties the difference between their purely transition metal counterpart are minimum. Electrical and magnetic properties are extremely sensitive to defects on the structure,[4] which lead to another important feature. TMCs present large structural defects, as commented above, deviations from ideal stoichiometric structures are fairly common, and can be up to 50%, usually more predominant on the nonmetal lattice sites.[4]

To predict which combinations of metal-carbon compounds can lead to stable structures, *i.e.*, those where the ratio, *r*, of nonmetal and metal radii is between 0.41 and 0.59., one could account on the long-used Hägg's rule.[5] For *r* values below 0.59, it is common to find the typical face-centred cubic (fcc), hexagonal closed packed (hcp), or simple hexagonal (hex) crystalline structures. On the other hand, for *r* values larger than 0.59, the metallic arrangement distorts to accommodate the nonmetal atoms and, in this way, be able to preserve the metal-metal interactions.[6] While Hägg's rule provides the geometric explanation of the common structure formation, the need of a more precise method was required to predict the crystal structure of TMCs. The Engel-Brewer Theory implied a considerable improvement on the crystalline structure prediction. This theory predicts stable structures accounting on the outer *sp* electrons for pure metals.[7] In the same way, TMCs behave similarly to their metal counterparts with some shifts usually explained because the interstitial nonmetal atoms increase the *sp* electrons on the alloy. While TMCs present a more predominant crystalline structure, more and more stable phases are being discovered of most of them in the recent years.[8-12] Advances on experimental procedures allow to synthesise these materials on extreme conditions leading to different crystalline structures.

The electronic properties of TMCs, *i.e.*, thermal and electrical conductivity, can be explained by their bonding nature, with contribution of strong covalent-nonmetal bonding, a less important ionic bonding and a relevant influence of metallic bonding.[13,14] This mixture of bonding features allows TMCs to perform in several applications and explain the main physical properties already commented. The electronic structure and bonding in bulk transition metal carbides has been studied by means of X-ray photoemission spectroscopy (XPS)[15] and recently by means of near edge X-ray adsorption fine structure spectroscopy (NEXAFS).[16] Nevertheless, the information

obtained seem contradictory and the main issue comes from the amount of charge transfer between carbon and metal atoms.[17,18] It is clear that there is always a certain amount of charge transfer probed by the relevant shifts on the concerning bands. Nonetheless, it is complicated to explicitly determine the amount of charge transfer just based on this shift. In an earlier work, Viñes *et al.*,[19] theoretically studied the electronic structure of a series of transition metal carbides focusing on both bulk and most stable surfaces by means of density functional theory (DFT) methods. For the bulk systems, the results clearly stated a primary covalent bond that tends to change into a metal bond moving to the right of the periodic table. For group 4 TMCs, the covalency prevail and, consequently, they could be seen as small band-gap semiconductors, but there exists a weak overlap between valence and conduction band, so they display a metallic character. On the other hand, group 5 TMCs show an enhanced metallic character due to partially filled *d* bands, with some exceptions where the metallic character comes from partially occupied metal *s* bands (NbC and δ-MoC). For the surface models, the results show a decrease in the gap due to a shift between bonding and antibonding levels which is generalized for all the studied TMCs. This shift implies that surface systems turn around their semiconductor character in the bulk to a more metallic character.

1.3 Synthesis of TMCs

This section will focus on the fundamental description of the different methods used to synthesize TMCs. Currently, there are several methods, mostly delimited by the TMC used in practice and the final structure sought, being the latter, the driven thread of this section. The effort carried out by Oyama *et al.*,[6] and Ahmad *et al.*,[20] on assembling all these methods for an easier documentation must be recognized.

1.3.1 Synthesis of low surface area TMCs

As described by Oyama,[6] there are four main methods to fabricate TMCs seeking large bulk/surface ratio structures. As it could seem apparent, these methods look for a more well-defined bulk composition than a given termination of the particle edges and surfaces. The first method is based on a direct reaction between the TM and elemental C. The merely contacting of metal and C powders in an inert atmosphere at high temperatures

(2300 K), propitiate the TM formation by diffusion of C atoms into the metal powder. The second method implies the reaction of a metal oxide in presence of solid carbon. It follows the same methodology as in the first case. The contacting of powders at high temperature (2300 K) reduces the metal oxide to metal, followed by the C diffusion into the metal. The latter could end up forming oxycarbides, which is the main downside of this method, as the final product could have impurities.

The third method implies a more subtle process than just applying high temperatures on all the material. It is a self-propagating high-temperature synthesis (SHS),[21,22] where a mix of Al, TM and, C is compressed and placed in an inert atmosphere. Then a small area of the pack is heated, which starts the reaction and continues inevitably as it has positive (exothermic) reaction heat. The reaction is based on the formation Al_xTi and Al_yC_z blocks, that with an increase in temperature end up forming liquid Al and solid TiC.[23] This method is appraised because does not require a high energy input. Finally, the fourth method is used to create single crystals. This method is based on techniques that imply the precipitation from liquid metals. Verneuil and the floating zone techniques are two examples of them.[6]

1.3.2 Synthesis of 2D TMCs

The 2D TMCs or MXenes[24] are compounds structured in layers of few atoms wide, arranged in a particular $M_{n+1}X_n$ structure, where M is the TM, X is either C or N, and normally have n = 1-3. On synthesis conditions MXenes are terminated with hydroxyl, fluorine, oxygen or hydrogen adatoms. As commented by Ahmad *et al.*,[20] there are three main methods to synthetize 2D TMCs.

The first method entails the formation of MXenes from MAX phases using the hydrofluoric acid etching method. MAX phases are 3D materials that follow a $M_{n+1}AX_n$ structure where M is a TM, A is a group 13 or 14 element (usually Al) and, X is either C or N.[20] The hydrofluoric acid etching method is based on the exfoliation of MXenes by combining a MAX phase and hydrofluoric acid. The acid reacts with the A element to form AF_x salt plus H_2, the remanent not dissolved material is the MXene, which ultimately reacts with water and more hydrofluoric acid to lead to the final MXene covered with fluorine, OH, O, and/or H. *In situ* HF generation by using LiF and HCl has also been used.[25]

The second method entails the usage of molten salts. Concretely, a mix of a MAX phase and salt (usually LiF, KF, or NaF) is heated to 823 K in an inert atmosphere. Once the salt is melted, it acts as an etching agent that remove the Al or A element of the MAX phase.[26] This method allows producing layers with larger lattice parameters.[27]

The third and final method family is an alternative method not requiring fluoride compounds, which are highly toxic and corrosive. It is based on an electrochemical etching to convert a MAX phase into the MXene. The MAX phase is used as both electrodes and submerged into a HCl solution for a long period of time with an applied potential of around 0.6 V. In this method the Cl^- etch Al and the cations intercalate and increase the *d*-spacing.[20] This method has an important drawback; it only produces etching on the surface of the MAX phase when kept on an acidic medium. To solve this problem, it can be kept in a binary electrolyte solution of ammonium chloride and tetramethylammonium hydroxide at a high pH (over 9).

1.3.3 Synthesis of TMC nanocomposites

Nano-composites are multiphase compounds where at least one phase is of the nm order.[28] Usually, one phase acts as a solvent matrix where a repetitive structure with one or more phases is embedded. Polymers, ceramics and metals can be found among the most used matrix elements. As summarized by Ahmad *et al.*,[20] there are three main methods to synthesis TMCs nano-composites.

The first method is a one-pot solvothermal method. In this method, the precursors are kept under magnetic stirring for a certain time to, later on, be kept into an oven for 24 hours. This method has been satisfactory used to synthetize a $Ni/Ni_3C/Ni_3N$ nano-composite.[29] The final products are spherical Ni nanoparticles surrounded by Ni_3C and Ni_3N. This method allows a controlled growth of Ni_3C and Ni_3N phases which has been an important challenge due to its metastable nature.

The second method is based on an electrospinning technique that allow to materialize thin nano-composite fibers.[20] Initially, precursors are kept under stirring into a strong electric field. Then, the sample is heated under air atmosphere and a nitrogen rich atmosphere. This technique has been used to generate MoC nanoparticles embedded

on carbon nanofibers, which are aimed to be used as anodes in Li-ion batteries due to its high stability and performance.[30]

The third method is based on a simple stirring.[20] This method has been used to obtain $AgTi_3C_2T_x$ from MAX phases. After etching the MAX phase with acid, the suspension is acclimatised by a de-ionizing process and then, a $AgNO_3$ solution is added under stirring.

1.3.4 Synthesis of TMC nano-particles

TMC nanoparticles have been extensively used due to their catalytic properties, proof of it is the large list of methods developed to synthetize them. Ahmad *et al.*[20] describe nine different methods, some of them with up to four variations in the synthesis procedure. In order to do not overly extend their description, only some synthesis strictly specific of a TMC have been summarized, leaving apart synthesis variations, for which we refer to the existing literature.[20]

The first method and its variations are based on the carbothermal method. It is a simple metal carburization where a carbon source is injected into the metal sample at high temperatures (over 1473 K). If the carbon source is a gas, it could be done at lower temperatures, around 1023 K, and the products are the TMC and H_2 reduced from the CH_x species. This method is the exact replica of the first method described by Oyama *et al.*, discussed in section 1.3.1. Nevertheless, in order to obtain nanoparticles, the metal is pre-treated with a mechanical polishing to obtain the desired nanoparticle size.[31] Method variations imply the obtention of metal plates and metal wires.

The second method is based on solid-state reactions. This involves a compilation of low temperature reactions that represent a greener alternative to the carburization methods. The usage of different salts plus a profound mill of the metal source allows obtaining TMCs at much lower temperatures (873–1073 K).[32,33] The third method is a liquid-phase method, that allows producing Ni_3C nanoparticles from Ni oleate, oleylamine and oleic acid. The mix is heated for 5 to 8 hours at around 523 K. Nanoparticles produced have a size around 18 nm.[34]

The fourth method implies the use of the sol-gel technique, where a solid is produced from a solution containing a TM salt that is passed through a gel acting as an

intermediate and source of C or N. Depending on the synthesis conditions, the gel can modulate the nanoparticles size. There are different variations that modify the synthesis route. The gel can be a biopolymer,[35] hydroxyl propyl cellulose (HPC),[36] or other macromolecules. This method is highly appraised as it allows to easily tune nanoparticle size, morphology and porosity and, moreover, it requires low temperatures.

The fifth method is based on the metal deposition onto a reactive multilayer of ethylene, using a technique called: Reactive layer assisted deposition (RLAD). The ethylene is initially physisorbed on an inert metal surface at low temperatures (<100 K). Then, TM atoms are deposited on the ethylene/Au surface and a temperature annealing is programmed. Upon increasing the temperature, the TM atoms react with ethylene to form TMC nanoparticles. Depending on the temperature annealing, it is possible to tune the nanoparticles Mo/C ratio. The final nanoparticles present a uniform size around 1.5 nm and amorphous structure. This method is the one used by the experimental group and provided the experimental information to the chapters in this work related to MoC_y nanoparticles.[37]

The sixth and last commented synthetic procedure is the laser ablation method. In this case, a sample of TM is submerged into an organic solvent and then, a laser pulse at high frequency is applied. The laser ablaze the metal liberating high temperature fragments into the solvent, which acts as C source. It is known that the solvent has a crucial impact on the composition and structure of nanoparticles.[38] This technique is a low-cost alternative that does not produce toxic waste and, can produce magnetic nanoparticles.[38]

Other techniques used to produce TMCs nanoparticles that have not been covered on this work are: the solvothermal technique, already explained in section 1.3.3,[39] the thermal reduction technique,[40] and the direct element combination technique.[41] These techniques are either not popular or they have been used in one TM only. As a summary, several methods to produce TMCs nanoparticles have been documented, where some present advantages over the others. The solid-state reaction technique is a greener approach than the conventional carburization and, the sol-gel technique allows to tune several aspects of the nanoparticles. All in all, the interest to obtain TMC nanoparticles is clear from the rather large number of techniques developed to this end.

1.4 Catalysis by TMCs

Since Levy and Boudart[2] disclosed that some TMCs were able to mimic platinum catalytic properties, these non-noble metal containing materials have gained great attention. Accounting on the scarcity of the typical noble metal catalysts, that typically translates into a higher cost, it is not surprising that a less expensive alternative could bring such awareness of TMCs catalytic performance although this is still far from competing with that of the noble metals. Nevertheless, in the past years, some catalytic applications have been found, mainly on hydrogenation reactions,[2] such as ammonia decomposition,[42] isomerization,[43] hydroprocessing,[44] and hydrazine decomposition.[45] Among these, there are other more recent applications that will be extensively covered on this section.

1.4.1 Catalytic conversion of biomass by TMCs

The upgrading of biomass chemicals to fine chemicals has been an important aspect of TMCs catalysis.[46] The major biomass components are hemicellulose and cellulose, that represent around 70% of plant cell. Cellulose is composed by a homogeneous polymer of cellobiose fused by glycosidic bonds.[47] In contrast, hemicellulose is a mix of heterogeneous polymers of pentoses, hexoses, and some sugar acids.[48] Cellulose conversion products are exceedingly dependent on reaction conditions and catalyst. This requires noble metals as catalysts and high temperatures to obtain more stable products with efficiency ranging from 5 to 30%,[46] which is far from being ideal. In contrast, Ji *et al.*,[49] developed a prominent Ni-W_2C catalyst able to transform cellulose to ethylene glycol with an efficiency of 61%, a true goal exceeding any prediction. The same authors tried with Mo_2C as well, nevertheless, this alternative did not culminate being as profitable as the W_2C catalyst. The high activity shown by the W_2C based catalyst has motivated its use in the catalysis of sugars, hemicellulose and other carbohydrates.[46]

The second most important biomass compound is lignin, a three-dimensional structure which purpose is to fill gaps between cellulose and hemicellulose.[46] Accounting on the results obtained on cellulose conversion by the W_2C catalyst and observing some lignin residual conversion on a previous work, Li *et al.*[50] studied the lignin conversion under the influence of the W_2C catalyst. Results showed that W_2C presents a high yield to split β-β bonds, which dominate the lignin structure, allowing its conversion to liquid

oils. Moreover, W_2C catalyst does not have the entire monopoly of lignin conversion, as demonstrated by Li *et al.*,[51] molybdenum carbide has shown interesting capabilities towards lignin conversion as well. All in all, both TMCs have shown promising capabilities on biomass catalysis and a recurrent effort is underway to improve their efficiency.

1.4.2 Electrochemical catalysis by TMCs

There exist two main applications for TMCs in the electrochemical field, as anode on fuel cells and electrocatalyst in hydrogen evolution reaction (HER). The search of a portable and high energy density fuel cell seems to have found a new promising alternative to the hydrogen fuel cells. The direct alcohol fuel cells (DAFCs) have revolutionized this field by displaying larger operational times, higher volumetric energy density and, much easier handling than other state-of-the-art fuel cells, like the already commented hydrogen fuel cell.[52,53] DAFCs use an alcohol (methanol, ethanol, glycerol…) in an acidic medium to generate carbon dioxide, water and energy. The main challenge in producing a DAFCs system is to determine the anode oxidation catalyst. The electrocatalyst anode has to fulfil at least two requirements: It must have a high activity for the electrooxidation of the fuel and high stability in aqueous environments at anodic potentials. Some electrocatalysts exists that largely fulfil these requirements, like Pt or Ru, nevertheless, these catalysts are expensive and can be poisoned by CO.[54] In contrast, some TMCs have shown their possibilities as alternative DAFC anode electrocatalysts. Particularly, WC appears to be the most successful replacement endorsed by several studies.[55-60]

In the HER a similar situation is observed. While Pt is considered the best option, its scarcity prohibits its use at a worldwide scale in the several applications where it could participate, *e.g.*, as electrolyser in fuel cell vehicles.[61] On the other hand, some studies have concluded that monolayers of Pt supported on TMCs could overcome this problem by using much less Pt while maintaining a similar performance.[56,62]

1.4.3 Water-gas shift catalysed by TMCs

It is well known that most commercial and industrial H_2 comes from hydrocarbons, representing up to 95% of the globally produced H_2.[63] The main inconvenient of obtaining

H_2 from hydrocarbons is that the final stream can contain up to 10% carbon oxide (CO),[64] and as commented above, it severely poisons the state-of-the-art electrodes on H_2 production, the Pt electrodes.[54] Consequently, the water-gas shift reaction (WGS), $CO+H_2O \rightarrow H_2+CO_2$, has acquired great attention as a must step to increase the reliability of the H_2 production procedure from hydrocarbons. Catalysts currently being used are based on mixtures of Fe-Cr and Zn-Al-Cu oxides,[65,66] nevertheless, these catalysts are pyrophoric and require complex activation steps before its use, withdrawing efficiency to the process.

Some alternatives have been studied to substitute the classical catalysts for ones that can undergo the WGS reaction. The most appealing alternative is the usage of metal nanoparticles (Pt, Au, Cu) supported on oxides (Ce_2O, Ti_2O and ZnO).[67-70] The mixture appears to be decisive to obtain high yields, being the appropriate balance when there is a 1-10% metal weight ratio.[71,72] However, even these prominent catalysts have some drawbacks. CO poisoning is not solved and appear after some usage time,[73,74] plus the elevated price of noble metals does not encourage their use.

At the end, one need compounds able to catalyse the WGS reaction, not poisoned by CO and, relatively cheaper. TMCs fulfil some of the requirements. As it has been already commented, TMCs present similar catalytic activity as to noble metals,[2,46,55-57] and they are undoubtably less expensive than noble metals. It is important to note, that even if TMCs are not poisoned by neither CO or S,[75,76] some oxycarbide species can be formed under catalysis conditions[77-81] and, on the long term, affect the TMCs performance. Nevertheless, theoretical studies have explored the catalytic activity of $Mo_2C(001)$ surface.[81,82] The results showed a complex redox mechanism, clearly different from the associative mechanism occurred on Cu surface. The catalytic activity appears to be much lower than that of the noble metal catalysts due to strong binding of O adatoms to C and Mo surface atoms.[81] At most, a C terminated $Mo_2C(001)$ surface covered by O atoms displayed a similar catalytic activity to that of noble metals. However, it appears that C removal after some cycles will deplete the high activity.

Yet another possibility could come from TiC, Viñes *et al.*,[83] theoretically studied the catalytic activity of the TiC(001) surface towards the WGS reaction. Results showed a relevant activity mainly driven by the carboxyl route that disables the formation of atomic O in the surface, hence, preventing the catalyst deactivation. Furthermore, two nanoparticle models were studied as well, although, their performance is clearly

discouraging. This large difference between the reactivity of the extended TiC(001) surface and that of the nanoparticle models is justified due to a different reaction mechanism, which is the same observed for Mo_2C surface. The redox path generates O adatoms than turn out to deactivate the catalysts. These authors concluded that the different mechanisms selectivity is promoted by the interaction of the adsorbed species with the catalyst. A too strong interaction, as encountered on the nanoparticles, enables the non-desired redox mechanism. Finally, they suggested the use of group 5 TMs as their resistance to O poisoning has been predicted.[84-86]

To conclude, TMCs remain prominent candidates for the WGS reaction and every day, new studies are published showing more and more optimistic results to finally apply these materials.

Chapter 2

Motivation and outline of the thesis

The incessant increase of methane (CH_4) and carbon dioxide (CO_2) concentration in the atmosphere is clearly threatening the future of mankind and many other Life forms.[87,88] The currently adopted measures to reduce these greenhouse gases concentration, mainly by reducing the usage of fossil fuels, are not enough to stop the already critical global warming progression. Every year, more and more evidences of exceedingly severe natural disasters are being reported, which not only are increasing in frequency, but their severity is hardly comparable to that of previous events.[89,90] Besides the commented measures, other strategies are being considered to rapidly reduce these two components from the atmosphere. One of these strategies is based on using compounds able to capture and transform CH_4 and CO_2 into more valuable compounds respectful with the environment. In this sense, the traditional reported catalysts for these gases are scarce and, in consequence, expensive. Nevertheless, in the recent years, TMCs have been proposed as plausible alternative catalysts for such reactions. Precisely, the present thesis focuses on the computational study of TMCs, specifically on MoC systems at nanoscopic scale, where the nanostructure ensemble effect to the catalytic capabilities of this TMC remains mostly unexplored. The novelty of the present subject invites to collaboratively tackle the disposed experimental results in order to bring some insights at the microscopic level. Therefore, the present thesis aims on unveiling valuable insights on the main mechanisms responsible for CH_4 and CO_2 capture and transformation by means of MoC NP catalysts. The theoretical studies have been focused on the main mechanisms responsible of the first scission for both molecules, which are considered bottleneck steps in their transformation. Moreover, in the CO_2 project, the theoretical part was not restricted to the study of its first scission. The experiments for the CO_2 project included the presence of hydrogen within the reaction environment, which turn out to be crucial to activate CO_2 in a stable manner. Thus, the hydrogen effect on the CO_2 activation was included on the theoretical part, where the obtained results revealed an unexpected Eley-Rideal reaction mechanism preference for the CO_2 activation. Overall, both experimental and theoretical evidences must be brought together in order to encourage further studies on the applicability of nanostructured TMCs at industrial levels.

Additionally, other related topics have been studied in the present Thesis, as the theoretical study of ethylene interaction with MoC NPs, the experimental and theoretical study of the hydrogen adsorption and scission on MoC NPs, and the theoretical study of TM carbides and nitrides surface reconstruction. In the case of ethylene interaction with

MoC NPs, the theoretical study aimed to encourage further experiments to validate the reported trends and determine whether MoC NPs are suitable olefin hydrogenation catalysts. The main study focused on the description of ethylene and MoC NPs interaction relying on several chemical descriptors. The subsequent results analysis unveiled the most critical NP parameters, such as NP size and stoichiometry, that could be tuned to enhance the catalytic capabilities of MoC NP for olefin hydrogenation reactions.

For the hydrogen adsorption and scission on MoC NPs study, the experimental and theoretical results were of great interest to explore further hydrogenation reactions, as in the case of CO_2 hydrogenation. The theoretical results revealed the presence of a particular hydrogen conformation named Kubas, which will be further described in Chapter 6. The Kubas conformation appeared crucial to understand the obtained experimental results in this project. Moreover, the same study revealed the main features affecting the outstanding capability of MoC NPs to capture H, which can be summarized as a feasible H adatom diffusion, lower scission energy barriers for H_2 and, as commented, the Kubas conformation.

Finally, the unexpected discovery of some TM carbides and nitrides surfaces reconstruction triggered a subsequent theoretical study aiming to determine the main driven force responsible for such phenomenon. Accounting on the obtained results and their subsequent analysis, it was suggested that the main driven force was the relative bulk instability of the present polymorphs with respect to the most stable one at standard conditions. Interestingly, the reconstruction phenomenon was revealed when studying methane adsorption on δ-MoC surface, where the mere interaction of methane with the surface was able to trigger a reconstruction of the latter.

Overall, this Thesis converges different studies aiming to inspire and motivate the use of TMC NPs as plausible catalysts for greenhouse gases transformation reactions. Some exceptions out of the scope proposed in last statement are included, nevertheless, their importance is clearly assessed throughout this work and their message is clearly bonded to the main purpose of this Thesis.

The experimental side has been carried out by Prof. J. A. Rodriguez at the Brookhaven National Laboratory, Upon, Nova York, USA. On the other hand, the computational side has been carried out in the Computational Material Science Laboratory (CSML) within the *Institut de Química Teòrica i Computacional* (IQTC) at

the *Universitat de Barcelona* (UB). Under the lead of Prof. Dr. Francesc Illas and Prof. Francesc Viñes which have a long baggage in the heterogeneous catalysis field as well as in the simulation of the aforementioned TMCs. Moreover, the main group has had the active contribution of several external members as well. Among them, emphasize the useful contribution of Profs. Carlos Jimenez-Orozco and Elisabet Flórez from *Universidad de Medellín*, Colombia.

Chapter 3

Objectives

The main objective of the present Thesis is to assess computational validation to the observed experimental evidences on MoC NPs as outstanding catalyst for greenhouse gases conversion. In a more specific manner, the objectives can be summarized as:

- Revealing the actual features and mechanisms affecting the experimentally observed outstanding capability of MoC NPs supported on Au(111) towards methane activation.
- Disclosing the main mechanisms and features responsible for the H_2 interaction with MoC NPs supported on Au(111).
- Assessing theoretical support to the experimental study on CO_2 interaction with MoC NPs supported on Au(111). The theoretical studies will focus on disclosing the main mechanism responsible for the CO_2 hydrogenation reaction.

Nevertheless, other complementary objectives were set for the present Thesis.

- Determining the existence of reconstruction phenomena on TM carbide and nitride surfaces.
- Unveiling the crucial features affecting MoC NPs catalytic capabilities towards olefin hydrogenation reactions.

Chapter 4

Methodology and models

The goal of this Chapter is to provide a minimal background on the theoretical methods and models used to achieve the proposed objectives. The Vienna *ab initio* simulation package (VASP)[91-93] is the main code used throughout the thesis, and, consequently, some insights on the implementation of the theoretical methods and algorithm used will be briefly discussed.

4.1 Theoretical Methods

4.1.1 The Schrödinger equation

First-principles calculations aim at describing the electronic structure of matter, most often relying on non-relativistic Quantum Mechanics.[94-99] Even though, relativistic effects can be essential to understand some aspect of the electronic nature, particularly when implying heavy elements, for the time being it will suffice to consider a static system driven by a non-relativistic time-independent Schrödinger equation:

$$\hat{H}\,|\Psi(R,r)\rangle = E\,|\Psi(R,r)\rangle \qquad (4.1),$$

where $\Psi(R,r)$ is a well-behaved wavefunction that describes the stationary states of a system of nuclei and electrons with positions described by vectors *R* and *r*, respectively, and $\hat{H}$ states for Hamiltonian operator. For a system composed by multiple atoms and electrons, the Hamiltonian operator can be defined as:

$$\hat{H} = -\sum_{i=1}^{N}\frac{1}{2}\nabla_i^2 - \sum_{A=1}^{M}\frac{1}{2m_A}\nabla_A^2 - \sum_{i=1}^{N}\sum_{A=1}^{M}\frac{Z_A}{r_{iA}} - \sum_{i=1}^{N}\sum_{j>i}^{N}\frac{1}{r_{ij}} - \sum_{A=1}^{M}\sum_{B>A}^{M}\frac{Z_A Z_B}{R_{AB}} \qquad (4.2),$$

where Z_A is the atomic charge of a nucleus *A*, m_A is the ratio between the mass of a nucleus *A* and the mass of an electron (in atomic units), ∇_i^2 is the Laplacian operator acting on the coordinates of the i-th electron, and ∇_A^2 is the Laplacian operator acting on the coordinates of the A-th nucleus. Every term in equation 4.2 corresponds to a different type of energy contribution. The first term is an operator aiming to account for energy contributions corresponding to the kinetic energy of the electrons; the second term is a similar operator but corresponding to the kinetic energy of the nuclei; the third term is an operator that accounts for the Coulomb interaction between nuclei and electrons; the fourth term is an operator accounting for the repulsion interaction between electrons; and the fifth and last operator includes the contribution corresponding to the repulsion interaction between nuclei.

To solve for the eigenvalues (energy levels) and eigenfunctions (wave functions) of the Hamiltonian operator as defined in equation 4.2 is a formidable task and the usual approach is to solve it in a two-step procedure. The reasoning is that nuclei are much heavier than electrons and one could consider that they move much slower than electrons, so that the latter adiabatically follow the nuclear motion. For a certain nuclear configuration, one can imagine all electrons adiabatically moving in the field of nuclei that remain static compared to the time scale in which electrons move around. Regarding the proposed situation, a new Hamiltonian can be defined in which the nuclei kinetic energy term is set to zero as nuclei remain static and, for a given nuclei configuration the repulsion energy term becomes a constant. This approximation is usually known as the Born-Oppenheimer approximation (BOA) and constitutes an important pilar of quantum chemistry and for the derived modern *ab initio* methods.[100] The remaining terms constitute the electronic Hamiltonian (EH), which describes a system of electrons moving on an external field of M point charges with charge Z_A:

$$\widehat{H}_{elec} = -\sum_{i=1}^{N}\frac{1}{2}\nabla_i^2 - \sum_{i=1}^{N}\sum_{A=1}^{M}\frac{Z_A}{r_{iA}} - \sum_{i=1}^{N}\sum_{j>i}^{N}\frac{1}{r_{ij}} \qquad (4.3).$$

By applying the EH to equation 4.1 and solving the Schrödinger equation, one obtains the electronic energy and the electronic wavefunction:

$$\widehat{H}_{elec}\,|\Psi(R,r)_{elec}\rangle = E_{elec}\,|\Psi(R,r)_{elec}\rangle \qquad (4.4).$$

Nevertheless, in order to obtain the total energy of the system with fixed nuclei, it is mandatory to consider the constant nuclear repulsion as well:

$$E_{Tot} = E_{elec} + \sum_{A=1}^{M}\sum_{B>A}^{M}\frac{Z_A Z_B}{R_{AB}} \qquad (4.5).$$

Applying these approximations solves half of the problem and exposes the remaining main difficulty. In fact, one still needs to solve the Schrödinger equation for the nuclear motion. Substituting the solutions of equation 4.4 into 4.1 reveals, not so directly, that the energy in the left hand-side of equation 4.5 is the potential that the nuclei feel in each electronic state, which leads to the concept of potential energy surface (PES), usually limited to the electronic ground state and opens the door to the quantum mechanical description of nuclear motion. Nevertheless, solving equation 4.4, even for the ground state only, is not trivial and several methods have proposed in the past fifty years or so. Most of these methods aim at approaching the exact wavefunction and allow

to systematically increase the accuracy at the cost of severely increasing the computational demand. At the end, any method based on finding an appropriate wavefunction must deal with 3*N* electron spatial coordinates plus *N* spin coordinates as spin must be included to account for the Fermionic nature of electrons and, consequently, to account for the antisymmetry principle. The overall procedure often results in an unfeasible task and more approximations are needed. On the other hand, there are methods that do not rely on a wavefunction defining the system state as a solution of the Schrödinger equation. Methods based on the DFT, allow to approach the ground state energy from the electron density only. Thus, instead of a wavefunction involving a 4*N* coordinate function, one deals with a 3-coordinate problem where at every point of real space corresponds an electron density value. DFT methods play an important role on this thesis and are described in the next section.

4.1.2 Density functional theory

The key quantity in any DFT method is the ground state electron density, $\rho(r)$, instead of the corresponding complex wavefunction. Nevertheless, one must know how to obtain the electron density without relying on the wave function and how to relate these two objects. The second problem is trivial to solve as in a quantum state defined by its wavefunction, the electron density probability is the probability of simultaneously finding each electron *i* between r_i and $r_i + dr_i$, being r_i a position on the real space. Therefore, the electron density probability can be easily derived from a wavefunction that describe a system of *N* electrons, $\Psi(r_1, r_2, r_{3,} \dots r_N)$. This is given simply by the scalar product of the wavefunction, $\Psi(r_1, r_2, r_{3,} \dots r_N)\Psi^*(r_1, r_2, r_{3,} \dots r_N)$. Since the electron density must give the probability of finding any electron *i* on a section of space independently of where all other electrons are, one must integrate the scalar product over all electrons but one:

$$\int \Psi(r_1, r_2, r_{3,} \dots r_N)\, \Psi^*(r_1, r_2, r_{3,} \dots r_N) d\mathrm{r}_2, d\mathrm{r}_3 \dots d\mathrm{r}_N \qquad (4.6),$$

where the integral runs for all the electrons coordinates but one, here electron 1 is considered as reference for convenience. The second aspect implies the indistinguishability of electrons and modifies the probability density as follows:

$$\rho(\mathrm{r}_1) d\mathrm{r}_1 = N d\mathrm{r}_1 \int \Psi(r_2, r_{3,} \dots r_N)\, \Psi^*(r_2, r_{3,} \dots r_N) d\mathrm{r}_2, d\mathrm{r}_3 \dots d\mathrm{r}_N \qquad (4.7).$$

Finally, one obtains the probability density to find any electron in a fraction of space independently of where the other electrons are. When this probability density is summed up for any point in the real space (r), one gets the total number of electrons. The definition of electron density, $\rho(r)$ is as in 4.7.

The first problem above commented is more complex as getting the density from the wavefunction is trivial, the opposite is not that easy. Hohenberg and Kohn (HK) provided on 1964,[101] a way to estimate the energy of the ground state relying on the electron density only. Their approach was given in the form of two theorems. The first one, proved that, for a non-degenerate ground state, the external potential (corresponding to the nuclei-electron interaction) is a functional of the electron density of the system which, as corollary implies that the electron density defines the Hamiltonian and, hence, all the information of the system. While this has some logics, it does not solve the problem as it does not provide a way to solve the Hamiltonian. Nevertheless, it follows that the energy of the ground state must be a functional of the electron density even if the exact form of this functional is unknown. The proof of this theorem is based on *reductio ad absurdum* by showing that is not possible for two different external potentials applied on a system of electrons to produce the same ground state density since they satisfy different Schrödinger equations. Thus, only a unique relation of the form:

$$\rho_0 \leftrightarrow V_{ext} \leftrightarrow \widehat{H} \leftrightarrow \Psi_0 \leftrightarrow \rho_0 \tag{4.8}$$

can exist.

This, in turn, shows that the ground state wavefunction is a unique functional of the electron density and that, as far as one electron properties is concerned, the ground state wavefunction contains the same information as the ground state electron density. Since the ground state density determines the Hamiltonian, it also determines the ground state energy as:

$$E[\rho] = \langle \Psi[n] | \widehat{H} | \Psi[n] \rangle = F_{HK}[\rho] + \int d\mathrm{r} V_{ext}\rho(\mathrm{r}) \tag{4.9},$$

where F_{HK} is the Hohenberg-Kohn functional, and can be described as:

$$F_{HK}[\rho] = T[\rho] + V_{ee}[\rho] \tag{4.10},$$

where $T[\rho]$ is the kinetic energy and, $V_{ee}[\rho]$ is the electron repulsion term. It must be pointed out that the F_{HK} functional is the same for any system with the same number of electrons, consequently, it has been named the universal functional.

The second theorem is crucial to lead to a practical method to estimate the ground state energy. This theorem states the validity of the variational principle applied to the energy functional, $E[\rho]$. Strictly speaking, this theorem establishes that "for any positively defined trial density, ρ_1, such that $\int \rho_1(\mathrm{r})d\mathrm{r} = N$ then:

$$E_0 \leq E[\rho(\mathrm{r})]" \tag{4.11},$$

where E_0 is the exact ground state energy, and $E[\rho(\mathrm{r})]$ is the energy given by the energy functional. It is important to note that $E[\rho(\mathrm{r})]$ will always give an upper bound of the ground state energy whenever the exact ground state density is not used. The proof of this theorem is a consequence of the first one. It is known that the trial density defines a unique Hamiltonian and, therefore, the wavefunction. Thus, it directly follows that the energy associated to the density obeys the variational theorem of the Schrödinger equation.

It is important to point out that the HK theorems provide a link between the ground state energy and the ground state electron density but do not provide any practical approach to determine the energy from the density.

4.1.3 Implementing DFT

The challenge now is to provide a recipe to obtain the ground state energy from the density alone: *i.e.*, to each of the terms in 4.10. One year after the HK theorems were published, Kohn and Sham were able to provide the practical way sought for. They argued that for any real system, there is a fictitious system of non-interacting electrons that has exactly the same density as the real system of interacting electrons which provides a way to estimate the kinetic energy term in 4.10, although this will still differ from that of the real system where the electrons do interact. For the fictious systems, the wave function is trivial as it corresponds to a single Slater determinant build up from one electron orbitals, hereafter referred as Kohn-Sham orbitals (ϕ_i). For the fictious system of non-interacting electrons the kinetic energy is as in 4.12.

$$T_s[\rho] = -\frac{1}{2}\sum_{i}^{N}\langle\phi_i|\nabla^2|\phi_i\rangle \tag{4.12}.$$

Since the contribution from the external potential, $\hat{v}_{ext}$, is as in 4.9 and the average classical Coulomb electron-electron can be estimated as

$$J[\rho] = \frac{1}{2}\int\int \frac{\rho(r_a)\rho(r_b)}{(r_a - r_b)}\, dr_a dr_b \quad (4.13),$$

and it follows that

$$F_{HK}[\rho] = T_s[\rho] + J[\rho] + E_{xc}[\rho] \quad (4.14),$$

where the first term is the non-interacting kinetic energy, the second term is the classical Coulomb repulsion functional and the last term is the exchange-correlation functional including all missing terms, *i.e.*, the fact that electrons are Fermions, the instantaneous electron-electron interactions, and contributions of interacting electrons to the kinetic energy. The $E_{xc}[\rho]$ functional in 4.14 is denoted as the exchange-correlation functional (some authors explicitly call it exchange-correlation-kinetic energy). The Kohn and Sham version of the universal functional ca be also defined as:

$$E_{xc}[\rho] = T[\rho] - T_s[\rho] + V_{ee}[\rho] - J[\rho] \quad (4.15),$$

where $T[\rho]$ and $V_{ee}[\rho]$ are the exact kinetic and electron repulsion energies of the real interacting system, and, $T_s[\rho]$ and $J[\rho]$ are the kinetic energy for the non-interacting system and the classical Coulomb repulsion energy, respectively. It must be pointed that the non-interacting system is used just to estimate $T_s[\rho]$, as it includes electron-electron repulsion. The major issue of DFT methods is that the explicit expression for $E_{xc}[\rho]$ term is unknown, consequently, it is not possible to calculate the exact ground state energy until the $E_{xc}[\rho]$ true form is disclosed.

In order to solve Kohn-Sham equations for an interacting system, it is necessary to rely on a variational self-consistent procedure. The main motive is that whatever functional approach is used, the $E_{xc}[\rho]$ functional ultimately relies on the derivative (variation) of $E_{xc}[\rho]$ with respect to the electron density. Therefore, an initial electron density must be guessed to define the exchange-correlation term. Then the $F_{HK}[\rho]$ is defined and can be used to calculated the set of Kohn-Sham orbitals. This new set of Kohn-Sham orbitals will lead to a new electron density that will redefine the $E_{xc}[\rho]$. This procedure must be repeated until the density reaches an arbitrary convergence criterion. Ultimately, the converged electron density can be used to compute the energy and other features.

It must be pointed out that the eigenvalues related to the self-consistent procedure do not have any physical meaning, although by their similitude it is customary to associate them to the Hartree-Fock orbitals. Note that the Kohn-Sham orbitals define the density of

the non-interaction fictious system but the energy is computed using 4.9 with the $F_{HK}[\rho]$ as in 4.14, *i.e.*, solving a set of one-electron Kohn-Sham equations for the interacting system. At self-consistency one obtains the ground-state energy and the electron density.

Several approaches have been developed aiming to mimic the unknown exchange-correlation functional. They are classified in function of their complexity, understanding complexity as how complete is their perception of the electron density. A visual and clear representation of this classification is the Jacob's ladder,[102,103] represented in Fig. 1, where every rung should be able to reproduce the results of the lower rung in certain limits and add more capabilities.

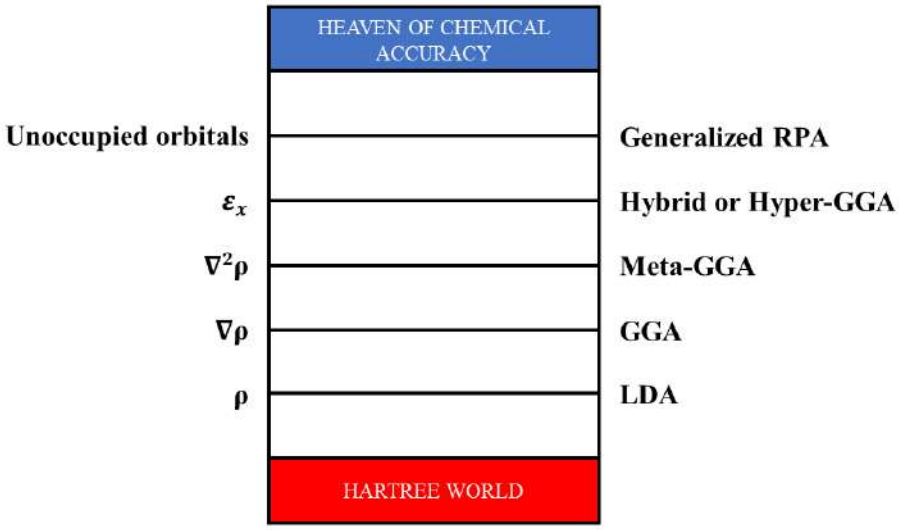

Figure 1. Jacob's ladder of density functional families as described by Perdew *et al.*[103]

At the end, the appropriate functional is extremely dependent on the tested problem, because the increase in accuracy held by higher rungs comes at a computational cost, usually as restrictive limitations about where the functional can be applied. Nevertheless, the computational cost is not always the main decisive feature. Several studies have been reported demonstrating that lower functional rungs imply more accurate results than higher functional rungs when limited to the calculation of some specific features.[104-107] Thus, confirming that the appropriate functional uses to depend on the system to be studied and, in some cases, in the specific property of interest. In the next section, the functional used and its group will be introduced.

4.1.4 Local and generalized gradient approximation

The local density approximation (LDA) constitutes the first implementation of DFT (beyond primitive related models as the Thomas-Fermi or the Slater SCF- xα) and follows from the work of Ceperley and Alder and Vosko-Wilk-Nussair, [108,109] who independently provided a functional form for the exchange-correlation functional for the uniform, homogeneous, density electron gas. This approach makes use of the density at each point of space and provides good molecular and crystal structures but poor thermochemistry.[110]

The generalized gradient approximation (GGA) functionals are a variety of mathematical expressions that use the density and its gradients in each point. These functionals are more accurate than the LDA functionals but at the cost of computing the density gradients. Their improvement is clearly observed when computing bond dissociation energies and transition-state energy barriers.[111] The main issue compared to LDA is that, while LDA has a universal form, GGA functionals have different forms to account the exchange and correlation contributions and, therefore, several forms exist for the GGA functionals. One of the most used GGA functionals is the PBE, called after the work of Perdew, Burke, and Ernzerhof.[112]

The general form of all GGA functionals is:

$$E_{xc}^{GGA}[\rho] = \int dr\ e_x^{HEG}(\rho(r))F_{xc}(\rho(r), \nabla\rho(r)) \qquad (4.16),$$

where e_x^{HEG} is the exchange contribution computed in a homogeneous electron gas (HEG) model, which can be calculated analytically as:

$$e_x^{HEG} = -\frac{3}{4}\left(\frac{3}{2\pi}\right)^{2/3}\frac{1}{r_s} \qquad (4.17),$$

where r_s is the Wigner-Seitz radius:

$$r_s = \left(\frac{3}{4\pi\rho}\right)^{1/3} \qquad (4.18).$$

The e_x^{HEG} term in equation 4.16 can be written as well as e_x^{LDA}, because it is how the LDA functional accounts the exchange contribution. The remanent term of equation 4.16, F_{xc}, is known as the enhancement factor because it takes into account deviations from the HEG model. The most popular enhancement factor is the PBE, which is the only GGA functional used along this work. The exchange part of PBE can be described as:

$$F_x^{PBE}(s) = 1 + k - \frac{k}{1 + \mu s^2/k} \quad (4.19),$$

where k and μ are parameters optimized to fulfil the Lieb-Oxford bound[113] and LDA linear response conditions, that the exact functional must fulfil and the s parameter is a dimensionless density gradient. Moreover, the correlation part can be described as:

$$F_c^{PBE}(r_s, \zeta, p) = e_c^{HEG}(r_s, \zeta) + H(r_s, \zeta, p) \quad (4.20),$$

where $e_c^{HEG}(r_s, \zeta)$ is the HEG correlation term, which depends on the Wigtner-Seitz radius (r_s) and the relative spin polarization (ζ). The $H(r_s, \zeta, p)$ term has the form:

$$H(r_s, \zeta, p) = g^3 \frac{\beta^2}{\alpha} ln\left[1 + \frac{p^2 + Ap^4}{1 + Ap^2 + A^2p^4}\right] \quad (4.21),$$

where g is a spin-scaling factor, β and α are constants, p is a dimensionless density and A is a complex term described as:

$$A = \frac{2\alpha}{\left(\beta exp^{\frac{-2\alpha e_c^{HEG}}{g^2\beta^2}} - 1\right)} \quad (4.22),$$

where all the terms have been already commented except the e_c^{HEG}, that is the correlation energy computed in the HEG model. In summary, when all these terms are taken into account, a simpler notation for the enhancement factor can be written as in 4.23,

$$F_{xc}^{PBE} = F_x^{PBE} + \frac{e_c^{HEG}}{e_x^{HEG}} F_c^{PBE} \quad (4.23),$$

which ultimately defines PBE. Other variants of the PBE functional, such as the PBE adapted for solids (PBE_{sol}) or the revised PBE (RPBE), have been developed aiming to overcome some intrinsic vulnerabilities of PBE, or VV and VVsol, adjusted for a better description of transition metals.[114] Still, PBE is a very robust functional performing especially well to describe the properties of bulk and surface transition metals[104,114] and broadly used in the computational heterogeneous catalysis field.[115] Note, however, that the description of bulk Fe, Co and Ni, and the corresponding NPs and extended surfaces requires taking spin polarization into account. With respect to the bulk of early transition metal carbides, the validity of GGA functionals to describe their main features has been stablished by Viñes *et al.*[19] Moreover, these materials exhibit a metallic behaviour with no evidence of magnetic moments, as reported in the landmark review published by Hwu and Chen[77] in 2005. Consequently, spin polarization does not need to be considered.

4.1.5 Basis sets

Before any definition of the main protagonists of this section, it is necessary to present some essential concepts that will appear useful to the reader. The one electron states (orbitals) entering into the Kohn-Sham determinant are usually represented as linear combinations of basis functions on the three-dimensional (3D) space as in the method proposed by Roothaan to numerically solve the Hartree-Fock equations. [116] There are different types of basis functions, although, the two most used options are the gaussian type orbitals (GTO) and the plane wave (PW) functions. The former is typically used in molecular calculations and there is at least one periodic code based on this approach.[117] In this basis, orbitals are represented by linear combinations of nuclei-centred gaussian functions carefully parametrized to reproduce atomic orbitals and nowadays available through the basis set exchange platform.[118] In short, GTOs provide a computationally convenient representation of orbitals and reduce the variational problem of finding the density minimizing the energy for the functional of choice, to a numerical problem. This just follows the approach brilliantly developed by Roothaan commented above, which originated modern quantum chemistry and also the methods of solid-state physics.

Alternatively, PWs are the main choice when dealing with periodic systems precisely because they are periodic in nature with concomitant numerical advantages, for instance the matrix representation of the kinetic energy in a PW basis set is diagonal. These basis functions are the main basis sets implemented in VASP, consequently, they are used in all calculations reported in the present work. Contrarily to GTOs, PWs are not nuclei-centred and a massive linear combination of PWs is required to mimic the accuracy obtained with fewer GTOs. In fact, this is probably the main drawback of PWs, but it is compensated by the advantages in applying it to periodic systems. The amount of PWs needed to obtain accurate results is sometimes prohibitive, specifically, on describing core electrons where dramatic oscillations of the wave function are required. Here is where pseudopotentials appear as an alternative to represent core electrons.

4.1.6 Pseudopotentials and the projector augmented wave method

The use of pseudopotentials (PP) is based on the assumption that most chemical processes are dominated by valence electrons, while core electrons remain almost unaffected to the environment changes. Therefore, a precise representation of core electrons can be

substituted by an effective core potential, while valence electrons remain as originally intended. This approximation is what is explicitly called a pseudopotential and are extensively used in VASP. The exact treatment is based on substituting the exact Hamiltonian by an effective Hamiltonian that contains a pseudopotential operator and which pseudo-eigenfunctions mimic, as close as possible, those of the exact Hamiltonian.[119] This general definition can be applied to any electron section within an atom, but for obvious interest, it will be restricted to core electrons. Thus, the mathematical definition of a pseudo-Hamiltonian for valence electrons is:

$$H_v = -\frac{1}{2}\sum_{i}^{n_v}\nabla_i^2 + \sum_{i<j}^{n_v}\frac{1}{r_{ij}} + \sum_{i}^{n_v}\sum_{a}^{n_c}\left[V_{PP}^{a}(r_{ai}) - \frac{Q_a}{r_{ia}}\right] + \sum_{a<b}^{n_c}\frac{Q_a Q_b}{r_{ab}} \qquad (4.24),$$

where n_v is the number of valence electrons, n_c is the number of core electrons, a, b indices account on all nuclei in the system, Q_a, Q_b are the core charges, *i.e.*, the sum of core electrons and, V_{PP}^{a} is the one-electron pseudopotential operator. There are several ways to approximate V_{pp}, but when dealing with GTO basis sets these are reduced to the so-called effective core potentials developed by Hay *et al.*[120,121] and the *ab initio* model potential developed by the Huzinaga group.[122]

PP approximation becomes unavoidable when aiming at describing periodic systems with a PWs basis set. Different types of pseudopotentials have been proposed with the ultrasoft family having been broadly used. This choice greatly contributes to minimize the computational cost by reducing the number of PWs needed. Nevertheless, it is important to take care when dealing with systems with core-valence correlation, core-overlap and, complex nodal structures effects because their use could be compromised.[119] PP main drawback can be summarised to the loss of information on the wave function close to the nuclei.

The earlier periodic codes using PWs basis sets used the so-called augmented-plane-wave (APW) method, where the real space is divided into atom-centred spheres. These spheres are filled with wave functions considered as atom-like partial waves that are restricted within the sphere region. Outside the sphere, there is a bonding region where envelope functions are defined. On the interfaces, partial waves and envelope functions are connected. Nevertheless, this approach was far from being user friendly and, consequently, its use was quite limited.

Finally, there is a method that combines the pseudopotential approximation and the APW approximation. This is the projector augmented wave (PAW) method initially proposed by Blöch in 1994.[123] This method transforms the rapidly oscillatory real wave function into a smooth wave function by applying a linear transformation. This linear transformation is only applied in a certain region close to the atomic core because the real wave function already presents a smooth character at a certain distance from the core. The region where the linear transformation occurs is defined as the augmentation region. It is important to carefully define this region to avoid overlap between augmentation spheres of different atoms. The true (one electron) wave functions inside the augmentation region are expanded into partial waves and transformed into smooth partial waves by applying the linear transformation. When the smooth partial waves form a complete set inside the augmentation region, it is possible to expand the complete smooth wave function into a sum of smooth partial waves multiplied by expansion coefficients. These expansion coefficients are the same that could be applied to the non-smooth partial functions to generate the real wave function. As the transformation must be linear, it has to be imposed to the expansion coefficients to be linear functionals. These linear functionals are defined as smooth projector functions and must fulfil some requirements that will not be further discussed in the present work. At the end, the linear transformation can be defined as:

$$\hat{T} = 1 + \sum_a \hat{T}^a = 1 + \sum_a \sum_i \left(|\phi_i^a\rangle - |\tilde{\phi}_i^a\rangle \right) \langle \tilde{p}_i^a | \qquad (4.25),$$

where a is the atom index, i is the expansion index, ϕ_i^a is a non-smooth partial function, $|\tilde{\phi}_i^a\rangle$ is a smooth partial function and, $\langle \tilde{p}_i^a|$ is the projector function. As a summary, the linear transformation can be understood as a decomposition of the original KS wave functions into two contributions: The total smooth wave function and, the subtraction of partial wave functions (smooth and non-smooth) projected to the total smooth wave function. The first contribution is smooth in all space while the second contribution has some rapid and small oscillations due to the contribution of the non-smooth partial wave functions. The final wave function of the system is much smoother than the original KS wave function and turns out to critically decrease the number of plane waves needed.

Finally, it is worth to point out that in conjunction with PAW approximation, it is usual to find the frozen core (FC) approximation. In this condition, core electrons remain represented by the real KS wave functions within the augmentation region, but remain

unaltered by the environment changes. This approximation is the default option implemented in VASP.

4.1.7 Reciprocal space and the Bloch theorem

The reciprocal lattice or momentum space is an essential mathematical construction that ease the obtention of information for periodic systems. Any crystalline lattice in a 3D space characterized by three lattice vectors (a_1, a_2, and a_3) has its own reciprocal lattice (b_1, b_2, and b_3), defined as:

$$b_i = 2\pi \frac{a_j \times a_k}{a_i \cdot (a_j \times a_k)} \qquad (4.26),$$

where *i, j,* and *k* are the indeces of the three main lattice vectors. The unit cell defined by (b_1, b_2, and b_3) has a volume equal to $(2\pi)^3/V$, where V is the volume of the direct unit cell. Hence, a large unit cell in real space, ends up being a smaller unit cell in the reciprocal lattice. The a_1, a_2, and a_3 vectors provide a basis for the 3D space so that any point in this space (here denoted as real space) can be described by an appropriate linear combination of these three vectors. The b_1, b_2, and b_3 vectors defining the reciprocal lattice do also define a 3D space, this is usually denoted as the reciprocal space.

Once the unit cell is defined, let us determine the meaning of any point on the reciprocal lattice. Let us imagine a plane within the real space unit cell, this plane can be characterized by its Miller indexes and it corresponds to an infinite family of planes with the same interplanar distance, d_{hkl}. The d_{hkl} can be calculated from the unit cell parameters, *i.e.*, vectors moduli and angles from the unit cell. Nevertheless, the Millers indexes are the main key parameter to understand the functionality of a point within the reciprocal lattice. From the Miller indexes, it is possible to form a vector, which moduli is reciprocal (inversely proportional) to d_{hkl} and defines a point in a 3D space. Now, including all Miller indexes that could be obtained from a crystalline structure, it is possible to form a periodic lattice that remain reciprocal to the original lattice, known as the reciprocal lattice. In other words, any point on the reciprocal lattice represents a family of planes with Miller indexes in the real space. This property explains the diffraction pattern obtained from crystalline structures. In general, the use of the reciprocal lattice in periodic systems can ease the obtention of some properties. Most calculations implying the reciprocal lattice

are restricted to the first Brillouin zone, that can be defined as the Wigner-Seitz cell of the reciprocal lattice.

Understanding the reciprocal lattice permits introducing the Bloch theorem.[124] This theorem states that any observable that can be obtained from a certain point of a crystalline lattice, will be the same in an infinite number of points due to the translational nature of a crystalline structure. Therefore, it is possible to describe a periodic potential which remains unaltered after a certain translational operation. In this sense, the periodic potential must retain the Bravais lattice periodicity,

$$U(r+\tau) = U(r) \qquad (4.27),$$

where U is the potential and τ is a translational vector. Accounting on the potential periodicity, Bloch stated, that any one-electron wavefunction must be expressed as the product of two functions:

$$\phi_{i,k}(r) = e^{ikr} u_i(r) \qquad (4.28),$$

where u_i is a local function and e^{ikr} is a plane wave and *k* is a vector of the reciprocal space. The local function must satisfy the periodicity of the Bravais lattice. When the basis set used is a plane wave, then the inner shape of the electronic Bravais cell is already assembled into the plane wave, hence, the local function term is reduced to 1 and the wave function can be written as:

$$\phi_{i,k}(r) = \sum_F C_{i,k+F} e^{i(k+F)r} \qquad (4.29),$$

where *F* is a vector in the reciprocal lattice that must satisfy that its scalar product with a unit cell vector of the Bravais lattice (a_i) has to be equal to a constant of the form $2\pi m$, where *m* is an integer number. On the other hand, when the basis set used is based on Gaussian functions, the u_i function form will be that of a Gaussian function.

Finally, the one-electron wave function describing an electron moving through a periodic potential has the form:

$$\phi_{i,k}(r+\tau) = e^{ik\tau} \Psi_i(r) \qquad (4.30),$$

where its energy just depends on the *k* points considered. The total energy of the periodic system is calculated as an average of different *k*-points within the first Brillouin zone. The number of *k* points considered must be enough to ensure a representative average result.

4.1.8 Reaction energy profiles: The nudged elastic band method

The ultimate goal in any theoretical study of a catalytic process is to characterise the molecular mechanism of the reaction of interest. By this one expects to obtain some features that precisely explain how reactants could become products. Usually, this process requires three major steps. First, it necessary to characterise minima within the potential energy surface (PES) for both adsorbed species, reactants and products, to determine the initial and final states. Several different minima can be encountered in both cases; however, it is a natural praxis to consider the most stable ones as, if there are no other effects involved, they will be the most probable to be populated. From this step, one can obtain the reaction energy which is simply defined as in 4.31. This is the energy difference between the initial state and the final state, and can be computed as:

$$E_{reac} = E_{cat+prod} - E_{cat+react} + \Delta ZPE \qquad (4.31),$$

where $E_{cat+prod}$ is the total energy of a system composed by the catalyst and the products, $E_{cat+react}$ is the total energy of a system composed by the catalyst and the reactants and, ΔZPE is the difference in zero-point energy between reactants and products. E_{reac} gives information about the exothermicity of a reaction.

The second step consists on typifying the interaction of reactants and products gas species with the catalyst. This step is typically characterised by the adsorption energy, which can be defined as:

$$E_{ads} = E_{cat+reac} - E_{cat} - E_{reac.gas} + \Delta ZPE \qquad (4.32),$$

where $E_{cat+reac}$ is the total energy of the system composed by the catalyst plus the reactant or product, E_{cat} is the total energy of the system without the reactant or product, $E_{reac.gas}$ is the total energy of the reactant or product in gas phase and, ΔZPE is the difference in zero-point energy contribution for the gas and adsorbed species. E_{ads} concept is intensely bonded to the ordering of minimums as it is a conceptually easy method to propose absolute values for the adsorbate-catalyst interaction.

Finally, the third step consists on the characterisation of the Transition State (TS), *i.e.*, the structure of maximum energy along the minimum energy reaction pathway.[125] There are different approaches to find a TS structure, nevertheless, the main method used in this work is the Nudged Elastic Band method (NEB).[126]

The NEB method is based on a combined optimization of intermediate images along a proposed reaction path. For each image a normal optimization is carried out but this is bonded to the two nearest images by spring forces that constraint its movement along the reaction path. Hence, one obtains a set of images equally spaced that can be interpreted as if a band or rope was adapting to the PES. This method alone is not enough to determine a TS structure, depending on the number of images, the highest energy image could still be spatially far from the TS structure. In order to find the TS structure, it is necessary to apply a different approach within the NEB method. The Climbing-Image NEB (CI-NEB), implies a small modification to the NEB method, where the highest energy image does not feel the spring forces. Instead, this image feels an opposite force along the tangent, consequently, it maximizes the energy along the band and minimize in all other directions. Once, it converges, the structure will be close to that of the saddle point sought for. Nevertheless, a frequency analysis is always required to find the single imaginary frequency defining a TS.

4.2 Models

This section focuses entirely on the models used to represent the materials of interest as they play a major role on the computational projects carried out in this Thesis. There are three main types of models which, for simplicity, will be discussed separately. The models can be divided into support surfaces, MoC nanoparticles, and MoC/MoN surfaces.

4.2.1 Support surfaces

Most experiments carried out by the experimental group of Jose A. Rodriguez, at the Brookhaven National Laboratory (BNL) used a Au(111) surface as support. In order to provide a realistic model the Au(111) surface is represented by *p*(6×6) slab including 4 atomic layers with 36 atoms each. Following a typical 2+2 scheme (Fig 2.), [127]the two outmost atomic layers are relaxed and the two bottommost are fixed as in the bulk to provide an appropriate bulk environment to the surface region. The slab area of this slab model, corresponding to that of the plane orthogonal to the Z axis, is large enough to ensure that adsorbates, in this case supported NPs, in the periodically repeated unit cells are at least separated by 15 Å and, hence, do not exhibit noticeable interactions.

Of course, the slab surface model has its own limitations, as the bulk/non-bulk transition is clearly quite abrupt. However, this can be minimized by adding more totally relaxed layers that will produce a smoother transition. The (2+2) scheme has been chosen to reach a compromise between accuracy of the model and computational resources. Moreover, this scheme has been proven to be sufficient in several works, justifying its use. [127-131]

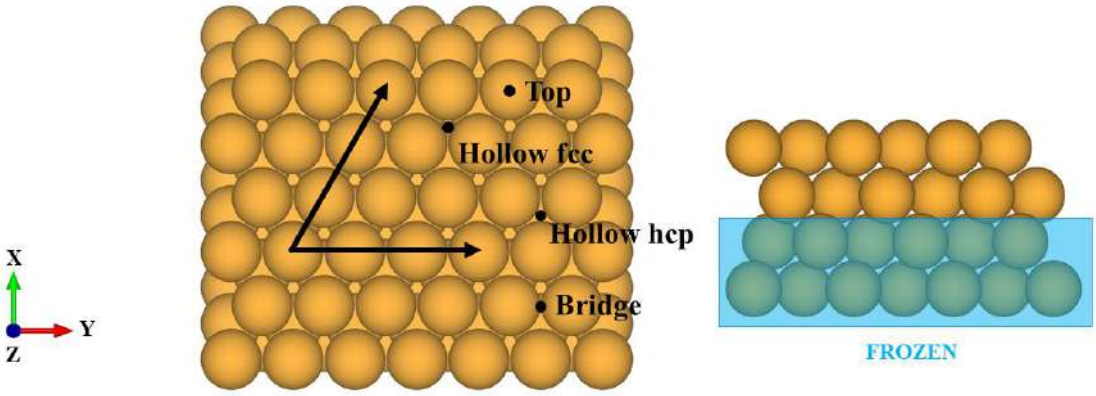

Figure 2. Au (111) slab in two different perspectives. The black arrows represent the lattice vectors. The black points are the different adsorption sites that can be encountered. The blue rectangle shows the frozen layers of a (2+2) scheme.

The Au(111) slab has four high symmetry adsorption sites illustrate in Fig 2 that are typically used when dealing with small adsorbates. These sites have been considered for each NP adsorption and also for some molecule adsorption, where its diffusion to the Au slab appeared plausible. NPs are too large to be placed above a given adsorption site, their rather large size implies simultaneously occupying several adsorption sites. Thus, to ensure a differently adsorption based on the four adsorption sites, it was required to determine a reference position within the NP. The reference position was chosen to be the centre of mass, so the centre of mass of each NP was initially placed above the four-adsorption sites. The adsorption site is not the only parameter to be considered when supporting the NPs. The nanoparticle orientation is relevant as well, and requires a meticulous systematic procedure to ensure that every NP is placed in every possible orientation.

4.2.2 MoC nanoparticles

Undoubtedly MoC_y NPs are the main players in this work, as they constitute the active part of the catalyst in all the studied chemical reactions. From the information provided by the experimental group of Jose Rodriguez, *i.e.*, size, morphology and, stoichiometry of the NPs, a series of models have been developed taking into account the specified parameters as much as possible. Again, a compromise between accuracy of the model and the computational resourced must be invoked. As a summary, the NPs size should be around 0.6-1.5 nm in diameter, they should exhibit an amorphous structure and, the stoichiometry largely depended on the studied case, as it can be easily moulded by the synthesis conditions. The experimental information does not overly restrict the search of appropriated structures, which ultimately difficult the whole process as it adds more variability to the problem. As it will be explained later, this aspect is significantly important on the stoichiometry feature.

The initial stoichiometric structures were obtained from mimicking the most stable gas-phase TiC NPs reported by Oriol *et al.*[132] They obtained the TiC NPs structures combining data from data mining searches, global optimization using interatomic potentials (IP), and geometry optimization by means of DFT of the most prominent candidates. They reported a total of 21 low-energy structures, for $(TiC)_6$ and $(TiC)_{12}$. On the present work, the 21 structures have been used as templates. A simple substitution of Ti by Mo atoms plus a full reoptimization were required to obtain the MoC NP models. It is important to remark that the shape of most MoC models, in special the most stable ones, remain unaltered when compared to their TiC counterparts. This is not shocking when one takes into account that both TiC and δ-MoC polymorph display the same rock-salt crystallographic structure.

Moreover, even if gas-phase MoC_y NPs exhibit magnetization, supporting these NPs on the Au(111) surfaces completely quenches the magnetism. Therefore, spin polarization has not been included for the supported NPs. In addition, one must point out that calculations for supported NPs showed that the spin polarized solution converges to the non-spin polarized one. Moreover, for several surface reactions on nonmagnetic substrates, Fajín *et al.*,[133] showed that the effect of spin polarization is negligible, the two solutions are indistinguishable, even if bond breaking and bond forming occurs. This is at variance of the situation encountered in gas-phase reactions where TS exhibit a strong radical character requiring the use of a multiconfigurational description or including spin

polarization if the reaction is studied by DFT based methods. In the latter case, one must be aware of limitations inherent to the single determinant nature of DFT. To summarize, reactions occurring at surfaces of non-magnetic systems, there is no need to account for spin polarization and most often this is the case in heterogeneous catalysis.

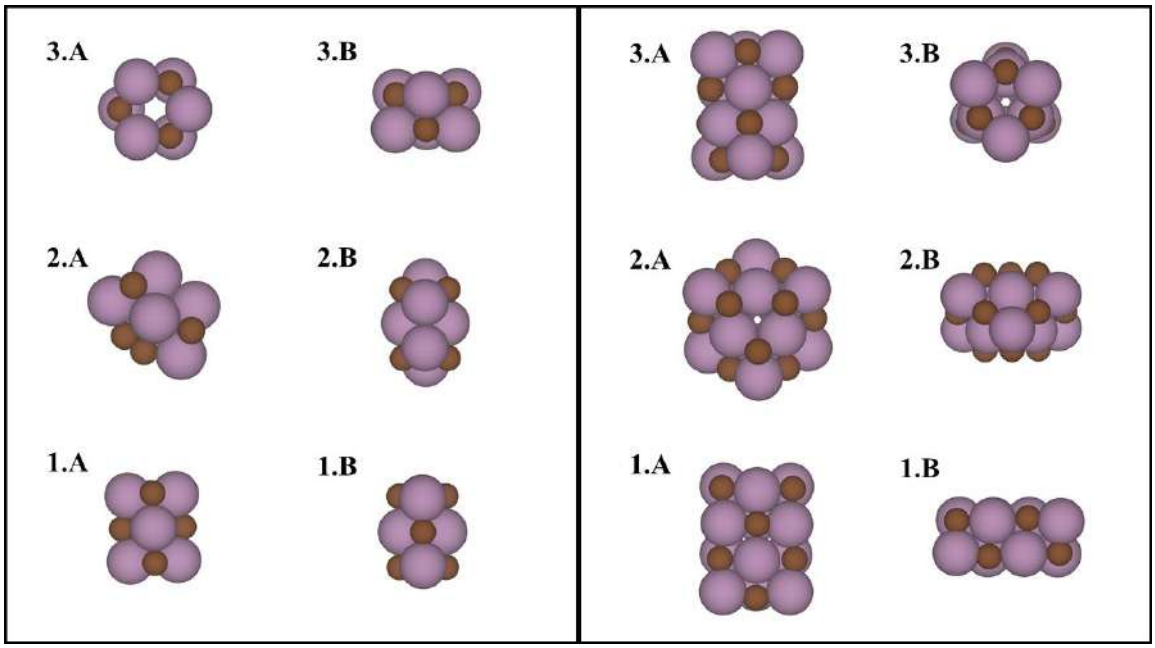

Figure 3. Left side: Three most stable structures of Mo_6C_6 isomers. Right site: Three most stable structures for $Mo_{12}C_{12}$ isomers. The indices {*1,2,3*} recall the stability order, being *1* the most stable and *3* the least stable. *A* and *B* letters denote different view orientation for the same NP.

Generally, only the two most stable structures of each stoichiometry have been considered through the present work, *i.e.*, Fig. 3 indices *1* and *2*. It appeared computationally unfeasible to systematically consider the 21 nanoparticles for each catalytic reaction, therefore, it became compulsory to restrict the number of models to be used. Among the most stable, there is a significant energy difference between the 2nd and 3rd models for each stoichiometry, a feature that has been used a restriction criterium to select the models to be used.

To generate the non-stoichiometric models, two straightforward possibilities exist. One could add atoms or remove them. Of course, other alternatives exist like the search of global minima for every considered stoichiometry, however, due to its complexity and computational cost they have not been considered. The addition option implies far more degrees of freedom as atoms can be placed in several positions within the same addition site. After the optimization, most addition sites will turn up inexistent and the variability will strongly decrease as most added atoms will end up in the same

position. Nevertheless, it is not possible to predict the final addition sites beforehand and, therefore, all possibilities must be computed, greatly increasing the computational cost. On the other hand, removing atoms implies to remove all non-equivalent atoms from the system, which number can be severally decreased when there exists symmetry within the NP. In the absence of other decisive aspects apart from the computational cost, the removing method has been chosen as the main source to obtain non-stoichiometric structures.

In the removing approach, all non-equivalent atoms were removed for the two most stable NPs of each size (Mo_6C_6 and $Mo_{12}C_{12}$), generating different $Mo_{x-1}C_x$ or Mo_xC_{x-1} structures. Afterwards, a full optimization is carried out to obtain the final non-stoichiometric structures. This procedure is repeated in a cascade manner to obtain larger deviations from the 1:1 stoichiometry, *i.e.*, all non-equivalent C atoms from all Mo_xC_{x-1} structures are removed in order to obtain suitable structures for the Mo_xC_{x-2} stoichiometry. As explained in Chapter 9, this procedure scales as $2 \cdot N^z$ per removal, where N is the average number of inequivalent atoms per removal, Z stands for the number of atoms that have been already removed, and the coefficient 2 is necessary as there are two species. Nevertheless, this expression must be considered as an upper bound. The generation of repeated structures from different parents or the appearance of new symmetric shapes that reduce the N value can severely decrease the number of different structures per removal. Nevertheless, it is clear that a fully cascade procedure implying several removals can rapidly became prohibitive. Thus, for large Z values only the most stable Z-1 parents have been considered to produce new structures. This approach is not fully arbitrary as it has been observed that, at least for the first iterations, the most stable Z structure was obtained from the most stable Z-*1* structure. Thanks to an ongoing work done by Prof. Elizabeth Flores in collaboration with our group, based on the study of low-energy Mo_yC_x structures by means of temperature annealing, has determined the validity of the cascade procedure for small Z values. Thus, the structures obtained by the cascade procedure appear among the most stable structures encountered by the temperature annealing method. For large Z values, it is clear that the obtained structures are not ideal and other more stable structures can easily appear. It could be easy to fall for rapid conclusions on this matter, however, the truth is that more future research has to be done in this topic. Nevertheless, one must remind that one does not pretend to

find out the most stable isomers for a given stoichiometry but just to provide reasonable models that can provide a fair representation of the experimental systems.

4.2.3 MoC and MoN surfaces

The study of MoC and MoN (001) surfaces is not addressed to the study of a particular catalytic reaction. In fact, their inclusion into this work was unexpected, as it will be commented on Chapter 6. Specifically, there are two more surfaces studied in Chapter 6 apart from MoC and MoN. WC and WN were considered after realizing that they exhibit the same particular behaviour as MoC and MoN. Nevertheless, the main discussion can be focused on the MoC system and then extrapolated to the other surfaces. Figure 4 gather the different MoC models used in Chapter 6.

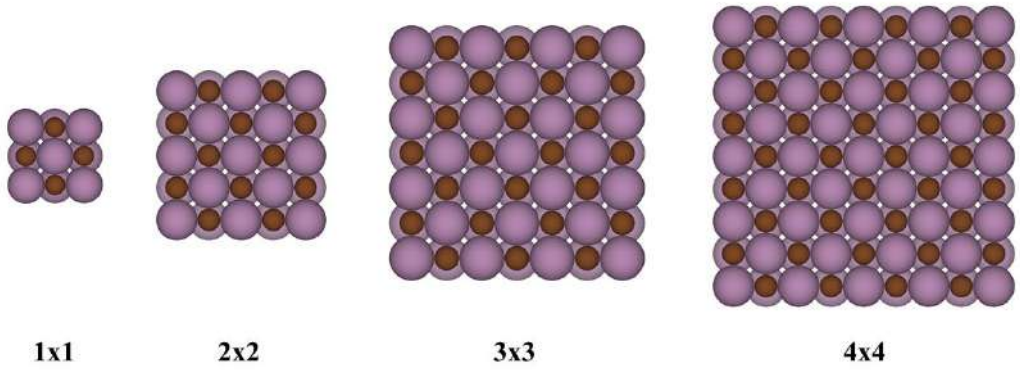

Figure 4. $\left(\sqrt{N} \times \sqrt{N}\right)R45°$ MoC(001) supercells with N ranging from 1 to 4. For simplicity these supercells are hereafter denoted as (N×N).

The MoC (001) surface was obtained by cutting the optimized δ-MoC bulk structure (Fm$\bar{3}$m-MoN/WN and γ-WC). The resulting surface was composed by four layers in the same fashion as in the Au surface, a (2+2) scheme where the two outermost layers were freely optimized and the two innermost were kept frozen at the bulk geometry. It must be pointed that, in this specific research, other schemes were included in order obtain information about the surface thickness effect. The thickest surface considered was an eight-layer surface following a (2+6) scheme, where the two innermost layers were kept frozen and the six outermost layers were freely optimized. Moreover, in this case the supercell size was a central parameter to be studied, therefore, different supercell sizes were considered, ranging from (1×1) to (4×4). Compared to Au surface where NPs had to be adsorbed, which implies an increase in vacuum space, a 15 Å vacuum distance

between MoC surfaces was enough to ensure the non-interaction condition. After the appropriate optimization, an artificial displacement was triggered in order to determine whether a reconstruction pattern exists. A full explanation will be found in Chapter 6.

Chapter 5

Methane activation on MoC nanoparticles supported on Au(111)

5.1 Introduction

Methane is the main component of natural gas and the first greenhouse gas treated in this work. It shows a high chemical stability (4.15 eV for its first C-H bond) plus its non-polar character strongly compromises its use or transformation into other species without greenhouse effect or industrial profitability. Nevertheless, recent efforts aiming to develop low temperature activation procedures for methane have found some promising catalysts in transition metals,[134] Ni and Co surfaces,[135,136] nanoporous carbons,[137] zeolites,[138] and metal-organic frameworks (MOFs).[139]

The present Chapter is focused on the capacity of MoC_y NPs supported on Au(111) to activate methane at room temperature. Both, experiments and theoretical calculations, were carried out to study the main mechanisms involved in this process. Along with the theoretical results on NPs models, the interaction with the bulk surfaces of Mo_2C and MoC were studied for comparison.

MoC nanoparticles were produced following the techniques explained in section 1.3.4, and their characterization was done using X-ray photoelectron spectroscopy (XPS), thermal desorption mass spectroscopy (TDS), and scanning tunnelling microscopy (STM) techniques. These confirmed that methane was adsorbed on the NPs and also that the molecule dissociates. Moreover, the synthesis procedure allows tuning the NPs stoichiometric ratio; consequently, it was possible to study the stoichiometry effect on the methane activation. To summarize, the experimental results showed that these systems adsorb and activate CH_4 at room temperature with a low methane partial pressure.

On the theoretical part, a set of MoC_y NPs supported on Au(111) were modelled, where *y* could range from 0.6 and 1.5. The actual stoichiometry obtained from experiments does not contemplate stoichiometric ratios larger than 1.1, nevertheless, this possibility was considered in the theoretical models to determine the effect of larger C concentrations. The energy profiles were obtained by means of DFT based calculations. Interestingly, DTF results showed a clear difference between MoC surfaces and MoC NPs interacting with methane. For the interaction and dissociation of methane on the different extended surfaces, a Brønsted-Evans-Polanyi (BEP) relationships[140,141] trend emerges that is not followed when analysing results for the supported NPs. Moreover, a detailed comparison between NPs and surfaces revealed the importance of the

contribution of the NP ensemble in lowering the energy barriers. Furthermore, other aspects affecting the methane activation are contemplated and discussed.

The present discovery opens the possibility to design new carbide catalysts for methane activation at room temperature that could represent an important contribution to mitigate methane effect in climate change.

5.2 Results

In order to ensure the inert nature of the support, a clean Au(111) surface was exposed to methane at 1 Torr and 300 K. The absence of a peak in the XPS spectra at C 1*s* binding energy range confirms the inexistence of methane adsorbed to Au(111). Moreover, another indispensable experiment was done in order to determine the incapacity of polycrystalline δ-MoC surface to activate methane, highlighting the importance of the NP shape. In this case, the polycrystalline δ-MoC surface was exposed to the same conditions specified for the Au(111) surface. XPS results revealed the typical signal of carbon atoms within a carbide and not a trace of CH_x species formation.

On the other hand, MoC_y (y = 0.6-1.1) NPs showed a completely different behaviour. The obtained results showed that this NPs are able to interact and react with methane at room temperature, where the strength of the interaction is connected to the NP C/Mo ratio. This feature becomes visible when observing the C(1*s*) XPS spectra of Au(111) covered with NPs of different stoichiometry. For $MoC_{0.6}$ system, the C(1*s*) spectra exhibits a significant peak around 284.8 eV after being exposed to methane at 300 K. This peak cannot be attributed to methane being adsorbed on the NP and indicates the presence of CH_x (x = 1, 2, 3) species, a clear demonstration of methane dissociation. The subsequent annealing to 500 and 600 K stimulated desorption of adsorbed species, nearly recovering the C(1*s*) XPS spectrum of the MoC_y NPs in the absence of methane. The impossibility to totally recover the clean NPs C(1*s*) XPS spectra suggests that the $MoC_{0.6}$ NPs are metastable in presence of methane. This possibility was confirmed by an increase in the NPs C/Mo ratio, which indicates the C enrichment of the NP. Subsequently, the low stability displayed by $MoC_{0.6}$ NPs indicated that they are not suitable as catalysts for reactions involving C atoms as these are attached to the C-deficient NP, thus changing their nature.

The same procedure was carried out for $MoC_{1.1}$ NPs, where results indicated that $MoC_{1.1}$ NPs still show a significant reactivity towards methane without the penalty of being metastable, as their C/Mo ratio does not change after exposure. Although, their interaction with the CH_x species is weaker when compared to that of $MoC_{0.6}$ NP. The weaker interaction is evident as a minor temperature increase inducted a hasty decrease in the CH_x species intensity signal in the XPS spectra. Nevertheless, $MoC_{1.1}$ NPs significant reactivity and capacity to withstand several adsorption/desorption cycles makes them useful as possible catalysts.

On the computational part, a set of models and reactions were studied to support the obtained experimental results and add some insight in the methane activation process. Accounting on the methodology already commented in Section 4.2.2, a set of eight low-energy NPs were selected with C/Mo ratios ranging from 0.67 to 1.50. For comparison, the same activation steps were studied on extended C- and Mo-terminated β-Mo_2C(0001) and δ-MoC(001). All NPs were systematically supported on the Au(111) surface accounting on the procedure explained in section 4.2.1. The obtained structures can be seen in Figure 5. A similar procedure was done to adsorb all the species involved in the reaction, *i.e.*, CH_4, CH_3, and H, in all inequivalent sites within the NP. CH_4 adsorption results showed its preference to adsorb on low-coordinated Mo atoms, with adsorption energies (E_{ads}) ranging from -0.38 to -1.16 eV. In comparison, the extended surfaces showed smaller values ranging from -0.17 to -0.39. Moreover, CH_3 adsorption results showed a similar preference as CH_4 for low-coordinated Mo atoms and, finally, H adsorption results showed its indifference to adsorb in either top-C or top-Mo sites.

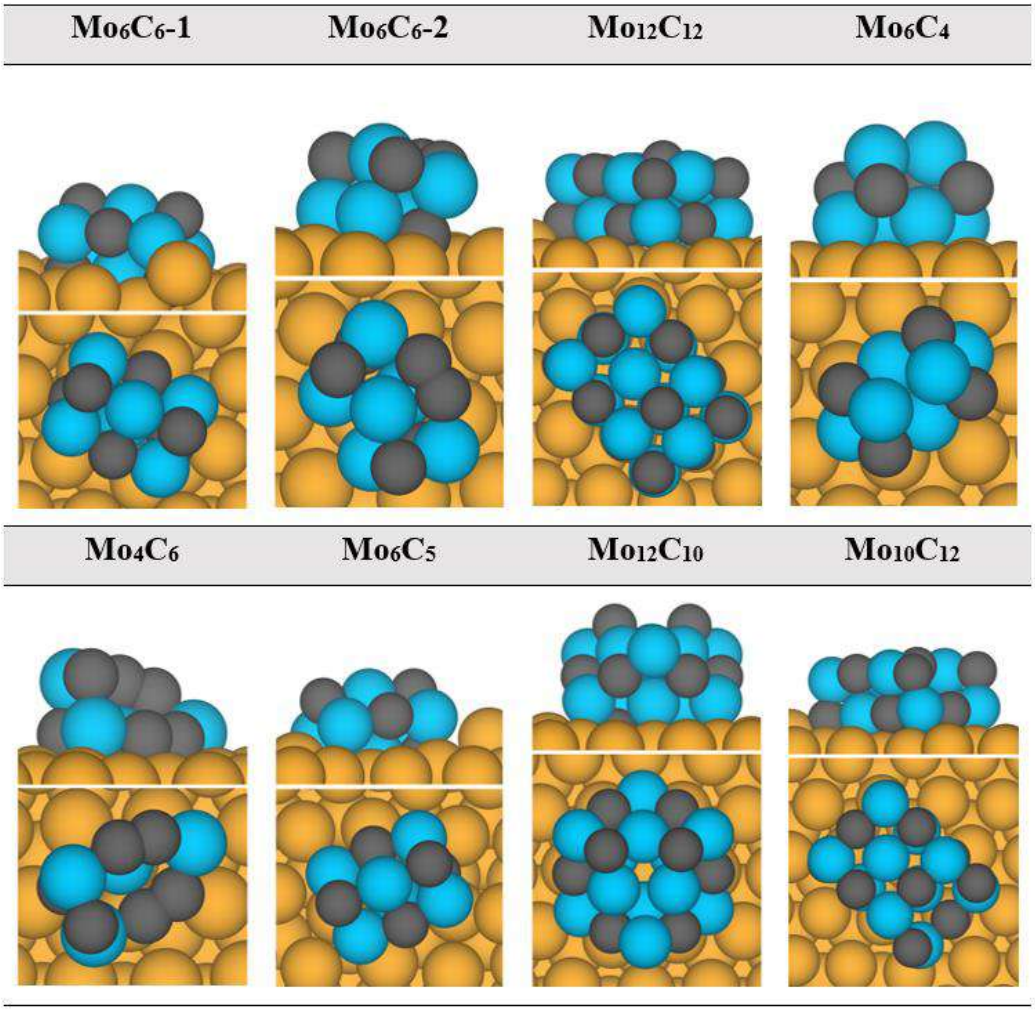

Figure 5. Top and side views for the fully optimized MoC_y/Au(111) systems considered. C, Mo, Au, and H are illustrated as black, blue, yellow and white spheres, respectively. All structures correspont the most stable isomer for such stoichiometry, except for Mo_6C_6, where the first and second most stable isomers were considered.

The reaction energy profiles were obtained by means of TS searches using the CI-NEB method. The main bottleneck step on methane transformation is the first scission of an H atom, which is precisely the step assumed in the experiments. Therefore, for the eight NPs and the extended surfaces, several reaction paths were computed studying the CH_4 dissociation into CH_3 and H. Analysing the results permits to unveil some interesting trends. First, the NP size does not seem to play a significant role, although, a larger set of NPs should be examined in order to ensure this statement. Second, the NP shape has a central role on methane activation. It appears clear comparing the two models with the same stoichiometry where one doubles the energy barrier value of the other. Third, the stoichiometry plays an important role as well., as commented in the experiments, where the carbon deficient NPs are the most reactive. Nevertheless, the reactivity stops

decreasing once the 1:1 carbon/metal ratio is reached. Finally, methane activation on MoC_y NPs supported on Au(111) does not display the typically featured linear correlation between the E_b and E_{reac} (*i.e.*, BEP relationship),[140,141] that otherwise is observed for the extended surfaces. The non-linearity displayed by the NP systems can be accused to a disproportionate lowering in the energy barriers for the methane activation, consequence of the existence of special low-coordinated Mo atoms in the vertices of the NP.

5.3 Conclusions

The experimental and theoretical results obtained clearly revealed an important enhancement in the catalytic properties towards methane activation for the MoC NPs systems compared to the extended MoC surfaces. Specifically, the experiments revealed that MoC_y (y = 0.6-1.1) NPs supported on Au(111) are capable to dissociate methane at room temperature where the stability and activity depend on the C/Mo ratio. The NP C/Mo ratio has a small impact on the activity; however, it has an important impact on the NP stability. Low C/Mo ratio NPs tend to strongly bind with the formed CH_x species, and increase their C/Mo ratio upon annealing, leading to the inevitable conclusion that $MoC_{0.6}$ NPs are not suited to be a catalyst. On the other hand, stoichiometric NPs are still able to dissociate methane and, in conjunction with their higher stability in a methane atmosphere, are great candidates towards methane capture and conversion.

For a more detailed description, the reader is referred to the publication included below. The supporting information of the present publication, can be found in Appendix A.

Contribution: models preparation, DFT based calculations, results interpretation, scientific discussion, and providing a first draft of the publication.

Note: There is an error in the abstract. "MoC_y (y = 0.5-1.3)" should be "MoC_y (y = 0.6-1.1)"

5.4 Publication

Boosting the activity of transition metal carbides towards methane activation by nanostructuring

PCCP

ROYAL SOCIETY OF CHEMISTRY

PAPER

View Article Online
View Journal | View Issue

Cite this: *Phys. Chem. Chem. Phys.*, 2020, **22**, 7110

Boosting the activity of transition metal carbides towards methane activation by nanostructuring†

Marc Figueras,[a] Ramón A. Gutiérrez,‡[bc] Hector Prats,[a] Francesc Viñes,[a] Pedro J. Ramírez,‡[c] Francesc Illas *[a] and José A. Rodriguez *[b]

Received 14th January 2020,
Accepted 12th March 2020

DOI: 10.1039/d0cp00228c

rsc.li/pccp

The interaction of methane with pristine surfaces of bulk MoC and Mo_2C is known to be weak. In contrast, a series of X-ray photoelectron spectroscopy (XPS) experiments, combined with thermal desorption mass spectroscopy (TDS), for MoC_y (y = 0.5–1.3) nanoparticles supported on Au(111)—which is completely inert towards CH_4—show that these systems adsorb and dissociate CH_4 at room temperature and low CH_4 partial pressure. This industrially-relevant finding has been further investigated with accurate density functional theory (DFT) based calculations on a variety of MoC_y supported model systems. The DFT calculations reveal that the MoC_y/Au(111) systems can feature low C–H bond scission energy barriers, smaller than the CH_4 adsorption energy. Our theoretical results for bulk surfaces of Mo_2C and MoC show that a simple Brønsted–Evans–Polanyi (BEP) relationship holds for C–H bond scission on these systems. However, this is not the case for methane activation on the MoC_y nanoparticles as a consequence of their unique electronic and chemical properties. The discovery that supported molybdenum carbide nanoparticles are able to activate methane at room temperature paves the road towards the design of a new family of active carbide catalysts for methane activation and valorisation, with important implications in climate change mitigation and carbon cycle closure.

Introduction

Natural gas is a common source of energy for heating, cooking, and electricity generation. In this gas, methane (CH_4) is the major component and its activation and transformation can have a major impact in industrial operations and environmental pollution control,[1] given that CH_4 greenhouse capabilities are ~23 times larger than those of carbon dioxide (CO_2),[2] making CH_4 a main role-player of global warming and climate change. Research endeavors have been undertaken to make it possible to use CH_4 as a C1 feedstock, an appealing approach for closing the C-cycle[3] while transforming methane into commodity chemicals such as methanol, ethylene, or benzene. However, the high strength of the C–H bonds in CH_4—4.51 eV mol^{-1} for the first bond dissociation energy—and the non-polar character of the molecule make the activation of this hydrocarbon particularly difficult. In this respect, it is well known that the methane monooxygenase enzyme is able to activate methane at room temperature. However, this biological system cannot be used in industrial-scale operations.[4,5] Moreover, to avoid the decomposition of the products and competing reactions, methane activation should proceed at low or medium temperatures.[4,5] These difficulties have triggered a significant amount of research aimed at examining fundamental and practical aspects associated to methane activation by inorganic catalysts, including transition metals, oxides, sulphides, carbides, and zeolites.[5–8]

On late transition metals surfaces, methane binds very weakly and the probability for dissociation is low.[6] For example, on Ni well-defined surfaces, methane dissociation is significant only at temperatures above 450 K;[9] with similar trends reported for Pt and Pd[8] surfaces. Interestingly, low-coordinated surface sites existing in metallic nanoparticles have been found to achieve CH_4 dissociation at or below room temperature even if the ratio of such enhanced activity sites may be too low to lead to large enough conversion.[10,11] In contrast, a few oxide and metal/oxide systems are able to activate methane at 300 K or even lower temperatures.[12,13] On these systems, cooperative interactions between cation and oxide sites are behind the dissociation of the first C–H bond in methane with energy

[a] *Departament de Ciència de Materials i Química Física & Institut de Química Teòrica i Computacional (IQTCUB), Universitat de Barcelona, Martí i Franquès 1-11, 08028 Barcelona, Spain. E-mail: francesc.illas@ub.edu*

[b] *Chemistry Department, Brookhaven National Laboratory, Upton, New York 11973, USA. E-mail: rodriguez@bnl.gov*

[c] *Facultad de Ciencias, Universidad Central de Venezuela, Caracas 1020-A, Venezuela*

† Electronic supplementary information (ESI) available: S1. C 1s and Mo 3d XPS data for the carbide nanoparticles. S2. Additional computational details. S3. Optimized structures for the transition states of CH_4 dissociation on MoC_y/Au(111) models. S4. Optimized structures for the transition states of CH_4 dissociation on δ-MoC or β-Mo_2C surfaces. See DOI: 10.1039/d0cp00228c

‡ Present address: Zoneca-CENEX, R&D Laboratories, Alta Vista, 64770 Monterrey, Mexico.

barriers below 0.5 eV.[12–14] Transition metal carbides (TMCs) have also been tested as possible catalysts for methane conversion,[7,15–18] although the most stable extended surfaces of typical TMCs such as MoC and TiC exhibit a very low reactivity towards methane with no evidence of dissociation.[7,19] Theoretical calculations suggested that metal-terminated metastable surfaces of carbides could be active for the dissociation of methane.[19,20] However, it is unlikely that such surfaces are exposed when dealing with a bulk TMC under typical reaction conditions although they could well be present in TMC nanoparticles thus representing an interesting possibility. In fact, it is known that TMC nanoparticles supported inside zeolites can catalyse the conversion of methane into ethane, benzene and other hydrocarbons.[16–18,21] In principle, both the structure of the nanoparticle and its carbon/metal ratio could affect its ability to bind and dissociate methane. However, there is no information regarding this point and no systematic study has been reported so far examining the interaction of methane with TMC nanoparticles.

In this article, we use a combination of experimental and theoretical techniques to investigate the reactivity of MoC_y nanoparticles towards CH_4 activation and dissociation. In particular, we focus on molybdenum carbide (MoC_y) nanoparticles which are growth on an inert Au(111) substrate[22] and employ X-ray photoelectron spectroscopy (XPS), thermal desorption mass spectroscopy (TDS), and density functional theory (DFT) based calculations to examine the interaction of methane with the supported MoC_y nanoparticles. We provide compelling evidence that the MoC_y/Au(111) systems are able to dissociate methane at room temperature. Moreover, for MoC_y nanoparticles with a carbon/metal ratio of 1.1, the CH_x surface groups generated by the adsorption of methane recombine upon heating to yield ethane and ethylene. Our results for bulk surfaces of Mo_2C and MoC show that, following the initial ideas of Pallassana and Neurock,[23] a simple Brønsted–Evans–Polanyi (BEP) relationship[24,25] holds for C–H bond scission on these systems. However, this is not the case for methane activation on the MoC_y nanoparticles as a consequence of their unique electronic and chemical properties.

Experimental details

The MoC_y/Au(111) systems were prepared following a procedure described in a previous study and established at Brookhaven National Laboratory.[22] On a Au(111) substrate, with the characteristic herringbone $(22\times\sqrt{3})$ reconstruction structure, inverse carbide/gold, sulfide/gold and oxide/gold systems have been generated for fundamental studies in catalysis.[22,26–29] In this case, the MoC_y nanoparticles were generated by deposition of Mo metal onto a reactive multilayer of ethylene, which was physisorbed on a Au(111) surface at 100 K.[22] The amount of Mo deposited was estimated using XPS and Mo/Au ratios seen in previous studies for the deposition of Mo on the herringbone structure of Au(111).[22,30,31] The Au(111) substrate does not react with ethylene but the deposited Mo does to form carbide nanoparticles. Upon heating to 750 K, the unreacted ethylene desorbed and MoC_y nanoparticles were left on the gold substrate (Fig. S1, ESI†). This process could be followed using XPS, TDS, and STM.[22] Following this approach, in XPS measurements, we found no O 1s signal and C 1s binding energies which were very different from those of regular hydrocarbons and very close to those reported for molybdenum carbides around 282.5–283 eV (see Fig. S1, ESI†).[32–34] For the Mo 3d core levels, we saw a small shift towards higher binding energy (see Fig. S2, ESI†), consistent with previous studies for molybdenum carbides and a Mo → C charge transfer.[32,33] In this synthetic process, by changing the initial amounts of Mo and C_2H_4 deposited on the Au(111) substrate, it is possible to control the C/Mo ratio in the carbide nanoparticles, and this was varied between 0.6 and 1.1. XPS was used to determine this ratio, and we utilized as reference previous values measured in our instrument for the C 1s and Mo 3d regions of bulk MoC and Mo_2C.[35] For the bulk sample of MoC our XPS measurements point to a C/Mo ratio of 0.98–0.96, in good agreement with the ratio typically observed for bulk samples of one-to-one carbides.[29,36–38] A set of the MoC_y/Au(111) surfaces had a C/Mo ratio close to this value but displayed a unique reactivity. Images acquired by scanning tunnelling microscopy (STM) have shown that the MoC_x nanoparticles are small (0.6–1.5 nm) and aggregate in the face-centred cubic (fcc) troughs located on either side of the elbows of the reconstructed Au(111) surface.[22] Previous and current images of STM indicate that the nanoparticles are essentially amorphous and do not have the typical structures of bulk MoC or Mo_2C.[22] Thus, due to their size and structure, these nanoparticles can have special chemical and catalytic properties.

The reactivity of the MoC_y/Au(111) surfaces towards methane was examined in a system which combines an ultrahigh-vacuum (UHV) chamber (base pressure $\sim 7 \times 10^{-10}$ mbar) and a batch reactor.[39–42] Within this system, the sample could be transferred between the reactor and UHV chamber without exposure to air. The UHV chamber was equipped with instrumentation for XPS, ultraviolet photoelectron spectroscopy (UPS), low-energy electron diffraction (LEED), ion scattering spectroscopy (ISS), and TDS. In the tests to study the interactions with methane, clean Au(111) and MoC_y/Au(111) surfaces were positioned in the batch reactor at ~300 K, then 1 Torr of CH_4 was introduced for a period of five minutes. After this exposure, the CH_4 gas was removed and each sample was transferred back to the UHV chamber for surface characterization with XPS and TDS.

Computational methods and models

Methane activation on MoC_y/Au(111) has been assessed by modelling different Au-supported MoC_y nanoparticles with C/Mo ratios ranging from 0.67 to 1.50, as in the experiments, and relying on periodic DFT based calculations. The initial stoichiometric structures of MoC nanoparticles in gas-phase were taken so as to mimic the most stable gas-phase TiC nanoparticles reported in previous work by Lamiel *et al.*,[43] formerly obtained by data mining searches combining interatomic potentials and DFT calculations. These authors reported

a total of nine Ti_6C_6 and twelve $Ti_{12}C_{12}$ low energy structures. In the present work, these structures were taken as initial guess for the gas-phase Mo_6C_6 and $Mo_{12}C_{12}$ nanoparticles by simply replacing all Ti atoms by Mo atoms followed by full PBE-D3 relaxation without any constraint. Interestingly, for both sizes, the structure of the most stable MoC isomer corresponds to the most stable one for the TiC nanoparticle. However, in some cases, the order of stability of the other (*i.e.*, less stable in gas-phase) MoC isomers differs from that of their TiC counterparts. To obtain suitable non-stoichiometric structures in gas-phase, mimicking the composition of the particles in the experiments, a cascade approach was used starting from the two most stable Mo_6C_6 and $Mo_{12}C_{12}$ structures. The different non-stoichiometric nanoparticles were created removing one of all non-equivalent (Mo or C) atoms at a time. This resulted in five Mo_5C_6, four Mo_6C_5, six $Mo_{11}C_{12}$, and other six $Mo_{12}C_{11}$ new structures with C/Mo ratios between 0.83 to 1.20. To fill the experimental ratio ranging from 0.6 to 1.1, structures resulting from successive extractions of one Mo or one C atom were considered as well. Overall, a full set of 148 gas-phase non-stoichiometric MoC_y structures were obtained and their structure fully optimized.

The two most stable Mo_6C_6 (Mo_6C_6-1 and Mo_6C_6-2) and the most stable $Mo_{12}C_{12}$ structures in gas-phase were supported on the Au(111) surface. This step implied numerous geometry optimizations due to the high number of possible orientations of the supported nanocluster and the presence of different adsorption sites on the Au(111) surface. All MoC_y/Au(111) systems were optimized, and the structure presenting the strongest adsorption energy was chosen to perform the study of CH_4 adsorption and dissociation. Similarly, the most stable non-stoichiometric Mo_6C_5, Mo_6C_4, Mo_4C_6, $Mo_{12}C_{10}$, and $Mo_{10}C_{12}$ structures in gas-phase were supported on Au(111). Again, for each non-stoichiometric structure, the optimized geometry presenting the strongest adsorption energy was chosen to perform the study of CH_4 adsorption and dissociation. In summary, three stoichiometric—two isomers of Mo_6C_6 and one of $Mo_{12}C_{12}$—and five non-stoichiometric nanoparticles supported on Au(111) were investigated, as shown in Fig. 1. These carbide nanoparticles have diameters which are within the range of sizes experimentally found with STM for MoC_y/Au(111) systems.[22] For comparison, the extended C- and Mo-terminated orthorhombic β-Mo_2C(0001) and cubic δ-MoC(001) surfaces have been studied as well.

All present DFT calculations employed the Perdew–Burke–Ernzerhof (PBE)[44] exchange–correlation (xc) functional, known to accurately describe molybdenum carbide and transition metal surfaces.[45,46] The dispersion—van der Waals, vdW—term was approximated through the D3 correction as proposed by Grimme.[47] Spin polarization was taken explicitly into account only for the systems containing non-stoichiometric MoC_y nanoparticles in gas phase as test calculations show that any spin polarization is quenched once the particles are supported on the Au(111) metallic surface. The transition state (TS) structures for methane dissociation were located using the climbing-image nudged-elastic-band (CI-NEB) method[48] employing five intermediate images, and the gained TS further characterized by appropriate frequency analysis. Initial guesses for those images were generated by means of the atomic simulation environment (ASE)[49] using the image dependent pair potential (IDPP).[50] All calculations were carried out using the Vienna *ab Initio* simulation package (VASP).[51] Further computational details and obtained geometries are provided in the ESI.† Note in passing by that favourable adsorption energies, E_{ads}, are defined negative, and all reported energy values include the zero-point energy (ZPE) term obtained within the harmonic approximation.

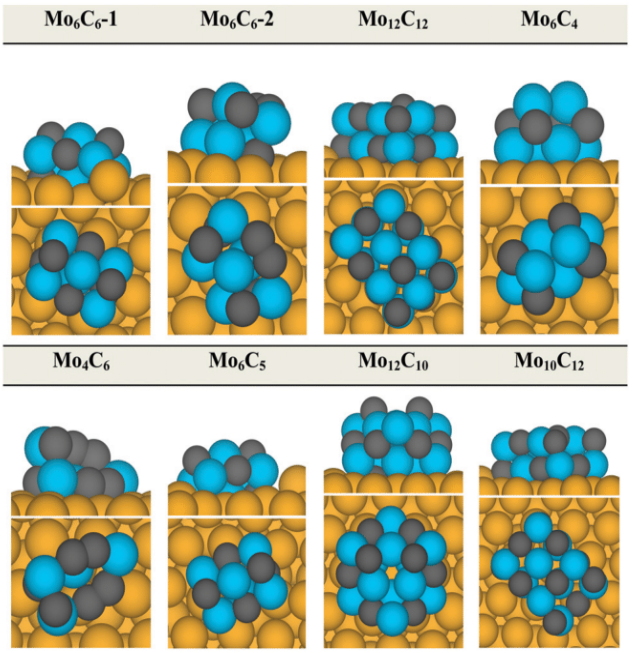

Fig. 1 Optimized geometries (top and side views) for the studied MoC_y/Au(111) systems. Au, Mo, C, and H atoms are shown as yellow, blue, black, and white spheres, respectively. In all cases, the most stable isomer has been studied, except for the Mo_6C_6, where the second most table structure was also studied (Mo_6C_6-2).

Results and discussion

Experiments

Fig. 2 shows a C 1s XPS spectrum obtained after exposing clean Au(111) to 1 Torr of methane at 300 K. The noble metal did not react with methane at room or elevated temperatures. This agrees with previous studies which show that this substrate also does not react with ethylene.[22] At low and high temperatures pure metallic gold is not able to break the C–H bonds in the hydrocarbon, even in presence of adsorbed atomic O.[52] Included in Fig. 2 is a C 1s spectrum collected after exposing bulk polycrystalline δ-MoC to 1 Torr of CH_4 at 300 K. Only features for the carbon atoms in the carbide are observed. In the region between 284 and 285 eV, where signal for CH_x fragments is usually seen,[7] no clear features are detected and one sees the plain C 1s spectrum of a metal carbide. From previous studies it is known that samples of bulk polycrystalline δ-MoC or TiC do not react with methane at room temperature.[7,19] The surface metal atoms of such bulk 1 : 1 TMCs are saturated with C atoms, and so do not attack the C–H bonds in methane,[7,19]

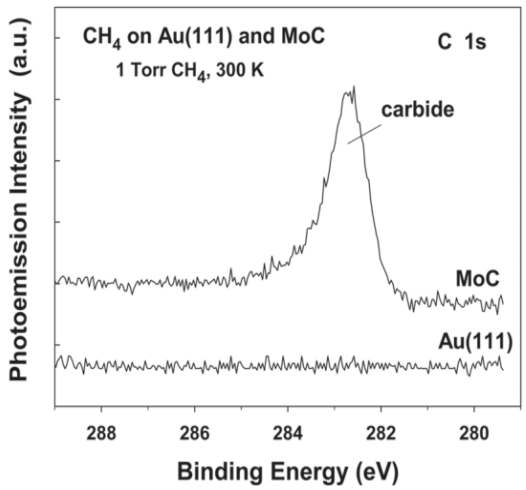

Fig. 2 C 1s XPS spectra collected after dosing methane to clean Au(111) and bulk polycrystalline δ-MoC. The dosage of methane was 1 Torr for 5 minutes.

Thus, the blank experiments in Fig. 2 show that neither Au(111) nor bulk δ-MoC is useful for methane activation. In contrast, we found a different behaviour for MoC_y (y = 0.6–1.1) nanoparticles dispersed on Au(111). These nanoparticles do react with methane at room temperature, and the strength of the interaction appears to be affected by the carbon/metal ratio of the studied system. Fig. 3 displays C 1s XPS spectra collected after dosing methane at 300 K to a Au(111) surface pre-covered with 0.3 monolayers (ML) of $MoC_{0.6}$. The fresh sample shows the typical C 1s XPS peak position at ~283 eV, expected for a molybdenum carbide.[22] Upon exposure to methane a second peak appears *circa* 284.8 eV, which cannot be attributed to adsorbed CH_4 and indicates the generation of CH_x (x = 1, 2, 3) species on top of the carbide surface.[7,13,14] This peak has a full width at half maximum (FWHM) of ~1.5 eV, very similar to that measured for bulk MoC and the carbide nanoparticles dispersed on gold. Annealing to 500 and 600 K induces the disappearance of the CH_x features while the features for MoC_y grow. Fig. 4 shows the relative changes in the CH_x and MoC_y signals as a function of temperature, and from it one deduces that the $MoC_{0.6}$/Au(111) seems to be metastable in the presence of CH_4, and while the Mo attacks the C atoms in CH_x the carbon/metal ratio in the carbide appears to increase. A similar behaviour has been seen for bulk Mo_2C in an atmosphere of methane or other hydrocarbons at high temperatures where a $Mo_2C \rightarrow MoC$ transformation was seen with *in situ* X-ray diffraction for powders of the carbide.[53] When compared to bulk Mo_2C, our results indicate that the $MoC_{0.6}$ nanoparticles are more chemically active, as they do react with CH_4 at room temperature, although their low stability gives them a limited use as catalysts.

In bulk molybdenum carbides, an increase in the carbon/metal ratio from 0.5 to 1 leads to a MoC compound which has a negligible reactivity towards methane, as seen in Fig. 2 and in previous studies.[7,19] In the case of the MoC_y nanoparticles, the reactivity towards CH_4 is also affected by the C/Mo ratio, but for these nanostructures, at ratios higher than one, there is still

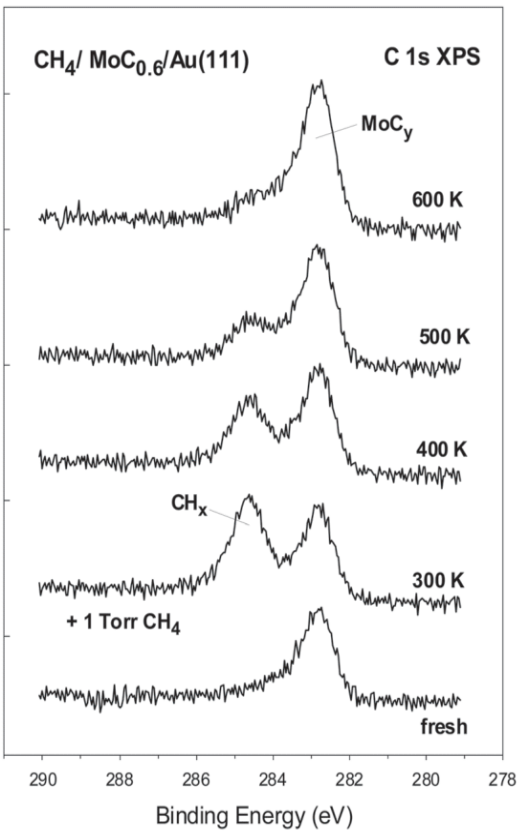

Fig. 3 C 1s XPS spectra collected before and after dosing methane to $MoC_{0.6}$/Au(111) at 300 K. This was followed by heating to 400, 500, and 600 K. The dosage of methane was 1 Torr for 5 minutes. The initial coverage of $MoC_{0.6}$ on the Au(111) substrate was 0.3 ML.

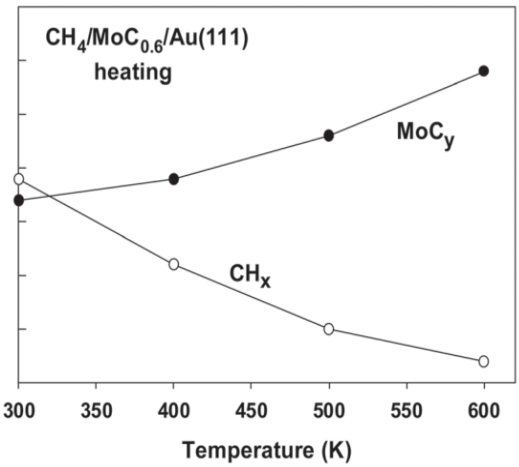

Fig. 4 Variation of the CH_x and MoC_y intensities as a function of temperature in CH_4/$MoC_{0.6}$/Au(111). Initially the surface was exposed to 1 Torr of methane for 5 minutes at 300 K, see Fig. 1.

significant reactivity towards methane. Fig. 5 shows the C 1s XPS spectra recorded after dosing methane at 300 K to a Au(111) surface pre-covered with 0.3 ML of $MoC_{1.1}$. The fresh sample shows again the typical C 1s features for a carbide near ~283 eV,[22] and the dosing of methane leads to the appearance as well of a second peak near 284.5 eV due to adsorbed CH_x. Thus, when going from C-meagre to C-rich nanoparticles—$MoC_{0.6}$ to $MoC_{1.1}$—the system is still able to dissociate methane

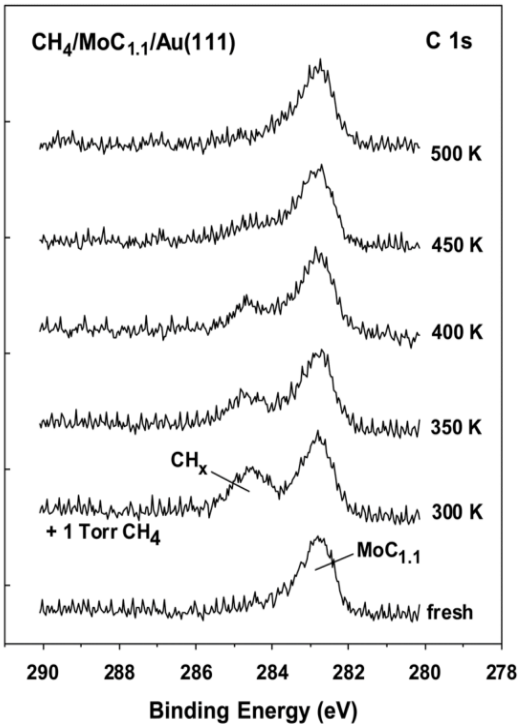

Fig. 5 C 1s XPS spectra collected before and after dosing methane to $MoC_{1.1}$/Au(111) at 300 K. This was followed by heating to 350, 400, 450, and 500 K. The dosage of methane was 1 Torr for 5 minutes. The initial coverage of $MoC_{1.1}$ on the Au(111) substrate was 0.3 ML.

at room temperature, although the adsorbed CH_x binding weakens, since, as shown in Fig. 5 and 6, a minor temperature increase triggers a rapid decrease in the CH_x signal intensity without significantly affecting the C 1s signal intensity assigned to the MoC_y carbide. Therefore, the $MoC_{1.1}$ nanoparticles appear to be stable under an atmosphere of methane. This behaviour is reminiscent of that observed for MoC powders[30] and bulk crystals of 1 : 1 TMCs.[5] Indeed, we found that the $MoC_{1.1}$/Au(111) system was able to sustain many CH_4 adsorption/desorption cycles without any significant change neither on the C/Mo ratio nor in the reactivity of the surface towards CH_4 (Fig. 7). Thus, in the

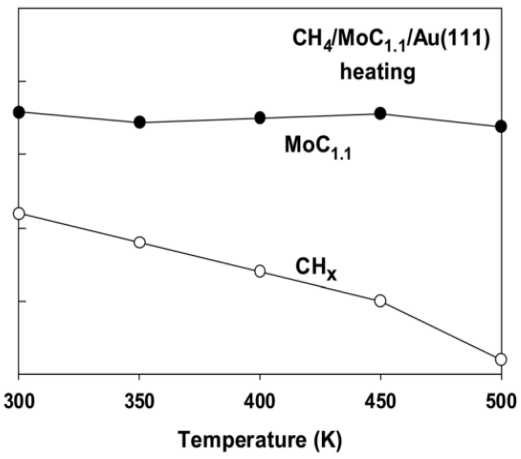

Fig. 6 Variation of the CH_x and MoC_y intensities as a function of temperature in CH_4/$MoC_{1.1}$/Au(111). Initially the surface was exposed to 1 Torr of methane for 5 minutes at 300 K, see Fig. 3.

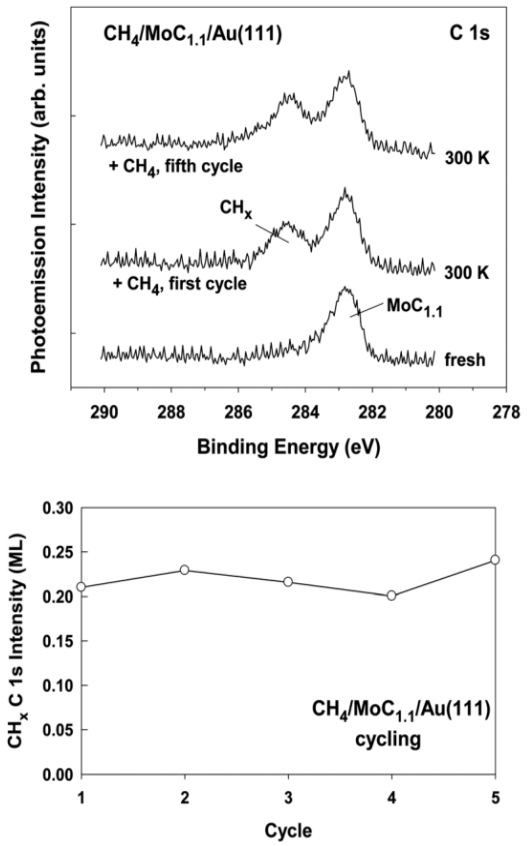

Fig. 7 Top panel: C 1s XPS spectra collected after 1 and 5 cycles of adsorption/desorption for the CH_4/$MoC_{1.1}$/Au(111) at 300 K. In each cycle, the surface was exposed to 1 Torr of CH_4 at 300 K for five minutes. Then, the gas was removed, the corresponding C 1s XPS spectrum was recorded, and finally the sample was heated to 500 K to desorb the CH_x deposited before the beginning of the next cycle. This was repeated for five cycles. Bottom: Amount of CH_x adsorbed in each cycle after dosing methane at 300 K. The initial coverage of $MoC_{1.1}$ on the Au(111) substrate was 0.3 ML and essentially remained constant after five cycles.

$MoC_{1.1}$ nanoparticles, one has the right balance of stability and activity making them useful as catalysts.

As far as the chemical behaviour of adsorbed CH_x is concerned, mass spectrometer signals detected mainly the evolution of CH_4 from the CH_x/$MoC_{1.1}$/Au(111) surface, as a consequence of a $CH_{x,ads} + (4 - x)\cdot H_{ads} \rightarrow CH_{4,gas}$ recombination, but with noticeable signals for C_2H_6 and C_2H_4, see Fig. 8. No CO or water desorption was found, consistent with a lack of an O 1s XPS signal after preparing the carbide overlayer or after dosing methane. In average, the relative amount of the desorbed hydrocarbons from the CH_x/$MoC_{1.1}$/Au(111) surface was methane (79%), ethane (15%), and ethylene (7%). Thus, it is clear that the species produced by the CH_4 dissociation are chemically active and so susceptible to be used for producing other, more complex hydrocarbons. Indeed, one can envision that nanoparticles of the $MoC_{1.1}$ type could be responsible for the activity seen over MoC_x/ZSM-5 catalysts when transforming methane into larger hydrocarbons.[16–18,21]

Computational study

To disclose the chemistry behind the described experiments for the MoC_x/Au(111) systems, methane adsorption and first C–H bond scission have been studied on eight different supported

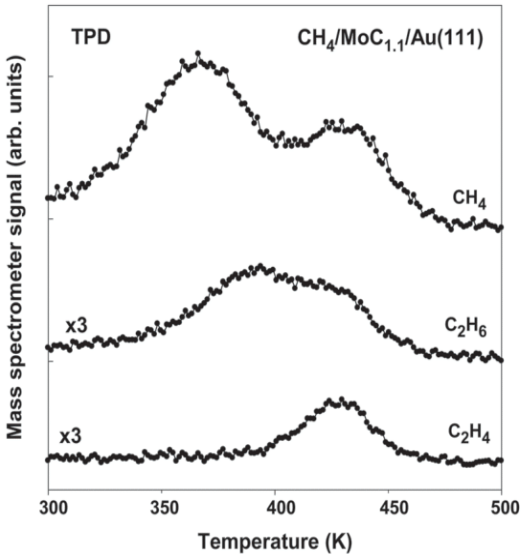

Fig. 8 Thermal desorption spectra collected after exposing a $MoC_{1.1}$/Au(111) surface to 1 Torr of methane for 5 minutes at 300 K in a micro-reactor. The gas was pumped out and the sample was transferred to a UHV chamber for a TDS study (heating ramp 2 K s^{-1}).

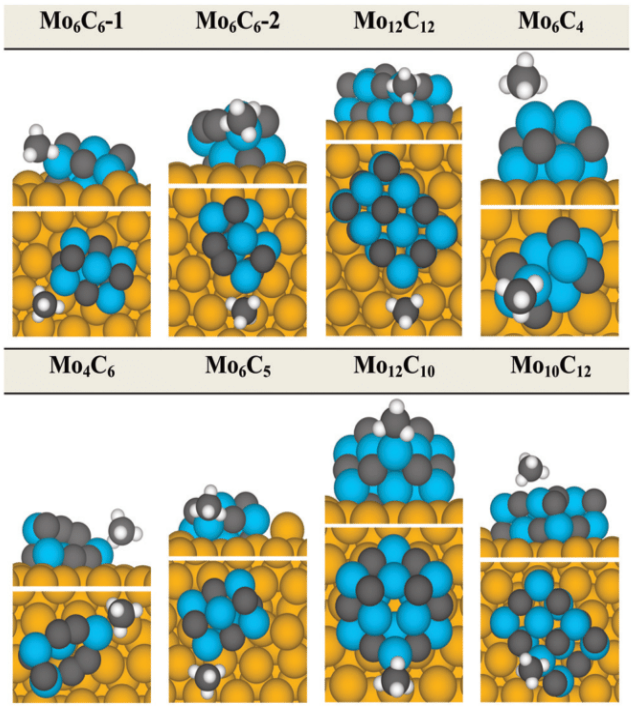

Fig. 9 Optimized geometries (top and side views) for the adsorption of CH_4 on all studied MoC_y/Au(111) systems. Au, Mo, C, and H atoms are shown as yellow, blue, black, and white spheres, respectively. In all cases, the most stable isomer has been studied, except for the Mo_6C_6, where the second most table structure was also studied (Mo_6C_6-2).

MoC_y nanoparticles with C/Mo ratios ranging from 0.67 to 1.50, as in the experiments. For comparison, similar calculations have been carried for the extended C- and Mo-terminated β-Mo_2C(0001) and δ-MoC(001) surfaces. The interaction of all the above stated nanoparticles with the Au(111) surface has been studied by explicitly and systematically placing the MoC_y center of mass above several non-equivalent sites (*i.e.*, top, bridge, and hollow sites) and exploring several orientations per site as described in the section on Computational methods and models. A similar procedure has been used to explore the structure of CH_4, CH_3, and H moieties when adsorbed on the supported clusters, where η^1, η^2, and η^3 connectivities have been considered for CH_4.[19]

The present calculations show that, in general, CH_4 prefers to adsorb on low-coordinated Mo atoms with η^2 connectivity, see Fig. 9, featuring surprisingly high adsorption energies, ranging from −0.38 to −1.16 eV, see PBE-D3 E_{ads} values listed in Table 1, thus suggesting a clear meeting point in between the Mo special affinity towards CH_4 and the low-coordination effect.[10,19] Clearly, the MoC_y nanoparticles exhibit E_{ads} values larger than the extended surface, which range from −0.17 to −0.39 eV only—see the optimized geometries in Fig. 10. Similarly, CH_3 species also prefer low-coordinated Mo atoms, which agrees with the experimental finding that C-poor MoC_y nanoparticles present a stronger binding towards CH_x species. Finally, atomic H can be adsorbed indistinguishably at both top-C or top-Mo sites. Note also that, since removing one carbon atom does not produce a significant structural reconstruction, the most stable Mo_6C_6 isomer (Mo_6C_6-1) and Mo_6C_5 structures are actually very similar, see Fig. 1. The CH_4 adsorption and subsequent dissociation in the latter structure has been studied by considering the most stable adsorption site near the C vacancy defect. The same strategy has been used on the $Mo_{10}C_{12}$ structure, since it is very similar to $Mo_{12}C_{12}$, except near the Mo vacancy defect.

Table 1 Methane adsorption energies (E_{ads}) and energy barriers (E_b) and reaction energies (E_{reac}) for CH_4 dissociation on all studied systems

System	E_{ads} (eV)	E_b (eV)	E_{reac} (eV)
Mo_6C_6-1	−1.16	0.58	−0.68
Mo_6C_6-2	−0.95	1.02	−0.79
$Mo_{12}C_{12}$	−0.61	0.60	−0.33
Mo_6C_4	−0.48	0.08	−1.98
Mo_4C_6	−0.38	0.63	−1.03
Mo_6C_5	−0.45	0.58	−0.55
$Mo_{12}C_{10}$	−0.51	0.37	−0.62
$Mo_{10}C_{12}$	−0.22	0.58	−1.57
δ-MoC(001)	−0.17	1.20	0.59
C-Terminated β-Mo_2C(0001)	−0.18	0.67	−0.66
Mo-Terminated β-Mo_2C(0001)	−0.39	0.48	−1.66

For the eight selected supported MoC_y structures, as well as for the above mentioned extended δ-MoC and β-Mo_2C surfaces, we have carried out TS searches for CH_4 dissociation by using the CI-NEB method. Specifically, the dissociation of an adsorbed CH_4 molecule from its most stable adsorption site to produce CH_3, typically remaining in the same site, and one atomic H typically ended adsorbed in the most stable nearby site, has been studied. Note that, for every structure, several dissociation energy paths—between 3 and 7 depending on the chosen structure—have been explored with different final configurations, so as to have a clear, unequivocal description of the CH_4 dissociation energy landscape. The optimized geometries for all obtained TSs are reported in Fig. S3 and S4 of the ESI.† The energy barriers values, reported in Table 1, are thus the lowest among the explored energy paths. Regarding the C-terminated β-Mo_2C(0001)

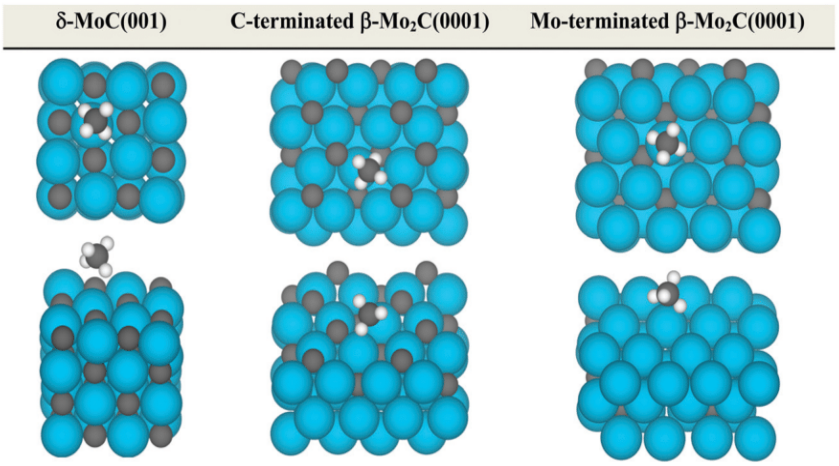

Fig. 10 Optimized geometries (top and side views) for the adsorption of methane on δ-MoC(001) and C/Mo-terminated β-Mo_2C(0001) surfaces. Colour code as in Fig. S1 (ESI†).

and δ-MoC(001) extended surfaces, the CH_4 adsorption energy is always much smaller than the energy barrier for dissociation, in agreement with experimental findings that these surfaces do not dissociate methane, and implying a preference for desorption rather than for dissociation. In the case of the Mo-terminated β-Mo_2C(0001) surface, the energy barrier is *circa* 0.1 eV larger that the adsorption energy, indicating that this particular surface may exhibit some activity towards methane, also in agreement with experiments. However, most of the studied MoC_y/Au(111) systems feature energy barriers for dissociation equal or lower than the adsorption energy of methane, with the only exceptions of Mo_4C_6 and $Mo_{10}C_{12}$, suggesting that MoC_y nanoparticles with $y > 1.2$ present a lower activity compared to other nanoparticles.

The analysis of DFT results also permits to identify the nanocluster size effect on the CH_4 dissociation energy barrier, *i.e.* by comparing results for most stable Mo_6C_6 and $Mo_{12}C_{12}$ structures. For both supported clusters, the energy barriers for CH_4 dissociation are quite similar, 0.58 and 0.60 eV, respectively. Consequently, the effect of nanoparticle size may not be significant, at least for stoichiometric structures, although, obviously, this preliminary statement would be confirmed when data for larger nanoparticles could be acquired. Nevertheless, the present results indicate that the effect of the nanocluster shape seems to play a dominant role. Take, for instance, the supported Mo_6C_6 nanoparticles, where the methane dissociation energy barriers for the most stable (Mo_6C_6-1) and second most stable (Mo_6C_6-2) supported structures are 0.58 and 1.02 eV, respectively. Clearly, the large difference in the calculated energy barriers is to be attributed to the large structural difference which is clearly seen in Fig. 1. Finally, the results reported in Table 1 suggest that the C–H scission energy barrier on Mo-deficient systems is very similar to their stoichiometric homologs. The case of C-meagre systems is especially interesting since feature much lower energy barriers which may be as low as 0.08 eV for Mo_6C_4, an exceptional result that perfectly agrees with the experimental observation that $MoC_{0.6}$ nanoparticles are the most reactive ones.

Unravelling trends for C–H bond activation on bulk surfaces and nanostructures of molybdenum carbides

To further investigate key points in the activation of the C–H bond in CH_4 on different systems of molybdenum carbide we investigated trends for the adsorption and dissociation of the hydrocarbon on the bulk surfaces and nanostructures examined. In a past study a clear correlation was found when comparing E_b for CH_4 dissociation *vs.* E_{reac} (*i.e.*, BEP relationship) on Ni/TiC(001) systems and on bare Ni(111).[7] Fig. 11 shows that this type of correlation holds well comparing the results for the adsorption and dissociation of methane on the bulk surfaces of δ-MoC and β-Mo_2C (the latter with two possible terminations). However, for the nanoparticles there are deviations of the linearity which are a strong indication of a different underlying chemistry. The results in Fig. 11 indicate that the reactivity of the finite nanoparticles cannot be extrapolated from the behavior seen for the extended bulk carbides.

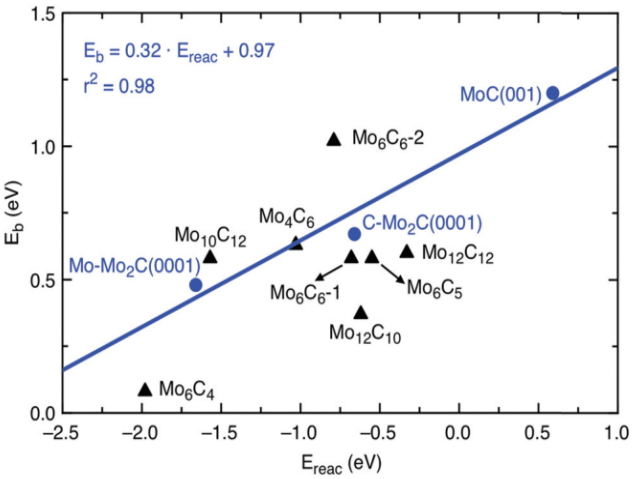

Fig. 11 Energy barrier (E_b) for CH_4 to CH_3 + H dissociation on different molybdenum carbide nanoparticles (black triangles) and extended surfaces (blue dots) *versus* the reaction energy (E_{reac}). The values used to construct the plot are reported in Table 1. The linear regression corresponds to the values from the extended surfaces only.

In general, the breakdown of the correlation is mainly a consequence of a lowering in the energy barrier for the $CH_4 \rightarrow CH_3 + H$ dissociation on the carbide nanoparticles, while keeping similar reaction energies to those for extended carbides. As discussed above, this lowering is a consequence of the existence of special low-coordinated Mo atoms in the vertices of the nanostructures. The energy barriers for methane dissociation on the most active MoC_y nanoparticles are close to those calculated on $IrO_2(110)$ and $Ni/CeO_2(111)$ surfaces.[12,13] On those systems, a concerted mechanism has been reported for low-temperature activation where the cleavage of the first C–H bond in methane involves simultaneous bonding interactions with a metal cation and an oxygen anion.[12,13] This type of dissociative interaction cannot take place on the MoC_y nanoparticles where the C centers do not have the very high negative charge present in the O centers of an oxide. Nevertheless, the η^2 connectivity on Mo atoms seen in Fig. 9 is very efficient for the activation of methane. Such a type of dissociative interaction probably occurs when nanoparticles of MoC_y are dispersed in the cages of zeolites and methane is transformed into ethane, benzene and other hydrocarbons.[16–18,21]

Conclusions

The present experimental and theoretical results point to a clear enhancement in the reactivity of the MoC based systems towards methane activation when going from extended surfaces to the case of MoC_y (y = 0.6–1.1) nanoparticles supported on Au(111). The supported MoC_y nanoparticles are able to dissociate CH_4 at room temperature, and the activity, the stability, and the strength of the interaction with CH_x species appears to depend on the C/Mo ratio. While C-deficient nanoparticles are very reactive, they feature low stability due to the strong binding of the adsorbed CH_x species, which leads to an increase in the C/Mo ratio upon annealing. On the other hand, Mo-deficient systems present the right balance of stability and activity. Although, Mo-deficient nanoparticles are less reactive, they are still able to dissociate methane at room temperature, and are stable under an atmosphere of methane, posing themselves as attractive catalytic systems towards CH_4 capture and catalytic conversion.

The present exciting and technologically relevant experimental result were explained by means of DFT based calculations on a broad enough set of supported MoC_y nanoparticles models with C/Mo ratios ranging from 0.67 to 1.50. The DFT calculations confirm that supported carbide nanoparticles feature stronger CH_4 adsorption energies than extended δ-MoC or β-Mo_2C surfaces, with adsorption energy values up to −1.16 eV. Moreover, the energy barrier for CH_4 dissociation on the nanoparticles gets substantially reduced, and can be as low as 0.08 eV for C-deficient systems, perfectly agreeing with the experimental findings. All in all, the present results open the way for the preparation of a new family of active catalysts for methane activation and conversion under mild conditions, thus widening the applications of existing natural gas resources.

Conflicts of interest

The authors declare no conflict of interest.

Acknowledgements

This manuscript has been authored by employees of Brookhaven Science Associates, with the financial support of the Office of Basic Energy Sciences in the U.S. Department of Energy under Contract No. DE-SC0012704. The work carried out at University of Barcelona has been supported by the MICIUN RTI2018-095460-B-I00 research grants and by the Spanish Structures of Excellence María de Maeztu program through grant MDM-2017-0767. The authors are also grateful to Generalitat de Catalunya for partial support through grants 2017SGR13 and XRQTC. F. I. acknowledges additional support from the 2015 ICREA Academia Award for Excellence in University Research. F. V. is thankful to Ministerio de Economía y Competitividad (MINECO) for his Ramón y Cajal (RYC-2012-10129) research contract. Authors are thankful for the computational time provided at Marenostrum-IV supercomputer at the Barcelona Supercomputing Centre (BSC) through the grants QCM-2019-1-0008 and QCM-2018-3-0010 awarded by the Red Española de Supercomputacion (RES).

References

1 P. Tang, Q. Zhu, Z. Wu and D. Ma, *Energy Environ. Sci.*, 2014, **7**, 2580–2591.
2 J. Feichter, U. Schurath and R. Zellner, *Chem. Unserer Zeit*, 2007, **41**, 138–150.
3 D. L. Woodard, S. J. Davis and J. T. Randerson, *Proc. Natl. Acad. Sci. U. S. A.*, 2019, **116**, 759–764.
4 S. I. Chan and S. S. Yu, *Acc. Chem. Res.*, 2008, **41**, 969–979.
5 M. Ravi, V. L. Sushkevich, A. J. Knorpp, M. A. Newton, D. Palagin, A. B. Pinar, M. Ranocchiari and J. A. van Bokhoven, *Nat. Catal.*, 2019, **2**, 485–494.
6 P. Khirsariya and R. K. Mewada, *Procedia Eng.*, 2013, **51**, 409–415.
7 H. Prats, R. A. Gutiérrez, J. J. Piñero, F. Viñes, S. T. Bromley, P. J. Ramírez, J. A. Rodriguez and F. Illas, *J. Am. Chem. Soc.*, 2019, **141**, 5303–5313.
8 T. V. Choudhary, E. Aksoylu and D. W. Goodman, *Catal. Rev.*, 2003, **45**, 151–203.
9 T. P. Beebe Jr., D. W. Goodman and B. D. Kay, *J. Chem. Phys.*, 1987, **87**, 2305–2315.
10 F. Viñes, Y. Lykhach, T. Staudt, C. Papp, H.-P. Steinrück, J. Libuda, K. M. Neyman and A. Görling, *Chem. – Eur. J.*, 2010, **16**, 6530–6539.
11 S. M. Kozlov and K. M. Neyman, *J. Catal.*, 2017, **336**, 111–121.
12 Z. Liang, T. Li, M. Kim, A. Asthagiri and J. F. Weaver, *Surf. Sci.*, 2017, **356**, 299–303.
13 Z. Liu, D. G. Grinter, P. G. Lustemberg, T.-D. Nguyen-Phan, Y. Zhou, S. Luo, I. Waluyo, E. J. Crumlin, D. J. Stacchiola, J. Zhou, J. Carrasco, H. F. Busnengo, M. V. Ganduglia-Pirovano, S. D. Senanayake and J. A. Rodriguez, *Angew. Chem., Int. Ed.*, 2016, **55**, 7455–7459.

14 P. G. Lustemberg, P. J. Ramírez, Z. Liu, R. A. Gutiérrez, D. G. Grinter, J. Carrasco, S. D. Senanayake, J. A. Rodriguez and M. V. Ganduglia-Pirovano, *ACS Catal.*, 2016, **6**, 8184–8191.
15 H. F. Li, Z.-Y. Li, Q.-Y. Liu, X.-N. Li, Y.-X. Zhao and S.-G. He, *J. Phys. Chem. Lett.*, 2015, **6**, 2287–2291.
16 F. Solymosi, A. Szöke and J. Cserény, *Catal. Lett.*, 1996, **39**, 157–161.
17 N. K. Razdan, A. Kumar and A. Bhan, *J. Catal.*, 2019, **372**, 370–381.
18 M. Rahman, A. Sridhar and S. J. Khatib, *Appl. Catal., A*, 2018, **558**, 67–80.
19 S. Posada-Perez, J. R. dos Santos Politi, F. Viñes and F. Illas, *RSC Adv.*, 2015, **5**, 33737–33746.
20 T. Zhang, X. Yang and Q. Ge, *Catal. Today*, 2019, **339**, 54–61.
21 W. Ding, S. Li, G. D. Meitner and E. Iglesia, *J. Phys. Chem. B*, 2001, **105**, 506–513.
22 J. M. Horn, Z. Song, D. V. Potapenko, J. Hrbek and M. G. White, *J. Phys. Chem. B*, 2005, **109**, 44–47.
23 V. Pallassana and M. Neurock, *J. Catal.*, 2000, **191**, 301–317.
24 J. N. Brønsted, *Chem. Rev.*, 1928, **5**, 231–338.
25 M. G. Evans and M. Polanyi, *Trans. Faraday Soc.*, 1938, **34**, 11–24.
26 T. Cai, Z. Song, J. A. Rodriguez and J. Hrbek, *J. Am. Chem. Soc.*, 2004, **126**, 8886–8887.
27 J. A. Rodriguez and J. Hrbek, *Surf. Sci.*, 2010, **604**, 241–244.
28 J. A. Rodriguez, P. Liu, J. Graciani, S. D. Senanayake, D. C. Grinter, D. Stacchiola, J. Hrbek and J. Fernandez-Sanz, *J. Phys. Chem. Lett.*, 2016, **7**, 2627–2639.
29 J. Kang, M. Mahapatra, N. Rui, I. Orozco, R. Shi, S. D. Senanayake and J. A. Rodriguez, *J. Chem. Phys.*, 2020, **152**, 054702.
30 Z. Song, T. Cai, J. A. Rodriguez, J. Hrbek, A. S. Y. Chan and C. M. Friend, *J. Phys. Chem. B*, 2003, **107**, 1036–1043.
31 Z. Song, T. Cai, Z. Chang, G. Liu, J. A. Rodriguez and J. Hrbek, *J. Am. Chem. Soc.*, 2003, **125**, 8059–8066.
32 P. Reinke and P. Oelhafen, *Surf. Sci.*, 2000, **468**, 203–215.
33 J. A. Rodriguez, J. Dvorak and T. Jirsak, *Surf. Sci.*, 2000, **457**, L413–L420.
34 T. P. St. Clair, T. Oyama, D. F. Cox, S. Otan, Y. Ishizawa, R. L. Lo, K. Fukui and Y. Iwasawa, *Surf. Sci.*, 1999, **426**, 187–198.
35 S. Posada-Perez, P. J. Ramirez, J. Evans, F. Viñes, P. Liu, F. Illas and J. A. Rodriguez, *J. Am. Chem. Soc.*, 2016, **138**, 8269–8278.
36 J. A. Rodriguez, P. Liu, J. Dvorak, T. Jirsak, J. Gomes, Y. Takahashi and K. Nakamura, *J. Chem. Phys.*, 2004, **121**, 465–474.
37 F. Frantz and S. V. Didziulis, *Surf. Sci.*, 1998, **412/413**, 384.
38 S. V. Didziulis, P. Frantz, S. S. Perry, O. El-bjeirami, S. Imaduddin and P. B. Merrill, *J. Phys. Chem. B*, 1999, **103**, 11129.
39 J. B. Park, J. Graciani, J. Evans, D. Stacchiola, S. Ma, P. Liu, A. Nambu, J. F. Sanz, J. Hrbek and J. A. Rodriguez, *Proc. Natl. Acad. Sci. U. S. A.*, 2009, **106**, 4975–4980.
40 J. A. Rodriguez, P. Liu, J. Hrbek, M. Pérez and J. Evans, *J. Mol. Catal. A: Chem.*, 2008, **281**, 59–65.
41 Y. Yang, J. Evans, J. A. Rodriguez, M. G. White and P. Liu, *Phys. Chem. Chem. Phys.*, 2010, **12**, 9909–9917.
42 J. A. Rodriguez, J. Evans, L. Feria, A. B. Vidal, P. Liu, K. Nakamura and F. Illas, *J. Catal.*, 2013, **307**, 162–169.
43 O. Lamiel, S. T. Bromley and F. Illas, *Theor. Chem. Acc.*, 2013, **132**, 1312.
44 J. P. Perdew, K. Burke and M. Ernzerhof, *Phys. Rev. Lett.*, 1996, **77**, 3865–3868.
45 J. R. d. S. Politi, F. Viñes, J. A. Rodriguez and F. Illas, *Phys. Chem. Chem. Phys.*, 2013, **15**, 12617–12625.
46 L. Vega, J. Ruvireta, F. Viñes and F. Illas, *J. Chem. Theory Comput.*, 2018, **14**, 395–403.
47 S. Grimme, J. Antony, S. Ehrlich and S. A. Krieg, *J. Chem. Phys.*, 2010, **132**, 154104.
48 G. Henkelman, B. P. Uberuaga and H. A. Jónsson, *Phys. Rev. B: Condens. Matter Mater. Phys.*, 2000, **113**, 9901–9904.
49 A. H. Larsen, J. J. Mortensen, J. Blomqvist, I. E. Castelli, R. Christensen, M. Dułak, J. Friis, M. N. Groves, B. Hammer, C. Hargus, E. D. Hermes, P. C. Jennings, P. B. Jensen, J. Kermode, J. R. Kitchin, E. L. Kolsbjerg, J. Kubal, K. Kaasbjerg, S. Lysgaard, J. B. Maronsson, T. Maxson, T. Olsen, L. Pastewka, A. Peterson, C. Rostgaard, J. Schiøtz, O. Schütt, M. K. S. Strange, T. Vegge, L. Vilhelmsen, M. Walter, Z. Zeng and K. W. Jacobsen, *J. Phys.: Condens. Matter*, 2017, **29**, 273002.
50 S. Smidstrup, A. Pedersen, K. Stokbro and H. Jónsson, *J. Chem. Phys.*, 2014, **140**, 214106.
51 G. Kresse and J. Furthmüller, *Phys. Rev. B: Condens. Matter Mater. Phys.*, 1996, **54**, 11169–11186.
52 J. S. Yoo, J. Schumann, F. Studt, F. Abild-Pedersen and J. K. Nørskov, *J. Phys. Chem. C*, 2018, **122**, 16023–16032.
53 W. Wu, P. J. Ramirez, D. Stacchiola and J. A. Rodriguez, *Catal. Lett.*, 2014, **144**, 1418–1424.

Chapter 6

Metal carbides and nitrides surface reconstruction

6.1 Introduction

This chapter and the subsequent publication were not initially intended to be part in the present Thesis, nevertheless, the main topic discussed had a crucial impact on the previous Chapter, which made its inclusion compulsory. On Chapter 6, the insights on methane activation catalysed by TMC NPs have been discussed, and their performance compared to that of the MoC bulk extended surfaces. This comparison was crucial to determine the importance of a NP ensemble on methane activation and, additionally, another feature was revealed while studying the MoC extended surfaces. Methane adsorption onto the δ-MoC surface seemed to be sufficient to trigger a surface reconstruction revealing a lower energy pattern. Since methane is a very stable molecule featuring physisorption only, one may wonder whether the reconstructed surface is indeed the most stable one. Note also that ignoring such a reconstruction could lead to misleading conclusions about the interaction of methane (or other adsorbates) and δ-MoC, *e.g.*, a mistakenly large E_{ads}. The unveiling of this feature motivated the study of the relative stability of the ideal and reconstructed δ-MoC surfaces. During the research, other similar transition metal carbides and nitrides (WC, MoN, and WN) were unveiled generating similar reconstruction patterns. The studied surfaces displaying reconstruction patterns are (001) cuts from cubic $Fm\bar{3}m$ rock-salt structures, which are not the most stable polymorph structures at standard conditions for any of the explored materials. Subsequently, one may wonder if the reconstruction process is a natural consequence of the metastable bulk structure from where the surfaces were obtained. In fact, for many other carbides or nitrides such as Ti, Zr, Hf, V, Nb, and Ta, the rock-salt structure is the most stable polymorph under standard conditions,[142] and the (001) surface is the most stable one.[19] Nevertheless, these surfaces do not feature any reconstruction, just some rumpling, which is the mere vertical relaxation of both metal and non-metal atoms with respect to their bulk positions.[19] Accounting on the obtained results and the already mentioned features for the remanent TMCs, this Chapter brings strong evidence of the driven force behind the reconstruction of the, in principle, more most stable surfaces, *i.e.*, (001), obtained from metastable bulk structures.

6.2 Results

In order to validate the obtained results, it is primordial to accurately model the cubic $Fm\bar{3}m$ structures of MoC, WC, MoN, and WN. In this sense, the first step implied the comparison of the presently optimized lattice parameters with those obtained from the literature, either experimental or computational.[8,11,143-147] In general, the present values were in concordance with the literature, just in some cases there existed a small discordance. Lattice parameters of MoC and WC are displaced 0.1 Å, and MoN presents a displacing of 0.2 Å with respect to experiment. These differences represent relative errors of only 2% up to 4% for MoN particular case, small variations that effectively validates the computed models.

Next, the surface energy of the different surfaces was computed in two different manners, fixed and relaxed. The former is calculated as

$$\gamma^{fix} = \frac{E_{slab}^{fix} - nE_{bulk}}{2A} \quad (6.1),$$

where E_{slab}^{fix} correspond to the bulk-truncated energy of the model slab with all atoms at the bulk environment positions, E_{bulk} stands for the bulk energy per formula unit, *n* is the number of formula units repeated in the slab model and, *A* corresponds to the area of on one of the slab model surfaces. The computation of this essentially theoretical value provides a self-check on the computational models and methods, because the same value must be obtained for the different supercells considered, *i.e.*, (1×1), (2×2), (3×3), (4×4), or any other supercells, defined as in section 4.2.3. The use of a PWs basis set may induce small discordances due to a different density of PWs in the supercell for a given cutoff. Nevertheless, the obtained results showed that the difference between γ^{fix} computed for the different supercell was, in each case, minimal, hence validating the present approach. The relaxed surface energy was calculated as

$$\gamma^{rel} = \frac{E_{slab}^{rel} - nE_{bulk}}{A} - \gamma^{fix} \quad (6.2),$$

where most parameters have been already commented except, the E_{slab}^{rel} that is the total energy of the fully relaxed slab. The difference between surface energies allows to quantify which is the relaxation energy. To keep it simple, the analysis of the obtained results derived from the difference in relaxation energies is only discussed for the δ-MoC surface.

The (1×1) unit cell of the δ-MoC surface relaxes just displaying the typical rumpling observed for most transition metal carbides.[19] The further frequency analysis of the relaxed layers, obtained by the diagonalization of the Hessian matrix obtained from discrete displacements of analytical gradients, showed positive eigenvalues only. Nevertheless, it has been shown that this surface can undergo reconstruction when interacting with Ni, Cu, and Au atoms in large supercells.[148] Again, the question that arises is whether the reconstruction is triggered by the adsorbate, as commented for methane above, or it is intrinsic of the surface and hidden when a small supercell is used to represent the surface. In the latter case, the use of larger supercells will unveil the reconstruction, if any. In order to determine which is the driven feature affecting the reconstruction, the unit cell was doubled and the overall structure fully relaxed by the corresponding geometry optimization. This showed that the symmetry displayed by the (1×1) supercell remained. Nevertheless, the frequency analysis revealed some imaginary frequencies, and a subsequent optimization displacing the atoms along the imaginary frequencies, leaded to a different structure with a lower surface energy and all frequencies displaying positive values. The obtained reconstructed structure for the (2×2) supercell is illustrated in Figure 6.

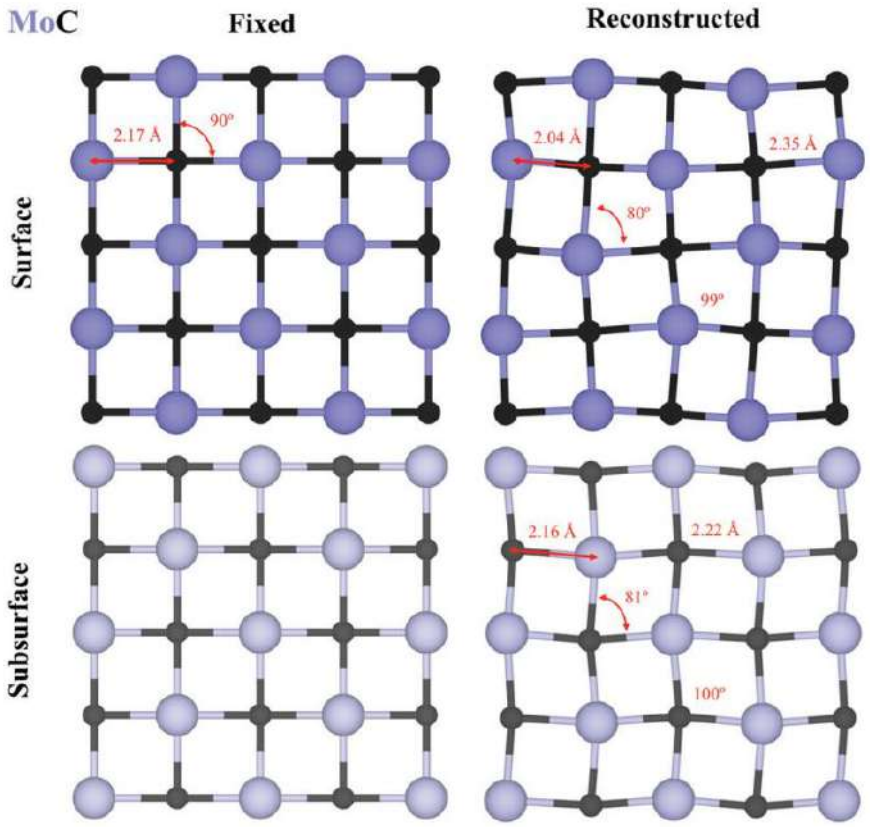

Figure 6. First (top) and second (bottom) layers of the δ-MoC(001) surface in the reconstructed structure (right) and as in the bulk-truncated structure (left). Black and violet spheres correspond to C and Mo atoms, respectively.

The same procedure was carried out for the (3×3) and (4×4) supercells leading to the same reconstruction without imaginary frequencies. However, it must be pointed out that the (3×3) supercell introduces an artificial distortion which becomes apparent as it displays a slightly larger surface energy. Analysing the (4×4) model it is clear that the artificial distortion comes from the impossibility for the (3×3) model to properly duplicate the reconstruction pattern observed in the (2×2) model.

Next, the effect of surface thickness was considered in order to determine its impact on determining the structure of the reconstructed surface, as the (2+2) scheme could be considered insufficient to ensure the results validity. Hence, a (6+2) scheme was considered, where the 6 outermost layers were fully relaxed and the 2 innermost layers were left fixed as in bulk. The non-relaxed model presents the same surface energy as in the (2+2) scheme model, which, as already mentioned, provides a self-check. On the other hand, the relaxed structures display a significant difference on the surface energy, where the thickest model (8 layers) shows a lower energy, making clear the limitation of the (2+2) scheme on regards of calculating the surface energy. Nevertheless, the optimized

structure obtained after the reconstruction remained unaltered, confirming the validity of the obtained trends on the (2+2) scheme models.

In general, the trends obtained for the δ-MoC surface model hold for all the studied materials, however, some special features appeared when analysing those that remain unexplained. WN does not display a different energy surface when comparing the (3×3) and (4×4) reconstructed models, as both patterns are identical, meaning that WN reconstruction pattern is already converged in the (3×3) supercell model. Another differential aspect is that all the other (2×2) surface models explored, directly reconstruct when relaxed without any prior action. Moreover, the N based materials showed negative surface energies, which can be explained because the surface reconstruction is determined by the bulk structure instability, which provokes that the surface reconstruction tends to change the surface phase to that of a hexagonal environment. Thus, the bulk instability is partially remediated when the surface atomic layers are reconstructed and the energy lowering largely contributes to the surface energy lowering.

Finally, a detailed comparison between the difference in energy between the more unstable cubic crystal and the most stable hexagonal structure, reveals that the more unstable the cubic cell is compared to its hexagonal counterpart, the larger the reconstruction is. This can be observed as well in the geometry changes. In other words, the larger the difference in bulk stability with respect to the most stable polymorph, the larger the distance and angle distortions. This trend seems to confirm, the already commented hypothesis that the reconstruction process is driven by the relative instability of these polymorph with respect to the most stable one. The distortions observed try to compensate the energetic and geometric difference with respect to the most stable structure.

6.3 Conclusions

The present Chapter summarize a purely theoretical work aiming to explain the main insights on the predicted reconstruction processes displayed by some transition metal carbides and nitrides. The modelling and further optimization allowed to reveal the reconstruction process and an inherent defect of those models too small to reproduce the reconstruction pattern. The obtained surface energies agree with an earlier observed trend for transition metal system, where the larger the bulk instability, the smaller the surface

energy. Furthermore, a detailed analysis of the relaxation degree, size, and energetic terms has been provided. The calculations indicated that the main driven force for such reconstructions seems to be the relative bulk instability of the present polymorphs with respect to the most stable ones at standard conditions.

For a more detailed description, the reader is referred to the publication included below. The supporting information of the present publication, can be found in Appendix B.

Contribution: models preparation, DFT based calculations, results interpretation, scientific discussion, and providing a first draft of the publication.

6.4 Publication

Bulk (in)stability as a possible source of surface reconstruction

PCCP

ROYAL SOCIETY OF CHEMISTRY

PAPER

View Article Online
View Journal | View Issue

Cite this: *Phys. Chem. Chem. Phys.*, 2020, **22**, 19249

Bulk (in)stability as a possible source of surface reconstruction†

Marc Figueras,‡ Anabel Jurado,‡ Ángel Morales-García, Francesc Viñes and Francesc Illas *

Received 17th July 2020,
Accepted 30th July 2020

DOI: 10.1039/d0cp03819a

rsc.li/pccp

A density functional theory based study is presented with the aim of addressing the surface energy stabilization mechanisms of transition metal carbide and nitride surfaces from a crystal structure different from that of the most stable polymorph. To this end, we consider the MoC(001), MoN(001), WC(001), and WN(001) surface of rocksalt structures, which, for these compounds, is not the most stable one. The geometry optimization of suitable slab models shows that all these surfaces undergo a sensible reconstruction. The energy difference per formula unit between the rock salt and the most stable polymorph seems to be the driving force behind the observed reconstruction. A note of caution is given in that certain small periodic boundary conditions can artificially restrain such reconstructions, for which at least (2×2) supercells are needed. Also, it is shown that neglecting such a surface reconstruction can lead to artifacts in the prediction of the chemical activity and/or reactivity of these surfaces.

Introduction

Well-defined surfaces can be experimentally prepared for a great variety of materials, including metals, oxides, nitrides and carbides, and their study and comprehension is actually one of the main focuses of the Surface Science field.[1] Most often the low Miller index surfaces are the most stable ones, where their surface atomic structure follows the periodicity of the corresponding bulk crystal structure. However, there are many cases where such ideally cut surfaces are not experimentally realized because they undergo relaxation and/or reconstruction processes. The former just implies a change in the atomic interlayer separation relative to the bulk crystal truncation, while the latter does involve a change in the periodic symmetry with respect to the bulk.[1] Both relaxation and reconstruction are ubiquitous with a large number of cases reported in the literature.[2] It is commonly accepted that relaxation and/or reconstruction processes occur because the ideal surface features an excessively large surface energy, which stems out from the energy cost of breaking the bonds of the surface atoms from their bulk environment so as to generate the surface.[3] As a result, a given surface gets further stabilized when undergoing such processes, reducing the surface formation energy costs. In other words, relaxation and reconstruction occur because the ideal surface is, intrinsically, unstable. This explanation must necessarily hold when, under normal working conditions, the corresponding bulk is the most stable polymorph. Recently, it has been shown for a series of transition metals in a higher-in-energy polymorph that they feature surfaces relaxed more than expected, thus lowering the surface energy so as to compensate the inherent bulk instability.[4] However, predicting whether a given well-defined surface will reconstruct or not is generally unfeasible without the help of a theory behind. For compounds with several stable polymorphs one may wonder whether the surfaces of the non-most stable polymorph inherit somehow the lack of stability, which, consequently, would lead as well to a further reconstruction.

In the present work, we explore the hypothesis of whether the surface reconstruction naturally emerges for metastable polymorphs by analyzing the stability of the most stable (001) surfaces of MoC, WC, MoN, and WN displaying a cubic $Fm3m$ rocksalt crystal structure. For binary transition metals and carbides and nitrides such as Ti, Zr, Hf, V, Nb, and Ta, such a rocksalt crystal structure is indeed the most stable polymorph under standard conditions of pressure and temperature,[5] and the (001) surface is the most stable one, exhibiting just a small rumpling in which metal and non-metal atoms relax vertically with respect to the surface, yet in opposite directions.[6] However, for the four compounds mentioned earlier, the most stable structure has a hexagonal symmetry, $P6_3/mmc$ for MoN[7] and $P\bar{6}m2$ for MoC, WC, and WN,[5] although their $Fm3m$ rocksalt cubic form also exists under other somewhat harsher conditions. For instance, cubic MoC—usually referred to as δ-MoC—is broadly used in model studies in catalysis even if, to

Departament de Ciència de Materials i Química Física & Institut de Química Teòrica i Computacional (IQTCUB), Universitat de Barcelona, c/Martí i Franquès 1-11, 08028 Barcelona, Spain. E-mail: francesc.illas@ub.edu

† Electronic supplementary information (ESI) available. See DOI: 10.1039/d0cp03819a

‡ Both authors contributed equally.

date, it has not been possible to prepare single crystals,[8,9] and it has only been acquired in the form of nanocrystallites. The rocksalt WC (γ-WC), though, has actually been prepared long ago and its crystal structure reported,[10] whereas the cubic form of MoN and WN has also been reported, although at high temperature conditions[11] or in the form of thin films.[12] The variety of cases of such compounds, but at the same time being of the same family of transition metal carbide or nitride compounds, makes them an ideal set to test the aforementioned hypothesis that the existence of a lower energy polymorph prompts a surface reconstruction, even in the most stable featured surfaces.

Computational details

The stability of the (001) surfaces of δ-MoC, γ-WC, and *Fm*3*m* MoN and WN has been studied by means of periodic density functional theory (DFT) based calculations employing the broadly used Perdew–Burke–Ernzerhof (PBE)[13] exchange–correlation functional within the generalized gradient approach (GGA). All calculations have been carried out with the Vienna *Ab Initio* Simulation Package (VASP) code,[14] where the valence electron density has been expanded by a plane wave basis set with a 415 eV cutoff for the kinetic energy, whereas the effect of the core electrons on the valence density has been accounted for through the projector augmented-wave (PAW) method.[15] Numerical integrations have been carried out in reciprocal space at the **k**-point nodes generated through optimal Monkhorst–Pack meshes. The variations in the total energy due to the use of a larger basis set or the use of denser **k**-point meshes have been found to be converged below 0.01 eV (see also Table S1 in the ESI†).

The (001) surfaces of interest have been represented by slab models cut from the PBE optimized bulk structure, using a regular cubic unit cell and a **k**-point mesh of 17×17×17 dimensions. The same **k**-point density has been used to optimize the hexagonal crystal cells of the explored materials. The (001) surface slab models have been constructed displaying four atomic layers, with the two outermost ones allowed to relax, and the two innermost frozen at the bulk geometry—the so-called 2+2 scheme—with a vacuum width of 15 Å between the interleaved slabs. For the purposes of the present work, these slab models should be enough to reach a sound conclusion, especially regarding the plane-wave kinetic energy cutoff and the vacuum width between the periodically repeated slabs. This is further supported by results reported in the ESI† involving a tighter energy cutoff and a larger vacuum width. The influence of the slab thickness has also been considered as described in detail in the next section.

Different supercells of increasing size have been used so as to tackle the surface stability. In particular, $(\sqrt{N}\times\sqrt{N})R45^\circ$ supercells have been considered, with N = 1–4. However, for simplicity, we denote these hereafter as (N×N) supercells, for whose numerical integrations we use optimal **k**-point meshes of 9×9×1, 5×5×1, and 3×3×1 for N = 1 to 3, respectively, and Γ point optimizations for the (4×4) supercell. Notice that, for a stable surface, the calculated surface energy does not depend on the size of the supercell used. However, for unstable surfaces the use of an excessively small supercell may lead to misleading results, as the structural optimization may be biased by the constraints imposed by an artificial periodic symmetry. In that case, a frequency (phonon) calculation will clearly show that the structure is not dynamically stable. On the other hand, larger supercells provide additional degrees of freedom so that the geometry optimization may result in a different surface structure with a lower surface energy; a clear fingerprint that the surface is likely to undergo a reconstruction. A plausible reconstruction pattern is proposed based on the minimization of the imaginary frequencies for every surface model. However, it must be pointed out that the encountered reconstruction pattern cannot, in any case, be considered as the global minimum, since following the imaginary frequency paths only ensures the characterization of a local minimum. The subsequent research of a global minimum is out of the current scope. Note, in addition, that this quest for a global minimum requires much larger models, which drive the computational cost excessively up. In any case, the stability of the reported reconstruction is supported by a series of additional calculations involving different initial reconstruction patterns in the (4×4) MoC supercell as shown in the ESI.† The fact that all proposed initial patterns converge to the reconstruction pattern displayed in Fig. 1, provides strong support for the claim that the ideal surface is unstable and if prepared in ultra high vacuum (UHV) conditions by appropriate cleavage it will undergo a reconstruction. To provide more quantitative data and support the abovementioned statements, we focus on the

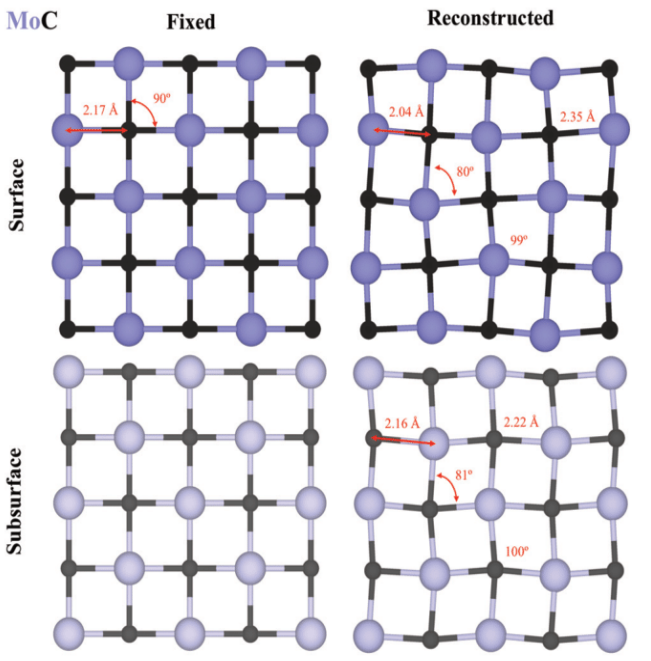

Fig. 1 First (top panels) and second (bottom panels) atomic layer for fixed (bulk-truncated) *vs.* reconstructed (2×2) supercells of the δ-MoC (001) surface. Violet and black spheres correspond to Mo and C atoms, respectively.

surface energy of the relaxed slab surface, γ^{rel}, usually defined as

$$\gamma^{rel} = \frac{E^{rel}_{slab} - nE_{bulk}}{2A} \quad (1)$$

where E^{rel}_{slab} is the total energy of the fully relaxed slab, while E_{bulk} stands for the bulk energy per formula unit, n is the number of formula units repeated in the slab model, and, finally, A corresponds to the created area on one side of the slab model. By construction, eqn (1) requires a full relaxation of the slab surface model and, since it must provide a suitable bulk environment for the surface atomic layers, this implies using a rather large number of atomic layers. Alternatively, one can provide the bulk environment to the surface region by keeping the bottom layers fixed, *i.e.*, the 2+2 scheme described earlier. In this type of models, γ^{rel} is computed in two steps:[16] first, the bulk-truncated surface energy is defined as

$$\gamma^{fix} = \frac{E^{fix}_{slab} - nE_{bulk}}{2A} \quad (2)$$

which is similar to eqn (1) but with E^{fix}_{slab} corresponding to the bulk-truncated energy of the slab model with all atoms at the bulk environment positions. Then, γ^{rel} is calculated as:

$$\gamma^{rel} = \frac{E^{rel}_{slab} - nE_{bulk}}{A} - \gamma^{fix} \quad (3)$$

This approach allows one to significantly reduce the computational burden since it involves slab models with a smaller number of atomic layers and, in addition, not all need to be relaxed. The computational saving is especially important for large supercells where the use of thicker slabs can become computationally prohibitive.

Results and discussion

We start the discussion of the results by commenting on the optimized lattice parameters for the cubic *Fm3m* structures of MoC, WC, MoN, and WN, listed in Table 1 and compared to experimental available data and previously calculated results.[16–22] Not surprisingly, the present values for the calculated lattice parameters are in good agreement with previous work and nicely agree with the available experimental data. However, in some cases the maximum absolute value is of ~0.1 Å for MoC and WC and ~0.2 Å for MoN, representing maximum relative errors of only ~2% in general, up to ~4% for the MoN particular case. For the latter, the error is larger than the average one for crystal structures predicted by DFT methods and, in view of the metastable character of these polymorphs and their synthesis difficulty, we attribute, at least in part, this discrepancy to a lack of accuracy due to problems in the experiments, which cannot be discarded.

Table 1 Calculated (PBE) and experimental (Exp.) lattice parameters for the cubic, rocksalt *Fm3m* crystal structures of MoC, WC, MoN, and WN, as well as comparison to previously calculated values found in the literature (Lit.). All values are given in Å

	MoC	WC	MoN	WN
Exp.	4.278[a]	4.266[b] 4.252[d]	4.110[c]	—
Lit.	4.373[e]	—	4.304[f]	4.351[g]
PBE	4.342	4.387	4.346	4.357

[a] Ref. 22. [b] Ref. 17. [c] Ref. 19. [d] Ref. 18. [e] Ref. 16. [f] Ref. 20. [g] Ref. 21.

Table 2 Calculated relaxed surface energies, γ^{rel}, in J m^{-2}, for the different supercells used to represent the different (001) surfaces. The bulk-truncated, fixed surface energies, γ^{fix}, are given in parentheses

Supercell		(1×1)	(2×2)	(3×3)	(4×4)
MoC	γ^{fix}	1.41	1.41	1.41	1.41
	γ^{rel}	0.77	0.67	0.70	0.67
WC	γ^{fix}	1.43	1.43	1.44	1.43
	γ^{rel}	0.66	0.59	0.62	0.61
MoN	γ^{fix}	1.11	1.11	1.09	1.11
	γ^{rel}	−0.77	−0.75	−0.67	−0.79
WN	γ^{fix}	1.07	1.06	1.07	1.06
	γ^{rel}	−1.57	−1.35	−1.81	−1.83

Next, we analyze first the bulk truncated surface energy for the four explored surfaces. As defined in the computational details, this quantity corresponds to the surface energy of the generated slab without allowing any surface relaxation or reconstruction. The reason to include this purely theoretical quantity is that it provides a self-check on the computational models and methods, as the obtained values for the (2×2), (3×3), and (4×4) supercells must coincide with that of the (1×1) supercell. In the case of using a plane wave basis set, small differences may be present because, for a given cutoff, the density of plane waves in the supercell differs, leading in each case to a somehow different quality of the basis set, and a similar slight change is to be expected in the **k**-point density. However, the γ^{fix} results compiled in Table 2 show that these differences are minimal, thus validating the present approach. Furthermore, the results align with those already found for transition metal surfaces,[4] insomuch the more unstable the cubic bulk crystal structure is with respect to the most stable hexagonal one, see Table 3, the lower the γ^{fix} surface energy. Thus, such a rule-of-a-thumb seems to be more general, and applicable beyond the transition metal material family.

Now we analyze the results corresponding to the surface energy as predicted from the different supercells. For the sake of simplicity we will focus on the case of δ-MoC (001), where the relaxation of the (1×1) unit cell after cleavage leads to the typical rumpling of the surface atoms as observed for most of the cubic transition metal carbides,[23] while preserving the *Fm3m* cubic symmetry. This structure has actually been often taken as the ground state for this particular surface as a frequency analysis of the relaxed layers, gained by Hessian matrix construction by discrete displacements of 0.03 Å and its diagonalization, displays only positive values. Interestingly, though, the interaction of Ni, Cu, and Au atoms on this surface has shown that adsorbate induced reconstruction takes place as revealed for low coverage situations and, hence, large supercells.[24]

At this point one may still wonder whether the reconstruction is really triggered by the adsorbate, or its absence was due

Table 3 Geometric parameters of the surface layer (surf) or the first subsurface layer (sub) for the different explored reconstructed (001) surfaces, including the variation of metal–carbon distances with respect to that of the unreconstructed surface, d(CO), in Å, and the changes of in-plane angles, α, in degrees. Finally, the difference in energy between cubic and hexagonal bulk structures, ΔE, is provided, given per formula unit and in eV

	MoC	WC	MoN	WN
$d(CO)^{surf}$	±0.18	±0.17	±0.07	±0.32
$d(CO)^{sub}$	±0.05	±0.05	±0.05	±1.24
α^{surf}	±10	±10	±13	±13
α^{sub}	±10	±12	±12	±37
ΔE	0.40	0.69	0.62	0.81

to the use of a too small a unit cell. Doubling the unit cell and relaxing the atomic structure of the top two layers still leads to a symmetric structure, preserving that of the (1×1) supercell. However, in this case, the frequency analysis reveals the presence of imaginary frequencies. Indeed, further geometry optimization starting from a slightly distorted structure along the imaginary vibration leads to a new energy minimum characterized by solely positive frequencies and resulting in a lower surface energy, as shown in Table 2.

This new structure does not preserve the original symmetry and can then be defined as the result of a surface reconstruction. To further confirm that this is a stable structure, the calculations have been repeated for larger (3×3) and (4×4) supercells. In both cases, the final reconstructed structures do not exhibit imaginary frequencies. In the case of the (3×3) supercell, though, the surface energy is slightly higher than the (2×2) one; we attribute this to the fact that this supercell does not fully duplicate the (2×2), and so one still introduces an artificial distortion. This is confirmed by the results obtained for the (4×4) supercell, which are identical to those of the (2×2), indicating that convergence is reached.

The reconstructed surface implies a rather large change in the position of the atoms of the relaxed layers (Fig. 1). At this point one may wonder whether the thickness of the slab surface model is enough to reach sound conclusions. To investigate the influence of the slab thickness on the present findings, a new series of calculations has been carried out by considering the (2×2) MoC supercell but including eight atomic layers with the six outermost fully relaxed and the two bottommost fixed as in the bulk, *i.e.*, a 6+2 scheme. For the starting structure, both models (four or eight atomic layers) lead to the same surface energy, as expected and clearly seen in Table S2 in the ESI.† For the relaxed structures there is a noticeable influence of the slab thickness, which, in view of the reconstruction of the upper atomic layers, is not at all surprising. The surface energy of the thicker slab becomes noticeably lower. However, this does not affect the reconstruction pattern and, hence, fully confirms the trends emerging from the four-layer models.

Even though the calculations outcome for the δ-MoC surface models is quite straightforward, the (001) surfaces of MoN, WC, and WN do not converge as flawless as δ-MoC (001). In fact, the WN (4×4) reconstruction pattern ends up being the same as in the (3×3) supercell, meaning that convergence has been reached anyway, but not in the same way as for δ-MoC (001). The structure of the unreconstructed and reconstructed (2×2) supercell of δ-MoC (001) is shown in Fig. 1, while the same information for the rest of the structures can be found in the ESI.† The fact that the δ-MoC (001) surface exhibits this type of reconstruction can have some implications for earlier studies where this surface reconstruction has not been taken into account. In particular, the somewhat stronger CO_2 and CH_4 adsorption on δ-MoC (001) compared to other transition metal carbides made it an outlier. Such CO_2 and CH_4 capture were explored at relatively low coverage[25] and so it seems that the stronger attachment of CO_2 and CH_4 is a consequence of utilizing a relatively large supercell. Computing the adsorption energy with respect to the reconstructed MoC (001) surface leads to a smaller value by 0.60 eV, which thus falls in line with that of the rest of the transition metal carbides.

The situation for the rest of the surfaces studied in the present work is very similar and so could be the consequence of their neglect. In all other cases, a reconstruction shows up when going from the (1×1) to the (2×2) supercell accompanied by a reduction of the surface energy, which is only slightly increasing for the (3×3) supercell, again because this implies an artificial distortion, and so the actual value converges to the (2×2) value for the largest (4×4) supercell, see Table 2, and a view of the structures in the ESI.† The only difference with respect to the case of δ-MoC is that the geometry optimization applied on the (2×2) directly leads to the reconstructed structures without further ado. A surprising point is that the nitrogen-based materials, MoN and WN, feature negative surface energies when relaxed; however, such a result should not be regarded as a degradation indication of such materials. What seems to happen is that the surface reconstruction is driven by the bulk crystal structure instability, see below, and so the surface reconstructs so as to partially change its phase back to a hexagonal environment. Consequently, part of the bulk instability is saved due to the reconstructions, and, so, this energy lowering is substantially contributing to the surface energy lowering.

One can thus take the (2×2) supercells to carry out a geometry analysis of the distortions, as shown in Fig. 1 and Fig. S2 (ESI†). The metal–carbon distances, d(MC), expand/contract across the surface and subsurface layers, which also happens with the angles, α. From the values in Table 3, one could argue that the reconstruction shape is kept when going to the subsurface layer, as the a values are kept just about constant; however, the degree of reconstruction, sized by d(MC), diminishes, and, so, the reconstruction is more of a surface process that dilutes when penetrating the material.

Last, it is important to relate the difference in energy between the more unstable cubic crystal cell and the most stable hexagonal one, listed as ΔE in Table 3, with the extent of the surface reconstruction. A detailed inspection reveals that, similarly to the aforementioned γ^{fix} trend, the more unstable the cubic cell, the lower γ^{rel}, and, therefore, the larger the reconstruction. This is also observable in the geometry changes, especially on the first surface layer, reported in Table 3; the larger the difference in bulk stability with respect to the most stable polymorph, the larger the

distance and angle distortions. Thus, this seems to be a clear indication that the observed reconstruction relates to the fact that the crystal structure of these polymorphs is not the most stable one, which *de facto* acts as a driving factor, likely implying distortions of the surface as much as possible so as to cover the energetic and geometric distance with respect to the hexagonal crystal cell environment, and, ultimately, expressing reconstructed surfaces whose activity may well be different from the regular rocksalt (001) ones, and different from the hexagonal crystal structure surfaces.

Conclusions

The present theoretical work addresses the relaxation or reconstruction processes occurring on the surfaces of transition metal carbide and nitride materials displaying a bulk crystallographic structure (rocksalt) higher in energy compared to the most stable one (hexagonal). In this sense, the (001) surfaces of rocksalt crystal structures of MoC, MoN, WC, and WN have been modeled and optimized, revealing that such undergo a surface reconstruction, which can be artificially masked when imposing certain small periodic boundary conditions. This is normally avoided when using larger supercell models, here revealing that convergence can be already reached by using (2×2) supercells.

The bulk truncated surface energies follow the trend of the larger the bulk instability, the smaller the surface energy, as earlier found on transition metal systems. Furthermore, the degree of relaxation, sized in energetic terms, in variations of the metal–carbon distances, or in variations of the layer angles, does follow the bulk instability, but it is shown that the extent of such reconstruction dilutes when going towards the interior of the material. All in all, the present study reveals that the proper depiction of such surfaces is necessary, as this can affect the overall material surface chemistry.

Conflicts of interest

There are no conflicts to declare.

Acknowledgements

The research in this work has been supported by the Spanish MICIUN RTI2018-095460-B-I00 and María de Maeztu MDM-2017-0767 grants, and, in part, by Generalitat de Catalunya 2017SGR13 grant and COST Action CA18234. A. M.-G. thanks Spanish MICIUN for a Juan de la Cierva postdoctoral grant (IJCI-2017-31979), and F. I. acknowledges additional support from the 2015 ICREA Academia Award for Excellence in University Research.

References

1 G. A. Somorjai and Y. Li, *Introduction to Surface Chemistry and Catalysis*, John Wiley & Sons, 2nd edn, 2010.
2 C. B. Duke, *Chem. Rev.*, 1996, **96**, 1237–1260.
3 J. Ruvireta, L. Vega and F. Viñes, *Surf. Sci.*, 2017, **664**, 45–49.
4 H. Lin, J.-X. Liu, H. Fan and W.-X. Li, *J. Phys. Chem. C*, 2020, **124**, 11005–11014.
5 J. G. Chen, *Chem. Rev.*, 1996, **96**, 1477–1498.
6 F. Viñes, C. Sousa, P. Liu, J. A. Rodriguez and F. Illas, *J. Chem. Phys.*, 2005, **122**, 174709.
7 C. L. Bull, P. F. McMillan, E. Soignard and K. Leinenweber, *J. Solid State Chem.*, 2004, **177**, 1488–1492.
8 S. Posada-Pérez, F. Viñes, P. J. Ramirez, A. B. Vidal, J. A. Rodriguez and F. Illas, *Phys. Chem. Chem. Phys.*, 2014, **16**, 14912–14921.
9 S. Posada-Pérez, P. Ramírez, F. Viñes, P. Liu, F. Illas and J. A. Rodriguez, *J. Am. Chem. Soc.*, 2016, **138**, 8269–8276.
10 R. H. Willens and E. Buehler, *Appl. Phys. Lett.*, 1965, **7**, 25.
11 L. E. Toth, *Transition Metal Carbides and Nitrides*, Academic, New York, 1971.
12 P. Hones, N. Martin, M. Regula and F. Lévy, *J. Phys. D: Appl. Phys.*, 2003, **36**, 1023.
13 J. P. Perdew, K. Burke and M. Ernzerhof, *Phys. Rev. Lett.*, 1996, **77**, 3865–3868.
14 G. Kresse and J. Furthmüller, *Phys. Rev. B: Condens. Matter Mater. Phys.*, 1996, **54**, 11169–11186.
15 P. E. Blöch, *Phys. Rev. B: Condens. Matter Mater. Phys.*, 1994, **50**, 17953–17979.
16 J. R. S. Politi, F. Viñes, J. A. Rodriguez and F. Illas, *Phys. Chem. Chem. Phys.*, 2013, **15**, 12617–12625.
17 A. S. Kurlov and A. I. Gusev, *Inorg. Mater.*, 2006, **42**, 121–127.
18 A. S. Kurlov and A. I. Gusev, *Russ. Chem. Rev.*, 2006, **75**, 617–636.
19 H. Jehn and P. Ettmayer, *J. Less-Common Met.*, 1978, **58**, 85–98.
20 M. B. Kanoun, S. Goumri-Said and M. Jaouen, *Phys. Rev. B: Condens. Matter Mater. Phys.*, 2007, **76**, 134109.
21 J. Qin, X. Zhang, Y. Xue, X. Li, M. Ma and R. Liu, *Comput. Mater. Sci.*, 2013, **79**, 456–462.
22 A. Fernández-Guillermet, J. Häglund and G. Grimvall, *Phys. Rev. B: Condens. Matter Mater. Phys.*, 1992, **45**, 11557–11567.
23 F. Viñes, C. Sousa, P. Liu, J. A. Rodriguez and F. Illas, *J. Chem. Phys.*, 2005, **122**, 174709.
24 G. Giacomo Asara, F. Viñes, J. M. Ricart, J. A. Rodriguez and F. Illas, *Surf. Sci.*, 2014, **624**, 32–36.
25 C. Kunkel, F. Viñes and F. Illas, *ACS Appl. Energy Mater.*, 2018, **1**, 43–47.

Chapter 7

H_2 adsorption and interaction on MoC nanoparticles supported on Au(111)

7.1 Introduction

At present, most hydrogenation reactions are catalysed by Pt-group metals,[149,150] although their scarcity and subsequent high prize seriously compromises their use in the near future. However, in the recent years, TMCs have been proposed as a valuable alternative to precious metals for several hydrogenation reactions.[2,77,130,150-153] The capabilities of these carbides are comparable or superior to those displayed by Pt-group metals, therefore, substantial efforts have been done in order to maximize their performance. Most of these efforts have been focused on studying the insights of H_2 adsorption on TMCs single crystal surfaces,[151,152] however, the effect of the NP ensemble is still unknown. In the present study, MoC_y NPs supported on Au(111) have been subjected to a H_2 rich atmosphere for an interval of increasing temperatures (300-500 K). The system characterization has been carried out at the Brookhaven National Laboratory by a combination of XPS and temperature programmed desorption (TPD). On the computational side, which is part of this thesis, several DFT based calculations have been carried out to unveil the insights in the interaction between H_2 and the MoC_y NPs. The obtained results provide strong evidence of the main aspects affecting the aforementioned interaction, such as, the easy H_2* dissociation, the rather easy diffusion of H* adatoms, the primarily role of low-coordinated Mo atoms and, the formation of Kubas complexes (adsorbed H_2 with elongated bond). The obtained results suggest that MoC_y NPs could be ideal candidates for hydrogenation catalytic reactions.

7.2 Results

In order to set a benchmark, the H_2 adsorption on a polycrystalline MoC surface was examined first. Accounting on previous studies, the C/Mo ratio of the present surface can be estimated to be around 0.98, close to the 1.0 value of the rock-salt δ-MoC.[154] Prior to the H_2 exposition, the MoC surface displayed a single peak (282.4 eV) in the C(1*s*) XPS spectra, corresponding to C atoms in the MoC surface. Upon exposure to 1 Torr of H_2 at 300 K, the C(1*s*) XPS spectra displayed and additional peak around 284.0 eV assigned to the formation of CH_x species on the MoC surface, which indicates the capacity of the MoC surface to adsorb and dissociate H_2. From C(1*s*) XPS peaks intensity, the estimated adsorbed hydrogen was around 0.2-0.3 monolayers (ML). Next, the TPD technique was applied to determine H_2 desorption between 300 and 500 K The results revealed a

complex TPD plot with numerous desorption peaks between 320 and 400 K, indicating the polycrystalline character of the surface and a concomitant large amount of defects. The H_2 total desorption occurs around 425 K. Comparing to the TPD of H_2 in Pt(111) surface, it is possible to estimate that the actual coverage of the MoC surface is 0.93 ML,[155,156] a much larger value than the 0.2-0.3 ML obtained in the XPS spectra. This feature indicates the presence of alternative adsorption sites that do not involve the formation of CH_x species.

Next, a new system composed by MoC_y NPs supported on a Au(111) surface was prepared following the same procedure commented in Chapter 5.[37] As a summary, the obtained NPs have a C/M ratio varying from 0.6 to 1.1 and the data collected from STM images indicates that their size range from 0.8 to 1.5 nm in diameter. In order to show that hydrogen does not-interact with the Au(111) surface, a TPD experiment was carried out after the exposure of a clean Au(111) surface to H_2 at 300 K. The absence of any peak in the TPD spectra indicates the inert nature of gold towards H. Next, both stoichiometries, $MoC_{0.6}$ and $MoC_{1.1}$, were prepared separately and characterized using the same techniques as in MoC surface case. After exposure to H_2, it is clear that the nanostructure shape displays a different behaviour from that of bulk MoC. Furthermore, the C/M ratio has a significant influence on the MoC_y NPs reactivity towards H_2. In the case of $MoC_{0.6}$/Au(111), the C(1*s*) XPS spectra at 300 K revealed a small amount of CH_x formed, around (0.05 ML). The obtained results could be explained due to the strong interaction between Mo and C atoms within the NPs, which is required to maintain their integrity. The TPD estimates that the H coverage in $MoC_{0.6}$/Au(111) surface is 0.27 ML, a substantially smaller coverage compared to that of the bulk MoC (0.93 ML).Nevertheless, it is consistent taking into account the fact that the amount of $MoC_{0.6}$ NPs in the gold substrate is of 0.3 ML only. Since Au does not interact with H_2, the same proportion is maintained.

On the other hand, a totally different behaviour was observed for the $MoC_{1.1}$/Au(111) system. The increase in C/M ratio implies an increase in reactivity towards H_2 adsorption and dissociation. The obtained C(1*s*) XPS spectra for the $MoC_{1.1}$/Au(111) system displayed two peaks with the same intensity, which implies that 50% of all C atoms in the system are involved in CH_x species. The adsorption and desorption processes are fully reversible as, once heated to 500 K, no trace of H remained and the process can be repeated several times without affecting the C/M ratio. The TPD

plot displayed different peaks indicating the presence of different active sites. Moreover, it can be estimated a total H coverage of 0.58 ML, which implies a H/C ratio of 2, a much larger value than the observed for both, $MoC_{1.1}$ NPs and δ-MoC surface. Hence, indicating the outstanding capacity of $MoC_{1.1}$/Au(111) to capture H_2 and pointing them as suitable systems for hydrogenation reactions.

To understand the outcome of the experiments, a series of DFT based calculations were carried out. The main goal here being to unveil the microscopic details of the interaction between H_2 and the MoC NPs/Au(111) system. The study was restricted to the stoichiometric NPs, the most valuable asset reported by the experiments. Accounting on the methodology reported in section Section 4.2.2, a low energy $Mo_{12}C_{12}$ NP structure was selected. The Au(111) support is as already reported in Chapter 5 and explained in Section 4.2.1. The total system consists of a Au(111) four-layered *p*(6×6) slab model with 30 Å vacuum, where the selected $Mo_{12}C_{12}$ NP was supported following the procedure reported in Section 4.2.1. Next, H_2 and H* adatoms were adsorbed in all non-equivalent sites within the supported NP. Results obtained indicate that both species attach with similar strength to the NP, but H_2 having a preference for low-coordinated Mo sites and H* adatoms displaying a preference for low-coordinated C atoms. The H* adatom stability was further analysed by comparing to that of H* adatom on δ-MoC (001). From the data in a previous study,[157] the observed H* E_{ads} in the present calculations was slightly larger than that of H* adatoms adsorbed on δ-MoC (001) surface (ΔE_{ads}=0.05 eV). Assuming order two desorption kinetics, $H^*+H^* \rightarrow H_2^* \rightarrow H_2$, and estimating desorption temperatures of the maximum desorption rates via Redhead equation, revealed a shift in the TPD spectra of 19-28 K between the $Mo_{12}C_{12}$/Au(111) system and δ-MoC surface, which is in perfect agreement with the obtained experiments shift (~30 K). Moreover, the large H* adsorption energy displayed by low-coordinated Mo atoms on $Mo_{12}C_{12}$/Au(111) system (-0.54 eV) contradicts the disadvantageous H* adsorption energy computed for Mo atoms on the δ-MoC surface (0.12 eV).[157] This aspect can be interpreted as an activity-killing effect held by neighbouring C atoms on Mo atoms that is countered by the low-coordination of Mo atoms in $Mo_{12}C_{12}$/Au(111) system. Nevertheless, it is not possible to discard the effect of a particular electronic arrangements to the nanoscale ensemble.

In order to study the hydrogen dissociation, several reaction paths were studied. The obtained results on the H_2 anchoring sites revealed dissociation energy barriers as

low as 0.2 eV on top of low-coordinated Mo atoms, a much lower value compared to the 0.39 eV energy barrier of the extended δ-MoC surface.[157] The promoted H_2* dissociation leads to a partial occupation of the MoC_y perimeter, suggesting that H* diffusion could occur. To investigate this possibility, all non-equivalent diffusions paths in the $Mo_{12}C_{12}$ were studied, and are displayed in Figure 7. The obtained results were analysed focusing on the largest energy barrier that should be overcame in order to fill the proposed sites. The largest diffusion barrier encountered was 0.76 eV, a much lower value compared to the extended δ-MoC surface (0.95 eV). Hence, implying that the H* diffusion is well promoted on the $MoC_{1.0}$/Au(111) system.

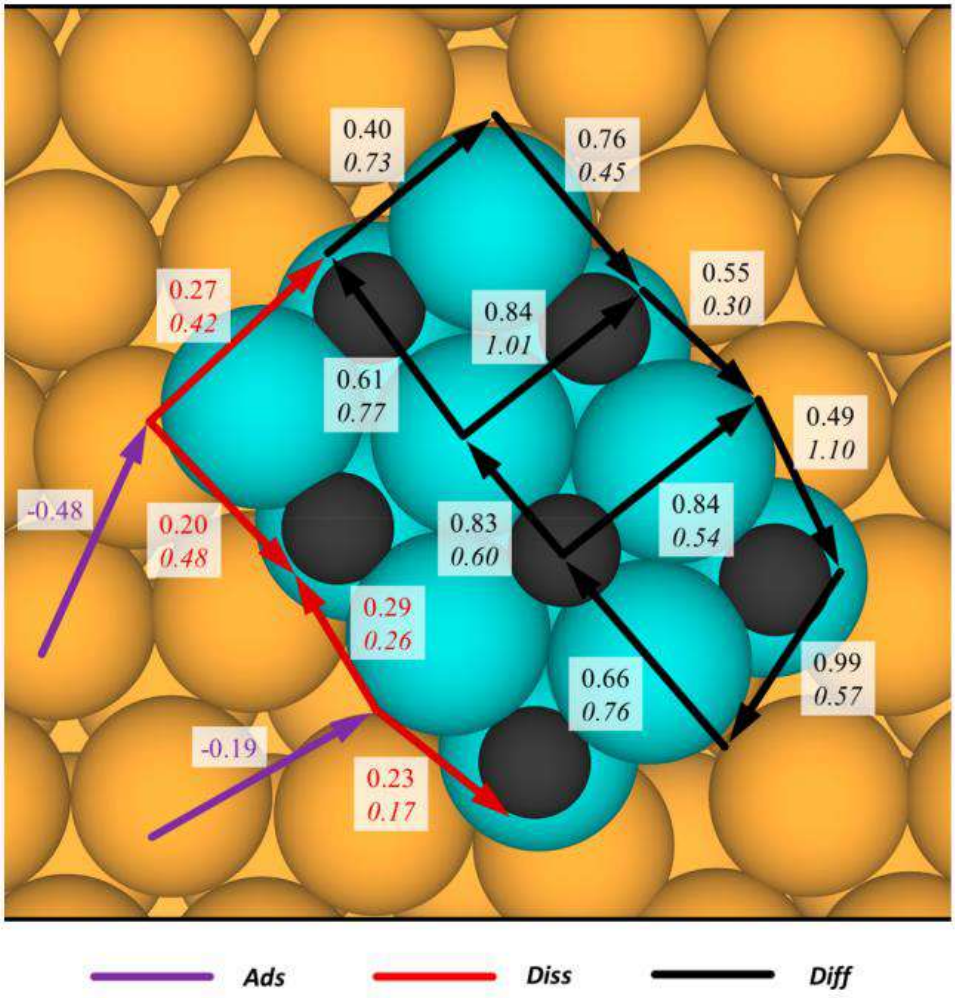

Figure 7. Top view of the explored system. Purple arrows show H_2 adsorption sites and purple values account for their respective adsorption energies. Red arrows show the H_2 dissociation paths, where one hydrogen atom remains in the adsorption site and the other moves to occupy a nearby site. Black arrows show H adatoms diffusions. The energy barrier values, either forward or backward, are shown in normal or italic fonts in the nearest square, respectively. Blue, black, and yellow spheres represent Mo, C, and Au atoms, respectively.

Finally, the possibility of having Kubas CH_2 structures, i.e., an elongated and adsorbed H_2 molecule over a substrate C atom was considered. From the obtained results, it was clear that the direct formation of Kubas can be rapidly rejected in these systems due to large energy barriers ranging from 1.2 to 1.8 eV. Nevertheless, Kubas structures can be formed from H* adatoms diffusion, as reported in Figure 8. The obtained results on this possibility revealed that the Kubas structure can be easily formed by H* diffusion as each considered site displayed rather small energy barriers, ranging from 0.18 to 0.55 eV. For comparison, the extended δ-MoC surface display much larger energy barriers ranging from 1.07 to 1.92 eV.[157] Moreover, the obtained results explain the different H sponginess capacity in function of stoichiometry. The H* preference for bonding to C atoms, either directly or in Kubas structure, is more limited in the $MoC_{0.6}$ NPs as they have fewer sites and C atoms are more saturated by Mo atoms. Thus, they are less active toward CH_x formation. All in all, it appears clear that the Kubas formation is key to understand the sponginess of $MoC_{1.0}$ systems supported on Au(111).

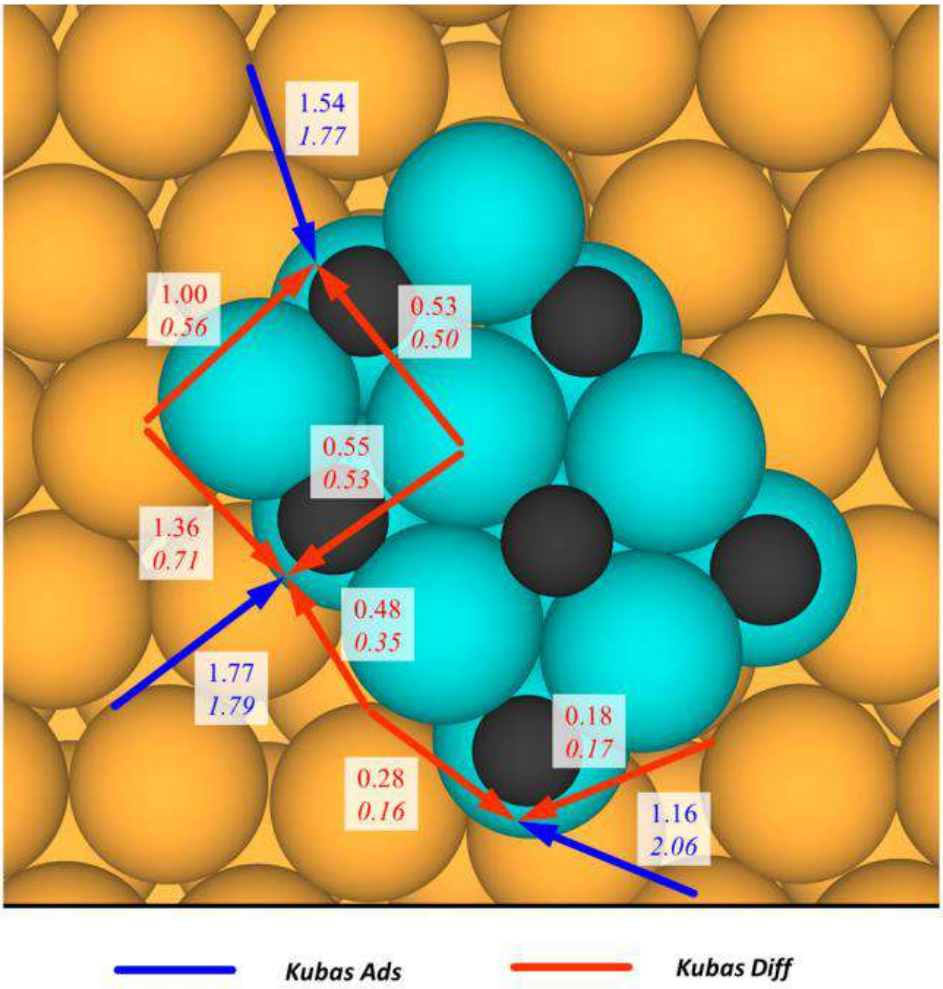

Figure 8. Top view of the explored system. Blue arrows show Kubas formation from gas-phase, where blue values account for their respective energy barriers, in the same manner as Figure 7. Orange arrows show Kubas formation from H adatom recombination, where orange values account for their respective energy barriers, in the same manner as Figure 7. Blue, black, and yellow spheres represent Mo, C, and Au atoms, respectively.

7.3 Conclusions

In the present Chapter, a combined theoretical and experimental study has shown the outstanding sponginess capabilities of MoC_y (y≈1.0) NPs supported on Au(111) surface when compared to the extended δ-MoC surface. The main features responsible for such difference can be summarized as the NPs stronger H_x affinity, significantly lower dissociation energy barriers, promoted H* adatom diffusion, and the formation of Kubas species. The other studied NP stoichiometry ($MoC_{0.6}$), do not follow this trend observed in the stoichiometric NPs. The decrease in active C sites appears to be the main cause to the observed activity decrease toward H. Nevertheless, $MoC_{0.6}$ NPs H activity is

comparable to that of the extended δ-MoC surface. All in all, the combination of experimental data and computational calculations have disclosed several insights behind the high H activity displayed by $MoC_{1.1}$/Au(111) system, placing them as plausible alternative catalysts for Pt-group TMs.

For a more detailed description, the reader is referred to the publication included below. The supporting information of the present publication, can be found in Appendix C.

Contribution: models preparation, DFT based calculations, results interpretation, scientific discussion, and providing a first draft of the publication.

7.4 Publication

Supported molybdenum carbide nanoparticles as hot hydrogen reservoirs for catalytic applications

THE JOURNAL OF PHYSICAL CHEMISTRY Letters

pubs.acs.org/JPCL

Letter

Supported Molybdenum Carbide Nanoparticles as Hot Hydrogen Reservoirs for Catalytic Applications

Marc Figueras, Ramón A. Gutiérrez, Francesc Viñes,* Pedro J. Ramírez, José A. Rodriguez,* and Francesc Illas

Cite This: *J. Phys. Chem. Lett.* 2020, 11, 8437−8441

Read Online

ACCESS | Metrics & More | Article Recommendations | Supporting Information

ABSTRACT: Transition metal carbides have been long proposed as replacements for expensive Pt-group transition metals as heterogeneous catalysts for hydrogenation reactions, featuring similar or superior activities and selectivities. Combining experimental observations and theoretical calculations, we show that the hydrogenating capabilities of molybdenum carbide can be further improved by nanostructuring, as seen on MoC_y nanoclusters anchored on an inert Au(111) support, revealing a more prominent role of Mo active sites in the easier H_2 adsorption, dissociation, H adatom diffusion, and elongated chemisorbed H_2 Kubas moieties formation when compared to the bulk δ-MoC(001) surface, thus explaining the observed stronger H_2 interaction and the larger formation of CH_x species, making these systems ideal to catalyze hydrogenation reactions.

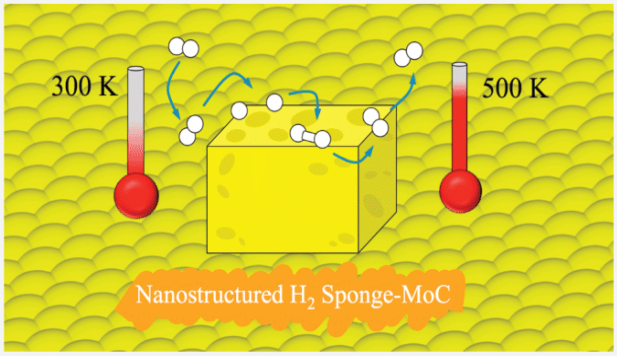

Hydrogenation reactions are common in many industrial processes, e.g., in the petrochemical plastic generation,[1] the saturation of vegetable oils polyunsaturated fat acids in food chemistry,[2] or in environmental chemistry, converting greenhouse carbon dioxide (CO_2) into greener chemicals.[3] Hitherto, hydrogenations have been mostly catalyzed using scarce and expensive Pt-group metals.[1,4] During the last decades, transition Metal Carbides (TMCs) have emerged as an alternative, often displaying superior activities and selectivities for a wide variety of relevant hydrogenation reactions.[3−9]

Consequently, considerable research efforts have been undertaken aimed at tailoring the TMCs hydrogenating capabilities. To this end, TMC nanoparticles (NPs) have been often used, deposited on oxide or zeolite-type supports.[10−12] Studies on the H_2 adsorption on TMCs extended single-crystal surfaces have shown complex phenomena related to H_2 adsorption and dissociation,[7,8] the diversity of easily interconvertible surface hydrogen species,[13] and the importance of H-coverage in lowering reaction energy barriers.[14] Unfortunately, it is yet not clear how to extrapolate this behavior to the supported TMC NPs, seriously hampering the rational design of novel hydrogenation catalysts.

We recently started a research program to investigate the intrinsic reactivity of free and Au-supported TMC nanoparticles.[15] Inspired by the tuning capabilities of the inverse oxide/metal catalysts,[16] MoC_y clusters were stabilized over an inert support, Au(111).[17] This produced systems able to dehydrogenate cyclohexene[18] and dissociate methane at room temperature.[15] The enhanced chemical activity is consistent with the CO_2 hydrogenation trends seen on carbon-supported TMC NPs.[19] Here, nanostructuring is exploited to tune the TMCs NPs reactivity on the basis of size, shape, and composition control. Combining X-ray Photoelectron Spectroscopy (XPS), Temperature-Programmed Desorption (TPD), and Density Functional Theory (DFT) based calculations, we show that $MoC_{1.1}$ nanostructures supported on Au(111) can act as hot H_2 reservoirs. We provide evidence that this behavior results from the combination of thermodynamic stability, diversity of H_x* species, easy H_2* dissociation and H* adatoms diffusion, an active role of low-coordinated Mo sites, and the promotion of Kubas complexes, all being the cornerstone of using MoC_y as ideal candidates for tailored hydrogenation catalytic reactions.

We start by examining the H_2 adsorption on a polycrystalline MoC surface reference. Previous studies showed a C/Mo ratio of 0.98 in this system,[20] very close to the 1.0 value for rocksalt δ-MoC. Figure 1 displays the C 1s XPS spectra collected before and after exposing bulk MoC to 1 Torr of H_2 at 300 K for 5 min. The initial C 1s peak at ∼282.4 eV corresponds to C

Received: August 26, 2020
Accepted: September 14, 2020
Published: September 22, 2020

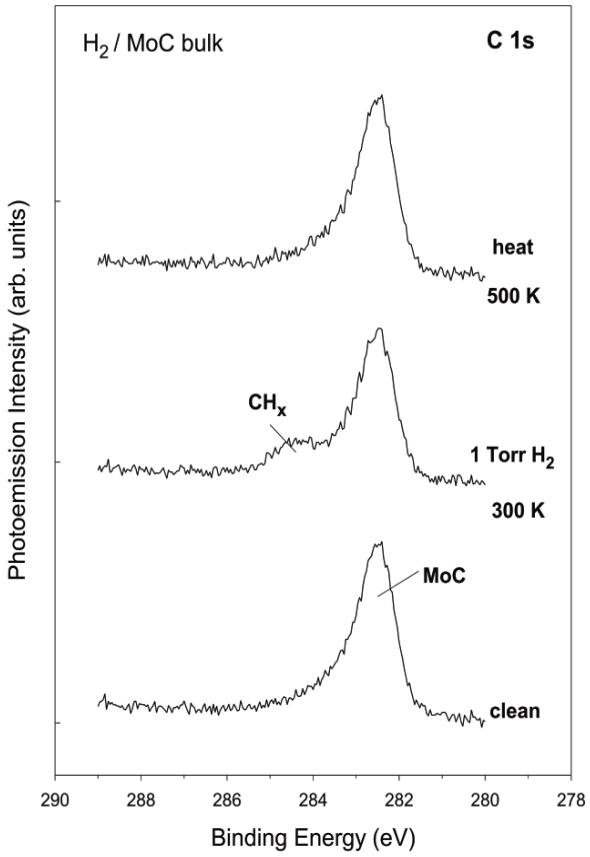

Figure 1. C 1s XPS spectra collected after dosing 1 Torr of H_2 to bulk MoC at 300 K with subsequent heating to 500 K. For comparison, the corresponding spectrum of the clean MoC is provided. The data were collected at an angle of 70° with respect to the surface normal to maximize surface contributions.

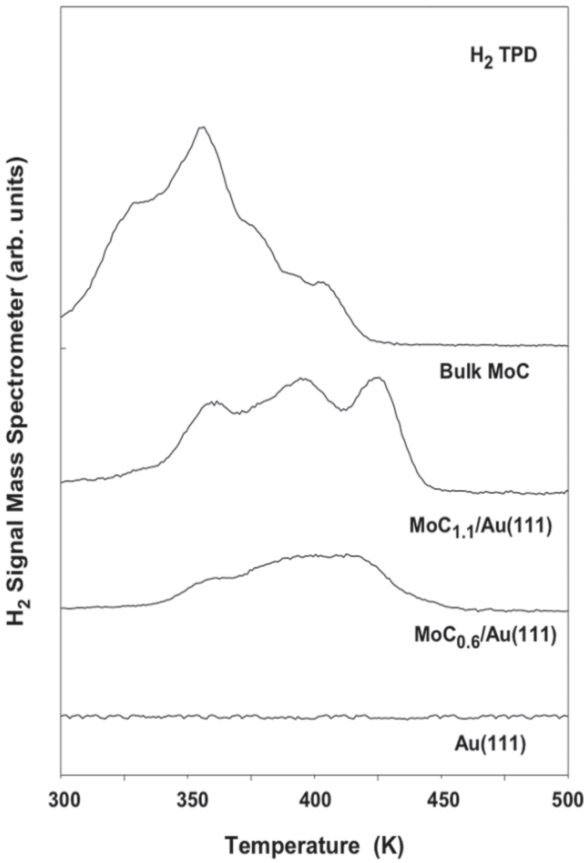

Figure 2. H_2 thermal desorption spectra collected after adsorbing hydrogen on bulk MoC, clean Au(111), and a gold substrate covered with 0.3 ML of $MoC_{1.1}$ or $MoC_{0.6}$. All the surfaces were exposed to 1 Torr of H_2 at 300 K for 5 min. The heating rate in the thermal desorption spectra is 2 K/s.

atoms in the δ-MoC surface.[15] There, H_2 adsorption and dissociation lead to a new feature at 284.0−284.5 eV assigned to the formation of CH_x groups on the MoC.[15,17,18] From the XPS peaks intensity, we estimate that the CH_x groups coverage is 0.2−0.3 monolayers (ML), which were removed by heating to 500 K for 1 min. Indeed, the TPD data in Figure 2 reveal that the hydrogen fully desorbs by 425 K, in a complex TPD spectrum where one can see clear peaks at 325, 350, and 400 K plus weak features at 370 and 380 K. This probably reflects the polycrystalline character of the MoC surface, which contains a large number of defective sites. By comparing to the TPD spectra of hydrogen on Pt(111),[21,22] one can estimate a hydrogen coverage of 0.93 ML, much larger than the 0.2−0.3 ML CH_x groups coverage seen in the XPS spectrum of Figure 1. Therefore, only a part of the surface hydrogen on the bulk MoC surface forms CH_x species, whereas a considerable amount involves H* adatoms on other active sites.

Au(111) surfaces were prepared containing 0.3 ML of either $MoC_{0.6}$ or $MoC_{1.1}$ nanoparticles following an earlier reported procedure.[15,17] This procedure leads to oxygen-free MoC nanoparticles where the C/Mo ratio varies from 0.6 to 1.1.[15,17] Scanning Tunnelling Microscopy (STM) images showed that these NPs are small (0.8−1.5 nm) and aggregate in the face-centered cubic (fcc) troughs located on either side of the elbows of the reconstructed Au(111) surface.[17] We found that the C/Mo ratio has a strong influence on the MoC_y NPs reactivity toward H_2, as seen in Figures 2 and 3, but in general the nanostructures displayed a behavior different from that of bulk MoC. In the case of $MoC_{0.6}$/Au(111), Figure 3A, a very small amount (0.05 ML) of CH_x was formed. This means that only a reduced fraction (~30%) of the C atoms present on the surface (0.18 ML) are involved in formation of CH_x species, probably due to the strong bonds between C and Mo atoms in the NPs required to maintain the cluster integrity. From the TPD in Figure 2, we estimate that the total coverage of hydrogen adsorbed on the $MoC_{0.6}$/Au(111) surface is only 0.27 ML, substantially smaller than that seen on bulk MoC but consistent with the fact that we only had 0.3 ML of $MoC_{0.6}$ on the gold substrate.

A distinct behavior is seen for the dissociative adsorption of H_2 on $MoC_{1.1}$/Au(111), where a larger C/Mo ratio of 1.1 did not lead to a reactivity decrease. On the contrary, C atoms in $MoC_{1.1}$ NPs were significantly more reactive than in either the $MoC_{0.6}$ NPs or in bulk δ-MoC. Figure 3B shows strong C 1s XPS features at a binding energy of ~284.6 eV, implying ca. 50% of the surface C atoms transformed into CH_x species. This process is fully reversible, as, upon heating to 500 K, H_2 desorbed without evolution of CH_4 or other light hydrocarbons. The reversible H_2 adsorption/desorption process was repeated several times (see Figure 3B and Figure S1 of the Supporting Information), and the C/Mo ratio was maintained in $MoC_{1.1}$/Au(111). The corresponding TPD spectrum in Figure 2 shows H_2 evolution at 360, 390, and 430 K, from which a total hydrogen coverage of 0.58 ML was estimated. This points to a H/C ratio close to 2, a value much larger than the one observed on bulk δ-MoC surfaces, posing $MoC_{1.1}$ NPs

https://dx.doi.org/10.1021/acs.jpclett.0c02608
J. Phys. Chem. Lett. 2020, 11, 8437−8441

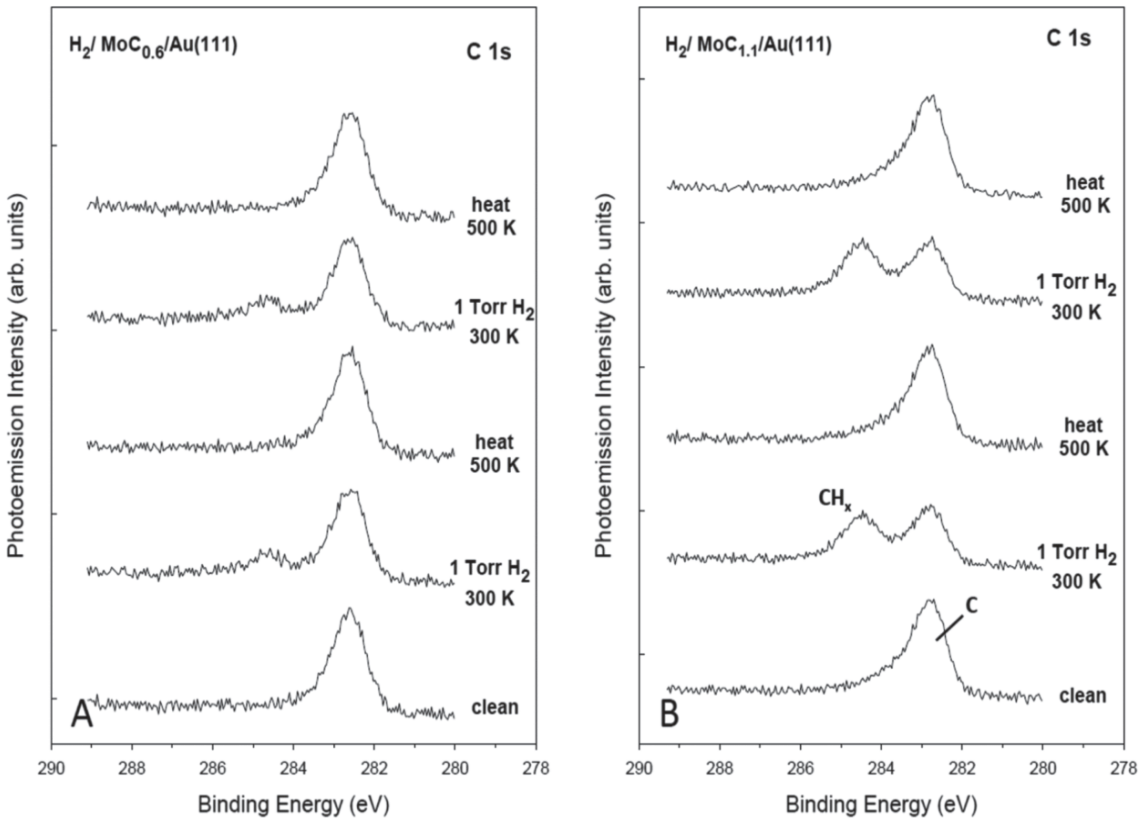

Figure 3. (A) C 1s XPS spectra collected after dosing 1 Torr of H_2 to $MoC_{0.6}$/Au(111) and (B) $MoC_{1.1}$/Au(111) at 300 K with subsequent heating to 500 K. The gold substrate was covered with 0.3 ML of $MoC_{0.6}$ or $MoC_{1.1}$ nanoparticles. The data were collected at an angle of 70° with respect to the surface normal to maximize surface contributions.

as hydrogen sponges, where H_2 can be easily adsorbed or desorbed, being hot hydrogen reservoirs for catalytic applications. The results for several cycles of hydrogen adsorption/desorption in Figure S1 indicate that the coverage for CH_x species on $MoC_{1.1}$/Au(111) was always close to 0.14 ML while being only near 0.04 ML on $MoC_{0.6}$/Au(111). This also points to $MoC_{1.1}$/Au(111) as an effective system for hydrogenation process.

To explain the remarkable results for $MoC_{1.1}$/Au(111), we carried out a DFT study using a stoichiometric $Mo_{12}C_{12}$ nanoparticle model supported on Au(111). Calculations were pushed toward a chemical accuracy below 0.04 eV using a Au(111) four-layered $p(6 \times 6)$ slab model with a 30 Å vacuum and using the Perdew–Burke–Ernzerhof (PBE)[23] exchange–correlation functional and including the D3 method proposed by Grimme to account for dispersion.[24] Further computational details are reported in the Supporting Information.

On the supported $Mo_{12}C_{12}$ NP, molecular H_2 and H adatoms attach with similar strength (see Figure 4), with H_2 preferring low-coordinated Mo sites, with an adsorption energy, E_{ads}, of up to −0.48 eV. Compared to a previous study for δ-MoC(001), which featured a stronger H_2 E_{ads} of −0.60 eV on-top of C atoms,[13] this involves here an active site switching from C to Mo. Aside, both δ-MoC(001) and $Mo_{12}C_{12}$/Au(111) prefer the H_2 dissociated state. Hence, the focus is on the stability of H*, which exhibits a preference toward corner C atoms, with an E_{ads} of −0.60 eV with respect to $1/2{\cdot}H_2$ and $Mo_{12}C_{12}$/Au(111), slightly stronger than on surface C atoms of δ-MoC(001), with an E_{ads} of −0.55 eV.[13] By assuming an order two desorption kinetics for H* — implying H* + H* recombination to H_2* prior to its desorption— and an estimate of desorption temperatures for the highest temperature peaks in Figure 1 via Redhead equation with pre-exponential values ranging 10^8–10^{13} s^{-1}, reveals a TPD shift toward higher temperatures of 28–19 K in $Mo_{12}C_{12}$/Au(111) relative to δ-MoC(001), in perfect agreement with the shift of ∼30 K as observed in Figure 2. Notice that the second peak of $MoC_{1.1}$/Au(111) could be assigned to H* on corner Mo atoms, with an E_{ads} of −0.54 eV, quite close, both in strength and in TPD peak position, to the low-coverage regular C sites on δ-MoC (001).[13] Finally, the peak at ∼355 K could be assigned to high-coverage H adatoms on regular (001) facet C atoms, sites in common for MoC_y NPs and δ-MoC (001) extended surfaces.

The distinct role of low-coordinated Mo sites on MoC_y for H adsorption relates to its E_{ads} of −0.54 eV, clearly stronger compared to the unfavorable interaction at Mo sites on δ-MoC(001),[13] which contributes to the to the aforementioned H_2 sponginess of supported MoC_y and the stronger interaction toward H adatoms upon or in the vicinity of low-coordinated Mo sites. It seems that the activity-killing ligand effect that C atoms have on neighboring Mo atoms, as featured on δ-MoC(001), gets counteracted by the lower Mo coordination, although particular electronic arrangements due to the nanoscale may play a role as well. Besides, on most stable H_2-anchoring Mo sites of $Mo_{12}C_{12}$/Au(111), H_2 features dissociation energy barriers as low as 0.2 eV (see Figure 4), thus halved compared to the extended δ-MoC(001) value of 0.39 eV.[13] Therefore, H_2 adsorption and dissociation is significantly promoted on supported MoC_y ($y > 1$) clusters, leading to a diversity of occupied C and Mo sites.

https://dx.doi.org/10.1021/acs.jpclett.0c02608
J. Phys. Chem. Lett. 2020, 11, 8437–8441

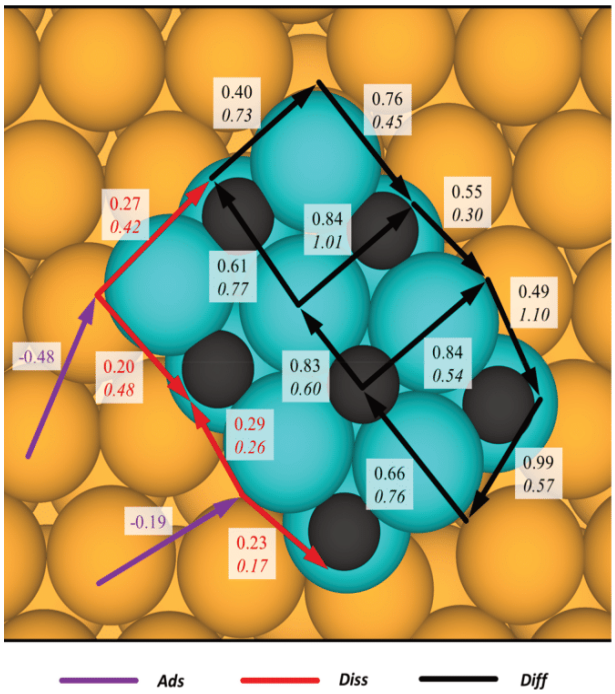

Figure 4. Top view of $Mo_{12}C_{12}$ supported on Au(111) surface. Black, blue, and orange spheres denote C, Mo, and Au atoms, respectively. H_2 adsorption sites are shown in purple, accompanied by adsorption energies, E_{ads}. Adsorbed H_2 dissociation energies are shown by red arrows, implying that one H adatom remains on-site, while the other moves to occupy a nearby site. H adatom diffusions are shown by black arrows, signaling initial to final locations. For H_2 dissociation and H diffusion, forward and backward energy barriers, E_b, are given in normal or italics fonts, respectively. All energy values are given in eV.

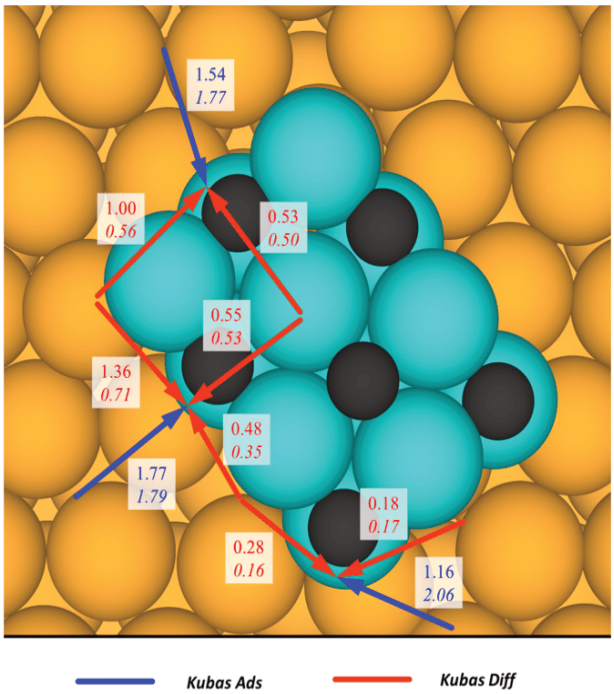

Figure 5. Top view of $Mo_{12}C_{12}$ supported on Au(111) surface. Kubas formation energy on low-coordinated C atoms are shown from gas-phase H_2 (blue) or through H adatoms recombination (red). In the latter a H adatom on a Mo site diffuses and interacts with the H-attaching surface C atom. Forward and backward energy barriers, E_b, are given in normal or italics fonts, respectively. All energy values are given in eV. Sphere color code as in Figure 4.

The mere H_2 dissociation on $Mo_{12}C_{12}$/Au(111) on the available aforementioned highly reactive sites would lead to a partial occupation of the MoC_y perimeter. Hence, a detailed analysis of the single H* diffusion has been performed, exemplified over the (001)-like facet; see Figure 4. The supported $Mo_{12}C_{12}$ nanoparticle features a rather complex network of H* diffusion steps, analyzed by having a look to the minimum barrier needed to be surmounted, so all sites could be occupied by H. For $Mo_{12}C_{12}$, this E_b is 0.76 eV, smaller than the equivalent value of 0.95 eV on δ-MoC(001),[13] implying that H* diffusion is also well promoted on nanostructured MoC_y model catalysts.

Finally, to explain the preferential CH_x formation on MoC_y nanoclusters with $y \sim 1$, the possibility of having a Kubas CH_2 structures has also been considered.[13] The direct Kubas formation on low-coordinated C atoms of $Mo_{12}C_{12}$ can be rapidly dismissed due to the large energy barriers involved, ranging 1.2−1.8 eV; see Figure 5. However, Kubas structures can be formed from diffusing H* adatoms on the MoC_y cluster. On each site, Kubas formation reaction paths exist with rather low energy barriers, from 0.18 to 0.55 eV, especially when compared to the equivalent barriers on δ-MoC(001) ranging 1.07−1.92 eV.[13] Thus, Kubas CH_2 structures can be easily formed on MoC_y NPs by H* diffusion processes, freeing neighboring Mo sites to further adsorb and dissociate H_2, a key aspect for the H_2 sponginess of MoC_y ($y \sim 1$) NPs and its high H_2 storage/release potential. Note that the present results permit us to understand the difference in H capacity of the two types of particles; since H prefers bonding to C atoms, either directly or as Kubas complexes, it appears that $MoC_{0.6}$ NPs, having fewer C atoms, have fewer active sites for H. Moreover, in such NPs, the carbons are more tightly bound to Mo, i.e., more saturated, and so less chemically active toward the CH_x formation.

All in all, on the basis of the above results, one can firmly state that, compared to δ-MoC(001), MoC_y ($y \sim 1$) NPs supported on Au(111) feature a stronger H_x affinity and a larger site diversity, with significantly reduced H_2 dissociation, H adatom diffusion, and CH_2 Kubas species formation energy barriers. These are key points in explaining the observed reversible H_2 sponginess on these systems Such inverse carbide/support catalysts are thus envisaged as promising hydrogenating catalysts, e.g., for ethylene hydrogenation, where both a high H coverage and easy H diffusion were found to be key for an easier and improved effective catalytic performance compared to late, Pt-group TMs.[14]

■ ASSOCIATED CONTENT

Supporting Information

The Supporting Information is available free of charge at https://pubs.acs.org/doi/10.1021/acs.jpclett.0c02608.

Experimental and computational details and a figure of the amounts of CH_x species generated on the MoC_y/Au(111) systems (PDF)

■ AUTHOR INFORMATION

Corresponding Authors

Francesc Viñes − *Departament de Ciència de Materials i Química Física & Institut de Química Teòrica i Computacional (IQTCUB), Universitat de Barcelona, 08028 Barcelona,*

https://dx.doi.org/10.1021/acs.jpclett.0c02608
J. Phys. Chem. Lett. 2020, 11, 8437−8441

Spain; orcid.org/0000-0001-9987-8654; Email: francesc.vines@ub.edu

José A. Rodriguez − *Chemistry Department, Brookhaven National Laboratory, Upton, New York 11973, United States;* orcid.org/0000-0002-5680-4214; Email: rodriguez@bnl.gov

Authors

Marc Figueras − *Departament de Ciència de Materials i Química Física & Institut de Química Teòrica i Computacional (IQTCUB), Universitat de Barcelona, 08028 Barcelona, Spain*

Ramón A. Gutiérrez − *Chemistry Department, Brookhaven National Laboratory, Upton, New York 11973, United States; Facultad de Ciencias, Universidad Central de Venezuela, Caracas 1020-A, Venezuela*

Pedro J. Ramírez − *Facultad de Ciencias, Universidad Central de Venezuela, Caracas 1020-A, Venezuela; Zoneca-CENEX, R&D Laboratories, Alta Vista, 64770 Monterrey, Mexico*

Francesc Illas − *Departament de Ciència de Materials i Química Física & Institut de Química Teòrica i Computacional (IQTCUB), Universitat de Barcelona, 08028 Barcelona, Spain;* orcid.org/0000-0003-2104-6123

Complete contact information is available at: https://pubs.acs.org/10.1021/acs.jpclett.0c02608

Notes

The authors declare no competing financial interest.

The data that support the findings of this study are available from the corresponding authors upon reasonable request.

■ ACKNOWLEDGMENTS

The research carried out at the Universitat de Barcelona has been supported by the Spanish MICIUN/FEDER RTI2018-095460−B-I00 and María de Maeztu MDM-2017-0767 grants and, in part, by Generalitat de Catalunya 2017SGR13 and XRQTC grants. This manuscript has been authored by employees of Brookhaven Science Associates, LLC under Contract No. DE-SC0012704 with the U.S. Department of Energy. F.I. acknowledges additional support from the 2015 ICREA Academia Award for Excellence in University Research. Computational resources provided by the Red Española de Supercomputación (RES) grants QS-2020-1-0007 and QS-2019-3-0004 are fully acknowledged.

■ REFERENCES

(1) Ebrahimi, M.; Simonovis, J. P.; Zaera, F. Near-Unity Reaction Probability in Olefin Hydrogenation Promoted by Heterogeneous Metal Catalysts. *J. Phys. Chem. Lett.* **2014**, *5*, 2121−2125.

(2) Emken, E. A.; Frankel, E. N.; Butterfield, R. O. Homogeneous Catalytic Hydrogenation of Unsaturated Fats: Metal Acetylacetonates. *J. Am. Oil Chem. Soc.* **1966**, *43*, 14−18.

(3) Posada-Pérez, S.; Ramírez, P. J.; Gutiérrez, R. A.; Stacchiola, D. J.; Viñes, F.; Liu, P.; Illas, F.; Rodriguez, J. A. The Conversion of CO_2 to Methanol on Orthorhombic β-Mo_2C and Cu/β-Mo_2C Catalysts: Mechanism for Admetal Induced Change in the Selectivity and Activity. *Catal. Sci. Technol.* **2016**, *6*, 6766−6777.

(4) Zhang, L.; Zhou, M.; Wang, A.; Zhang, T. Selective Hydrogenation over Supported Metal Catalysts: From Nanoparticles to Single Atoms. *Chem. Rev.* **2020**, *120*, 683−733.

(5) Levy, R. B.; Boudart, M. Platinum-Like Behavior of Tungsten Carbide in Surface Catalysis. *Science* **1973**, *181*, 547−549.

(6) Hwu, H. H.; Chen, J. G. Surface Chemistry of Transition Metal Carbides. *Chem. Rev.* **2005**, *105*, 185−212.

(7) Koverga, A. A.; Flórez, E.; Dorkis, L.; Rodriguez, J. A. CO, CO_2, and H_2 Interactions with (0001) and (001) Tungsten Carbide Surfaces: Importance of Carbon and Metal Sites. *J. Phys. Chem. C* **2019**, *123*, 8871−8883.

(8) Silveri, F.; Quesne, M. G.; Roldán, A.; de Leeuw, N. H.; Catlow, C. R. A. Hydrogen Adsorption on Transition Metal Carbides: a DFT Study. *Phys. Chem. Chem. Phys.* **2019**, *21*, 5335−5343.

(9) Schaidle, J. A.; Thompson, J. A. Fischer−Tropsch Synthesis over Early Transition Metal Carbides and Nitrides: CO Activation and Chain Growth. *J. Catal.* **2015**, *329*, 325−334.

(10) Shou, H.; Davis, R. J. Multi-Product Steady-State Isotopic Transient Kinetic Analysis of CO Hydrogenation over Supported Molybdenum Carbide. *J. Catal.* **2013**, *306*, 91−99.

(11) Vo, D.-V. N.; Adesina, A. A. Fischer−Tropsch Synthesis over Alumina-Supported Molybdenum Carbide Catalyst. *Appl. Catal., A* **2011**, *399*, 221−232.

(12) Gao, J.; Zheng, Y.; Fitzgerald, G. B.; de Joannis, J.; Tang, Y.; Wachs, I. E.; Podkolzin, S. G. Structure of Mo_2C_x and Mo_4C_x Molybdenum Carbide Nanoparticles and Their Anchoring Sites on ZSM-5 Zeolites. *J. Phys. Chem. C* **2014**, *118*, 4670−4679.

(13) Prats, H.; Piñero, J. J.; Viñes, F.; Bromley, S. T.; Sayós, R.; Illas, F. Assessing the Usefulness of Transition Metal Carbides for Hydrogenation Reactions. *Chem. Commun.* **2019**, *55*, 12797−12800.

(14) Jiménez-Orozco, C.; Flórez, E.; Viñes, F.; Rodriguez, J. A.; Illas, F. Critical Hydrogen Coverage Effect on the Hydrogenation of Ethylene Catalyzed by δ-MoC(001): An *Ab Initio* Thermodynamic and Kinetic Study. *ACS Catal.* **2020**, *10*, 6213−6222.

(15) Figueras, M.; Gutiérrez, R. A.; Prats, H.; Viñes, F.; Ramírez, P. J.; Illas, F.; Rodriguez, J. A. Boosting the Activity of Transition Metal Carbides Towards Methane Activation by Nanostructuring. *Phys. Chem. Chem. Phys.* **2020**, *22*, 7110−7118.

(16) Graciani, J.; Mudiyanselage, K.; Xu, F.; Baber, A. E.; Evans, J.; Senanayake, S. D.; Stacchiola, D. J.; Liu, P.; Hrbek, J.; Sanz, J. F.; Rodriguez, J. A. Highly Active Copper-ceria and Copper-ceria-titania Catalysts for Methanol Synthesis from CO_2. *Science* **2014**, *345*, 546−550.

(17) Horn, J. M.; Song, Z.; Potapenko, D. V.; Hrbek, J.; White, M. G. Characterization of Molybdenum Carbide Nanoparticles Formed on Au(111) Using Reactive-Layer Assisted Deposition. *J. Phys. Chem. B* **2005**, *109*, 44−47.

(18) Potapenko, D. V.; Horn, J. M.; White, M. G. The Reactions of Cyclohexene on Au(111)-supported Molybdenum Carbide Nanoparticles. *J. Catal.* **2005**, *236*, 346−355.

(19) Baddour, F. G.; Roberts, E. J.; To, A. T.; Wang, L.; Habas, S. E.; Ruddy, D. A.; Bedford, N. M.; Wright, J.; Nash, C. P.; Schaidle, J. A.; Brutchey, R. L.; Malmstadt, N. An Exceptionally Mild and Scalable Solution-Phase Synthesis of Molybdenum Carbide Nanoparticles for Thermocatalytic CO_2 Hydrogenation. *J. Am. Chem. Soc.* **2020**, *142*, 1010−1019.

(20) Posada-Pérez, S.; Ramírez, P. J.; Evans, J.; Viñes, F.; Liu, P.; Illas, F.; Rodriguez, J. A. Highly Active Au/δ-MoC and Cu/δ-MoC Catalysts for the Conversion of CO_2: The Metal/C Ratio as a Key Factor Defining Activity, Selectivity, and Stability. *J. Am. Chem. Soc.* **2016**, *138*, 8269−8278.

(21) Piñero, J. J.; Ramírez, P. A.; Bromley, S. T.; Illas, F.; Viñes, F.; Rodriguez, J. A. Diversity of Adsorbed Hydrogen on the TiC(001) Surface at High Coverages. *J. Phys. Chem. C* **2018**, *122*, 28013−28020.

(22) Christmann, K.; Ertl, G.; Pignet, T. Adsorption of Hydrogen on a Pt(111) Surface. *Surf. Sci.* **1976**, *54*, 365−392.

(23) Perdew, J. P.; Burke, K.; Ernzerhof, M. Generalized Gradient Approximation Made Simple. *Phys. Rev. Lett.* **1996**, *77*, 3865−3868.

(24) Grimme, S.; Antony, J.; Ehrlich, S.; Krieg, S. A. A Consistent and Accurate *Ab Initio* Parametrization of Density Functional Dispersion Correction (DFT-D) for the 94 Elements H-Pu. *J. Chem. Phys.* **2010**, *132*, 154104.

Chapter 8:

CO_2 activation and hydrogenation on MoC nanoparticles supported on Au(111)

8.1 Introduction

This Chapter comes back to one of the main goals of this Thesis, the study of catalytic reactions to transform greenhouse gases by means of TMCs based catalysts. In the same line as described in Chapter 5, involving CH_4 activation by MoC NPs, and relying on the obtained results from Chapter 7, studying H_2 adsorption and dissociation on MoC NPs as well, the present Chapter focuses on the hydrogenation reaction of CO_2 catalysed by MoC NPs supported on Au(111). Experimental and computational evidences are brought together to reveal the capabilities of MoC NP/Au(111) to adsorb and hydrogenate CO_2.

On the experimental side, a series of techniques involving XPS, TPD, and ion-scattering spectroscopy (ISS) were used to characterize and monitor the evolution of the studied systems. The consideration of two different NP C/M ratios revealed the important role of stoichiometry. Carbon deficient NPs are unstable under the hydrogenation reaction of CO_2, mainly due to its transformation into a highly stable oxycarbide that only produces significant amounts of CO. Nevertheless, rich carbon NPs are well suited to be used as catalysts for the hydrogenation reaction of CO_2, as they remain stable under such reaction producing a significant amount of methanol.

On the computational part, a series of DFT based calculations brought important insights regarding the main mechanisms responsible for CO_2 hydrogenation. The obtained results suggest that, even if the CO_2*+H*→ CO*+OH* mechanism could have some importance on the proposed reaction, the main outcome seems to involve an Eley-Rideal mechanism, where CO_2 reacts with a previously adsorbed H* moiety. Moreover, role of the Au(111) support was studied by comparing the reaction profiles obtained by explicitly including it to those involving just gas-phase NP models. The obtained results show that, even though the support has a certain impact on the products stability, it does not have a relevant effect on the main reaction path and energy barriers, suggesting that its inclusion in the present work is not necessary to unveil the main trends.

8.2 Results

First, the MoC NPs supported on Au(111) were synthetized by the group of Prof. Jose Rodriguez at the Brookhaven National Laboratory, following the same protocol already commented in Chapter 5 and Chapter 7.[37] This method allows to tune the C/M ratio in the

obtained NPs and, hence, two different stoichiometries were studied. These are $MoC_{0.6}$/Au(111) and $MoC_{1.1}$/Au(111), hereafter called, C-deficient and C-rich, respectively. Next, the carbon dioxide adsorption on C deficient, $MoC_{0.6}$/Au(111), and C rich, $MoC_{1.1}$/Au(111), NPs supported on Au(111) was monitored by means of XPS at 300 K. The obtained C(1*s*) and O(1*s*) spectra for the C deficient system revealed the presence of C, O, and CO species, indicating the total and partial CO_2 decomposition. On the other hand, the obtained C(1*s*) and O(1*s*) spectra for the rich C system displayed a totally different behaviour. There was no evidence of CO_2 decomposition and just one signal appeared in the O(1*s*) spectra, meaning that CO_2 was molecularly adsorbed without undergoing any further reaction. The subsequent heating revealed that CO_2 desorbs around 450 K, without any further evidence of reactivity. As in previous cases, the adsorbate, CO_2 in this case, interaction with the clean Au(111) surface was studied. Upon exposure of CO_2 to the Au(111) surface, a flat C(1*s*) spectra was collected, indicating the non-interaction of CO_2 on the Au(111) surface.

Next, experiments were carried out to study the reactivity of CO_2 with H_2 on MoC NPs supported on Au(111). The study of hydrogenation reaction relies on the results obtained in Chapter 7, where it was demonstrated the capabilities of MoC NPs to store and bind H. In order to monitor the aforementioned reaction, CO_2 and H_2 species were injected into a reactor at partial pressures of 0.5 atm and 4.5 atm, respectively. The catalyst was already placed in the reactor before exposure to the gases. Then the catalyst was heated to the reaction temperature around 500-600 K Next, the gas composition inside the reactor was characterized by a gas chromatograph with a flame ionization detector during 16 h.[154] The obtained results for the C-deficient systems showed that the main product formed was methane and, secondly, CO with traces of methanol. From the collected O(1*s*) spectra, it is possible to explain this behaviour. The O(1*s*) spectra during the reaction process, showed an increase in O adatoms signal overtime, indicating the accumulation of O adatoms on the catalyst. Therefore, even if at the beginning, the total dissociation of CO_2 produces C atoms that are suitable to be hydrogenated and become methane, the accumulation of O adatoms on the catalyst shifts the selectivity towards CO, making it the main reaction product. At the end, the carbide NP was transformed into an oxicarbide due to the accumulation of O adatoms.

On the other hand, the obtained results for the C-rich system showed that the main product was CO with a significant amount of methanol being also produced. Moreover,

the product distribution did not change overtime and there was not any trace of methane production. From the post-reaction O(1*s*) spectra, it can be concluded that the amount of O adatoms in the surface was halved compared to the C-deficient case. Most O adatoms were rapidly hydrogenated and become gaseous water. Furthermore, from the post-reaction C(1*s*) spectra, one can conclude that the surface was basically clean, as there was not any trace of C-containing molecules. From the described features, it is clear that the C/M ratio is an essential parameter for CO_2 hydrogenation on MoC/Au(111) systems.

Finally, the data collected from the gas chromatograph was used to determine the activation energy for methanol production via Arrhenius plots. The obtained activation energy for methanol production was 14 kcal/mol, a lower value compared to those of bulk δ-MoC (17 kcal/mol) and Cu(111) (25 kcal/mol).

To better understand the microscopic details of the experiments, the computational part focused on explaining the observed capabilities of $MoC_{1.1}$/Au(111) systems to hydrogenate CO_2 and produce methanol. First, the most stable stoichiometric NP structure, obtained following the procedure commented in Section 4.2.2, was selected. Next, the NP was supported on the Au(111) surface following the procedure explained in Section 4.2.1. Then, the adsorption of CO_2 on $MoC_{1.1}$/Au(111) was studied considering all non-equivalent sites of the NP. The obtained results showed CO_2 adsorption energies ranging from 0.5 to 1.4 eV, where the largest value corresponds to a low-coordinate C atom. The adsorption energy values obtained were compared to those of the bulk δ-MoC surface,[128] where the adsorption energies range from 1.0 to 1.2 eV using the same approach as in the present study, *i.e.*, PBE-D3. Nevertheless, these bulk δ-MoC surface values are much larger than those computed on rather equivalent sites on the present models. From results reported in Chapter 6, it can be suggested that the surface model used on the δ-MoC study could have reconstructed and go unnoticed, leading to a much larger adsorption energy simply because the energy of the bare surface was too high. In fact, taking into account that the reconstruction energy for this model is around 0.6 eV, the adsorption energies could end up being as low as 0.4 to 0.6 eV, a much more similar value compared to the currently obtained values for the rather equivalent sites on $MoC_{1.1}$/Au(111). A clear indication that, in previous work, the reconstruction of the clean δ-MoC(001) surface went unnoticed.

Next, a systematic series of reaction pathways was considered so as to explore the direct CO_2 dissociation mechanism. Neglecting a very specific and hardly frequent low-

coordinated C site and a similar low-coordinated Mo site, all sites displayed rather large energy barriers, in agreement with the experiments where it was concluded that C-rich systems do not dissociate CO_2. The observed low-coordinated sites reporting low energy barriers are interpreted as limitations of the specific model used to represent the real system. The concentration of these corner sites is assumed to be very small and, probably, due to their high reactivity, they will be rapidly passivated by C or O atoms. The aforementioned pathways are shown in Figure 9.

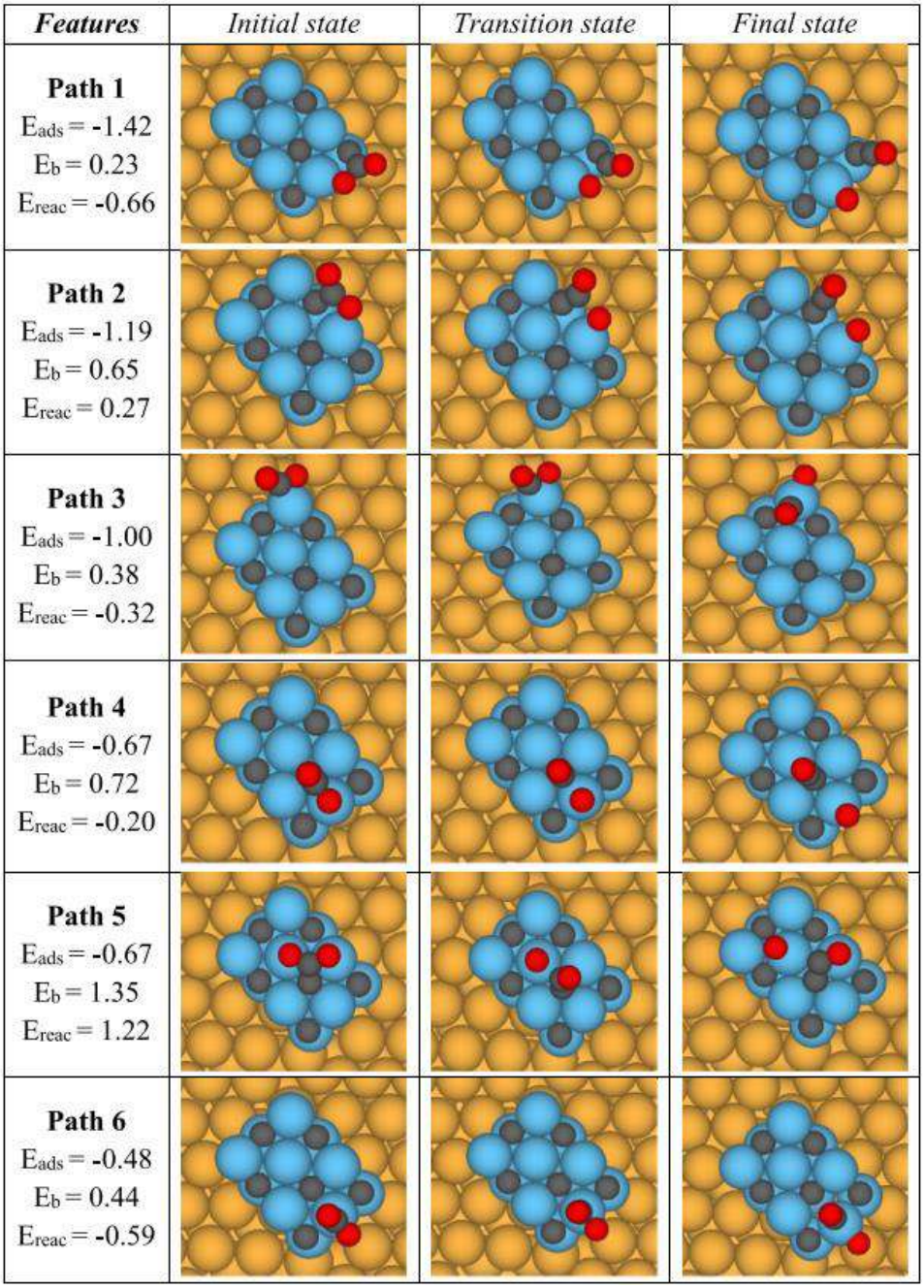

Figure 9. Paths considered for CO_2 direct dissociation on the studied system. Black, blue, red, and yellow spheres correspond to C, Mo, O, and Au atoms, respectively. All energies are given in eV.

In addition, the effect of the support Au(111) surface in the reactivity was studied in detail. The same pathways explored in the supported model for the direct CO_2 dissociation, were considered for gas-phase models (without including the Au support) in three different variants; totally frozen, partially relaxed, and totally relaxed. The obtained results revealed that the energy barriers and the CO_2 adsorption energies remain almost unaffected in the absence of a support. However, more significant discrepancies were

observed for the reaction energies. In order to determine the impact of the NP structure in such discrepancies, the structural difference between gas and supported models when reactants and products are adsorbed was studied. To this aim, the total energy of the NPs at the same structure but without reactants and products was computed. For simplicity, the $Mo_{12}C_{12}$-supported NP structure in reactants and products structure is referred as SupR and SupP, respectively. The same notation is used for the fully relaxed gas model, in this case referred as FreeR and FreeP. From these definitions, the influence of the NP structural differences caused by the absence of a support in the reaction energy was computed as

$$\Delta_{sup} = \frac{\left(E_{supP} - E_{supR}\right) - \left(E_{freeP} - E_{freeR}\right)}{E_{sup}^{Reac} - E_{free}^{Reac}} \qquad (8.1),$$

where E_{sup}^{Reac} and the E_{free}^{Reac} are the actual reaction energies of the free and supported models. From Eq. 8.1, it is deducted that to fully ascribe the reaction energy difference between the supported model and the free model to structural changes in the NP structure, the Δ_{sup} value should be 1. Nevertheless, the closest Δ_{sup} value reported was 0.8 for one of the cases. The other two considered path displayed values of 2.1 and -0.7, meaning that the differences observed in the reaction energies between supported and gas-phase cannot be attributed to structural changes of the NP. Instead, the observed discrepancies were attributed to the presence of the support, meaning that a full description of the energy profiles, including the reaction energy, requires to explicitly incorporate the Au support. Nevertheless, the supported and totally relaxed gas-phase models provide an almost equivalent description of the CO_2 adsorption and dissociation energy barrier. These parameters are considered bottleneck parameters on CO_2 activation, which justifies the use of the totally relaxed gas-phase model regardless of the observed discrepancies in the reaction energy. Consequently, the H reactivity towards CO_2 on the MoC/Au(111) systems was studied on the totally relaxed gas-phase model. It must be pointed that the two other gas-phase models, *i.e.*, frozen and partially relaxed, are not suited to represent the supported NP due to lack of a minimal reconstruction required to regain its catalytic capabilities towards CO_2.

The use of the totally relaxed gas-phase models was initially used in the exploration of additional CO_2 dissociation pathways. The obtained results revealed the same conclusions observed for their supported counterparts, where CO_2 direct dissociation is not favoured as reported in the experiments. In fact, experiments only

report the CO_2 transformation in a H-rich atmosphere. Hence, the next logic step was to explore the CO_2 dissociation in an environment with coadsorbed H adatoms. This new situation was explored relying on gas-phase models only, which is justified by the aforementioned reported trend which validates the conclusions extracted from gas-phase models. Additionally, the hydrogen adsorption was considered relying on the results reported in Chapter 7. For this new situation, several path ways were carried out at different H-coverages. The minimum H coverage considered was modelled by placing one H adatom in every C atom, the most preferable site as reported in Chapter 7. For the CO_2 molecule, the same previously encountered adsorption sites were used. The obtained hydrogenation pathways involved an initial CO_2 scission to form CO + O and next, the hydrogenation of the O adatom to form a hydroxyl (OH) group. It is interesting to point out, the unexpected encountered difficulty to converge on a carboxylate intermediate, a key specie on the water-gas shift mechanism.[154] Most hydrogenation paths failed to converge into the carboxylate or, if converged, the corresponding energy barrier was exceedingly large. Moreover, the predominant double step mechanism, allows for a meaningful comparison with the direct CO_2 dissociation in absence of H. The obtained results indicated that both, H-free and low H regime, mechanisms involved similar energy barriers, implying that the presence of low H quantities do not affect the CO_2 activation process.

Therefore, in order to unveil the insights on the reported experiments, a high H regime was considered. The high H regime has been considered by incorporating H adatoms in a Kubas conformation, a favoured structure reported in Chapter 7. The same paths for the CO_2 hydrogenation were carried out in the present situation. The obtained results show that an increase in H adatoms in a Kubas form, implies a significant energy barrier decrease in the hydrogenation process. Moreover, the reaction mechanism remains unaltered, an increase of H adatoms do not favour the formation of a carboxylate intermediate, instead, the two-step mechanism prevails. From the obtained trends, it is clear the significant influence of H coverage for the CO_2 hydrogenation on MoC/Au(111). A clear summary can be observed in Figure 10.

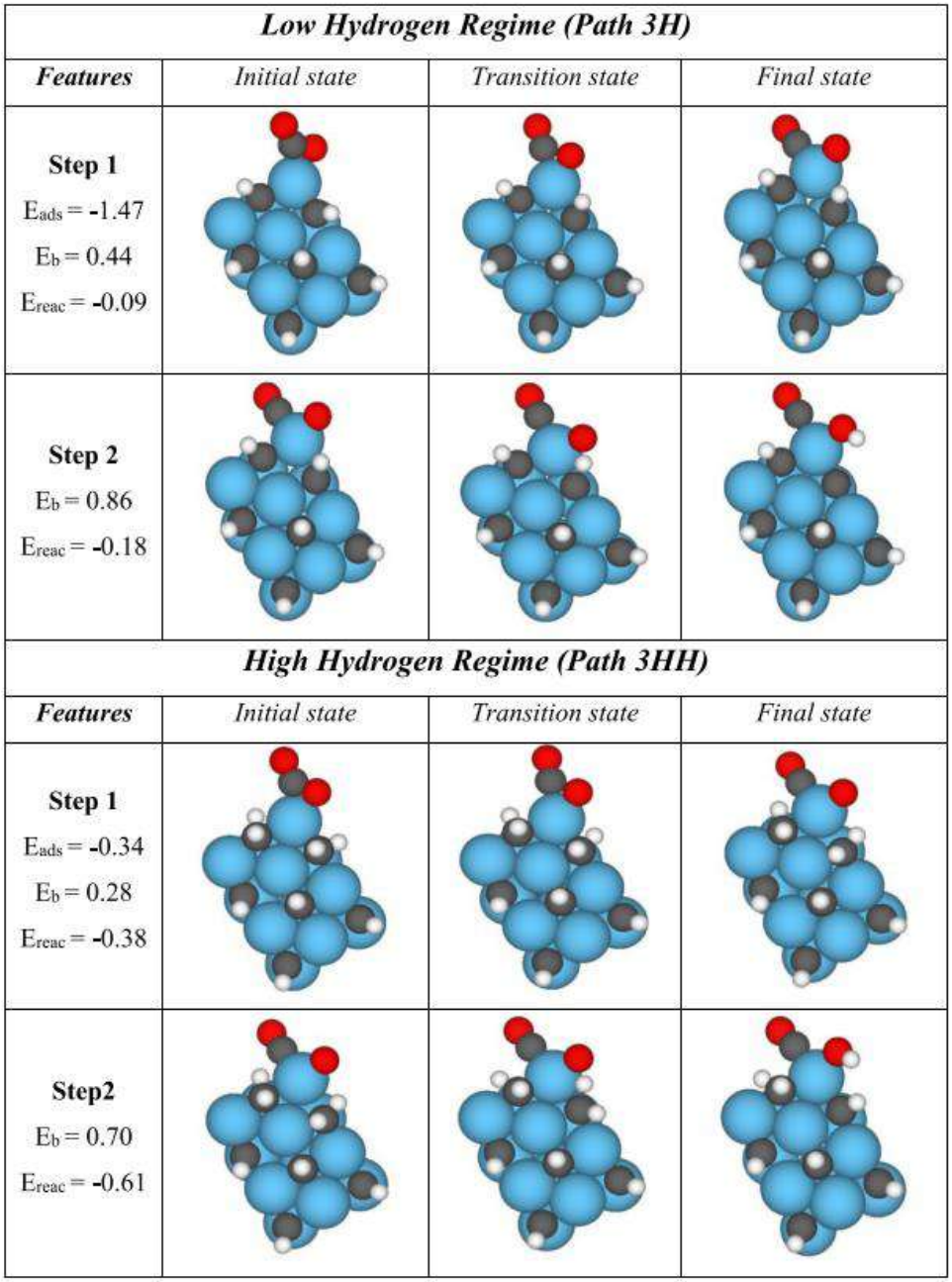

Figure 10. Specific hydrogenation path converged in two different hydrogen regimes. Top panel describes the low H regime, while the bottom panel describes the high H regime. Black, red, white, and blue sphere represent C, O, H, and Mo atoms, respectively. All values are in eV.

Finally, the study was completed by exploring an alternative model in better agreement with the experiments. The reported relation of H_2/CO_2 partial pressures in the experiments is 9, which suggest that most of the NP adsorption sites could be covered with H adatoms. In this sense, a H fully covered NP was considered, where the gas-phase CO_2 reacts with the adsorbed H adatoms to form a formate moiety (HCOO) following an Eley-Rideal mechanism. The obtained energy barriers are significantly small, comparable to those observed for in the high H regime and smaller than those observed for the direct

CO_2 dissociation. All in all, the reported DFT calculations indicate that the presence of substantial amounts of adsorbed H atoms, lowers the energy barriers for the CO_2 dissociation. Moreover, there are two favoured reaction mechanisms in presence of H, *i.e.*, the adsorbed CO_2 direct dissociation and the CO_2 transformation to formate *via* an Eley-Rideal mechanism.

8.3 Conclusions

In the present Chapter, a set of experiments and density functional calculations on suitable models have been reported evidencing the catalytic activity of MoC/Au(111) systems towards CO_2 hydrogenation. The C/M ratio plays a major role on the system stability and the final reaction products obtained. On the stability order, the $MoC_{0.6}$/Au(111) system appears to not be stable in presence of CO_2 due to O poisoning, which derives into its transformation to an oxycarbide. Contrarily, the $MoC_{1.1}$/Au(111) system remains stable through the reaction process, displaying small amounts of O adatoms adsorbed on the NP. On the reaction products side, $MoC_{0.6}$/Au(111) system produces mostly CO and methane, where the former is the major product obtained at large reaction times due to O poisoning. On the other hand, the $MoC_{1.1}$/Au(111) system produces mostly CO and significant amounts of methanol, without any trace of alkanes as reaction products. Moreover, the reported activation energies calculated *via* Arrhenius plots, indicate the superior capability of MoC/Au(111) systems to activate CO_2 compared to Cu(111) and δ-MoC bulk surfaces. All in all, experiments concluded that both MoC stoichiometries considered are highly active towards CO_2 transformation. Nevertheless, the instability displayed by the C-deficient system discourages its use as catalyst, placing the C-rich system as the only valid option for such reactions.

On the computational part, the DFT calculations, which constitute the main contribution of this Thesis Chapter, focused on the C-rich model. These found large energy barriers for the direct dissociation of CO_2 in absence of H, which is in agreement with the experiments. Moreover, the comparable results for the supported and gas-phase models show the same qualitative trends in the adsorption energy and energy barrier features. This aspect opens the possibility to use gas-phase systems on the study of the hydrogenation process, at least as far as activation energies is concerned. Subsequently, the hydrogenation process studied on the gas-phase models indicates the importance of

high H coverages in order to decrease the energy barriers for the CO_2 hydrogenation. Finally, the model calculations suggest that the main hydrogenation mechanism could involve an Eley-Rideal mechanism, which leads to formate intermediate.

For a more detailed description, the reader is referred to the publication included below. The supporting information of the present publication, can be found in Appendix D.

Contribution: models preparation, DFT based calculations, results interpretation, scientific discussion, and providing a first draft of the publication.

8.4 Publication

Supported molybdenum carbide nanoparticles as an excellent catalyst for CO_2 hydrogenation

ACS Catalysis

pubs.acs.org/acscatalysis Research Article

Supported Molybdenum Carbide Nanoparticles as an Excellent Catalyst for CO_2 Hydrogenation

Marc Figueras, Ramón A. Gutiérrez, Francesc Viñes, Pedro J. Ramírez, José A. Rodriguez,* and Francesc Illas*

Cite This: *ACS Catal.* 2021, 11, 9679−9687 Read Online

ACCESS | Metrics & More | Article Recommendations | Supporting Information

ABSTRACT: Experiments under controlled conditions show that MoC_x nanoclusters supported on an inert Au(111) support are efficient catalysts for CO_2 conversion, although with a prominent role of stoichiometry. In particular, C-deficient nanoparticles directly dissociate CO_2 and rapidly become deactivated. On the contrary, nearly stoichiometric nanoparticles reversibly adsorb/desorb CO_2 and, after exposure to hydrogen, CO_2 converts predominantly to CO with a significant amount of methanol and no methane or other alkanes as reaction products. The apparent activation energy for this process (14 kcal/mol) is smaller than that corresponding to bulk δ-MoC (17 kcal/mol) or a Cu(111) benchmark system (25 kcal/mol). This trend reflects the superior ability of $MoC_{1.1}$/Au(111) to bind and dissociate CO_2. Model calculations carried out in the framework of density functional theory provide insights into the underlying mechanism suggesting that CO_2 hydrogenation on the hydrogen-covered stoichiometric MoC_x nanoparticles supported on Au(111) proceeds mostly under an Eley−Rideal mechanism. The influence of the Au(111) is also analyzed and proven to have a role on the final reaction energy but almost no effect on the activation energy and transition state structure of the analyzed reaction pathways.

KEYWORDS: *CO_2 hydrogenation, MoC_x nanoparticles, XPS, TPD, DFT*

INTRODUCTION

Since the 1970s, transition-metal carbides have been suggested as an alternative to catalysts based on expensive late transition metals for a wide variety of hydrogenation reactions.[1−4] In many new catalysts, metal carbides nanoparticles (NPs) are dispersed on oxides and zeolites[5,6] but little is known about the specific phenomena which determine the hydrogenation capabilities of these systems. In principle, size effects and the carbon/metal ratio could affect the behavior of a NP.[2,7,8] Experimental studies for H_2 adsorption on NPs of $MoC_{0.6}$ and $MoC_{1.1}$ supported on Au(111), complemented by computational modeling, have shown that these systems are extremely efficient for the cleavage of the H−H bond at room temperature and the storage of H adatoms.[9] For H_2/$MoC_{1.1}$/Au(111), the results of temperature-programmed desorption (TPD) showed H_2 evolution between 350 and 450 K and a H/C ratio close to two, a value much larger than the one observed on bulk rock-salt δ-MoC surfaces, thus pointing out that $MoC_{1.1}$ NPs can act as H sponges, where H_2 can be easily adsorbed or desorbed, posing them as hot hydrogen reservoirs for catalytic applications.[9]

In this study, we examine the performance of MoC_x/Au(111) surfaces in the catalytic hydrogenation of carbon dioxide. This chemical transformation was chosen as a test due to its relevance for the control of air pollution and the production of high value chemicals in C_1 catalysis.[10,11] It is nowadays well-accepted that many activities involving the burning of fossil fuels in our industrial society have led to an excessive concentration of CO_2 in the atmosphere and major environmental problems.[10] In order to mitigate these harmful effects, CO_2 capture, storage, and, specially, its conversion to valuable chemicals or commodity goods have become an urgent need.[11,12]

Previous research has shown that metal carbides can hydrogenate CO_2 to give CO, oxygenates, and alkanes.[13,14] This diversity of products comes as a result of the effects of the carbon/metal ratio on the reactivity of a carbide toward CO_2. For example, on an orthorhombic β-Mo_2C(001) surface, the CO_2 molecule is strongly adsorbed, the first C−O breaks below 200 K, and the second around room temperature.[2] A more detailed study showed that the effect of the surface termination is also important. In fact, density functional theory (DFT) calculations predicted, and experiments confirmed, that the orthorhombic β-Mo_2C(001) Mo-terminated polar surface leads to a spontaneous cleavage of a C−O bond in CO_2 and

Received: April 16, 2021
Revised: July 7, 2021

https://doi.org/10.1021/acscatal.1c01738
ACS Catal. 2021, 11, 9679−9687

the carbon monoxide formation.[15] The same study showed that on a β-$Mo_2C(001)$ C-terminated polar surface or on a δ-MoC(001) nonpolar surface, the CO_2 molecule is activated, yet the C−O bond prevails. These results illustrate the huge impact the carbon/metal ratio has on the chemical and catalytic properties of molybdenum carbides and explains why the hydrogenation of CO_2 on β-Mo_2C powders produces a large amount of CO, methane, and light alkanes.[13,16] On the other hand, bulk δ-MoC exhibits a promising behavior for the conversion of CO_2 into methanol.[14] On carbides with a carbon/metal ratio close to one such as ZrC, TaC, NbC, HfC, TiC, or δ-MoC, the CO_2 molecule does not undergo spontaneous dissociation.[14,15,17] It adsorbs on C sites of the carbide surface with the formation of C═CO_2 bonds and its dissociation is assisted by hydrogen adatoms.[14]

The large amounts of H that can be accumulated in the MoC_x/Au(111) systems[8] may give the carbide NPs special properties for the catalytic conversion of CO_2, arising from the diversity of easily interconvertible surface hydrogen species and the catalytic smoothness achieved by H-coverage effects.[9] In this work, we use a combination of catalytic testing, X-ray photoelectron spectroscopy (XPS) measurements, and calculations based on DFT to investigate the hydrogenation of CO_2 on carbon-poor ($MoC_{0.6}$) and carbon-rich ($MoC_{1.1}$) NPs supported on Au(111) and present evidence that the latter constitute efficient catalysts for CO_2 decomposition to CO and methanol with a large selectivity to the former. The theoretical study consistently shows that the effect of preadsorbed H is crucial. The calculations evidence a systematic qualitative trend, preadsorbed H leads to a decrease in the energy barriers involved in the CO_2 hydrogenation steps, and even triggers an Eley−Rideal mechanism for the H-assisted CO_2 dissociation.

EXPERIMENTAL PROCEDURE

The catalytic performance of the carbon-poor ($MoC_{0.6}$) and carbon-rich ($MoC_{1.1}$) NPs supported on Au(111) was investigated in an instrument which combined a batch reactor with an ultrahigh-vacuum (UHV) chamber for surface characterization with XPS, TPD, and ion-scattering spectroscopy. The sample could be moved between the UHV chamber and the microreactor without exposure to air.

The MoC_x/Au(111) systems were prepared following a methodology described in previous works, where the interaction of these systems with methane and molecular hydrogen was examined.[8,9,18] In short, the NPs were synthesized by deposition of the Mo metal onto a reactive multilayer of ethylene (C_2H_4), which was resting physisorbed on a Au(111) substrate at low temperatures (90−100 K).[18] Upon heating to 750 K, the unreacted C_2H_4 desorbed and the MoC_x NPs were left on the gold substrate. The Mo → MoC_x transformations could be followed using a combination of XPS, TPD, and scanning tunneling microscopy (STM).[18] In this synthetic approach, one can control the C/Mo ratio in the NPs from 0.6 (C-poor) to 1.1 (C-rich).[8,9] XPS was used to determine this ratio and we utilized as reference previous values measured in our instrument for the C 1s and Mo 3d regions of bulk MoC and Mo_2C.[14] For the bulk sample of MoC, our XPS measurements pointed to a C/Mo ratio of 0.98−0.96 in good agreement with the ratio typically observed for bulk samples of one-to-one carbides.[19−21] Images acquired using STM have shown that the generated NPs by this synthetic procedure are relatively small (0.8−1.5 nm) and grew over the face-centered cubic (fcc) troughs located on either side of the elbows of the reconstructed Au(111) support.[18] Previous works have examined the reactivity of these MoC_x/Au(111) surfaces toward cyclohexene,[22] methane,[8] and H_2.[9]

The catalytic activity for CO_2 hydrogenation of the MoC_x/Au(111) systems was examined at temperatures in the range of 500−600 K. After characterization in the UHV chamber, the sample was transferred to the batch reactor at room temperature, the reactant gases were introduced [0.049 MPa (0.5 atm) of CO_2 plus 0.441 MPa (4.5 atm) of H_2], and finally, the catalyst was rapidly heated to the reaction temperature. The evolution of the gas composition inside the reactor was followed using a gas chromatograph with a flame ionization detector,[14] collecting data (CH_3OH, CH_4, and CO production) at intervals of 10 to 15 min for up to 16 h. The yields of carbon monoxide, methane, and methanol in the catalytic tests were normalized by the active area exposed by the sample and the total reaction time. The kinetic experiments to obtain the data for the Arrhenius plots were performed in the limit of low conversion (<5%).

MATERIALS, MODELS, AND COMPUTATIONAL DETAILS

The direct and hydrogen-assisted CO_2 dissociation on MoC_x/Au has been studied using a series of suitable models and DFT calculations. The models start from $Mo_{12}C_{12}$ NPs supported on a $p(6 \times 6)$ supercell of Au(111) following the approach described in a previous work investigating the hydrogen storage capability of these systems.[9] In view of the huge amount of possible adsorption sites, several pathways were first considered for the CO_2 direct dissociation on the $Mo_{12}C_{12}$/Au(111) model, and then, a set of these pathways were explored on the same $Mo_{12}C_{12}$ NPs but removing the Au(111) support, that is, ignoring the direct support effect. Results entail a clear resemblance between gas and supported models, and, in consequence, the effect of hydrogen coverage on the reaction profile was studied on the gas-phase models. This strategy is based on the observed ability of carbide NPs to store hydrogen[9] and allows one to tackle a vast number of reaction pathways under different hydrogen coverage at a reasonable computational cost. For the MoC_x/Au(111) systems, the main modifier of the surface chemistry on the carbide NPs should be hydrogen and not the inert gold substrate.[9]

The corresponding models are referred to as $Mo_{12}C_{12}$-sup (supported) and $Mo_{12}C_{12}$-free (in vacuum). In addition, for the $Mo_{12}C_{12}$-free model, we considered three different situations where the CO_2 to CO + O elementary step is explored. In the first one, the atomic structure of the $Mo_{12}C_{12}$ NPs is frozen as in the $Mo_{12}C_{12}$-sup and will be denoted as $Mo_{12}C_{12}$-free-1; in the second one, the position of the atoms that would be in contact with the Au surface is frozen as in $Mo_{12}C_{12}$-sup and the rest are allowed to relax ($Mo_{12}C_{12}$-free-2) and, finally, all atoms in the $Mo_{12}C_{12}$-free NP are free to relax ($Mo_{12}C_{12}$-free). The initial atomic structure of the NP model was obtained by mimicking largely stable gas-phase TiC NPs as previously reported.[23] These TiC NP models were acquired through interatomic potentials and the resulting atomic structure used as input for geometry optimization by means of DFT calculations. For the 21 low-energy structures of $Ti_{12}C_{12}$ reported by Lamiel-Garcia *et al.*,[23] Ti atoms were substituted by Mo atoms and the resulting structure was fully reoptimized by DFT calculations using the approaches described below. Resulting models are undoubtedly similar

https://doi.org/10.1021/acscatal.1c01738
ACS Catal. 2021, 11, 9679−9687

to their TiC counterparts, an expected outcome as both TiC and the δ-MoC polymorph exhibit the same rock-salt structure. For additional information regarding the structure of this type of NPs, we refer the reader to recent work describing a rather large set and their interaction with ethylene.[24]

All energy values reported in this work were obtained through periodic DFT calculations using large enough supercells so that the interaction between the supported NPs in periodically repeated images is negligible. The supercell size and **k**-point grid used depend on whether the Au(111) support is included or not. Thus, for the explicitly supported $Mo_{12}C_{12}$ NPs models, a 3×3×1 Monkhorst−Pack grid of special **k**-points was used, while calculations involving unsupported NPs were carried out at the Γ point only. The Au(111) support was represented using slab models including four atomic layers with the two upmost layers allowed to relax and the two bottommost ones kept frozen so as to provide a bulk environment to the surface region. This type of modeling metal surfaces is a rather standard approach employed by many authors; see, for instance, the kinetic Monte Carlo study of CO_2 hydrogenation on Ni(111),[25] the electroreduction of CO by Cu surfaces,[26] and references therein. Further details can be found in two very recent reviews.[27,28]

All calculations were carried out using the Vienna *Ab initio* Simulation Package (VASP) code,[29] employing the Perdew−Burke−Ernzerhof (PBE) exchange−correlation functional,[30] which has been determined as a suitable functional to describe Mo-based carbides.[31] Moreover, dispersion terms have been accounted by the Grimme D3 correction.[32] The Kohn−Sham equations were solved within a plane-wave basis set with a cutoff of 415 eV, while the effect of core electrons into the valence electron density was included through the projected augmented wave method as implemented by Kresse and Joubert.[33] Spin polarization has been found to be negligible on supported cases but accounted for in the gas-phase models as there it might have a significant effect. Convergence thresholds for the total energy and atomic forces were set to 10^{-5} eV and 0.01 eV $Å^{-1}$, respectively. Finally, transition state (TS) structures have been located by means of the climbing-image nudged-elastic-band (CI-NEB) method[34] and characterized by frequency analysis through the diagonalization of the corresponding block of the Hessian matrix with elements computed with finite differences of 0.03 Å of analytic gradients.

RESULTS AND DISCUSSION

Adsorption of CO_2 on MoC_x/Au(111) Surfaces: XPS Studies. In a first set of experiments, we investigated the adsorption of carbon dioxide on C-poor, $MoC_{0.6}$/Au(111), and C-rich, $MoC_{1.1}$/Au(111), NPs of molybdenum carbide dispersed on a gold substrate. Figure 1 displays C and O 1s XPS spectra collected after dosing CO_2 at 300 K. The Au(111) substrate does not adsorb the CO_2 molecule. A drastic change in reactivity is seen after the deposition of $MoC_{0.6}$ NPs. In the C 1s and O 1s regions, features are detected that denote the presence of C, O, and CO species on the surface.[35] These features indicate that the carbon dioxide undergoes partial ($CO_2 \rightarrow CO + O$) and complete ($CO_2 \rightarrow C + 2O$) decomposition on the $MoC_{0.6}$/Au(111) surface. In this system, the behavior is very similar to that found for CO_2 adsorbed on a bulk β-Mo_2C(001) surface where the C/Mo ratio is 0.5.[35]

$MoC_{1.1}$/Au(111) exhibited a reactivity toward CO_2 which was very different from that found on $MoC_{0.6}$/Au(111). In $MoC_{1.1}$/Au(111), the XPS data in Figure 1 indicate that CO_2

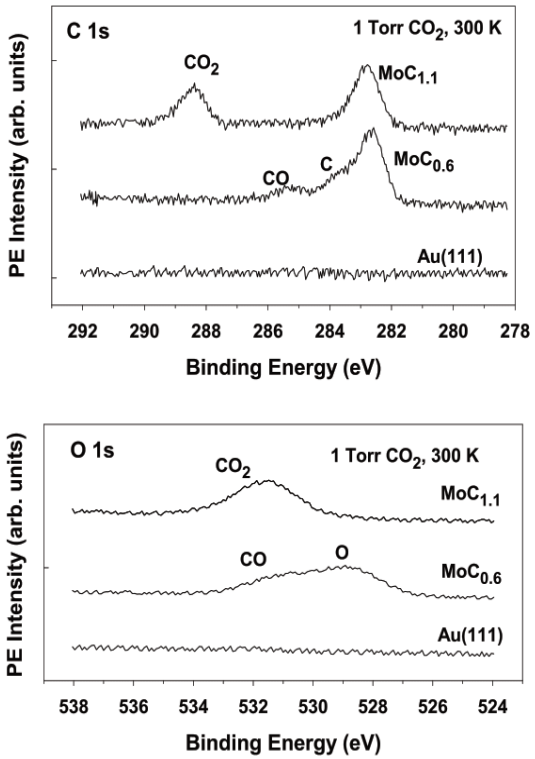

Figure 1. C 1s (top panel) and O 1s (bottom panel) XPS spectra recorded after exposing Au(111), $MoC_{0.6}$/Au(111), and $MoC_{1.1}$/Au(111) surfaces to 1 Torr of CO_2 at 300 K for 5 min in a microreactor. After exposure to CO_2, the gas was pumped out from the microreactor and the samples were transferred to a UHV chamber to collect the XPS spectra. In the surfaces with MoC_x NPs, the coverage of Mo was close to 0.3 monolayer (ML) in both cases.

was adsorbed molecularly at 300 K and desorbed intact upon heating to 450 K. After increasing the C/Mo ratio to 1.1, the carbide still binds CO_2 well, but it does not dissociate the C−O bonds of the molecule. It has a behavior very similar to that observed for bulk δ-MoC,[14] but in $MoC_{1.1}$/Au(111), the adsorption bond of CO_2 is stronger. As we will see below, this difference facilitates the activation and conversion of CO_2 to methanol on the $MoC_{1.1}$/Au(111) surface upon reaction with hydrogen.

Conversion of CO_2 to CO and CH_3OH on MoC_x/Au(111) Surfaces: Kinetic Studies. On a previous study, we have shown that MoC_x NPs are extremely active for the binding and dissociation of H_2.[9] The hydrogen on the MoC_x/Au(111) surfaces can be present as adatoms, molecules in a *Kubas* adsorption mode or form CH_x species that easily release hydrogen upon heating.[9] In principle, these systems are ideal for hydrogenation processes. Consequently, in the present study, we have investigated the hydrogenation of CO_2 on C-poor, $MoC_{0.6}$/Au(111), and C-rich, $MoC_{1.1}$/Au(111), systems. Both of them act as sponges for hydrogen adsorption/desorption.[9]

Figure 2 summarizes the results for the hydrogenation of CO_2 on $MoC_{0.6}$/Au(111). Initially, the main product of the reaction is methane, with CO as a secondary product, and a trace of methanol. This result can be explained using the CO_2 adsorption data reported in Figure 1 for the $MoC_{0.6}$/Au(111) system. The full dissociation of CO_2 produces C atoms that eventually are hydrogenated to yield methane. The pristine $MoC_{0.6}$/Au(111) surface is a very good catalyst for CO_2 methanation, but the accumulation of O adatoms, bottom

https://doi.org/10.1021/acscatal.1c01738
ACS Catal. 2021, 11, 9679−9687

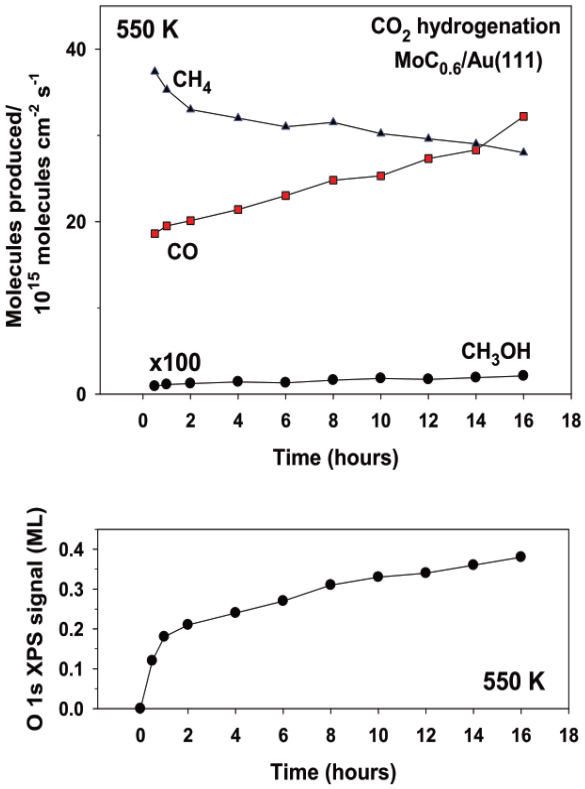

Figure 2. Top panel: Production of CH_4, CO, and CH_3OH during the hydrogenation of CO_2 on a Au(111) surface precovered with 0.3 ML of $MoC_{0.6}$. Bottom panel: Amount of oxygen measured with XPS after different CO_2 hydrogenation times on the $MoC_{0.6}$/Au(111) catalyst. T = 550 K, $P(CO_2)$ = 0.5 atm, and $P(H_2)$ = 4.5 atm.

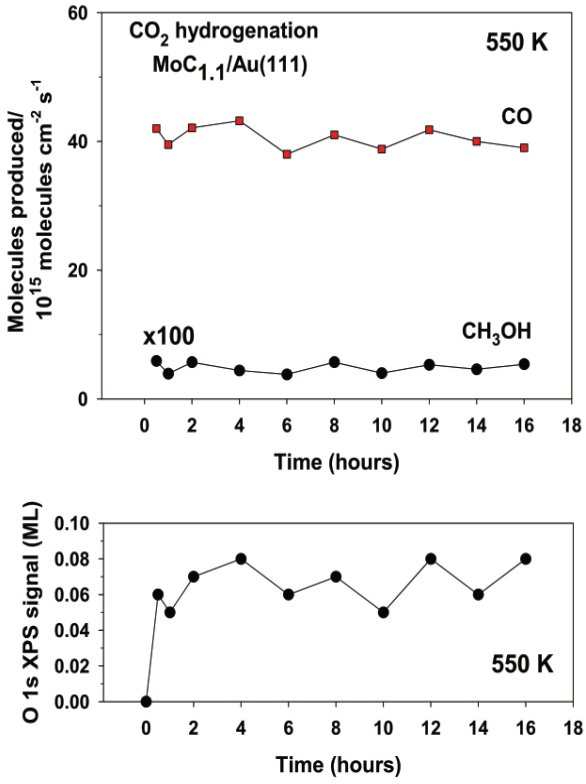

Figure 3. Top panel: Production of CH_4, CO, and CH_3OH during the hydrogenation of CO_2 on a Au(111) surface precovered with 0.3 ML of $MoC_{1.1}$. Bottom panel: Amount of oxygen measured with XPS after different CO_2 hydrogenation times on the $MoC_{1.1}$/Au(111) catalyst. T = 550 K, $P(CO_2)$ = 0.5 atm, and $P(H_2)$ = 4.5 atm.

panel in Figure 2, changes the selectivity of the catalyst and eventually CO becomes the main reaction product. The O adatoms probably block the highly active sites that fully decompose CO_2 on the $MoC_{0.6}$/Au(111) surface. Post-reaction characterization with XPS showed that O adatoms were always the dominant species on this surface with a very small amount (<0.05 ML) of a carbonate. The hydrogen atoms generated by H_2 dissociation on this system are not reactive enough to remove the O adatoms yielded by CO_2 decomposition, the catalyst is metastable, and the carbide NPs transform into a highly stable oxycarbide which also has been detected on surfaces and powders of bulk Mo_2C.[14,16,36,37] The product distribution seen for the hydrogenation of CO_2 on $MoC_{0.6}$/Au(111) is similar to that reported for NPs of Mo_2C which are mainly methanation or Fischer−Tropsch catalysts.[13]

On the other hand, Figure 3 summarizes the results for the hydrogenation of CO_2 on $MoC_{1.1}$/Au(111). Conversely, here, no production of methane was detected. The distribution of reaction products did not change with time, and the main product of the catalytic process was CO with a significant amount of methanol also being produced. As seen in Figure 1, the dissociation of CO_2 on $MoC_{1.1}$/Au(111) is negligible and the system cannot be a good methanation catalyst. The theoretical calculations described below indicate that the hydrogen present in $MoC_{1.1}$/Au(111)[9] facilitates the dissociation of CO_2 into CO by the reverse water−gas shift reaction. Post-reaction characterization with XPS showed that the amount of oxygen deposited on the $MoC_{1.1}$/Au(111) catalyst was very small, see the bottom panel in Figure 3, and most of the O atoms generated by the partial dissociation of CO_2 were rapidly hydrogenated to evolve as gaseous water. According to post-reaction XPS, the surface of the $MoC_{1.1}$/Au(111) catalyst was essentially clean ($\theta_O \sim 0.06$ ML) without carbonates or other C-containing molecules. A comparison of the results in Figures 2 and 3 indicates that the C/Mo ratio in the MoC_x NPs has a tremendous effect on the surface reactivity and the product distribution for CO_2 hydrogenation. The behavior seen for C-rich $MoC_{1.1}$/Au(111) is very different from that seen on C-poor $MoC_{0.6}$/Au(111) or for unsupported NPs of Mo_2C.[13] Thus, the C/Mo ratio can be a quite useful parameter to tune when dealing with CO_2 hydrogenation on carbide NPs.

Since the $MoC_{1.1}$/Au(111) catalyst is stable with time, see Figure 3, one was able to study, in a reproducible way, the hydrogenation of CO_2 at different temperatures. Figure 4 displays an Arrhenius plot for CO_2 hydrogenation to methanol on $MoC_{1.1}$/Au(111). The plain Au(111) substrate is not active for a $CO_2 \rightarrow CH_3OH$ conversion. For comparison, we also include in Figure 4 results for methanol synthesis on Cu(111), a common benchmark, and on bulk δ-MoC.[14] In addition, using the surface atomic density of Au(111) and assuming that all the Mo sites are active, we estimated that minimum TOFs of 0.41 CH_3OH produced molecules $site^{-1}$ s^{-1} at 600 K and 0.07 CH_3OH produced molecules $site^{-1}$ s^{-1} at 500 K. These TOF values are significantly bigger than those reported for Cu(111), Cu(110), polycrystalline Cu, and Cu/ZnO powder catalysts.[38,39] Clearly, $MoC_{1.1}$/Au(111) is a very good catalyst for methanol synthesis. This remarkable result highlights the importance of controlling the C/Mo ratio when dealing with MoC_x NPs as catalysts.

As can be seen in Figure 4, the apparent activation energy for methanol production is reduced from 25 kcal/mol on

https://doi.org/10.1021/acscatal.1c01738
ACS Catal. 2021, 11, 9679−9687

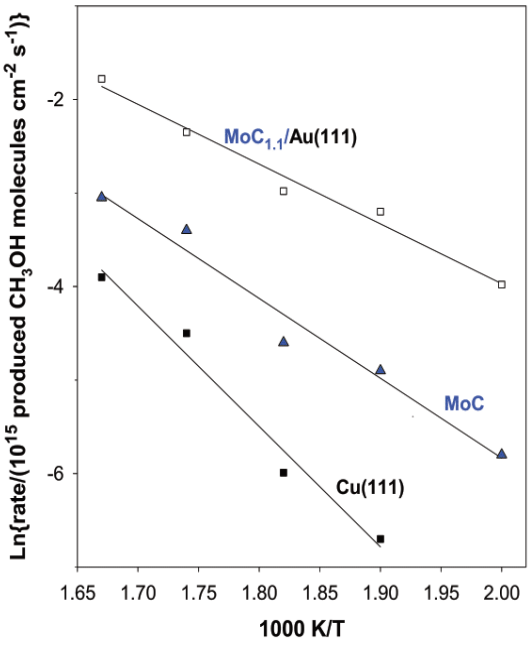

Figure 4. Arrhenius plots for CO_2 hydrogenation on Cu(111), bulk δ-MoC, and a Au(111) surface with 0.3 ML of $MoC_{1.1}$. $P(CO_2)$ = 0.5 atm and $P(H_2)$ = 4.5 atm.

Cu(111) to 17 kcal/mol on bulk δ-MoC and 14 kcal/mol on the $MoC_{1.1}$/Au(111) surface. The atoms in the $MoC_{1.1}$ NPs are orders of magnitude more efficient for the $CO_2 \rightarrow CH_3OH$ hydrogenation than the atoms in the Cu(111) benchmark. Furthermore, the $MoC_{1.1}$/Au(111) system exposed a much lower concentration of carbide sites per surface area than bulk δ-MoC, but it had a much better catalytic performance. These trends probably reflect the superior ability of $MoC_{1.1}$/Au(111) to bind and dissociate H_2.[9]

Adsorption and Activation of CO_2 on C-rich MoC_x/Au(111) Surfaces: DFT Studies. The experimental results in Figures 1−4 indicate that C-rich ($MoC_{1.1}$) carbide NPs are the systems to focus when attempting a controlled and stable conversion of CO_2 into CO and methanol. In a first step, the adsorption mode and energy of CO_2 have been studied at various distinct sites of the $Mo_{12}C_{12}$ NP supported on Au(111)—the $Mo_{12}C_{12}$-sup model—which were compared to previous results for CO_2 adsorption on the extended δ-MoC(001) surface. For this extended surface, calculations with the PBE-D2 method predicted adsorption energy values ∼1.5 eV;[15] the use of a more accurate parametrization of the contribution dispersion by means of the PBE-D3 approach reduces these values to the 1.0−1.2 eV range depending on the site.[17] These values have been obtained by considering a minimum unit cell for the δ-MoC(001) slab model and, hence, with an atomic structure that closely resembles that of the ideal, bulk-cut, surface. However, recent work has shown that this surface exhibits a noticeable reconstruction and, hence, the adsorption energy with respect to the ideal surface is overestimated by ∼0.6 eV.[40] Consequently, a better estimate of the adsorption energy of CO_2 on the reconstructed δ-MoC(001) surface is 0.4−0.6 eV, again depending on the site. For the $Mo_{12}C_{12}$-sup model, the CO_2 adsorption energy ranges from 0.5 to 1.4 eV, the stronger adsorption corresponding to a quite unique site involving a highly undercoordinated C atom, see Figure 5. The concentration of this type of site is likely to be very small and probably biased using the used model. Nevertheless, discarding this special site still leaves several sites

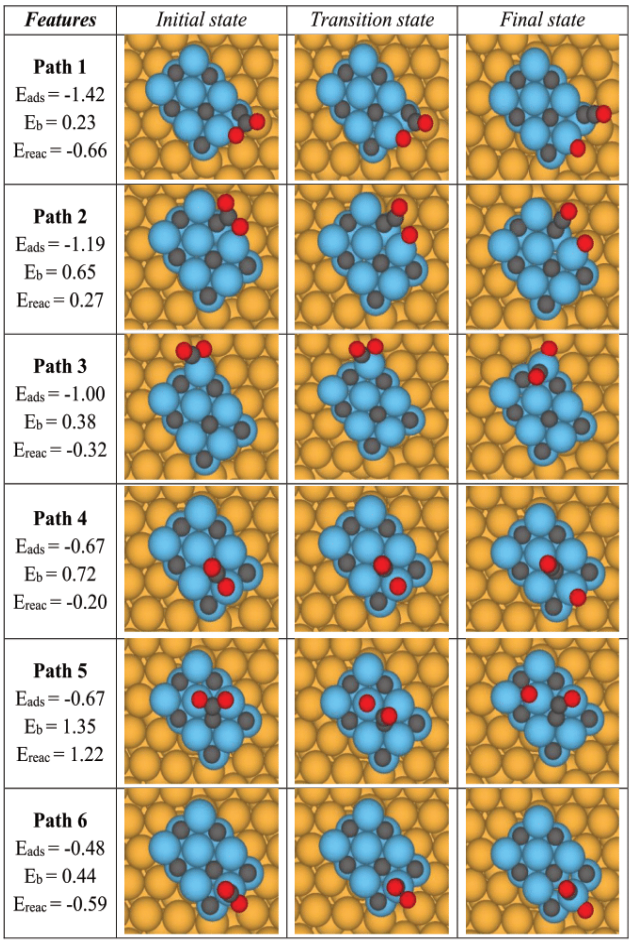

Figure 5. Main considered paths for CO_2 direct dissociation on $Mo_{12}C_{12}$/Au(111). Blue, black, red, and yellow spheres correspond to Mo, C, O, and Au atoms, respectively. Listed on the left side of the figure are calculated results for the adsorption energy (E_{ads}), energy barrier for CO_2 dissociation (E_b), and the reaction energy (E_{reac}). All energies are given in eV.

where the CO_2 adsorption energy is noticeably larger than for the extended surface, in agreement with experimental results.

Next, we consider a series of well-defined pathways for the CO_2 direct dissociation on $Mo_{12}C_{12}$-sup starting from each of the adsorption sites mentioned above and displayed in Figure 5. Excluding the rather infrequent sites involving a highly undercoordinated C atom and a very low coordinated Mo site, the direct CO_2 dissociation to CO and O involves rather large energy barriers, which is in agreement with experiments indicating that CO_2 does not directly dissociate on the C-rich $MoC_{1.1}$/Au(111) system. The quite low-energy barrier for the mentioned undercoordinated sites is interpreted here as a limitation of the present model as, even if eventually present in the experiment, the number of this type of sites will be very small and they are likely to be immediately passivated by C or O atoms produced by dissociation of CO_2.

To investigate the effect of the underlying Au(111) surface into the chemistry of the $Mo_{12}C_{12}$ NPs, we considered the different models where the structure of the NPs is as in the supported case but without the support and either frozen ($Mo_{12}C_{12}$-free-1), partially relaxed ($Mo_{12}C_{12}$-free-2), or totally relaxed ($Mo_{12}C_{12}$-free), as indicated above. Table 1 summarizes the results for these three types of unsupported particles which evidence small variations both in the adsorption energies and energy barriers. The reaction energies are somehow more

https://doi.org/10.1021/acscatal.1c01738
ACS Catal. 2021, 11, 9679−9687

Table 1. Effect of the Au Substrate on the Energy Profile for Representative Pathways for CO_2 Dissociation[a]

energy barrier	path 2	path 3	path 5
$Mo_{12}C_{12}$-sup	0.65	0.38	1.35
$Mo_{12}C_{12}$-free-1	0.83	0.36	1.03
$Mo_{12}C_{12}$-free-2	0.97	0.35	1.19
$Mo_{12}C_{12}$-free	0.79	0.44	1.52
CO_2 adsorption energy	path 2	path 3	path 5
$Mo_{12}C_{12}$-sup	−1.19	−1.00	−0.68
$Mo_{12}C_{12}$-free-1	−1.82	−1.37	−1.03
$Mo_{12}C_{12}$-free-2	−1.38	−1.25	−0.72
$Mo_{12}C_{12}$-free	−1.21	−1.09	−0.41
CO*+O* adsorption energy	path 2	path 3	path 5
$Mo_{12}C_{12}$-sup	−0.92	−1.32	0.54
$Mo_{12}C_{12}$-free-1	−1.49	−1.57	−0.40
$Mo_{12}C_{12}$-free-2	−0.91	−1.48	−0.22
$Mo_{12}C_{12}$-free	−0.61	−1.25	0.25
reaction energy	path 2	path 3	path 5
$Mo_{12}C_{12}$-sup	0.27	−0.32	1.22
$Mo_{12}C_{12}$-free-1	0.33	−0.21	0.63
$Mo_{12}C_{12}$-free-2	0.47	−0.23	0.50
$Mo_{12}C_{12}$-free	0.60	−0.16	0.67

[a]The different models are described in the main text. All values are given in eV.

affected, but the analysis of the results shows that this can, in part, be explained from the fact that the supported NP is partly stabilized by the presence of the Au substrate. To estimate the influence of the NP structure on the reaction energy, we analyzed the structural difference in the $Mo_{12}C_{12}$ NP when reactants (CO_2) or products (CO + O) are adsorbed. To this end, we computed the energy of the $Mo_{12}C_{12}$ NP at each geometry once reactants and products have been removed from the fully optimized $Mo_{12}C_{12}$-free model. For the $Mo_{12}C_{12}$-sup structure, the underlying Au support has also been removed. For convenience, we use SupR and SupP to refer to the structure of the $Mo_{12}C_{12}$-sup NP that is obtained once the reactants, products, and substrate are removed from the optimized structure in the $Mo_{12}C_{12}$-sup model. Following the same logic, the corresponding notation for the $Mo_{12}C_{12}$-free model is FreeR and FreeP. With these definitions, the influence of the Au substrate in the reaction energy, Δ_{sup}, can be obtained as

$$\Delta_{sup} = \frac{(E_{SupP} - E_{SupR}) - (E_{FreeP} - E_{FreeR})}{E_{sup}^{Reac} - E_{free}^{Reac}} \quad (1)$$

where E_{sup}^{Reac} and E_{free}^{Reac} are the actual reaction energies in the supported model and free model that can be extracted from Table 1. From eq 1, it turns out that a Δ_{sup} value close to 1 implies that the differences in reaction energy between the $Mo_{12}C_{12}$-free and $Mo_{12}C_{12}$-sup models can be completely ascribed to the structural differences between the $Mo_{12}C_{12}$-free and $Mo_{12}C_{12}$-sup models with the adsorbed reactants and products. It turns out that Δ_{sup} is 0.8 just for one of the cases in Table 1 indicating that the differences in reaction energy between the $Mo_{12}C_{12}$-free and $Mo_{12}C_{12}$-sup models cannot always be fully attributed to structural changes, which implies that a full description of the energy profiles, including the reaction energy value, requires taking the Au support into account. Besides, for the other two cases studied, Δ_{sup} becomes 2.1 and −0.7. The large deviation from 1 meaning that the difference in reaction energy is not driven by the structural changes in the NP, instead they are induced by the support. Nevertheless, the positive part of this comparison is that $Mo_{12}C_{12}$-free and $Mo_{12}C_{12}$-sup provide a very similar description of the CO_2 adsorption and energy barrier, considering the bottleneck parameters on CO_2 activation, which justifies the use of the $Mo_{12}C_{12}$-free model to explore the reactivity of the H-covered NPs. It is also worth pointing out that the partially relaxed $Mo_{12}C_{12}$-free-1 and $Mo_{12}C_{12}$-free-2 models do not adequately represent the situation for the supported particle as, in the absence of a support, a minimal reconstruction is required to recover the capability of the $Mo_{12}C_{12}$ NP to adsorb and activate CO_2.

Next, we make use of the $Mo_{12}C_{12}$-free models to systematically explore additional reaction pathways always with the same conclusion, the CO_2 direct dissociation is not favored which, again, is in line with experimental findings where no methane is detected, and CO and methanol are the only products, see Figure 3. Since CO_2 dissociation is experimentally observed when a significant amount of hydrogen is present (cf., Figures 3 and 4), a new series of calculations were carried out to explore the effect of coadsorbed atomic H on the CO_2 dissociation energy profile. For the situations where one H atom is present close to the adsorbed CO_2 molecule, the energy barrier for dissociation is still large, above 0.4 eV, essentially as when H is not present.

This is clear when comparing the direct dissociation through the named path 3 with an almost equivalent activation pathway for a low hydrogen regime, hereafter referred to as path 3H. This pathway involves two steps, the first one corresponds to the dissociation of adsorbed CO_2, which is equivalent to the process observed when hydrogen is not present, and the second step involves hydrogenation of adsorbed O, as schematically shown in Figure 6 top. Consequently, the formation of a carboxylate (COOH) adsorbed species, a key species in the reverse water−gas shift mechanism,[14] is circumvented. The same situation is encountered when analyzing other pathways involving different sites. Most explored hydrogenation steps either failed to converge to the carboxylate intermediate leading instead to adsorbed CO and OH directly, or involved exceedingly large energy barriers. In any case, path 3 and path 3H allow a meaningful comparison between direct and hydrogen-assisted CO_2 activation as both mechanisms involve similar elementary steps with nearly equal energy barriers, 0.38 and 0.44 eV for path 3 and path 3H, respectively. These energy barriers are sufficiently high to prevent easy dissociation which agrees with the experimental findings that, in the absence of a sufficient amount of hydrogen, these Mo_2C NPs are not active for CO_2 dissociation.

Therefore, we analyzed the situation involving a high hydrogen regime already studied with experiment and theory in a previous work showing that the interaction between hydrogen and the MoC NPs supported on Au(111) occurs either *via* adsorption on top of C atoms in a *Kubas* mode as well as on top-Mo.[9] The model calculations carried out for the interaction of CO_2 with the $Mo_{12}C_{12}$-free NPs covered with more H atoms reveal a systematic lowering of the energy barrier for CO_2 dissociation. In particular, the formation of a *Kubas* complex—an elongated H_2 moiety—has an important impact on the energy barrier for CO_2 dissociation which becomes significantly reduced with values as low as 0.2−0.3 eV, and always involving the direct formation of CO and OH, again with no evidence of stable adsorbed COOH, at least at a

https://doi.org/10.1021/acscatal.1c01738
ACS Catal. 2021, 11, 9679−9687

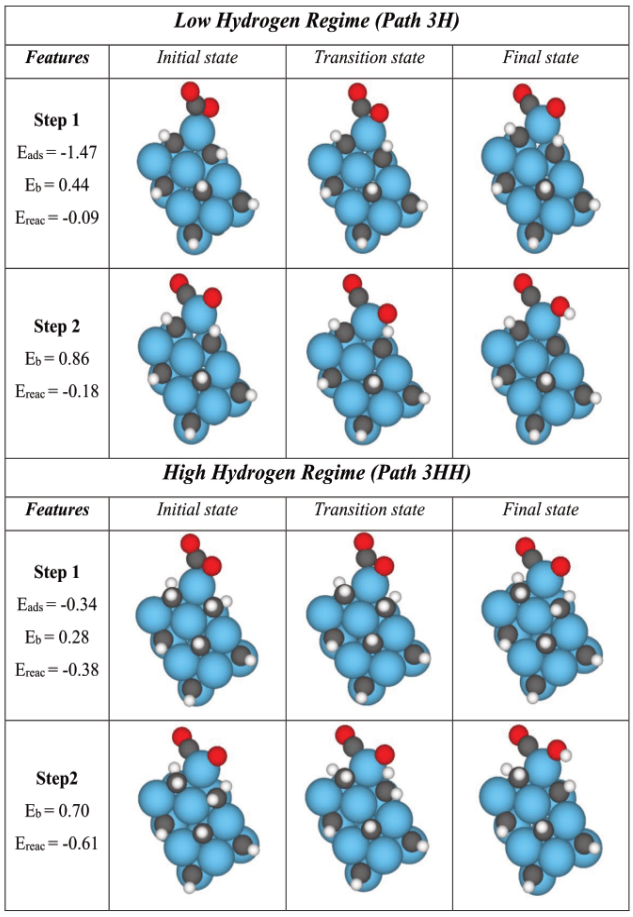

Figure 6. CO_2 hydrogenation paths on different hydrogen regimes for the $Mo_{12}C_{12}$-free model. Top and bottom panels correspond to the low and high H regime situations, respectively. Blue, black, red, and white spheres correspond to Mo, C, O, and H atoms, respectively. Values listed in the left side are as in Figure 5. All energies are given in eV.

competitive level. The differences with respect to the cases with no adsorbed H or with low H coverage are small but significative. Moreover, the computational setup explained in the previous section allows us to rule out the possibility of a numerical artifact. Nevertheless, to directly examine the influence of a high hydrogen regime in an analogous situation to the already mentioned example, we consider again path 3 but in a high hydrogen regime (path 3 HH). For this situation, the relevant results are reported in Figure 6 bottom. For path 3 HH, the molecular mechanism is in the low hydrogen regime path 3 H but with a significant drop in the energy barrier for CO_2 direct dissociation from 0.44 to 0.28 eV. This is an additional clear indication of the important effect of H coverage on the mechanism for CO_2 conversion.

To complete the study and to better model the experimental situation where the partial pressure ratio for CO_2 and H_2 gases is 19, a full H coverage model has been investigated where 19 H atoms are incorporated to the $Mo_{12}C_{12}$-free, where gas-phase CO_2 reacts with the adsorbed H atoms to form a formate intermediate following an Eley–Rideal mechanism. Interestingly, the energy barrier for such an elementary step is significantly small, of only 0.2 eV, and smaller than those corresponding to direct CO_2 dissociation in the absence of adsorbed H, see Figure 7. In conclusion, in spite of inherent limitations of the models used to represent the C-rich MoC_x/Au(111) system, the present DFT calculations consistently

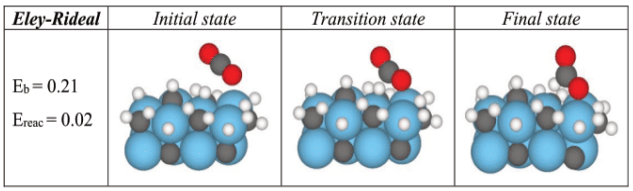

Figure 7. Eley–Rideal mechanism for CO_2 hydrogenation on a H-covered $Mo_{12}C_{12}$-free. Note that the bottom layer does not contain H because it is the region that should be in contact with the Au support. Color code as in Figure 6. All energies are given in eV.

predict that the presence of a significant amount of adsorbed atomic H significantly lowers the energy barrier for CO_2 dissociation leading to CO either *via* direct dissociation or through a formate intermediate, the latter implying an Eley–Rideal mechanism. Therefore, the predictions from the present model calculations are in qualitative agreement with experimental findings and provide consistent insights into the involved molecular mechanism evidencing the important effect of preadsorbed H on the CO_2 conversion to CO, although the calculated energy barriers should not be taken as estimates of the experimental values. In particular, the mentioned Eley–Rideal mechanism is likely to explain the formation of methanol as this requires continued hydrogenation steps to the adsorbed formate intermediate.

CONCLUSIONS

Carbon-poor ($MoC_{0.6}$) and carbon-rich ($MoC_{1.1}$) carbide NPs supported on Au(111) are active for the hydrogenation of CO_2. The molecule underwent partial ($CO_2 \rightarrow CO + O$) and complete ($CO_2 \rightarrow C + 2O$) decomposition on the $MoC_{0.6}$/Au(111) surface. This system was highly active but unstable under CO_2 hydrogenation conditions, producing CO and methane as main products with a very minor amount of methanol. In contrast, the nearly stoichiometric NPs in $MoC_{1.1}$/Au(111) reversibly adsorbed/desorbed CO_2 and, after exposure to hydrogen, CO_2 was converted predominantly to CO with a significant amount of methanol and no methane or other alkanes as reaction products. The apparent activation energy for this process (14 kcal/mol) was smaller than that corresponding to bulk δ-MoC (17 kcal/mol) or a Cu(111) benchmark system (25 kcal/mol). This trend reflects the superior ability of $MoC_{1.1}$/Au(111) to bind and dissociate H_2.

DFT calculations carried out for free or supported $Mo_{12}C_{12}$ NPs showed that, in the absence of preadsorbed H, the direct dissociation involves rather large energy barriers, which is in agreement with the experiment. The fact that calculations for the Au-supported and free $Mo_{12}C_{12}$ NP models lead to the same qualitative description of the reaction mechanism, with almost quantitative agreement for the adsorption energy and energy barrier for CO_2 dissociation, opens the way to the use of the unsupported model to investigate the catalytic properties of these NPs. These show that the large reservoir of H adatoms present in a $Mo_{12}C_{12}$ NP led to a considerable reduction in the energy barrier for the CO_2 dissociation to CO and OH without evidence of a carboxylate intermediate, thus providing a detailed insight into the experimental observations. Nevertheless, we must point out that the energy barriers predicted with the present models featuring different hydrogen coverages have to be taken as an indication of the overall effect and should not be directly compared to experimentally derived values. For the high H coverage situation, the present model

https://doi.org/10.1021/acscatal.1c01738
ACS Catal. 2021, 11, 9679–9687

calculations suggest that the pathway to methanol is likely to involve an Eley−Rideal mechanism leading to a formate intermediate that, we speculate, undergoes a series of hydrogenation steps.

■ ASSOCIATED CONTENT

Supporting Information

The Supporting Information is available free of charge at https://pubs.acs.org/doi/10.1021/acscatal.1c01738.

Atomic coordinates for representative models (PDF)

■ AUTHOR INFORMATION

Corresponding Authors

José A. Rodriguez − *Chemistry Division, Brookhaven National Laboratory, Upton, New York 11973, United States;* orcid.org/0000-0002-5680-4214; Email: rodrigez@bnl.gov

Francesc Illas − *Departament de Ciència de Materials i Química Física & Institut de Química Teòrica i Computacional (IQTCUB), Universitat de Barcelona, 08028 Barcelona, Spain;* orcid.org/0000-0003-2104-6123; Email: francesc.illas@ub.edu

Authors

Marc Figueras − *Departament de Ciència de Materials i Química Física & Institut de Química Teòrica i Computacional (IQTCUB), Universitat de Barcelona, 08028 Barcelona, Spain*

Ramón A. Gutiérrez − *Facultad de Ciencias, Universidad Central de Venezuela, 1020-A Caracas, Venezuela; Chemistry Division, Brookhaven National Laboratory, Upton, New York 11973, United States*

Francesc Viñes − *Departament de Ciència de Materials i Química Física & Institut de Química Teòrica i Computacional (IQTCUB), Universitat de Barcelona, 08028 Barcelona, Spain;* orcid.org/0000-0001-9987-8654

Pedro J. Ramírez − *Facultad de Ciencias, Universidad Central de Venezuela, 1020-A Caracas, Venezuela;* Present Address: Zoneca-CENEX, R&D Laboratories, Alta Vista, 64770 Monterrey, Mexico

Complete contact information is available at: https://pubs.acs.org/10.1021/acscatal.1c01738

Notes

The authors declare no competing financial interest.

■ ACKNOWLEDGMENTS

The research carried out at the Universitat de Barcelona has been supported by the Spanish MICIUN/FEDER RTI2018-095460-B-I00 and María de Maeztu MDM-2017-0767 grants and, in part, by Generalitat de Catalunya 2017SGR13 grants. This manuscript has been authored by employees of Brookhaven Science Associates, LLC under contract no. DE-SC0012704 with the U.S. Department of Energy. F.I. acknowledges additional support from the 2015 ICREA Academia Award for Excellence in University Research. Computational resources provided by the Red Española de Supercomputación are fully acknowledged.

■ REFERENCES

(1) Levy, R. B.; Boudart, M. Platinum-Like Behavior of Tungsten Carbide in Surface Catalysis. *Science* **1973**, *181*, 547−549.

(2) Hwu, H. H.; Chen, J. G. Surface Chemistry of Transition Metal Carbides. *Chem. Rev.* **2005**, *105*, 185−212.

(3) Shou, H.; Davis, R. J. Multi-Product Steady-State Isotopic Transient Kinetic Analysis of CO Hydrogenation over Supported Molybdenum Carbide. *J. Catal.* **2013**, *306*, 91−99.

(4) Silveri, F.; Quesne, M. G.; Roldán, A.; de Leeuw, N. H.; Catlow, C. R. A. Hydrogen Adsorption on Transition Metal Carbides: a DFT Study. *Phys. Chem. Chem. Phys.* **2019**, *21*, 5335−5343.

(5) Vo, D.-V. N.; Adesina, A. A. Fischer-Tropsch Synthesis over Alumina-Supported Molybdenum Carbide Catalyst. *Appl. Catal., A* **2011**, *399*, 221−232.

(6) Gao, J.; Zheng, Y.; Fitzgerald, G. B.; de Joannis, J.; Tang, Y.; Wachs, I. E.; Podkolzin, S. G. Structure of Mo_2C_x and Mo_4C_x Molybdenum Carbide Nanoparticles and Their Anchoring Sites on ZSM-5 Zeolites. *J. Phys. Chem. C* **2014**, *118*, 4670−4679.

(7) Prats, H.; Piñero, J. J.; Viñes, F.; Bromley, S. T.; Sayós, R.; Illas, F. Assessing the Usefulness of Transition Metal Carbides for Hydrogenation Reactions. *Chem. Commun.* **2019**, *55*, 12797−12800.

(8) Figueras, M.; Gutiérrez, R. A.; Prats, H.; Viñes, F.; Ramírez, P. J.; Illas, F.; Rodriguez, J. A. Boosting the Activity of Transition Metal Carbides Towards Methane Activation by Nanostructuring. *Phys. Chem. Chem. Phys.* **2020**, *22*, 7110−7118.

(9) Figueras, M.; Gutiérrez, R. A.; Viñes, F.; Ramírez, P. J.; Rodriguez, J. A.; Illas, F.; Rodriguez, J. A. Supported Molybdenum Carbide Nanoparticles as Hot Hydrogen Reservoirs for Catalytic Applications. *J. Phys. Chem. Lett.* **2020**, *11*, 8437−8441.

(10) Anderson, T. R.; Hawkins, E.; Jones, P. D. CO_2, the greenhouse effect and global warming: from the pioneering work of Arrhenius and Callendar to today's Earth System Models. *Endeavour* **2016**, *40*, 178−187.

(11) Porosoff, M. D.; Yan, B.; Chen, J. G. Catalytic reduction of CO_2 by H_2 for synthesis of CO, methanol and hydrocarbons: challenges and opportunities. *Energy Environ. Sci.* **2016**, *9*, 62−73.

(12) Aresta, M. *Carbon Dioxide as Chemical Feedstock*; Wiley-VCH: New York, 2010.

(13) Baddour, F. G.; Roberts, E. J.; To, A. T.; Wang, L.; Habas, S. E.; Ruddy, D. A.; Bedford, N. M.; Wright, J.; Nash, C. P.; Schaidle, J. A.; Brutchey, R. L.; Malmstadt, N. An Exceptionally Mild and Scalable Solution-Phase Synthesis of Molybdenum Carbide Nanoparticles for Thermocatalytic CO_2 Hydrogenation. *J. Am. Chem. Soc.* **2020**, *142*, 1010−1019.

(14) Posada-Pérez, S.; Ramírez, P. J.; Evans, J.; Viñes, F.; Liu, P.; Illas, F.; Rodriguez, J. A. Highly Active Au/δ-MoC and Cu/δ-MoC Catalysts for the Conversion of CO_2: The Metal/C Ratio as a Key Factor Defining Activity, Selectivity, and Stability. *J. Am. Chem. Soc.* **2016**, *138*, 8269−8278.

(15) Posada-Pérez, S.; Viñes, F.; Ramirez, P. J.; Vidal, A. B.; Rodriguez, J. A.; Illas, F. The Bending Machine: CO_2 Activation and Hydrogenation on δ-MoC(001) and β-Mo_2C(001) Surfaces. *Phys. Chem. Chem. Phys.* **2014**, *16*, 14912−14921.

(16) Xu, W.; Ramirez, P. J.; Stacchiola, D.; Rodriguez, J. A. Synthesis of α-MoC_{1-x} and β-MoC_y Catalysts for CO_2 Hydrogenation by Thermal Carburization of Mo-oxide in Hydrocarbon and Hydrogen Mixtures. *Catal. Lett.* **2014**, *144*, 1418−1424.

(17) Kunkel, C.; Viñes, F.; Illas, F. Transition Metal Carbides as Novel Materials for CO_2 Capture, Storage, and Activation. *Energy Environ. Sci.* **2016**, *9*, 141−144.

(18) Horn, J. M.; Song, Z.; Potapenko, D. V.; Hrbek, J.; White, M. G. Characterization of Molybdenum Carbide Nanoparticles Formed on Au(111) Using Reactive-Layer Assisted Deposition. *J. Phys. Chem. B* **2005**, *109*, 44−47.

(19) Rodriguez, J. A.; Liu, P.; Dvorak, J.; Jirsak, T.; Gomes, J.; Takahashi, Y.; Nakamura, K. The interaction of oxygen with TiC(001): Photoemission and first-principles studies. *J. Chem. Phys.* **2004**, *121*, 465−474.

(20) Frantz, P.; Didziulis, S. V. Detailed spectroscopic studies of oxygen on metal carbide surfaces. *Surf. Sci.* **1998**, *412*−*413*, 384.

(21) Didziulis, S. V.; Frantz, P.; Perry, S. S.; El-bjeirami, O.; Imaduddin, S.; Merrill, P. B. Substrate-Dependent Reactivity of Water on Metal Carbide Surfaces. *J. Phys. Chem. B* **1999**, *103*, 11129.
(22) Potapenko, D.; Horn, J.; White, M. The Reactions of Cyclohexene on Au(111)-supported Molybdenum Carbide Nanoparticles. *J. Catal.* **2005**, *236*, 346−355.
(23) Lamiel-Garcia, O.; Bromley, S. T.; Illas, F. Low-energy Nanoscale Clusters of $(TiC)_n$ n = 6, 12: A Structural and Energetic Comparison with MgO. *Theor. Chem. Acc.* **2013**, *132*, 1312−1318.
(24) Jiménez-Orozco, C.; Figueras, M.; Flórez, E.; Viñes, F.; Rodriguez, J. A.; Illas, F. Size and Stoichiometry Effects on the Reactivity of MoC_y Nanoparticles Towards Ethylene. *J. Phys. Chem. C* **2021**, *125*, 6287−6297.
(25) Lozano-Reis, P.; Prats, H.; Gamallo, P.; Illas, F.; Sayós, R. Multiscale Study of the Mechanism of Catalytic CO_2 Hydrogenation: Role of the Ni(111) Facets. *ACS Catal.* **2020**, *10*, 8077−8089.
(26) Piqué, O.; Viñes, F.; Illas, F.; Calle-Vallejo, F. Elucidating the structure of ethanol-producing active sites at oxide-derived Cu electrocatalysts. *ACS Catal.* **2020**, *10*, 10488−10494.
(27) Chen, B. W. J.; Xu, L.; Mavrikakis, M. Computational Methods in Heterogeneous Catalysis. *Chem. Rev.* **2021**, *121*, 1007−1048.
(28) Morales-García, A.; Viñes, F.; Gomes, J. R. B.; Illas, F. Concepts, models and methods in computational heterogeneous catalysis illustrated through CO_2 conversion. *Wiley Interdiscip. Rev.: Comput. Mol. Sci.* **2021**, *11*, No. e1530.
(29) Kresse, G.; Furthmüller, J. Efficient Iterative Schemes for ab initio Total-energy Calculations Using a Plane-wave Basis Set. *Phys. Rev. B: Condens. Matter Mater. Phys.* **1996**, *54*, 11169−11186.
(30) Perdew, J. P.; Burke, K.; Ernzerhof, M. Generalized Gradient Approximation Made Simple. *Phys. Rev. Lett.* **1996**, *77*, 3865−3868.
(31) Politi, J. R. D. S.; Viñes, F.; Rodriguez, J. A.; Illas, F. Atomic and Electronic Structure of Molybdenum Carbide Phases: Bulk and Low Miller-index Surfaces. *Phys. Chem. Chem. Phys.* **2013**, *15*, 12617−12625.
(32) Grimme, S.; Antony, J.; Ehrlich, S.; Krieg, H. A consistent and accurate ab initio parametrization of density functional dispersion correction (DFT-D) for the 94 elements H-Pu. *J. Chem. Phys.* **2010**, *132*, 154104.
(33) Kresse, G.; Joubert, D. From ultrasoft pseudopotentials to the projector augmented-wave method. *Phys. Rev. B: Condens. Matter Mater. Phys.* **1999**, *59*, 1758−1775.
(34) Henkelman, G.; Uberuaga, B. P.; Jónsson, H. A Climbing Image Nudged Elastic Band Method for Finding Saddle Points and Minimum Energy Paths. *Phys. Rev. B: Condens. Matter Mater. Phys.* **2000**, *113*, 9901−9904.
(35) Posada-Pérez, S.; Ramírez, P. J.; Gutiérrez, R. A.; Stacchiola, D. J.; Viñes, F.; Liu, P.; Illas, F.; Rodriguez, J. A. The Conversion of CO_2 to Methanol on orthorhombic β-Mo_2C and Cu/β-Mo_2C Catalysts: Mechanism for Admetal Induced Change in the Selectivity and Activity. *Catal. Sci. Technol.* **2016**, *6*, 6766−6777.
(36) Likith, S. R. J.; Farberow, C. A.; Manna, S.; Abdulslam, A.; Stevanović, V.; Ruddy, D. A.; Schaidle, J. A.; Robichaud, D. J.; Ciobanu, C. V. Thermodynamic Stability of Molybdenum Oxycarbides Formed from Orthorhombic Mo_2C in Oxygen-Rich Environments. *J. Phys. Chem. C* **2018**, *122*, 1223−1233.
(37) Kurlov, A.; Huang, X.; Deeva, E. B.; Abdala, P. M.; Fedorov, A.; Müller, C. R. Molybdenum carbide and oxycarbide from carbon-supported MoO_3 nanosheets: phase evolution and DRM catalytic activity assessed by TEM and in situ XANES/XRD methods. *Nanoscale* **2020**, *12*, 13086.
(38) Yoshihara, Y.; Campbell, H. Methanol Synthesis and Reverse Water-Gas Shift Kinetics over Cu(110) Model Catalysts: Structural Sensitivity. *J. Catal.* **1996**, *161*, 776−782.
(39) Schumann, J.; Tarasov, A.; Thomas, N.; Schlögl, R.; Behrens, M. Cu,Zn-based catalysts for methanol synthesis: On the effect of calcination conditions and the part of residual carbonates. *Appl. Catal., A* **2016**, *516*, 117.
(40) Figueras, M.; Jurado, A.; Morales-García, Á.; Viñes, F.; Illas, F. Bulk (in)stability as a possible source of surface reconstruction. *Phys. Chem. Chem. Phys.* **2020**, *22*, 19249−19253.

https://doi.org/10.1021/acscatal.1c01738
ACS Catal. 2021, 11, 9679−9687

Chapter 9:

Ethylene adsorption on MoC nanoparticles

9.1 Introduction

The interaction of ethylene (C_2H_4) with TMC surfaces has been explored in some previous studies to determine their practicability as alternative catalysts to the Pt-group metals. [158-160] Nevertheless, the effect of the nanostructure ensemble still remains unexplored and, as seen in previous Chapters of this Thesis, a nanostructure ensemble could significantly improve the inherent catalytic capabilities of TMCs. Moreover, the results in Chapter 8 show that the effect of the Au(111) support on the catalytic activity of the MoC nanoparticles is not dominant. Therefore, the chemistry of their interaction with ethylene can be safely studied using models that do not include the metallic support. In the present Chapter, a purely theoretical study aiming to describe the interaction between MoC NPs and ethylene, which can be taken as a model for larger olefins, is reported. A series of DFT based calculations were carried out to study several chemical descriptors revealing the insights of ethylene and MoC NPs interaction. The 14 NPs models used in the present Chapter have M/C ratios ranging from 0.67 to 2.0, thus covering a broad stoichiometries range, including those prepared experimentally and discussed in the previous Chapter regarding CO_2 activation and conversion.

The detailed analysis of the obtained results revealed some insights on the ethylene interaction with MoC_y NPs in gas-phase which may be also important to understand the chemistry of these NPs when supported on Au(111) or similar substrates. Particularly, the most relevant results are those indicating the superior capabilities of MoC_y NPs to bind ethylene compared to the δ-MoC(001) surface. Nevertheless, some NPs displayed rather large deformation energies and ethylene distortion energies, which are not a desired feature to consider MoC_y as possible hydrogenation catalysts. Large values in these descriptors imply the distortion of the C=C bond, which is considered key in such reactions as long as it remains unaltered. However, a rigorous analysis determined that for Mo/C ratios lower than 1.08, can avoid such difficulties and still display large adsorption energies. The obtained theoretical results determine the optimal MoC_y composition for ethylene binding, providing a benchmark encouraging further experimental studies to develop MoC_y based catalysts for hydrogenation reactions.

9.2 Results

The NPs models were selected accounting on the methodology described in Section 4.2.2, however, in this case the set of models was enlarged. The additionally considered models comprises a series of larger models or especially stable structures like the MetCar (Mo_8C_{12}) or the Nanocube ($Mo_{14}C_{13}$).[161,162] First, the bare selected NPs were analysed in order unveil some insights concerning the stoichiometry or size effects. The first chemical descriptor considered is the formation energy, E_{form}, as it provides an estimation of the thermodynamic stability. The obtained results reveal that for a constant C/M ratio, an increase in size implies a linear decrease of the E_{form}, as expected from the increased stability. The second chemical descriptor considered for the bare NPs is the band gap, E_{gap}, which does not show any relevant correlation between size or stoichiometry. In fact, it remains mostly constant around 0.15 eV, implying that these NPs do not have a clear metallic character which is typical of finite systems since even very large metallic nanoparticles exhibit discrete energy levels and a concomitant band gap.

Next, ethylene adsorption was considered in all 14 models, in all non-equivalent sites and all possible adsorption modes, implying a total of 500 different initial C_2H_4 adsorption structures. After optimization, the 500 different structures were reduced to 221 topologically different ethylene adsorption structures. The subsequent analysis focused on the most stable adsorption structure only, as the second most stable adsorption structure was always located, at least, more than 0.1 eV higher. The obtained results revealed that for the stoichiometric NPs, the E_{ads} values were significantly larger than those observed for the δ-MoC surfaces,[158,159] and similar to those obtained for β-Mo_2C surfaces.[160] From conformational point of view, the most common adsorption binding mode was π-M, which implies that both ethylene C atoms are bonded to the same low-coordinated Mo atom, usually at the NP corner sites. Other common adsorption modes are σ-M and μ-M, both implying a direct bond of a C atom with a Mo atom. The obtained results revealed the major role played by low-coordinated Mo atoms in the ethylene adsorption. Additionally, the elongation of the C=C bond was studied, revealing significant elongations ranging from 0.09 to 0.25 Å. Interestingly, the largest elongations were found on those adsorption modes implying C binding, *i.e.*, the bonding of ethylene C with NP C atoms. From the obtained results, one can suggest that bond elongations are more correlated to certain adsorption modes rather than to larger E_{ads}, *i.e.*, interaction strength.

The results were also analysed focusing only on the stoichiometric NPs so as to establish possible trends. A comparison between E_{ads} and NP size reveals a poor correlation between both properties. Nevertheless, this behaviour can be consequence of the inherent E_{ads} nature, which is a balance of different energy contributions, i.e., the ethylene distortion energy, E_{dis}, the NP deformation energy, E_{def}, and, the attachment energy, E_{att}, the result of considering both E_{dis} and E_{def} contributions. The resulting plots reveal the same uncorrelated oscillations displayed by the E_{ads}, with the exception of the E_{att}, indicating that the driving force is the intrinsic nature of the nanoscale regime, where features observed for small structures are usually not scalable to larger ones.[163] Precisely, for E_{att}, an increase in size represents a decrease of this value with the sole outlier of $Mo_{32}C_{32}$, mostly due to a different adsorption mode. When the same adsorption mode is considered, there is an almost perfect correlation between size and E_{att}, where an increase in the former evokes a decrease in the latter as expected, indicating once again the major role played by the adsorption mode. The poor correlation between E_{ads} and size can be attributed to just one case, the $Mo_{24}C_{24}$ NP, that distorts the linear correlation. The $Mo_{24}C_{24}$ special behaviour could be consequence of its particular atomic structure, where its higher symmetry leads to some unexpected values for the computed descriptors, *i.e.*, remarking the non-scalable regime present at these small sizes.

A similar study was carried out focusing on only on the non-stoichiometric NPs, aiming to unveil some different trends. Even though, their comparison is difficult, in the sense that there are a mix of size and C/M ratio features involved, some trends emerged. First, for M/C ratios smaller than 1, the E_{ads} dispersion is rather small, of 0.2 eV. On the other hand, for M/C ratios larger than 1, the E_{ads} dispersion is larger, around 1.1 eV. There is not a clear explanation for this aspect. Moreover, the size effect, in terms of C content, seems to be relevant as a larger size implies a weaker ethylene binding energy, with some pronounced outliner changes that can be accounted on a different adsorption mode. Additionally, for most of the considered NPs, the distortion energy triggered by ethylene adsorption was above 1 eV, which could imply the scission of the C=C bond in hydrogenation reaction, which is to be avoided. Another analysed feature was the charge transfer from the NP to ethylene. The obtained results indicated that charge transfer increase with the Mo/C ratio. In fact, the Mo enrichment has appeared relevant as well when analysing the largest NPs. The Mo enrichment appears to induce a rise in the E_{ads} for such NPs. Nevertheless, Mo/C ratios larger than 1.1 appear to not be favourable for

ethylene activation. The increase of Mo/C above 1.0 implies higher E_{dis} and E_{def}, which lowers the E_{att}. Consequently, the only desirable Mo/C ratios to bind ethylene are those close to the stoichiometric ratio.

Finally, the electronic structure resulting from the ethylene interaction with the NPs was studied by means of Charge Density Difference (CDD) and Electronic Localization Function (ELF) plots. The main conclusion appear when accounting for the different bonding modes. For instance, the σ-M and μ-M modes favour a large charge transfer from the NP to the ethylene molecule as shown in the ELF plots from Figure 11, which clearly correlates with the large -0.61 *e* Bader charge computed. Contrarily, the main observed binding mode, π-M, displays less electron density within the adsorbate, in concordance with the -0.30 *e* Bader charge computed. This behaviour could indicate that the ethylene adsorption on MoC NPs has some ionic character. Moreover, the electron density increase within ethylene occupies the lowest unoccupied molecular orbital (LUMO) anti-bonding orbitals, which induces a decrease in the bond order, elongating the C-C bond. On the other hand, the δ-MoC(001) surface reveals a continuous flux of electron density within its layers,[158] a behaviour that can be extrapolated to other TMCs.[164] Interestingly, ethylene on δ-MoC(001) displays negligible elongations of 0.03 Å, consequence of an easy perturbation in the Mo and C atoms arrangement upon interacting with ethylene.

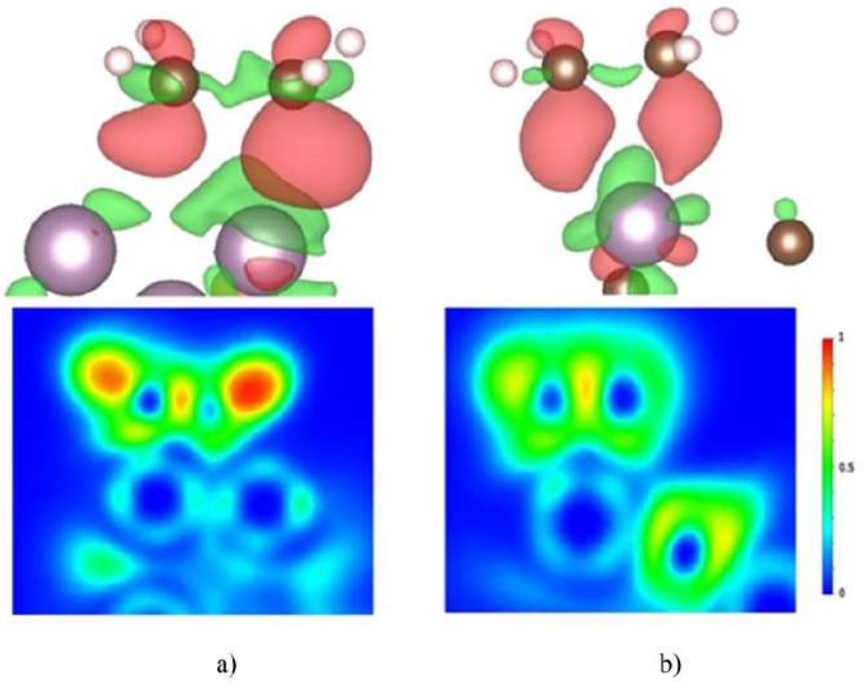

Figure 11. Top part: CDD plots for bonding via (a) σ-M, μ-M ($Mo_{12}C_6$) and (b) π-M ($Mo_{12}C_{12}$) modes. Bottom part: ELF illustration for the same bonding modes considered in the top part. C, H and Mo atoms are represented by brown, white and magenta spheres, respectively. In the CDD plots, red and green areas represent where charge was lost or gained, respectively. ELF illustration describes the likelihood of finding a pair of electrons in function of colour, being blue the least probable areas, and red the most probable ones.

9.3 Conclusions

In the present Chapter, a systematic study was carried out in order to reveal the insights of the ethylene binding to MoC_y NPs. The explored models account for a large range of M/C ratio (0.67-2.00) and NP structures obtained from different sources. The results of the DFT based calculations reveal that a major classification can be described accounting on the adsorption modes, as this plays a major role in the bonding strength. Furthermore, the ethylene adsorption strongly perturbs the NP electron density, which induces larger adsorption energies and higher charge densities migrations to ethylene compared to those observed for the δ-MoC surface. Moreover, C-C bond elongations of 0.09-0.25 Å have been reported, where the largest elongations are found on C binding sites.

Apart from the adsorption energy, the present Chapter precisely describe the aforementioned interaction as observed from several other descriptors and features, including the NPs stoichiometry, size, ethylene distortion energy, NP deformation energy

and ethylene attachment energy. Taking these properties as possible descriptors, one can predict that the highest performance on the ethylene hydrogenation reaction will be obtained using NPs with Mo/C ratios below 1.08, as larger ratios easily distort the C=C bond eventually breaking it and leading to undesired subproducts of the hydrogenation process. The main underlying reason for such distortion is that an excess of Mo atoms and, therefore, a low coordination of these atoms, imply that Mo atoms adsorption sites will bind ethylene too strongly in order to compensate their uncoordinated nature.

All in all, the present study unveiled several aspects of the ethylene binding on MoC_y NPs, contributing to the already established idea that MoC NPs can be excellent catalysts for hydrogenation reactions.

For a more detailed description, the reader is referred to the publication included below. The supporting information of the present publication, can be found in Appendix E.

Contribution: models preparation, results interpretation, and contribute to the writing of the publication.

9.4 Publication

Size and stoichiometry effects on the reactivity of MoC_y nanoparticles toward ethylene

THE JOURNAL OF PHYSICAL CHEMISTRY C
A JOURNAL OF THE AMERICAN CHEMICAL SOCIETY

pubs.acs.org/JPCC

Article

Size and Stoichiometry Effects on the Reactivity of MoC_y Nanoparticles toward Ethylene

Carlos Jimenez-Orozco,* Marc Figueras, Elizabeth Flórez, Francesc Viñes, José A. Rodriguez, and Francesc Illas*

Cite This: *J. Phys. Chem. C* 2021, 125, 6287−6297

Read Online

ACCESS | Metrics & More | Article Recommendations | Supporting Information

ABSTRACT: Molybdenum carbides are promising alternative catalysts to Pt-group metals for the hydrogenation of unsaturated hydrocarbons. Nanostructuring has been shown to be an efficient way to boost the catalytic activity of these materials with MoC_y nanoparticles (NPs) exhibiting a good performance when encapsulated inside zeolites or dispersed on inert supports such as carbon or gold. Hereby, we focus on a systematic DFT study of the interaction of MoC_y NPs with ethylene (C_2H_4) as a general and simple approach for examining binding and activation of C=C bonds. Models for 14 NPs, with a Mo/C ratio in the 0.67−2.00 range, have been built following a cascade procedure. Several chemical descriptors, including the adsorption energy, structural NPs distortion, C=C deformation, and C_2H_4 attachment energy, have been analyzed along with a meticulous geometric and electronic characterization of bare NPs and C_2H_4 binding. The present results show that 1:1 stoichiometric Mo_6C_6, $Mo_{12}C_{12}$, and $Mo_{24}C_{24}$ and the nonstochiometric Mo_4C_6, Mo_8C_{12} (MetCar), and $Mo_{14}C_{13}$ (nanocube) are excellent systems for the binding and activation of ethylene, exhibiting a much larger reactivity than a bulk δ-MoC(001) surface with a similar Mo/C ratio. In addition, C_2H_4 binding on the NPs with a Mo/C < 1.08 is advantageous because, apart from a rather large adsorption energy, it implies low energy values for NPs deformation (from 0.00 to 0.31 eV), C=C distortion (from 0.30 to 0.52 eV), and C_2H_4 attachment (from −2.12 to −2.58 eV). These theoretical results point to the ideal MoC_y size and composition for C_2H_4 binding, providing a background for further experimental studies aimed at the preparation of MoC_y NPs as hydrogenation catalysts.

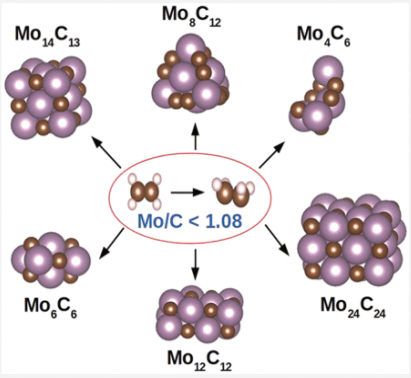

1. INTRODUCTION

The use of catalysts is key for producing clean fuels and several commodities, particularly by means of hydrogenation reactions of C=C double bonds in olefins, where Pt, Pd, Ru, Rd, Os, and Ir —sometimes termed Pt-group elements— are so far the most used catalyst due to their good performance.[1] In practice, these metals are supported on oxides, zeolites, and activated carbon, and exhibit a high catalytic activity.[2−11] However, the scarcity of these metals in the Earth's crust, together with their sensitivity to sulfur poisoning in the petrochemical industry, has motivated the search for alternative catalysts.[2]

Several studies have shown that transition metal carbides have excellent catalytic properties and appear as a good alternative to replace Pt-group-based catalysts, especially on several hydrogenation reactions. Among them, molybdenum carbides are highlighted as promising materials because of their remarkable interaction with hydrocarbons and with several successful applications in hydrogenation reactions.[12−16] Not surprisingly, several studies have been reported on the interaction of C_2H_4 with molybdenum carbides surfaces, precisely to explore the capability of these materials as a potential alternative catalyst to Pt-group metals.[17−20] The binding and hydrogenation of the ethylidyne species on δ-MoC(001) have also been considered[20] because these species have been found to be responsible of poisoning in Pt-based catalysts. Interestingly, there is evidence that this material could avoid surface poisoning, in contrast to Pt and Pd extended surfaces.[20]

The good performance of molybdenum carbides in catalysis has triggered new research aimed at investigating their possible improvement by nanostructuring. Recently, Figueras et al.[21] presented experimental and theoretical evidence that MoC_y nanoparticles supported on Au(111) can dissociate methane at room temperature. Additionally, this inverse catalyst system appears to be a good candidate for hydrogenation reactions as H_2 can easily dissociate and be stored on the supported nanoparticles[22] in a rather broad temperature range. Both the activation of methane and the activity toward hydrogen suggest that these nanoparticles (NPs) could be useful for hydro-

Received: November 29, 2020
Revised: February 8, 2021
Published: March 10, 2021

https://dx.doi.org/10.1021/acs.jpcc.0c10689
J. Phys. Chem. C 2021, 125, 6287−6297

genation of olefins. In addition, MoC_y NPs can be easily synthesized,[23] thus overcoming the problems encountered when aiming at preparing MoC or Mo_2C single crystal surfaces. Furthermore, it is known that MoC_y NPs encapsulated inside zeolites or dispersed on supports such as carbon or oxides exhibit good catalytic properties.[24−27]

At the present time, very little is known about the intrinsic reactivity of MoC_y NPs toward olefins or unsaturated hydrocarbons in general. The fact that the MoC_y NPs are frequently dispersed on zeolites, oxides, metals, and carbon-based supports raises the question about the possible influence of the substrate on their intrinsic chemical properties. To answer this question, we have performed a computational study, based on density functional theory (DFT), aimed at examining the bonding and activation of ethylene on a series of MoC_y NPs with different shapes and Mo/C atomic ratios; ethylene can be taken as a model for larger olefins. Our results show that the MoC_y NPs display a behavior which cannot be extrapolated from those seen for bulk δ-MoC(001) and β-Mo_2C(001) surfaces, with a substantial boost in chemical activity.

2. NANOPARTICLE MODELS AND COMPUTATIONAL DETAILS

The interaction of ethylene (C_2H_4) with gas-phase MoC_y NPs has been studied by using a series of models of increasing size, considering also different stoichiometries, as shown in Figure 1. The NPs models contain up to 64 atoms where the Mo/C ratio varies from 0.67 to 2.00. Note that this comprises usual MoC and Mo_2C stoichiometries as well as C-rich NPs like the well-known Mo_8C_{12} MetCar. The initial stoichiometric structures of MoC_y nanoparticles have been obtained from different sources. For instance, the Mo_6C_6 and $Mo_{12}C_{12}$ NPs have been gained by mimicking most stable gas-phase TiC NPs as previously reported.[28] These were acquired through data mining searches, global optimization using interatomic potentials (IP), and subsequent geometry optimization by DFT calculations. There, the authors reported a total of 21 low-energy structures for each Ti_6C_6 and $Ti_{12}C_{12}$ stoichiometry. Here, these TiC NP structures have been used as templates, substituting Ti by Mo and fully reoptimizing the atomic structure by using the methodology described below. Remarkably, the shape of most stable MoC_y isomers of both sizes coincides with that of their TiC counterparts. This is not surprising as both TiC and the δ-MoC polymorph exhibit the same rock-salt structure. This bottom-up approach revealed a quite fast convergence toward cubic, δ-MoC bulk-like shapes. Thus, a complementary top-down approach has been also considered creating cubic-like arrangements for $Mo_{24}C_{24}$ and $Mo_{32}C_{32}$ NPs, following a Wulff construction shape[29] and relying on the computed δ-MoC surface energies.[30,31]

Moreover, nonstoichiometric NPs have been considered and built from different sources as well. First, the Mo_8C_{12} magic cluster, usually known as MetCar,[32] and the $Mo_{14}C_{13}$ nanocube[33] have been selected from the literature. Then, other small MoC_y clusters have been considered through a cascade procedure, where for the two most stable isomers of Mo_6C_6 and $Mo_{12}C_{12}$ all inequivalent atoms have been sequentially removed, generating different $Mo_{x-1}C_x$ or Mo_xC_{x-1} structures. After optimizing the resulting structures, we repeated the cascade procedure to reach suitable structures for other Mo/C ratios. This methodology approximately scales

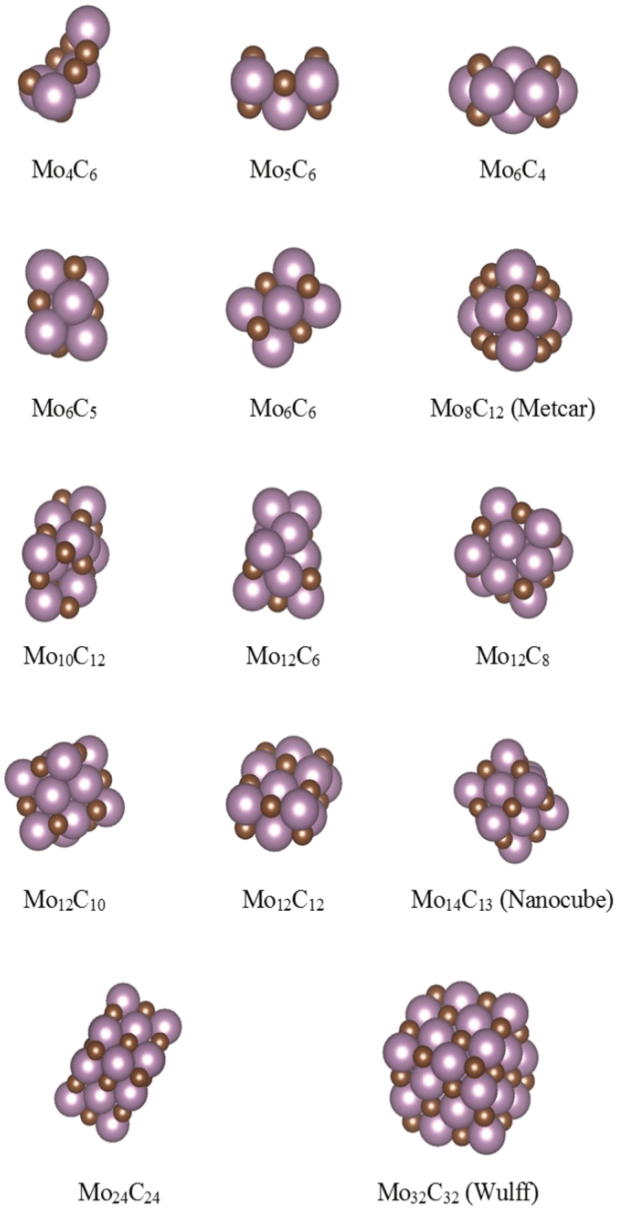

Figure 1. Geometry for the bare MoC_y NPs. The Mo and C atoms are represented by magenta and brown color, respectively.

as $2{\cdot}N^Z$ per removal, where N is the average number of inequivalent atoms per removal, Z states for the number of atoms that have been already removed, and the coefficient 2 is necessary as there are two different kinds of species. For instance, seven inequivalent C atoms exist for the most stable $Mo_{12}C_{12}$ isomer. Thus, removing one atom leads to seven structures, and a second removal leads to 49 new structures that need to be considered for subsequent geometry optimization. In any case, the actual number of isomers to explore on each batch depends on the new number of inequivalent atoms, yet the adoption of particularly symmetric shapes may reduce this number. Regardless of the previous, the $2{\cdot}N^Z$ expression should be taken as an upper bound. Clearly, a full cascade procedure becomes computational prohibitive for Z larger than two, especially for larger NPs such as $Mo_{12}C_{12}$. Thus, further Z steps have been explored only departing from the $Z-1$ most stable isomer. This strategy is not entirely arbitrary, as systematically for the first round the most stable isomers are obtained from previous most stable ones.

https://dx.doi.org/10.1021/acs.jpcc.0c10689
J. Phys. Chem. C 2021, 125, 6287−6297

The total energy of the studied MoC_y models described in the previous subsection has been obtained through periodic density functional theory (DFT) calculations using large enough supercells so that the interaction between the periodically repeated nanoparticles becomes negligible. Thus, the MoC_y nanoparticles have been placed inside a large cubic box, ensuring a minimum vacuum region of 10 Å in all directions and, obviously, considering the Γ point only. The calculations were performed by using the Vienna *Ab Initio* Simulation Package (VASP) code,[34] employing the Perdew–Burke–Ernzerhof (PBE) exchange-correlation functional,[35] as found to be especially well-suited in the description of Mo-based carbides.[36] In addition, the contribution of dispersion terms was accounted by adding the Grimme D3 correction, i.e., PBE-D3,[37] especially adequate for the interaction of molecules with such molybdenum carbide systems.[19,36,38,39] The Kohn–Sham equations were solved by expanding the valence electron density in a plane-wave basis set with 415 eV cutoff, whereas the effect of the inner electrons in the valence electron density has been taken into account by the Projected Augmented Wave (PAW) method[40] as implemented by Kresse and Joubert.[41] The convergence criteria ensures changes in total energies lower than 10^{-5} eV and variations in interatomic forces lower than 0.01 eV $Å^{-1}$. With this setup, total energies converge below the chemical accuracy of 1 kcal mol^{-1}, i.e., ~0.04 eV.

Regarding the used approach to choose the structures of the MoC_y NPs described above, one must acknowledge recent proposals in the literature aimed at exploring the landscape for several isomers.[42−44] These rely on geometry optimization and consideration of low-lying isomers being able to scrutinize the role of possible higher energy isomers in a given reaction at a given temperature. These approaches can provide detailed information about the contribution of each isomer to the overall reactivity. Nevertheless, the importance of high-energy isomers becomes relevant for subnanometer NPs only and, in general, becomes less and less important for larger NPs where the energy difference between structural isomers gradually increases with the NP size (see Table S1 of the Supporting Information). In addition, exploring the importance of different isomers for a set of nanoparticles becomes computationally too demanding and is, hence, beyond of the scope of the present work. Yet, the present approach, focusing on relatively low energy isomers, hopefully close to the global minima, allows one to extract meaningful information about the chemistry of these catalytically active MoC_y nanoparticles. Consequently, for each stoichiometry, the most stable cluster was selected to analyze the interaction with ethylene.

Once the optimum structure of the MoC_y NPs has been obtained, the interaction of each of them with the C_2H_4 molecule has been studied by using the same computational setup. All conceivable binding sites and connectivities have been explicitly considered. The notation for the adsorption modes is as earlier reported.[17,18,45] Briefly, π-M relates to ethylene binding atop a metal site; di-σ-MM, di-σ-CM, and di-σ-CC correspond to the binding bridging metal–metal, carbon–metal, and carbon–carbon bond, respectively; and finally, σ-M, μ-M stand for a situation in which one has one C atom of C_2H_4 atop a metal atom (σ-M) and one C_2H_4 C atom located perpendicularly atop a M–M bridge (μ-M). For every NP, several initial adsorption geometries were evaluated to cover all binding possibilities, so that a complete scanning of the potential energy surface for C_2H_4 binding in every NP can be assured. In total, the number of studied initial adsorption geometries was ca. 500. The final structures —bare nanoparticles and nanoparticles with adsorbed ethylene— were characterized as energy minima in the potential energy surface through pertinent vibrational analysis. The vibrational frequencies were gained within the harmonic approximation, accounting only the adsorbate vibrational frequencies, obtained through the building up and diagonalization of the Hessian matrix, constructed by finite differences of analytical gradients with atomic displacements of 0.03 Å.

The ethylene adsorption energy, E_{ads}, was calculated as

$$E_{ads} = E_{C_2H_4/MoC_y} - E_{MoC_y} - E_{C_2H_4} \quad (1)$$

where $E_{C_2H_4/MoC_y}$ stands for the energy of the system with the C_2H_4 adsorbed on the MoC_y NP, the term E_{MoC_y} refers to the MoC_y optimized energy, and $E_{C_2H_4}$ represents the isolated ethylene molecular energy. The first and third terms in eq 1 include the ethylene related vibrational zero-point energy (ZPE) contribution.

To investigate the bonding between ethylene and the MoC_y nanoparticles, a charge density difference (CDD) analysis, $\Delta\rho$, has been carried out, along with the electron localization function (ELF). In the CDD $\Delta\rho$ is defined as

$$\Delta\rho = \rho_{C_2H_4/MoC_y} - \rho_{MoC_y} - \rho_{C_2H_4} \quad (2)$$

where $\rho_{C_2H_4/MoC_y}$ refers to the electron density of the ethylene adsorbed on the MoC_y NP, and ρ_{MoC_y} and $\rho_{C_2H_4}$ correspond to the electron density of the nanoparticle and ethylene at the geometry they have in the adsorbed minimum. In addition, net charges on the adsorbed molecule are also obtained through the atoms-in-molecules topological analysis of Bader.[46]

3. RESULTS AND DISCUSSION

3.1. Geometry and Characterization of Bare MoC_y Nanoparticles. In Figure 1, the arrangement of carbon and molybdenum atoms within the MoC_y NPs is found to be different for each Mo/C ratio, and even for the same Mo/C ratio the relaxed geometries can be completely different. Thus, being in the nonscalable regime of NPs sizes,[29,47] their performance toward the binding of adsorbates is expected to be significantly different between the explored NPs. The geometries for the most stable structures of each of the 14 MoC_y NPs are the ones displayed in Figure 1. To separate stoichiometry from size effects, the MoC_y NPs analysis is split into stoichiometric and nonstoichiometric cases. The employed descriptors to unveil the properties of bare NPs are formation energies, computed by taking the energy per atom in bulk Mo and graphite as atomic references (see Figure S1 and Table S2) and the band gap (see Tables S2 and S3), which open the door toward the geometry and electronic properties characterization, respectively.

As far as stability is concerned, we first focus on the formation energy, E_{form}, as this quantity provides an estimate of the thermodynamic stability of a given NP, either stoichiometric or not. However, to have a meaningful comparison, it is convenient to somehow normalize this quantity. For the stoichiometric NPs this can be done simply by considering E_{form} per MoC unit, i.e., E_{form}/N. Here, a clear size effect is found where E_{form} linearly decreases as the size grows (see Table S2 and Figure S1). Interestingly, the band gap, E_{gap}, estimated in an approximate way from the Kohn–Sham orbital

https://dx.doi.org/10.1021/acs.jpcc.0c10689
J. Phys. Chem. C 2021, 125, 6287−6297

energies, exhibits a much less marked dependence with respect to the NP size and irrespective of whether these are stoichiometric or not (see Tables S2 and S3). For all NPs E_{gap} is close to 0.15 eV although with some oscillations of the energy levels that eventually lead to the valence and conduction band limits. In any case, from the calculated E_{gap} for these NPs, it is clear that they are still a bit far from metallic character predicted for the extended δ-MoC (001) surface.[31] Test studies were performed for Mo_6C_6 and the MetCar, which are representative of stoichiometric and nonstoichiometric NPs, to calculate E_{gap} by using the range-separated hybrid HSE06 functional. In both cases, the changes with respect to the PBE value are of 0.01 eV only.

Assuming that the frontier orbitals dominate the chemistry of these NPs, one would deduce that the binding of adsorbates on stoichiometric NPs in the range from Mo_6C_6 to $Mo_{32}C_{32}$ will be quite similar. However, the adsorbate binding strength does also depend on other factors, including (i) the adsorbate nature, (ii) the electronic arrangement with respect to the NP model, (iii) the anchoring site, and even (iv) the adsorbate molecular conformation.

3.2. C_2H_4 Adsorbed on MoC_y Nanoparticles. Once all 14 stoichiometric MoC_y NPs were described, a thorough exploration sampling ca. 500 different initial C_2H_4 adsorption geometries was performed, covering all conceivable binding possibilities, revealing 221 final topologically different structures. The subsequent analysis, however, focuses on most stable adsorption conformation for each NP, as summarized in Table 1 and shown in Figure 2. Note that for each case the second most stable adsorption conformations are located more than 0.1 eV higher in energy (see Table S5), with

Table 1. Adsorption Energy, E_{ads}, for the Ethylene Adsorption on the Studied MoC_y Nanoparticles, for the Most Stable Site, and Evaluating the Distortion (Activation) by the C_2H_4 C=C Bond Length, d(CC)[a]

MoC_y	site	E_{ads}/eV	d(CC)/Å
	stoichiometric		
Mo_6C_6	π-M	−1.76	1.43
$Mo_{12}C_{12}$	π-M	−1.65	1.42
$Mo_{24}C_{24}$	π-M	−1.84	1.42
$Mo_{32}C_{32}$	di-σ-CM	−1.54	1.55
	nonstoichiometric		
Mo_4C_6	π-M	−1.98	1.44
Mo_5C_6	di-σ-CC	−1.97	1.56
Mo_6C_4	σ-M, μ-M	−2.88	1.51
Mo_6C_5	σ-M, μ-M	−1.99	1.51
Mo_8C_{12}	π-M	−1.80	1.43
$Mo_{10}C_{12}$	di-σ-CM	−1.78	1.58
$Mo_{12}C_6$	σ-M, μ-M	−2.08	1.48
$Mo_{12}C_8$	σ-M, μ-M	−1.86	1.49
$Mo_{12}C_{10}$	σ-M, μ-M	−1.76	1.50
$Mo_{14}C_{13}$	π-M	−1.85	1.44
	surface references		
δ-MoC(001)[b]	π-M	−0.44[d]	1.36
β-Mo_2C(001)-C[c]	C-top, Mo-h_1	−1.49	1.51
β-Mo_2C(001)-Mo[c]	Mo-top, C-h_2	−2.50	1.48

[a]Energy values include the ZPE contribution. Reference data on most stable δ-MoC(001) and β-Mo_2C(001) surfaces, either C- or Mo-terminated, as provided. See complete Table S4. [b]References 17 and 19. [c]Reference 18. [d]Reoptimized by using the present computational setup.

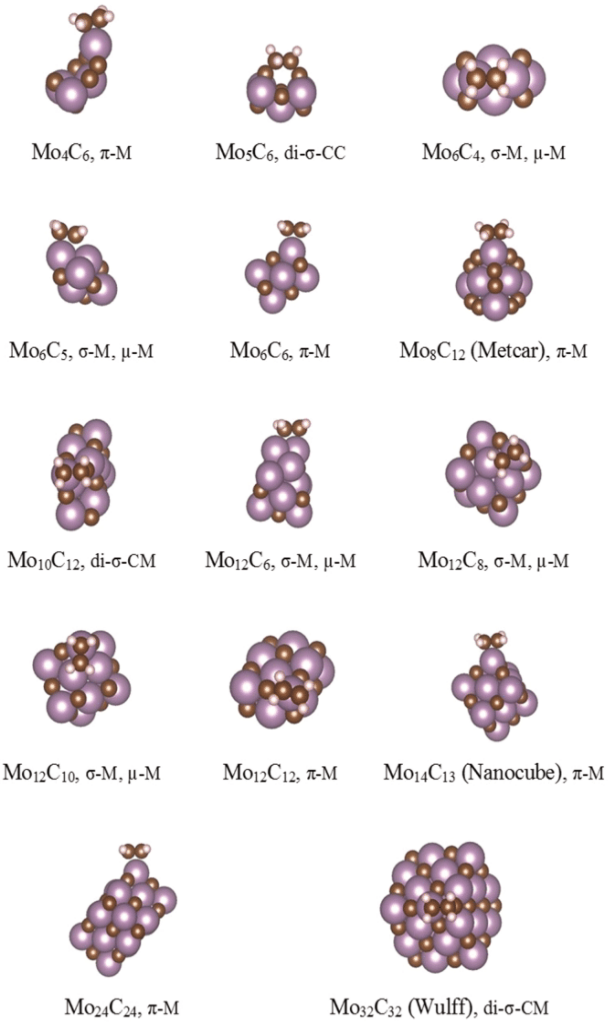

Figure 2. Most stable geometry of C_2H_4 adsorbed on every NP. The Mo, C, and H atoms are represented by magenta, brown, and light gray, respectively. The binding mode is tagged along the structure.

the sole exception of the MetCar, with rotated conformers around the NP tetrahedron vertex axis. Indeed, in most of the explored NPs, the second isomer is less stable by at least 0.2 eV, a behavior observed in 62% of the NPs listed in Table S5. However, one must advert that in 38% of NPs the adsorption conformations for both first and second most stable adsorption modes should be thermally accessible at the high temperatures typical in catalytic experiments, particularly for C_2H_4 binding on Mo_5C_6, $Mo_{12}C_8$, $Mo_{12}C_{10}$, Mo_8C_{12}, and $Mo_{32}C_{32}$. Therefore, future studies should carefully address the existence of low-lying isomers and possibly include them whenever considering the reactivity of these systems. For NPs with a 1:1 (Mo:C) atomic ratio, the E_{ads} values are sensibly stronger than on the δ-MoC(001) surface, but within the range of values found for C- and Mo-terminated surfaces of β-Mo_2C(001) surfaces, as seen in Figure 3. The results in this figure indicate that the binding capabilities of the MoC_y NPs cannot be extrapolated from the behavior of the bulk δ-MoC(001) and β-Mo_2C(001) surfaces.

For comparison purposes, the C_2H_4 adsorption on extended δ-MoC(001) and C- and Mo-terminated β-Mo_2C(001) surfaces, denoted as β-Mo_2C(001)-C and β-Mo_2C(001)-Mo, are included in Table 1.[17−19] The adsorption energies, E_{ads}, on the NPs are in the −1.54 to −2.88 eV range, comparable to the

https://dx.doi.org/10.1021/acs.jpcc.0c10689
J. Phys. Chem. C 2021, 125, 6287−6297

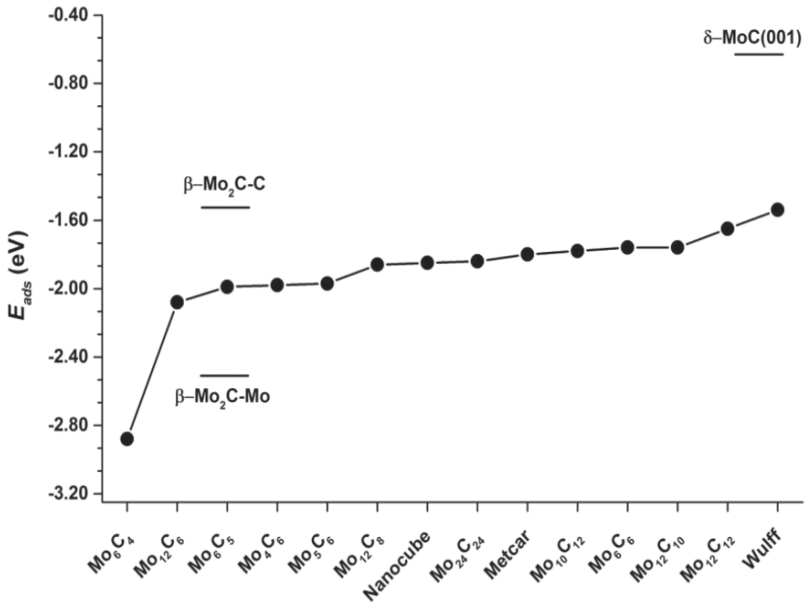

Figure 3. Adsorption energies, E_{ads}, for the most stable C_2H_4 structure adsorbed in every NP, sorted in terms of the energy strength. Extended surface values are shown as references.

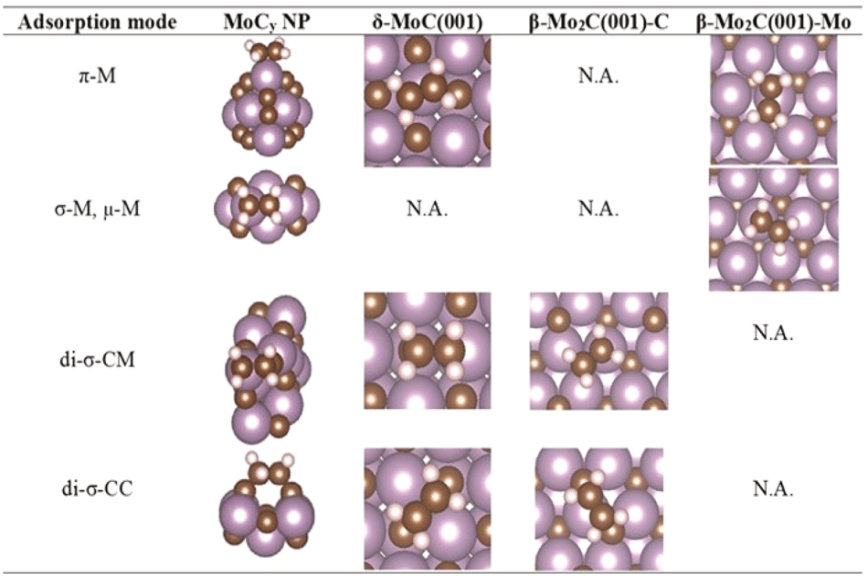

Figure 4. Comparative geometry binding of C_2H_4 on NPs and surfaces for the four adsorption modes found on NPs.

strong binding on polar β-$Mo_2C(001)$-Mo surfaces, ranging from −1.63 to −2.50 eV. On the other hand, the E_{ads} on polar β-$Mo_2C(001)$-C —with E_{ads} from −1.29 to −1.49 eV— and on the δ-MoC (001) surfaces —with E_{ads} up to −1.03 eV— are clearly weaker than on the studied NPs. Thus, the C_2H_4 E_{ads} binding strength decays as β-$Mo_2C(001)$-Mo ≈ NPs > β-$Mo_2C(001)$-C > δ-MoC(001). Notice that for the latter the most stable reconstructed surface has been used as reference.[21] Interestingly, the reported values for C_2H_4 adsorption energy on a Pt(111) surface, −1.78 eV,[45] and on Pt_x (x = 7−10) clusters, ranging from −1.4 to −1.7 eV,[48,49] are within the range found in this work for the MoC_y NPs. Notice that the adsorption energy on platinum clusters and the Pt(111) surface is very similar, which is in agreement with their similar catalytic performance toward ethylene hydrogenation.[50] In other words, nanostructuring Pt could not be advantageous for this particular hydrogenation process. However, a different behavior exists when comparing ethylene adsorption on MoC_y NPs and on TMC surfaces, where the current work is the basis to further explore this possibility.

Analyzing the adsorptive landscape in Table 1, the most common binding mode is π-M, closely followed by σ-M, μ-M, unfolding the main role played by Mo metal centers. The analogous geometry sites for binding on surfaces[17,18] is shown in Figure 4. Metal sites involved in bridge di-σ-CM are dominant on $Mo_{10}C_{12}$ and $Mo_{32}C_{32}$, while bridge di-σ-CC is only found for Mo_5C_6 case. Indeed, C-interaction is only found for Mo/C ratio of 0.8, with the sole exception of the $Mo_{32}C_{32}$ nanoparticle. The C_2H_4 preference toward Mo seems to be ruled by its lower electronegativity compared to that of C.[24]

The strong C_2H_4 adsorption on the NPs implies an elongation of the C═C double bond, d(CC), estimated to be 1.33 Å in gas phase. The d(CC) thus elongates from 0.09 to 0.25 Å for the studied NPs (see values in Table 1 and Table S4), and the largest elongations are found for MoC_y NPs involving C binding modes, such as in Mo_5C_6, $Mo_{10}C_{12}$, and

https://dx.doi.org/10.1021/acs.jpcc.0c10689
J. Phys. Chem. C 2021, 125, 6287−6297

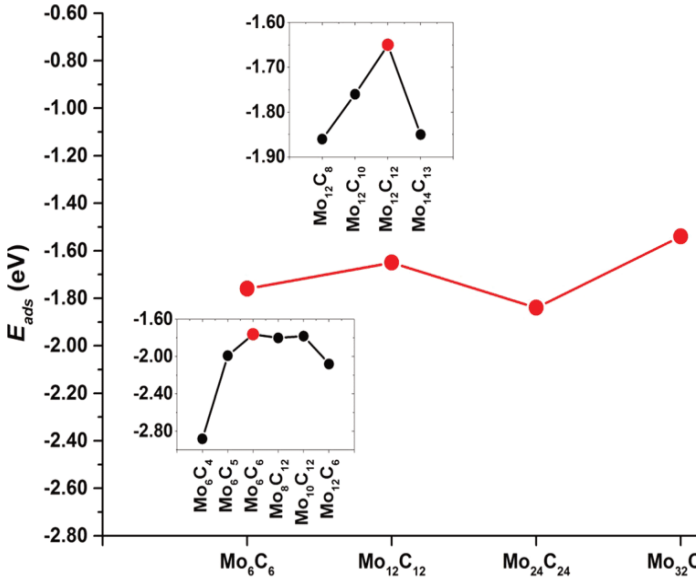

Figure 5. C_2H_4 adsorption on stoichiometric NPs (red points), while values on related nonstoichiometric NPs (black points) are shown in the insets.

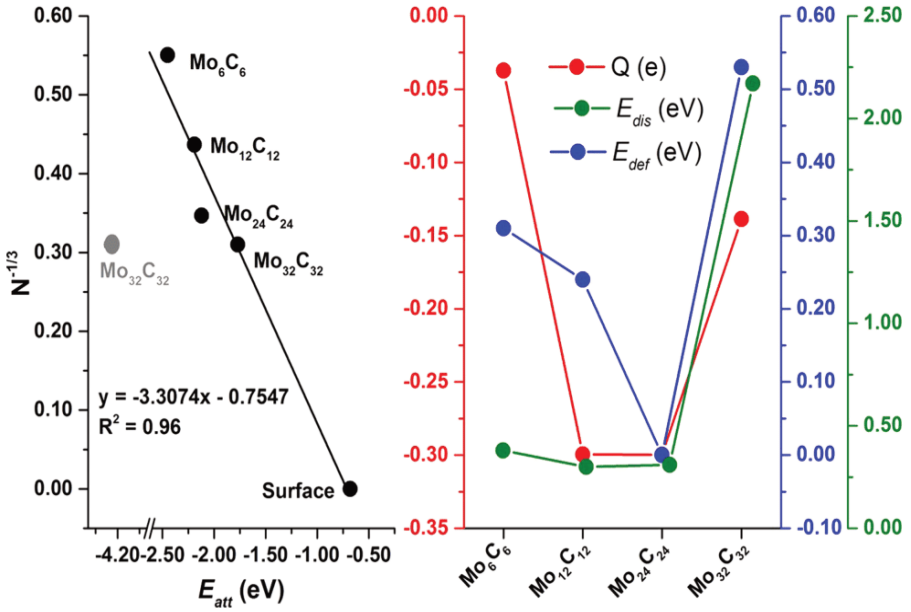

Figure 6. Left panel: evolution with respect to size, measured as $N^{-1/3}$, of the attachment energy, E_{att}. The second most stable structure for $Mo_{32}C_{32}$ is shown in gray. Right panel: Bader charge, Q, C_2H_4 distortion energy, E_{dis}, and NP deformation energy, E_{def}.

$Mo_{32}C_{32}$, with elongations of 0.22−0.25 Å. The C_2H_4 binding involving two Mo sites via the σ-M, μ-M mode displays still moderate elongations of 0.15−0.18 Å, while the π-M mode has a smaller, yet still noticeable lengthening of 0.09−0.10 Å. In this sense, the C_2H_4 carbon−carbon bond length distortion decreases with the binding mode as di-σ-CC, di-σ-CM > σ-M, μ-M > π-M. Notice in Table 1 that d(CC) bond length elongations are linked to the adsorption mode rather than to its strength.

3.3. Analysis of C_2H_4 Interaction with Stoichiometric MoC_y NPs. In this section we analyze the chemical nature of C_2H_4 adsorption on stoichiometric MoC_y NPs. At first sight, there is no clear trend for adsorption energy evolution with respect to NP size, having ups and downs, as seen in Figure 5. This behavior could be explained because the interaction is a balance of energy contributions, including (i) the C_2H_4 distortion energy when adsorbed, E_{dis}, as seen in the elongated d(CC) values of Table 1; (ii) the NP deformation energy, E_{def}, so as to better accommodate the C_2H_4 moiety and the concomitant changes in the NP; and (iii) the resulting attachment energy, E_{att}, as the binding energy of the distorted C_2H_4 on the deformed MoC_y NP, following a lock-and-key anchoring. The three different contributions are listed in Table S6, revealing that the oscillations in the E_{ads} are also observed in the E_{att}, which is reminiscent of the fact that the studied NPs are in the nonscalable regime.[29] In any case, a slight trend is observed in Figure 5, as E_{ads} decreases as the NP size increases. Here the size is measured by $N^{-1/3}$, with N being the number of MoC units (see also Table S7). Figure 5 also reports the effect of nonstoichiometry for Mo_6C_6 and $Mo_{12}C_{12}$, where it clearly can be stated that the presence of Mo or C vacancies strengthens the adsorption.

https://dx.doi.org/10.1021/acs.jpcc.0c10689
J. Phys. Chem. C 2021, 125, 6287−6297

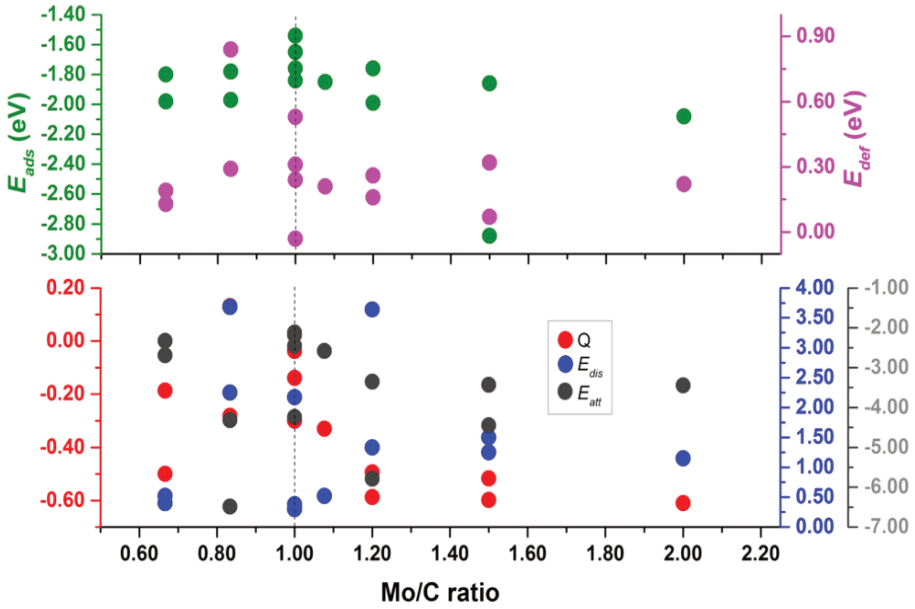

Figure 7. Effect of Mo/C ratio in nonstoichiometric NPs on the adsorption energy, E_{ads}, and NP deformation energy, E_{def} (upper panel). Adsorbed C_2H_4 Bader charge (in e), C_2H_4 distortion energy E_{dis}, and ethylene attachment energy, E_{att} (lower panel), both in eV.

Apart from the E_{ads} evolution, the size and attachment energy are useful descriptors to unveil the behavior of stoichiometric NPs as shown in Figure 6. Overall, an increase in size leads to a lowering of the E_{att}, with the sole outlier of $Mo_{32}C_{32}$, which has as a different signature displaying a di-σ-CM C_2H_4 mode, while others have a π-M mode. Indeed, the second most stable structure in $Mo_{32}C_{32}$ is a π-M mode, shown in gray in Figure 6, and nicely fitting to the trend, to the point of being almost linear with a regression coefficient, R^2, of 0.96. Another distinct point for $Mo_{32}C_{32}$ is that the E_{dis} relates to a decrease of charge for the adsorbed C_2H_4 moiety, given the formation of a C−C covalent bond (see CDD and ELF plots in Figure S2).

With regard to Figure 5 again, one could argue that solely the $Mo_{24}C_{24}$ NP is an outlier in the observed trend. This exception may obey to its particular atomic structure. Even if while comparing to $Mo_{12}C_{12}$ both the adsorption mode and the d(CC) elongations are similar, the $Mo_{24}C_{24}$ NP is more symmetric, leading to a negligible NP distortion upon C_2H_4 adsorption (see Figure 6). However, the charge transfer from the MoC_y NP to the C_2H_4 molecule is quite large for $Mo_{12}C_{12}$ and $Mo_{24}C_{24}$ only, −0.30 e for both cases, while for Mo_6C_6 and $Mo_{32}C_{32}$ NPs the charge transfer from the adsorbate is below −0.15 e. Interestingly, the distortion energy is the same, 0.30 eV, for both $Mo_{12}C_{12}$ and $Mo_{24}C_{24}$ NPs. Overall, the maximum in E_{ads} relates to the minimum in E_{dis}. Therefore, the different $Mo_{24}C_{24}$ behavior obeys its strong stability, favoring a higher charge transfer toward C_2H_4 and requiring a lower energy for elongating the C_2H_4 C═C bond. In fact, among all the 14 evaluated NPs, the distortion of $Mo_{24}C_{24}$ NP is almost negligible. Furthermore, the use of another descriptor other than the adsorption energy could help to understand the trends from Mo_6C_6 to $Mo_{24}C_{24}$. An increase in size leads to a drop in E_{att}, following a clear linear trend, although with R^2 = 0.90 only, within the studied range, having a clearer behavior compared to the adsorption energy.

3.4. Analysis of C_2H_4 Interaction with Nonstoichiometric MoC_y NPs. Several of the studied NPs are nonstoichiometric, with a Mo/C ratio in the range of 0.67−2.00. Even though there is diversity in terms of geometries and Mo/C ratios, the systems with Mo/C < 1 (see top of Figure 7) exhibit E_{ads} within the −1.78 to −1.98 eV range, i.e., in a narrow range of 0.20 eV. For the cases with Mo/C > 1, the binding energy variations are in the −1.76 to −2.88 eV range, i.e., in a broader range of 1.12 eV. Clearly, a large diversity is found for the latter cases. Aside from that, the decrease in the NPs size does not imply a clear trend in terms of the adsorption energy, and the only notes of distinction are particular reconstructions as observed on the Mo_4C_6 and Mo_5C_6 NPs cases (see Figures S3 and S4), forcing an sp^3 hybridization of C_2H_4 C atoms in the former and the formation of C−C bonds in the latter. Notice that the catalyst reconstruction is an important issue that should be addressed, especially when in small NPs as recently reported by Sun et al.[51] Therefore, in further studies related to ethylene hydroconversion, the NPs reconstruction must be considered, particularly for the smallest ones.

For four Mo/C ratios —0.67, 0.83, 1.20, and 1.50— there are particularly two different structures for each case, with different size; e.g., Mo_5C_6 and $Mo_{10}C_{12}$ for the case of Mo/C = 0.83. As generally seen in the top of Figure 3, the larger the size —in terms of C content— the weaker the C_2H_4 binding energy, where by doubling the size the E_{ads} weakens ∼0.2 eV, except for the Mo/C = 1.50 ratio, where the drop is ∼1 eV. Thus, it seems that size effects get pronounced particularly at Mo/C ratios larger than 1.20. Even though the major change in E_{ads} corresponds to NPs with Mo/C = 1.50 ratio, E_{def} values are merely 0.06 eV, which is quite small compared to the value for Mo/C = 0.83 of 0.58 eV (see top of Figure 3). This difference seems to be linked to a different adsorption mode. For Mo/C = 1.50, the C_2H_4 binding mode is π-M, while for Mo/C = 0.83 di-σ-CC and di-σ-CM modes. The C_2H_4 interaction on 75% of the nonstoichiometric NPs has a distortion energy of ∼0.2 eV, in the range of ratio Mo/C = 0.67−2.00, with the sole exception of Mo_6C_4, that with a deformation energy of 0.07 eV could be negligible, implying an almost rigid NP structure upon C_2H_4 adsorption.

https://dx.doi.org/10.1021/acs.jpcc.0c10689
J. Phys. Chem. C 2021, 125, 6287−6297

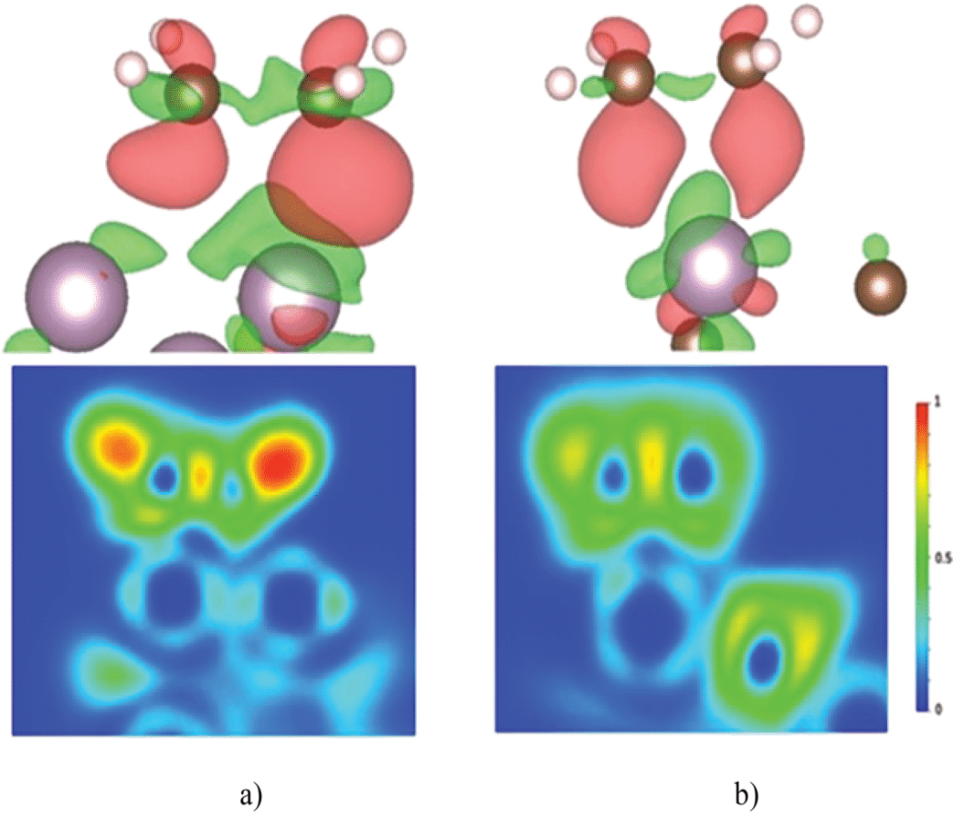

Figure 8. CDD plot (top) and ELF (bottom) for binding via (a) σ-M, μ-M ($Mo_{12}C_6$), E_{ads} = −2.08 eV, and (b) π-M mode ($Mo_{12}C_{12}$), E_{ads} = −1.65 eV. For the CDD, red and green colors represent the regions where the charge (0.05 e/Å^3) was lost and earned, respectively, after ethylene adsorption. The Mo, C, and H atoms are represented by magenta, brown, and light gray color, respectively. In the ELF, blue, green, and red colors represent low (0), intermediate (0.5), and high (1) likelihood of finding an electron pair, respectively.

Among the evaluated NPs, E_{dis} is above 1 eV for several cases, which may not be advantageous for further hydrogenation reactions as could imply the breaking of the C═C bond. However, E_{dis} is lower than 0.53 eV for the particular Mo/C ratios of 0.67, 1.00, and 1.08. It is worth to mentioning that E_{dis} and E_{att} follow a similar trend as a function of the Mo/C ratio. Hence, E_{att} depends on E_{dis}, which is thus a better descriptor than the adsorption energy. Therefore, the NPs attachment energies should also follow Le Sabatier's principle; i.e., the C_2H_4 binding should be not too strong, as ethylene could remain molecularly adsorbed or dissociated on the NP, nor too weak, as C_2H_4 could not get hydrogenated. Moreover, C_2H_4 should bind on the MoC_y NPs with moderate activated E_{dis} while having a low NP deformation, E_{def}. The NPs which comply with the previous criteria are Mo_4C_6, Mo_8C_{12} (MetCar), and $Mo_{14}C_{13}$ (nanocube), together with stoichiometric Mo_6C_6, $Mo_{12}C_{12}$, and $Mo_{24}C_{24}$ systems.

Aside from the previous considerations, the interaction of C_2H_4 with the NP triggers a charge transfer from the NP to ethylene (see bottom of Figure 7). Such accumulated charge in the adsorbed C_2H_4 increases with the Mo/C ratio, i.e., with an enrichment of Mo atoms in the system. Indeed, the amount of Mo in the NPs modulates their activity toward different elements in diverse chemical environments.[24] This behavior relates to the NP E_{def} and C_2H_4 E_{dis} energies, with an oscillating profile, pointing to a convergence toward the surface for larger sizes (see Figure S5). This rapidly oscillating behavior is typical of small NPs,[29] but increasing the number of Mo favors convergence, particularly from $Mo_{12}C_6$ onward.

Focusing on the largest nonstoichiometric NPs, i.e., the $Mo_{12}C_x$, the Mo enrichment over the stoichiometric point modulates the chemical activity of Mo atoms toward the carbons of C_2H_4, as seen by a major extent of charge transfer from the NP Mo atoms toward C_2H_4 (see the bottom of Figure 7). For the $Mo_{12}C_x$-based NPs, the increase of the Mo/C ratio leads to a rise in the E_{ads} (see the top of Figure S6). In other words, the NP size decrease and the larger share of Mo atoms lead to an increase of the C_2H_4 adsorption. The C═C bond in C_2H_4 gets also activated in $Mo_{12}C_x$ systems, but its extent is different only for the stoichiometric NP, being 0.09 Å, and similar for the rest of ratios, in the 0.15−0.17 Å range. This behavior is also related to the E_{dis}, which in turn relates to the Bader charge on the adsorbate (see Figure S6), showing that an increase in the Mo/C ratio favors a higher charge transfer from the NPs to C_2H_4.

Mo/C ratios above 1.08 are not advantageous for activating C_2H_4, even if key in hydrogenation processes. Increasing the Mo/C ratio up to 1.5 implies higher E_{def} and E_{dis} with concomitant lower E_{att} as in going from $Mo_{12}C_6$ to $Mo_{12}C_{12}$. Therefore, the only desired ratios to bind ethylene are 1.00 and 1.08, i.e., having only a small content of C deficiencies or, in other words, as close to stoichiometry as possible.

The results for the MetCar highlight another complex interplay between the Mo/C ratio and the chemical properties of a MoC_y NP. In this C-rich system, there are 1.5 atoms of C per each Mo atom, but the special structure and electronic properties of the NP allow it to bind ethylene better than δ-MoC(001) or β-Mo_2C(001)-C surfaces. In the structure of the MetCar, Figures 1 and 2, multiple bonds exist between the

https://dx.doi.org/10.1021/acs.jpcc.0c10689
J. Phys. Chem. C 2021, 125, 6287−6297

carbon atoms and the system exhibits C_2 dimers. It has been argued that the presence of C_2 dimers leads to special chemical properties.[52,53] With the exception of Mo_4C_6, C_2 dimers are not present in the other MoC_y NPs examined neither in the bulk δ-MoC(001) nor in β-Mo_2C(001) surfaces. Nevertheless, it is worth mentioning that the C_2 dimers in Mo_4C_6 and the MetCar have different nature. In Mo_4C_6 these are formed upon interaction with ethylene as a product of a significant structural rearrangement (see Figure S4), with a concomitant energy lowering of 0.6 eV. On the contrary, the isolated MetCar structure already contains C_2 dimers, and upon interaction with C_2H_4, the structure is not reconstructed. Therefore, the reactivity of the MetCar obeys not only to the presence of C_2 dimers but also to its particular pyramidal-like geometry. Among the evaluated NPs, only Mo_4C_6 and Mo_5C_6 (the smallest ones) suffer changes in cluster geometry upon C_2H_4 adsorption which is a typical behavior in small size clusters. In fact, this behavior was not seen in the larger NPs Thus, in C-poor and C-rich MoC_y NPs, there are phenomena that are not possible in a bulk surface and can lead to high reactivity toward ethylene.

3.5. Electronic Structure Organization. The electron density rearrangement between the MoC_y NPs and the C_2H_4 molecule is further illustrated by the Bader atoms-in-molecules analysis in Figure 6 (and also Figure S6). This is here complemented by CDD and ELF analyses. Four representative NPs were taken because they embody different adsorption modes and Mo/C ratios, leading to descriptors differences as above explained. The chosen NPs are $Mo_{12}C_6$ (σ-M, μ-M), $Mo_{12}C_{12}$ (π-M), $Mo_{10}C_{12}$ (di-σ-CM), and Mo_5C_6 (di-σ-CC), with Mo/C ratios of 2.00, 1.00, and 0.83 for two last cases, respectively.

The CDD and ELF plots for the adsorption on metal sites via π-M and σ-M, μ-M modes are displayed in Figure 8. The binding via the σ-M, μ-M mode favors a high charge migration from the NP toward C_2H_4, as shown by the accumulation regions within the adsorbate, also observable in the ELF plot. Indeed, this high electron density correlates with the Bader charge of −0.61 *e*. Overall, the largest adsorbate charges were seen for the σ-M, μ-M binding mode. On the contrary, the adsorption via the π-M mode has less electron density within the C_2H_4, in accordance with the smaller Bader charge of −0.30 *e*. Such a behavior may indicate that the C_2H_4 adsorption on the MoC_y NPs has some ionic contribution to the bonding.

The aforementioned electron density migration occupies the C_2H_4 lowest unoccupied molecular orbital (LUMO) antibonding orbitals, decreasing the bond order, and, consequently, elongating the C−C bond length. Indeed, the extent of the Bader charge relates to the d(CC) increase, as binding via the σ-M, μ-M mode is higher, ranging from 0.15 to 0.18 Å, compared to the binding via the π-M mode, with increases of ca. 0.10 Å. The largest d(CC) elongation is seen on MoC_y-$C_{ethylene}$ sites, i.e., binding via di-σ-CX−X = C or Mo. This is a direct consequence of the formation of new C−C covalent bond with the NP C atom, as clearly seen in the CDD and ELF plots of Figure S7, even if one has to regard that Coulombic interactions play a role. Notice that on Mo_5C_6 not only d(CC) is elongated but also a sp^3 hybridization emerges due to a molecular distortion. This explains the highest E_{dis} of 3.68 eV, among the evaluated NPs (see Table S6).

The ethylene binding on the NPs and on the extended δ-MoC(001) surface via π-M mode has clear differences in terms of charges (see Figure S8). In the δ-MoC(001) surface there is a continuous flux of electron density within the layers[17] —a general behavior seen on other TMCs.[45] The electronic arrangement between Mo and C atoms is perturbed upon C_2H_4 adsorption, leading to an almost negligible d(CC) elongation of 0.03 Å, with both ionic and covalent contributions. On the NPs the electron density is more affected due to the stronger adsorption, higher Bader charge in C_2H_4, and a larger d(CC) elongation of 0.09−0.25 Å.

4. CONCLUSIONS

The present systematic DFT study analyzed the ethylene binding on a series of MoC_y NPs, considering a broad Mo/C ratio range of 0.67−2.00. Overall, 14 NPs have been explored with structures derived from a cascade procedure. The most stable structures were then used to analyze C_2H_4 adsorption sampling ca. 500 adsorptive sites. The results show that a general classification can be established of the C_2H_4 binding related to the C−C bond length elongation and the NP active site. Thus, group I is for π-M mode adsorption, group II is for the σ-M, μ-M mode, and finally group III involves NP C sites, via di-σ-CX−X = Mo or C. Overall, the C_2H_4 adsorption strongly affects the whole NP electron density, resulting in a stronger adsorption energy, higher negative charge on the C_2H_4 adsorbate, and a d(CC) elongation of 0.09−0.25 Å as compared to the respective behavior on an extended δ-MoC(001) surface, revealing a complex mixture of ionic and covalent bond.

The reported analysis involved differentiating stoichiometric and nonstoichiometric NPs, a decomposition of the interaction in terms of C_2H_4 distortion energy, NP deformation energy, and C_2H_4 attachment energy in a lock-and-key fashion, considering cohesive energies, Mo/C ratios, and the explicit number of MoC units as possible interaction descriptors. Thus, the NPs with low distortion, deformation, and attachment energies are the nonstoichiometric Mo_4C_6, Mo_8C_{12} (MetCar), and $Mo_{14}C_{13}$ (nanocube) together with the stoichiometric Mo_6C_6, $Mo_{12}C_{12}$, and $Mo_{24}C_{24}$ NPs. These are promising systems to further support on metal surfaces, in a closer approach to a practical catalyst. The best predicted performance for C_2H_4 binding is for a Mo/C ratio below 1.08, as larger ratios are not advantageous for distorting the C=C bond, which is key in the hydrogenation processes. The reasons rely on the above-mentioned descriptors analysis, accompanied by a geometric issue at high Mo/C ratios above 1.1, as an excess of Mo atoms leads to a lower coordination of Mo atoms, which is not advantageous since Mo binds C_2H_4 just to compensate its undercoordination instead of favoring the C_2H_4 C−C lengthening, thus ultimately limiting its performance toward further hydrogenation reactions.

■ ASSOCIATED CONTENT

Supporting Information

The Supporting Information is available free of charge at https://pubs.acs.org/doi/10.1021/acs.jpcc.0c10689.

Table S1: total energy difference between the lowest and second lowest structures per stoichiometry; Table S2: formation energies, E_{form}, for each stoichiometric NP per MoC unit and band gap related energies; Table S3: band gap energy, E_{gap}, for the nonstoichiometric MoC_y NPs; Table S4: adsorption of C_2H_4 on MoCy NPS; Table S5: two most stable C_2H_4 adsorption energies and structures

https://dx.doi.org/10.1021/acs.jpcc.0c10689
J. Phys. Chem. C 2021, 125, 6287−6297

on every MoC_y NP; Table S6: energy contributions to the C_2H_4 adsorption energy on the different studied MoC_y NPs; Table S7: cohesive energies for the studied stoichiometric MoC NPs; Figure S1: formation energies per MoC unit for each of the studied stoichiometric MoC NPs as a function of the MoC units; Figure S2: CDD and ELF for the C_2H_4 binding on $Mo_{32}C_{32}$ NP; Figure S3: geometry changes in the Mo_5C_6 NP upon C_2H_4 adsorption; Figure S4: geometry changes in the Mo_4C_6 NP upon C_2H_4 adsorption; Figure S5: NP deformation energy and C_2H_4 distortion energy on nonstoichiometric NPs sorted relative to the amount of Mo in the explored NPs; Figure S6: effect of Mo/C ratio of $Mo_{12}C_x$ NPs in adsorption energy and size; Figure S7: CDD and ELF for the C_2H_4 binding through di-σ-CC on Mo_5C_6 NP; geometry coordinates of bare NPs and C_2H_4 adsorbed on them (PDF)

AUTHOR INFORMATION

Corresponding Authors

Carlos Jimenez-Orozco − *Facultad de Ciencias Básicas, Grupo de Materiales con Impacto (Mat&mpac), Universidad de Medellín, Medellín, Colombia*; Email: cjimenez@udem.edu.co

Francesc Illas − *Departament de Ciència de Materials i Química Física & Institut de Química Teòrica i Computacional (IQTCUB), Universitat de Barcelona, 08028 Barcelona, Spain*; orcid.org/0000-0003-2104-6123; Email: francesc.illas@ub.edu

Authors

Marc Figueras − *Departament de Ciència de Materials i Química Física & Institut de Química Teòrica i Computacional (IQTCUB), Universitat de Barcelona, 08028 Barcelona, Spain*

Elizabeth Flórez − *Facultad de Ciencias Básicas, Grupo de Materiales con Impacto (Mat&mpac), Universidad de Medellín, Medellín, Colombia*; orcid.org/0000-0002-8301-8550

Francesc Viñes − *Departament de Ciència de Materials i Química Física & Institut de Química Teòrica i Computacional (IQTCUB), Universitat de Barcelona, 08028 Barcelona, Spain*; orcid.org/0000-0001-9987-8654

José A. Rodriguez − *Chemistry Department, Brookhaven National Laboratory, Upton, New York 11973, United States*; orcid.org/0000-0002-5680-4214

Complete contact information is available at: https://pubs.acs.org/10.1021/acs.jpcc.0c10689

Notes

The authors declare no competing financial interest.

ACKNOWLEDGMENTS

The research performed at the Universitat de Barcelona has been supported by the Spanish MICIUN RTI2018-095460-B-I00 and María de Maeztu MDM-2017-0767 grants and, in part, by the Generalitat de Catalunya 2017SGR13 grant and COST Action CA18234. C.J.-O. and E.F. acknowledge the Universidad de Medellín for financial support under the internal project 1143. F.I. acknowledges additional support from the 2015 ICREA Academia Award for Excellence in University Research. Part of this research used resources of the Center for Functional Nanomaterials, which is a U.S. DOE Office of Science Facility, and the Scientific Data and Computing Center, a component of the Computational Science Initiative, at Brookhaven National Laboratory under Contract DE-SC0012704.

REFERENCES

(1) Wilson, J. N.; Otvos, J. W.; Stevenson, D. P.; Wagner, C. D. Hydrogenation of Olefins over Metals. *Ind. Eng. Chem.* **1953**, *45*, 1480−1487.

(2) Dhandapani, B.; St. Clair, T.; Oyama, S. T. Simultaneous Hydrodesulfurization, Hydrodeoxygenation, and Hydrogenation with Molybdenum carbide. *Appl. Catal., A* **1998**, *168*, 219−228.

(3) Bus, E.; Ramaker, D. E.; van Bokhoven, J. A. Structure of Ethene Adsorption Sites on Supported Metal Catalysts from in Situ XANES Analysis. *J. Am. Chem. Soc.* **2007**, *129*, 8094−8102.

(4) Binder, A.; Seipenbusch, M.; Muhler, M.; Kasper, G. Kinetics and Particle Size Effects in Ethene Hydrogenation Over Supported Palladium Catalysts at Atmospheric Pressure. *J. Catal.* **2009**, *268*, 150−155.

(5) Tsung, C.; Kuhn, J. N.; Huang, W.; Aliaga, C.; Hung, L.; Somorjai, G. A.; Yang, P. Sub-10 nm Platinum Nanocrystals with Size and Shape Control: Catalytic Study for Ethylene and Pyrrole Hydrogenation. *J. Am. Chem. Soc.* **2009**, *131*, 5816−5822.

(6) Aboul-Gheit, A. K.; Aboul-Fotouh, S. M.; Aboul-Gheit, N. A. K. Hydroconversion of Cyclohexene Using Catalysts Containing Pt, Pd, Ir, and Re Supported on H-ZSM-5 Zeolite. *Appl. Catal., A* **2005**, *283*, 157−164.

(7) Sapi, A.; Thompson, C.; Wang, H.; Michalak, W. D.; Ralston, W. T.; Alayoglu, S.; Somorjai, G. A. Recovery of Pt Surfaces for Ethylene Hydrogenation-Based Active Site Determination. *Catal. Lett.* **2014**, *144*, 1151−1158.

(8) Rioux, R. M.; Komor, R.; Song, H.; Hoefelmeyer, J. D.; Grass, M.; Niesz, K.; Yang, P.; Somorjai, G. A. Kinetics and Mechanism of Ethylene Hydrogenation Poisoned by CO on Silica-supported Monodisperse Pt Nanoparticles. *J. Catal.* **2008**, *254*, 1−11.

(9) Cunha, D. S.; Cruz, G. M. Hydrogenation of Benzene and Toluene Over Ir Particles Supported on γ-Al_2O_3. *Appl. Catal., A* **2002**, *236*, 55−66.

(10) Guil, J. M.; Masiá, A. P.; Paniego, A. R.; Menayo, J. M. T. Energetics of H_2 and O_2 Adsorption on Ir/γ-Al_2O_3 and Ir/SiO_2 Catalysts. Dependence on Support and on Metal Particle Size. *Thermochim. Acta* **1998**, *312*, 115−124.

(11) Piegsa, A.; Korth, W.; Demir, F.; Jess, A. Hydrogenation and Ring Opening of Aromatic and Naphthenic Hydrocarbons Over Noble Metal (Ir, Pt, Rh)/Al_2O_3 Catalysts. *Catal. Lett.* **2012**, *142*, 531−540.

(12) Levy, R. B.; Boudart, M. Platinum-Like Behavior of Tungsten Carbide in Surface Catalysis. *Science* **1973**, *181*, 547−549.

(13) Ardakani, S. J.; Liu, X.; Smith, K. J. Hydrogenation and Ring Opening of Naphthalene on Bulk and Supported Mo_2C Catalysts. *Appl. Catal., A* **2007**, *324*, 9−19.

(14) Hwu, H. H.; Chen, J. G. Surface Chemistry of Transition Metal Carbides. *Chem. Rev.* **2005**, *105*, 185−212.

(15) Posada-Pérez, S.; Viñes, F.; Ramirez, P. J.; Vidal, A. B.; Rodriguez, J. A.; Illas, F. The Bending Machine: CO_2 Activation and Hydrogenation on δ-MoC(001) and β-Mo_2C(001) Surfaces. *Phys. Chem. Chem. Phys.* **2014**, *16*, 14912−14921.

(16) Rocha, A.S.; Rocha, A.B.; da Silva, V. T. Benzene Adsorption on Mo_2C: A Theoretical and Experimental Study. *Appl. Catal., A* **2010**, *379*, 54−60.

(17) Jimenez-Orozco, C.; Florez, E.; Moreno, A.; Liu, P.; Rodriguez, J. A. Systematic Theoretical Study of Ethylene Adsorption on δ-MoC(001), TiC(001), and ZrC(001) Surfaces. *J. Phys. Chem. C* **2016**, *120*, 13531−13540.

(18) Jimenez-Orozco, C.; Florez, E.; Moreno, A.; Liu, P.; Rodriguez, J. A. Acetylene and Ethylene Adsorption on a β-Mo_2C(100) Surface: A Periodic DFT Study on the Role of C- and Mo-Terminations for

Bonding and Hydrogenation Reactions. *J. Phys. Chem. C* **2017**, *121*, 19786−19795.
(19) Jimenez-Orozco, C.; Flórez, E.; Viñes, F.; Rodriguez, J. A.; Illas, F. Critical Hydrogen Coverage Effect on the Hydrogenation of Ethylene Catalyzed by δ-MoC(001): An *Ab Initio* Thermodynamic and Kinetic Study. *ACS Catal.* **2020**, *10*, 6213−6222.
(20) Jimenez-Orozco, C.; Flórez, E.; Moreno, A.; Rodriguez, J. A. Platinum *vs.* Transition Metal Carbide Surfaces as Catalysts for Olefin and Alkyne Conversion: Binding and Hydrogenation of Ethylidyne. *J. Phys.: Conf. Ser.* **2019**, *1247*, 012003.
(21) Figueras, M.; Jurado, A.; Morales-Garcia, Á.; Viñes, F.; Illas, F. Bulk (in)stability as a Possible Source of Surface Reconstruction. *Phys. Chem. Chem. Phys.* **2020**, *22*, 19249−19253.
(22) Figueras, M.; Gutiérrez, R. A.; Viñes, F.; Ramírez, P. J.; Rodriguez, J. A.; Illas, F. Supported Molybdenum Carbide Nanoparticles as Hot Hydrogen Reservoirs for Catalytic Applications. *J. Phys. Chem. Lett.* **2020**, *11*, 8437−8441.
(23) Horn, J. M.; Song, Z.; Potapenko, D. V.; Hrbek, J.; White, M. G. Characterization of Molybdenum Carbide Nanoparticles Formed on Au(111) Using Reactive-Layer Assisted Deposition. *J. Phys. Chem. B* **2005**, *109*, 44.
(24) Gao, J.; Zheng, Y.; Fitzgerald, G. B.; de Joannis, J.; Tang, Y.; Wachs, I. E.; Podkolzin, S. G. Structure of Mo_2C_x and Mo_4C_x Molybdenum Carbide Nanoparticles and Their Anchoring Sites on ZSM-5 Zeolites. *J. Phys. Chem. C* **2014**, *118*, 4670−4679.
(25) Dai-Viet, N. V.; Adesina, A. A. Fischer−Tropsch synthesis over alumina-supported molybdenum carbide catalyst. *Appl. Catal., A* **2011**, *399*, 221−232.
(26) Shou, H.; Davis, R. J. Multi-product steady-state isotopic transient kinetic analysis of CO hydrogenation over supported molybdenum carbide. *J. Catal.* **2013**, *306*, 91−99.
(27) Baddour, F. G.; Roberts, E. J.; To, A. T.; Wang, L.; Habas, S. E.; Ruddy, D. A.; Bedford, N. M.; Wright, J.; Nash, C. P.; Schaidle, J. A.; Brutchey, R. L.; Malmstadt, N. Exceptionally Mild and Scalable Solution-Phase Synthesis of Molybdenum Carbide Nanoparticles for Thermocatalytic CO_2 Hydrogenation. *J. Am. Chem. Soc.* **2020**, *142*, 1010−1019.
(28) Lamiel-Garcia, O.; Bromley, S. T.; Illas, F. Low-energy Nanoscale Clusters of $(TiC)_n$ n = 6, 12: A Structural and Energetic Comparison with MgO. *Theor. Chem. Acc.* **2013**, *132*, 1312.
(29) Viñes, F.; Gomes, J. R. B.; Illas, F. Understanding the Reactivity of Metallic Nanoparticles: Beyond the Extended Surface Model for Catalysis. *Chem. Soc. Rev.* **2014**, *43*, 4922−4939.
(30) Quesne, M.; Roldán, A.; De Leeuw, N. H.; Catlow, C. R. A. Bulk and surface properties of metal carbides: implications for catalysis. *Phys. Chem. Chem. Phys.* **2018**, *20*, 6905−6916.
(31) Viñes, F.; Sousa, C.; Liu, P.; Rodriguez, J. A.; Illas, F. A systematic Density Functional Theory Study of the Electronic Structure of Bulk and (001) Surface of Transition-metals Carbides. *J. Chem. Phys.* **2005**, *122*, 174709.
(32) Guo, B. C.; Kerns, K. P.; Castleman, A. W., Jr. Ti_8C^{12+}-Metallo-Carbohedrenes: A New Class of Molecular Clusters? *Science* **1992**, *255*, 1411.
(33) Pilgrim, J. S.; Duncan, M. A. Beyond Metallo-carbohedrenes: Growth and Decomposition of Metal-carbon Nanocrystals. *J. Am. Chem. Soc.* **1993**, *115*, 9724−9727.
(34) Kresse, G.; Furthmüller, J. Efficient Iterative Schemes for *ab initio* Total-energy Calculations Using a Plane-wave Basis Set. *Phys. Rev. B: Condens. Matter Mater. Phys.* **1996**, *54*, 11169−11186.
(35) Perdew, J. P.; Burke, K.; Ernzerhof, M. Generalized Gradient Approximation Made Simple. *Phys. Rev. Lett.* **1996**, *77*, 3865−3868.
(36) Politi, J. R. D. S.; Viñes, F.; Rodriguez, J. A.; Illas, F. Atomic and Electronic Structure of Molybdenum Carbide Phases: Bulk and Low Miller-index Surfaces. *Phys. Chem. Chem. Phys.* **2013**, *15*, 12617−12625.
(37) Grimme, S.; Antony, J.; Ehrlich, S.; Krieg, H. A consistent and accurate *ab initio* parametrization of density functional dispersion correction (DFT-D) for the 94 elements H-Pu. *J. Chem. Phys.* **2010**, *132*, 154104.
(38) Kunkel, C.; Viñes, F.; Illas, F. Transition Metal Carbides as Novel Materials for CO_2 Capture, Storage, and Activation. *Energy Environ. Sci.* **2016**, *9*, 141−144.
(39) Liu, X.; Kunkel, C.; Ramírez de la Piscina, P.; Homs, N.; Viñes, F.; Illas, F. Effective and Highly Selective CO Generation from CO_2 Using a Polycrystalline α-Mo_2C Catalyst. *ACS Catal.* **2017**, *7*, 4323−4335.
(40) Blöchl, P. E. Projector Augmented-wave Method. *Phys. Rev. B: Condens. Matter Mater. Phys.* **1994**, *50*, 17953−17979.
(41) Kresse, G.; Joubert, D. From ultrasoft pseudopotentials to the projector augmented-wave method. *Phys. Rev. B: Condens. Matter Mater. Phys.* **1999**, *59*, 1758−1775.
(42) Ha, M.; Baxter, E. T.; Cass, A.; Anderson, S. L.; Alexandrova, A. N. Boron Switch for Selectivity of Catalytic Dehydrogenation on Size-Selected Pt Clusters on Al_2O_3. *J. Am. Chem. Soc.* **2017**, *139*, 11568−11575.
(43) Gorey, T. J.; Zandkarimi, B.; Li, G.; Baxter, E. T.; Alexandrova, A. N.; Anderson, S. L. Coking-Resistant Sub-Nano Dehydrogenation Catalysts: Pt_nSn_x/SiO_2 (n = 4, 7). *ACS Catal.* **2020**, *10*, 4543−4558.
(44) Li, G.; Zandkarimi, B.; Cass, A.; Gorey, T. J.; Allen, B. J.; Alexandrova, A. N.; Anderson, S. L. Sn-modification of Pt_7/alumina model catalysts: Suppression of carbon deposition and enhanced thermal stability. *J. Chem. Phys.* **2020**, *152*, 024702.
(45) Jimenez-Orozco, C.; Flórez, E.; Montoya, A.; Rodriguez, J. A. Binding and Activation of Ethylene on Tungsten Carbide and Platinum Surfaces. *Phys. Chem. Chem. Phys.* **2019**, *21*, 17332−17342.
(46) Bader, R. *Atoms in Molecules: A Quantum Theory*; Oxford University Press: New York, 1990.
(47) Bromley, S.; Moreira, I. P. R.; Neyman, K. M.; Illas, F. Approaching Nanoscale Oxides: Models and Theoretical Methods. *Chem. Soc. Rev.* **2009**, *38*, 2657−2670.
(48) Shen, J.; Hill, J. M.; Watwe, R. M.; Spiewak, B. E.; Dumesic, J. A. Microcalorimetric, Infrared Spectroscopic, and DFT Studies of Ethylene Adsorption on Pt/SiO_2 and $Pt-Sn/SiO_2$ Catalysts. J. *J. Phys. Chem. B* **1999**, *103*, 3923−3934.
(49) Watwe, R. M.; Spiewak, B. E.; Cortright, R. D.; Dumesic, J. A. Density Functional Theory (DFT) Studies of C_1 and C_2 Hydrocarbons Species on Pt Clusters. *J. Catal.* **1998**, *180*, 184−193.
(50) Crampton, A. S.; Rötzer, M. D.; Schweinberger, F. F.; Yoon, B.; Landman, U.; Heiz, U. Controlling Ethylene Hydrogenation Reactivity on Pt_{13} Clusters by Varying the Stoichiometry of the Amorphous Silica Support. *Angew. Chem., Int. Ed.* **2016**, *55*, 8953−8957.
(51) Sun, G.; Fuller, J. T., III; Alexandrova, A. N.; Sautet, P. Global Activity Search Uncovers Reaction Induced Concomitant Catalyst Restructuring for Alkane Dissociation on Model Pt Catalysts. *ACS Catal.* **2021**, *11*, 1877−1885.
(52) Liu, P.; Rodriguez, J. A.; Muckerman, J. T. The Ti_8C_{12} Metcar: A New Model Catalyst for Hydrodesulfurization. *J. Phys. Chem. B* **2004**, *108*, 18796−18798.
(53) Liu, P.; Rodriguez, J. A. Effects of carbon on the stability and chemical performance of transition metal carbides: A density functional study. *J. Chem. Phys.* **2004**, *120*, 5414.

https://dx.doi.org/10.1021/acs.jpcc.0c10689
J. Phys. Chem. C 2021, 125, 6287−6297

Chapter 10:

General conclusions

This Thesis focuses on the study of nanoparticles of transition metal carbides, and more specifically on MoC nanoparticles, and on the effect of nanostructuring on their performance as catalysts for the conversion of greenhouse gases on useful chemicals. This work constitutes a continuation of previous works carried out in the host research group of this Thesis, where transition metal carbides surfaces were considered as catalysts for the mentioned reactions as well as supports of metallic nanoparticles.

This Thesis is composed of a theoretical/computational part and an experimental one. The latter was carried out in the Brookhaven National Laboratory by the group of Prof. J. A. Rodriguez. Their contribution implied the synthesis of all systems composed of MoC nanoparticles supported on Au(111), their subsequent characterization, and the monitoring of all the reactivity reported in this thesis. On the other hand, the theoretical part has been carried out in the present institution, *Universitat de Barcelona*, and has implied the analysis of both experimental and theoretical results in addition to carrying out all the computational calculations. At the end, the obtained results have been published jointly.

With respect to the comparison of theory and experiments, the main conclusions are as follows:

- MoC_y nanoparticles supported on Au(111) present an outstanding capability to activate methane that can be explained thanks to the obtained theoretical results and predicted trends.
- These nanoparticles act as excellent H_2 sponges due to the viability of Kubas formation in addition to other features theoretically revealed.
- Furthermore, they are excellent candidates for the hydrogenation of CO_2 at high hydrogen concentrations under mild conditions.

In addition, motivated by the experimental findings and on the anticipated Au(111) support inactivity towards greenhouse gases transformation reactions, the intrinsic chemical nature of clean MoC_y nanoparticles has been studied. Moreover, the comparison between nanoparticles and extended surfaces of transition metal carbides revealed unexpected features. Thus, two more general conclusions have been obtained:

- Unsupported MoC_y nanoparticles can be considered as proficient catalysts for olefin hydrogenation reactions when some restrictions involving structural features are accounted, for such as the C/Mo ratio.

- The extended surfaces of some polymorphs of transition metal carbides and nitrides can undergo reconstruction, this is the case when they are not the most stable polymorph at standard conditions.

All in all, the present Thesis has provided detailed information on the effect of the nanostructuring in the catalytic performance of MoC_y nanoparticles on some greenhouse gases transformation reactions and other related topics. The expected outcome is to encourage further studies on the applicability of these materials as proficient greenhouse gases transformation catalysts.

List of publications

- Figueras, M.; Gutiérrez, R. A.; Prats, H.; Viñes, F.; Ramírez, P. J.; Illas, F.; Rodriguez, J. A. Boosting the activity of transition metal carbides towards methane activation by nanostructuring. *Phys. Chem. Chem. Phys.* **2020**, *22*, 7110-7118.

- Figueras, M.; Jurado, A.; Morales-García, A.; Viñes, F.; Illas, F. Bulk (in)stability as a possible source of surface reconstruction. *Phys. Chem. Chem. Phys.* **2020**, *22*, 19249-19253.

- Figueras, M.; Gutiérrez, R. A.; Viñes, F.; Ramírez, P. J.; Rodriguez, J. A.; Illas, F. Supported Molybdenum Carbide Nanoparticles as Hot Hydrogen Reservoirs for Catalytic Applications. *J. Phys. Chem. Lett.* **2020**, *11*, 19, 8437-8441.

- Figueras, M.; Gutiérrez, R. A.; Viñes, F.; Ramírez, P. J.; Rodriguez, J. A.; Illas, F. Supported Molybdenum Carbide Nanoparticles as an Excellent Catalyst for CO_2 Hydrogenation. *ACS Catal.* **2021**, *11*, 15, 9679-9687.

- Jimenez-Orozco, C.; Figueras, M.; Floréz, E.; Viñes, F.; Rodriguez, J. A.; Illas, F. Size and Stoichiometry Effects on the Reactivity of MoC_y Nanoparticles toward Ethylene. *J. Phys. Chem. C* **2021**, *125*, 11, 6287-6297.

Appendix A

Supporting information to "Boosting the activity of transition metal carbides toward methane activation by nanostructuring"

Boosting the activity of transition metal carbides towards methane activation by nanostructuring

Marc Figueras,[a] Ramón A. Gutiérrez[b,c,d] Hèctor Prats,[a] Francesc Viñes,[a] Pedro J. Ramírez,[c,d] Francesc Illas,[a,*] and José A. Rodriguez[b,*]

[a]*Departament de Ciència de Materials i Química Física & Institut de Química Teòrica i Computacional (IQTCUB), Universitat de Barcelona, Martí i Franquès 1-11, 08028 Barcelona, Spain.*

[b]*Chemistry Department, Brookhaven National Laboratory, Upton, New York 11973, United States of America.*

[c]*Facultad de Ciencias, Universidad Central de Venezuela, Caracas 1020-A, Venezuela.*

[d] *Present address: Zoneca-CENEX, R&D Laboratories, Alta Vista, 64770 Monterrey, Mexico*

Electronic Supplementary Information

S1. C 1s and Mo 3d XPS data for the carbide nanoparticles

Figure S1. C 1s spectra collected during the preparation of the $MoC_{1.1}$/Au(111) system. A multilayer of ethylene was adsorbed on the gold substrate at 100 K, 0.3 ML of Mo were vapor-deposited and then the sample was annealed to 750 K to induce the desorption of the excess hydrocarbon and the formation of $MoC_{1.1}$.

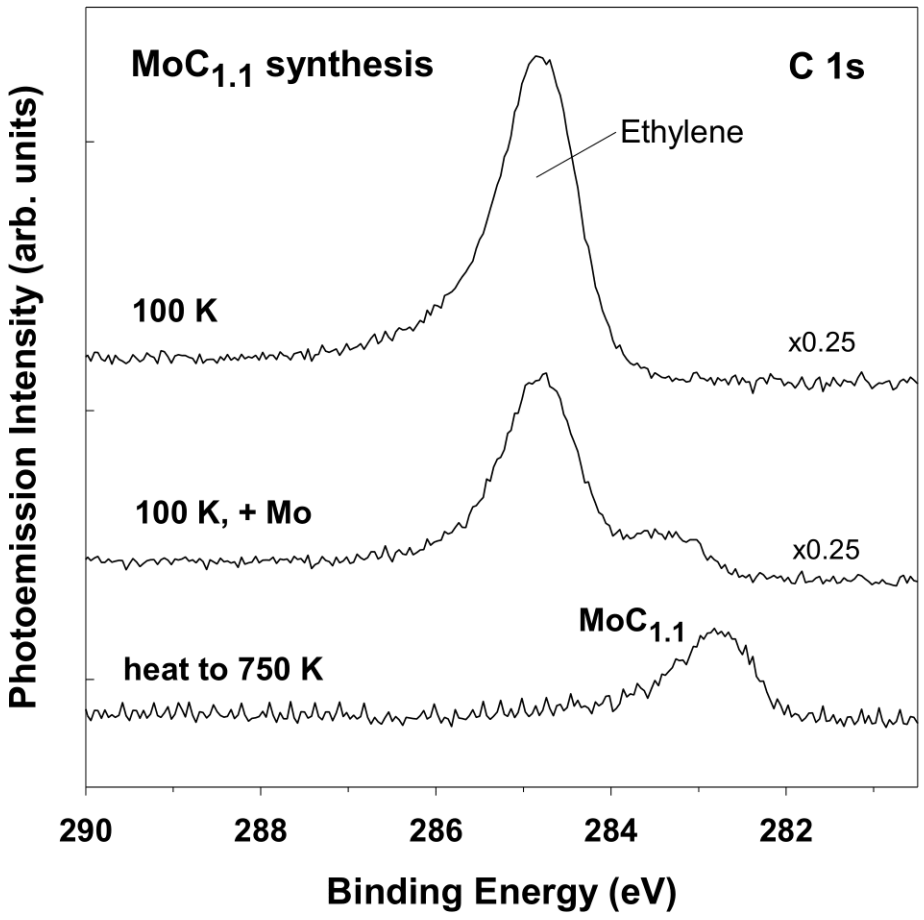

Figure S2. Mo 3d XPS spectra for metallic Mo, $MoC_{0.6}$/Au(111) and $MoC_{1.1}$/Au(111) systems

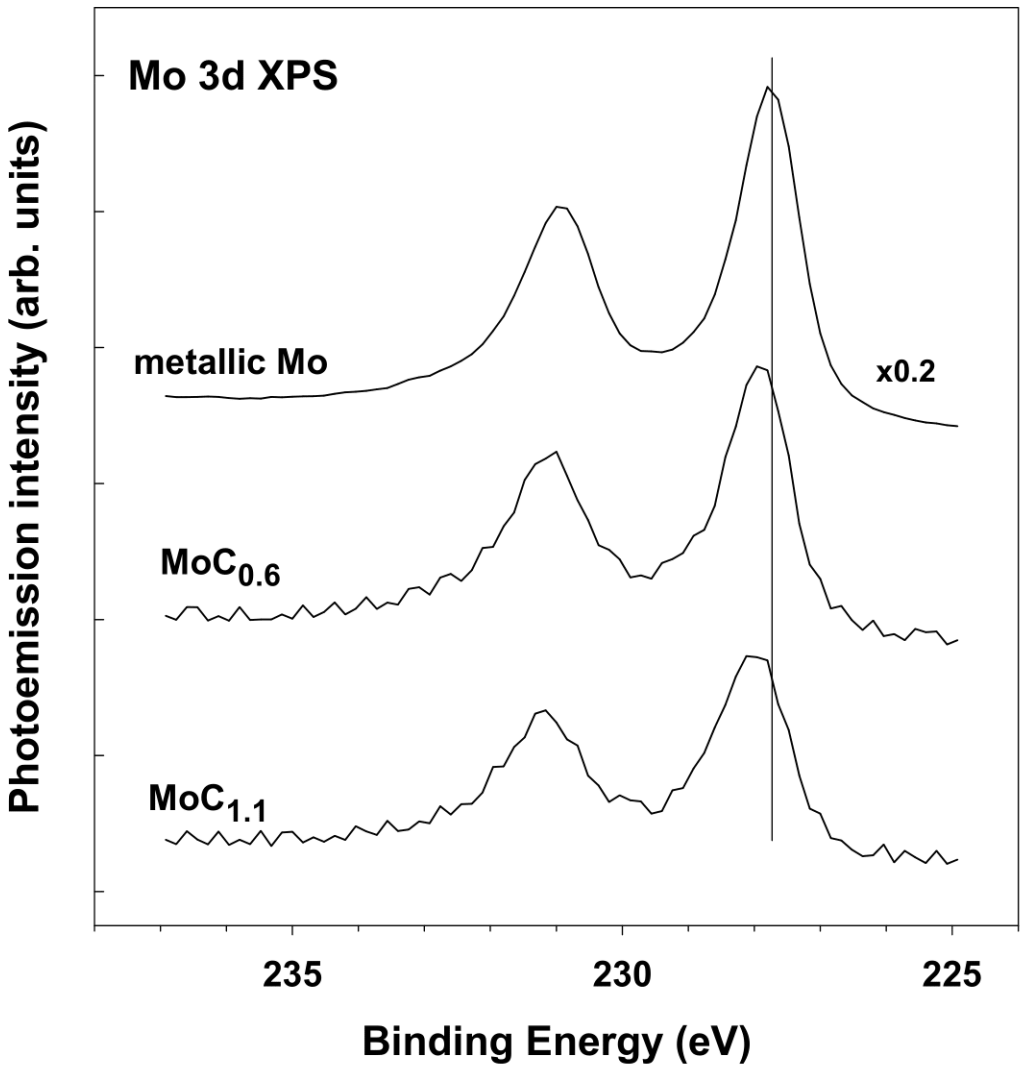

S2. Computational details

The periodic density functional theory (DFT) calculations have used a valence electron density expanded in a plane wave basis set with a kinetic energy cutoff of 415 eV, chosen to yield total energy variations below 0.01 eV. The effect of core electrons on the valence electron density has been described by the projector augmented wave (PAW) method of Blöchl,[1] as implemented in the VASP code by Kresse and Joubert.[2] The Au(111) surface slab model was built from the pre-optimized bulk unit cell, and contains four atomic layers with the two bottommost fixed as in the bulk to provide an appropriate environment to the fully relaxed two uppermost atomic layers defining the surface region.[3] To avoid interactions between periodic images in the direction perpendicular to the surface, a vacuum region of 30 Å was added. The MoC_y nanoparticles were supported on a (6×6) supercell of Au(111) containing 144 Au atoms, and their structure fully relaxed using a conjugate-gradient algorithm with convergence criteria for electronic and atomic updates of 10^{-5} eV and 0.01 eV·Å^{-1}, respectively. Several initial geometries were tested for each adsorbed MoC_y nanoparticle, and the most stable structure for each size was chosen to study the CH_4 dissociation reaction thereon. The optimization procedure used to gain the minimum energy structure of the nanoparticles was also used to optimize the geometry of the different species adsorbed on the supported nanoparticles. Note that, due to the large number of possible orientations of the nanoparticle and the presence of different adsorption sites on the Au(111) surface, a considerable number of geometry optimization runs was necessary.

The δ-MoC(001), and C- and Mo-terminated β-Mo_2C(0001) surface slabs were constructed using the lattice parameter taken from the optimized bulk TMC crystal.[4] The δ-MoC(001) $(2\sqrt{2}\times2\sqrt{2})R45^{o}$ slab contains four atomic layers; the two uppermost ones have been allowed to fully relax, whereas the two bottom layers were fixed at optimized bulk crystal positions to simulate the material bulk. The C- and Mo-terminated β-Mo_2C(0001) slabs contains six atomic; the three uppermost ones have been allowed to fully relax, whereas the three bottom layers were fixed at optimized bulk crystal positions. All surface geometries were optimized before placing any adsorbate. The initial guesses for adsorbate geometries were obtained by placing the adsorbate at different sites. Such optimized geometries were characterized as minima on the potential energy surface by appropriate frequency analysis involving diagonalization of the corresponding block of the Hessian matrix with elements obtained through finite differences of analytic gradients of 0.03 Å length. The necessary numerical integrations in the reciprocal space were carried out using an optimal 3×3×1 **k**-point mesh selected following the Monkhorst-Pack scheme[5] for the MoC_y/Au(111) systems, a 9×9×1 **k**-point mesh for δ-MoC(001), and a 5×5×1 **k**-point mesh for the β-Mo_2C(0001) slabs.

The energy of the isolated gas phase CH_4 molecule was obtained by placing it in an asymmetric periodic box of 9×10×11 Å and considering the Γ-point only. The initial guess for adsorbate geometries was obtained by directly placing the adsorbate at different sites which depends on each chosen system. Methane adsorption energy E_{ads}, was then calculated as:

$$E_{ads} = E_{CH_4/slab} - \left(E_{slab} + E_{CH_4}\right) \quad (1)$$

where $E_{CH_4/slab}$ is the energy of the CH_4 species adsorbed on the corresponding slab model, E_{slab} is the energy of the relaxed, pristine slab, and E_{CH_4} the energy of an isolated CH_4 molecule. In the studied MoC_y/Au(111) cases, the slab includes the supported carbide nanoparticle. All energy values include the zero-point energy (ZPE) term, estimated by considering both gas and adsorbed phases, obtained within the harmonic approximation. The reaction energy, E_{reac} has been calculated assuming that the final products are at infinite separation. Hence, it can be calculated from the formation energies of the different adsorbed species (CH_4, CH_3, and H):

$$\Delta E_{reac} = E^f_{CH_3} + E^f_H - E^f_{CH_4} \quad (1),$$

where details on the calculation of formation energies can be found elsewhere.[6]

S3. Optimized structures for the transition states of CH_4 dissociation on MoC_y/Au(111) models

Figure S3. Optimized geometries (top and side views) for the transition states of methane first C-H bond scission on all studied MoC_y/Au(111) systems. Colour code as in Figure S1.

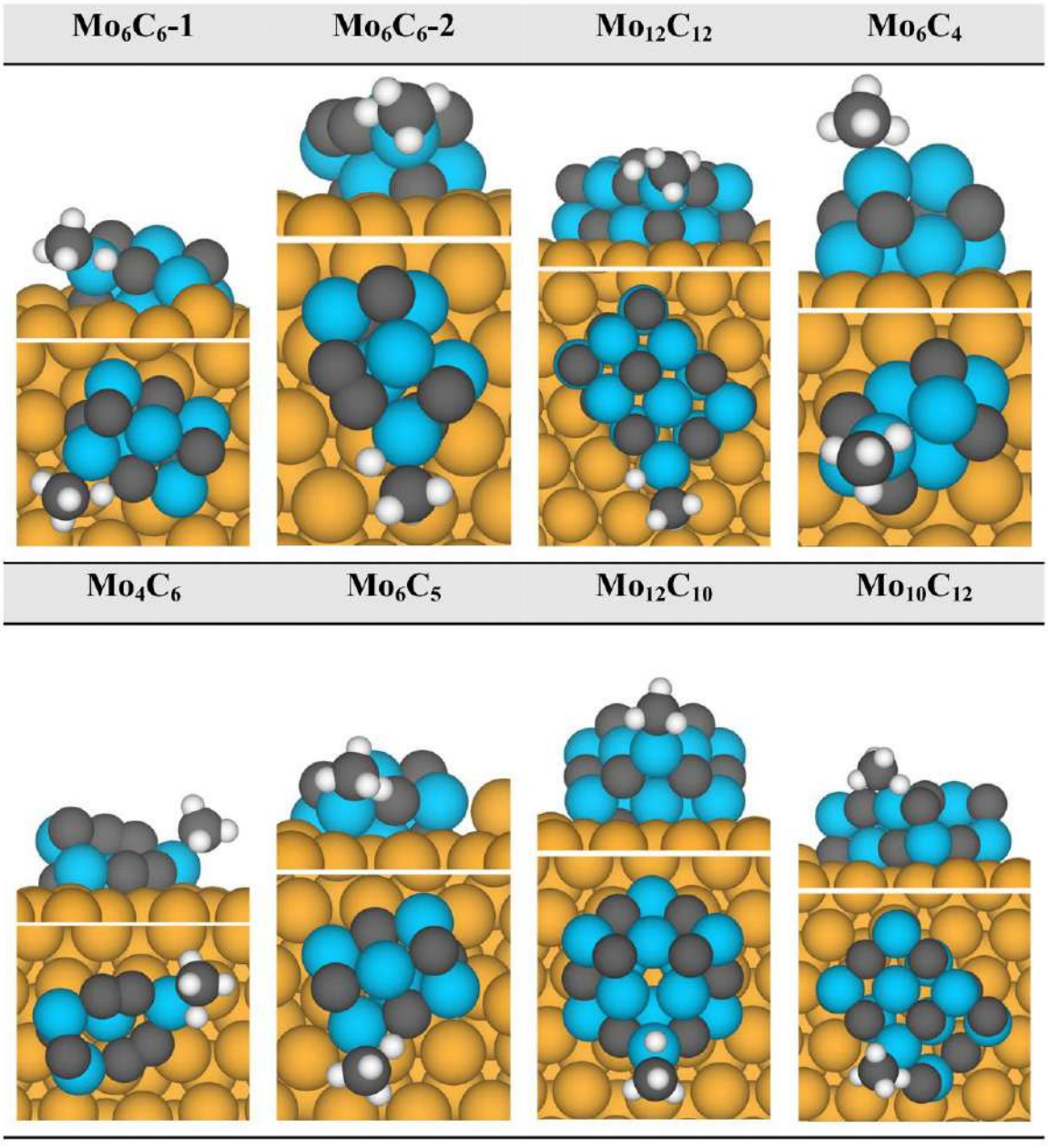

S4. Optimized structures for the transition states of CH_4 dissociation on δ-MoC and β-Mo_2C surfaces

Figure S4. Optimized geometries (top and side views) for the transition states of methane activation on δ-MoC(001) and C/Mo-terminated β–Mo_2C(0001) surfaces. Colour code as in Figure S1.

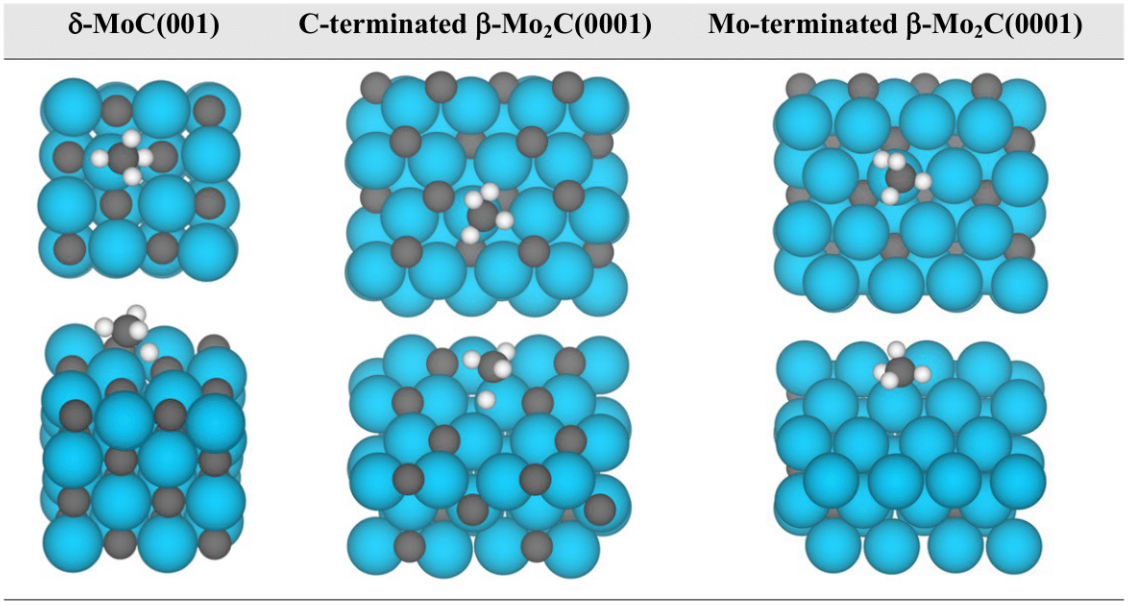

References and Notes

[1] P. E. Blöchl, *Phys. Rev. B,* 1994, **50**, 17953–17979.

[2] G. Kresse and D. Joubert, *Phys. Rev. B,* 1999, **59**, 1758–1775.

[3] C. Kunkel, F. Viñes and F. Illas, *Energy Environ. Sci.,* 2016, **9**, 141–144.

[4] J. R. d. S. Politi, F. Viñes, J. A. Rodriguez and F. Illas, *Phys. Chem. Chem. Phys.,* 2013, **15**, 12617-12625.

[5] H. J. Monkhorst and J. D. Pack, *Phys. Rev. B,* 1976, **13**, 5188–5192.

[6] H. Prats, R. A. Gutierrez, J. J. Piñero, F. Viñes, S. T. Bromley, P. J. Ramirez , J. A. Rodriguez and F. Illas, *J. Am. Chem. Soc.*, 2019, **141**, 5303-5313.

Appendix B

Supporting information to "Bulk (in)stability as a possible source of surface reconstruction"

Electronic Supporting Information

Bulk (in)stability as a possible source or surface reconstruction

Marc Figueras,‡ Anabel Jurado,‡ Ángel Morales-García, Francesc Viñes and Francesc Illas*

Departament de Ciència de Materials i Química Física & Institut de Química Teòrica i Computacional (IQTCUB), Universitat de Barcelona. c/ Martí i Franquès 1-11, 08028 Barcelona, Spain

* Corresponding author e-mail: francesc.illas@ub.edu

‡ Both authors equally contributed

Table. S1. Influence of the plane-wave kinetic energy cutoff and vacuum width on the surface energy for a (2×2) MoC supercell surface model containing four atomic layers. All surface energy values are in J/m^2.

Plane Wave kinetic energy Cutoff	**415 eV**	**500 eV**
Relaxed surface energy	0.67	0.67
Fixed surface energy	1.41	1.41
Vacuum width	**15 Å**	**20 Å**
kinetickiRelaxed surface energy	0.67	0.67
Fixed surface energy	1.41	1.41

Table. S2. Influence of the slab model thickness on the surface energy. Calculations are reported for two (2×2) supercell models, one with 4 atomic layers (2 relaxed + 2 frozen) and one with 8 atomic layers (6 relaxed + 2 frozen). All surface energy values are in J/m^2.

Thickness	**4 layers (2+2)**	**8 layers (2+6)**
Fixed surface energy	1.41	1.44
Relaxed surface energy	0.67	0.48

Figure S1. Initial configurations of the alternative reconstruction patterns studied in the (4×4) supercell of MoC (001) surface. Purple and black spheres correspond to Mo and C atoms, respectively. Atoms displacements are shown by arrows.

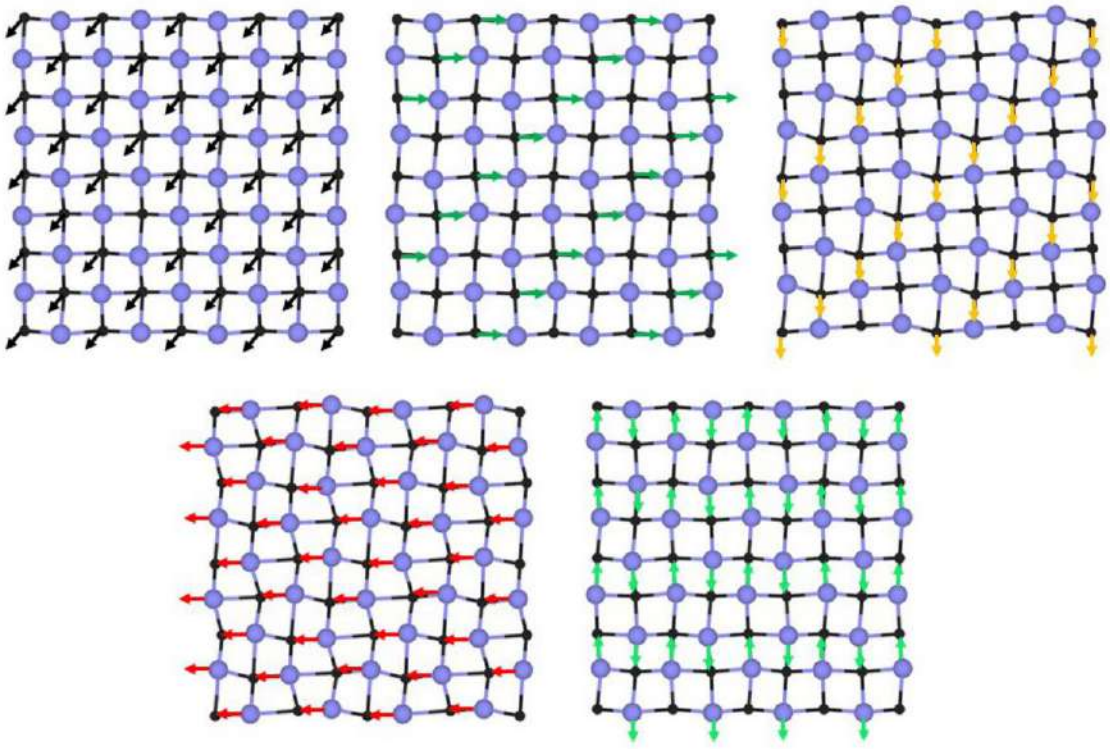

Figure. S2. First (top panels) and second (bottom panels) atomic layer for fixed (bulk-truncated) *vs.* reconstructed (2×2) supercells of the MoN (001) surface. Violet and cyan spheres correspond to Mo and N atoms, respectively.

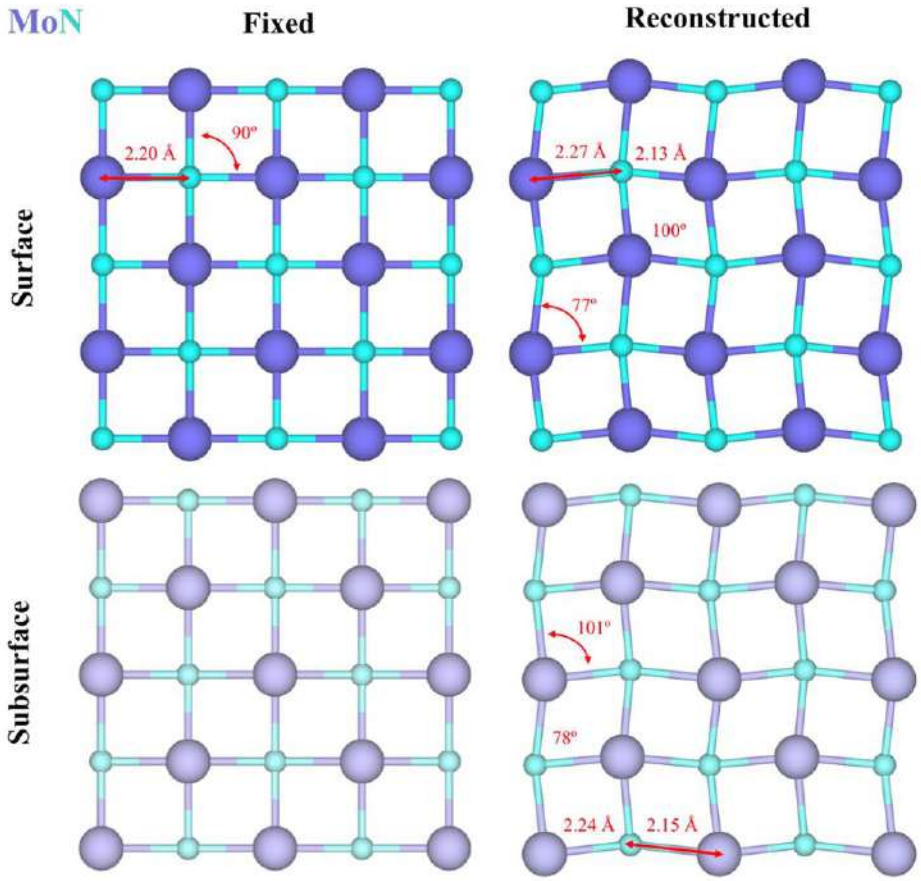

Figure S3. First (top panels) and second (bottom panels) atomic layer for fixed (bulk-truncated) *vs.* reconstructed (2×2) supercells of the γ-WC (001) surface. Grey and black spheres correspond to W and C atoms, respectively.

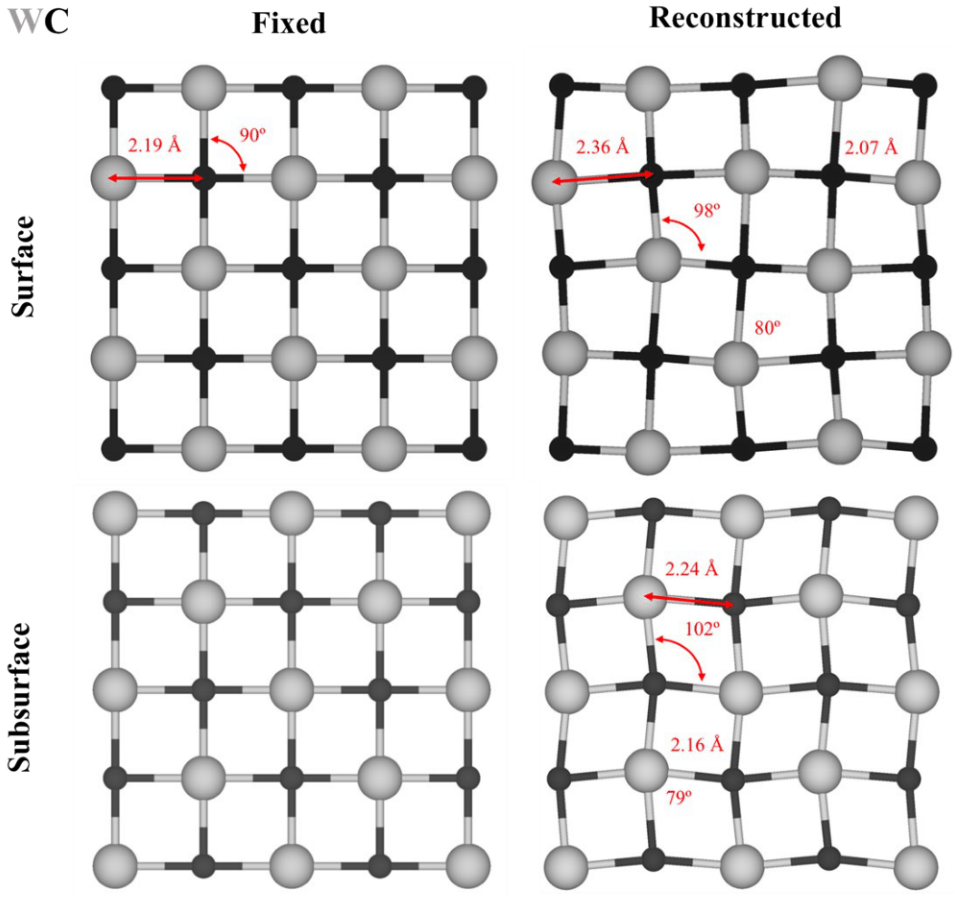

Figure S4. First (top panels) and second (bottom panels) atomic layer for fixed (bulk-truncated) *vs.* reconstructed (2×2) supercells of the WN (001) surface. Grey and cyan spheres correspond to W and N atoms, respectively.

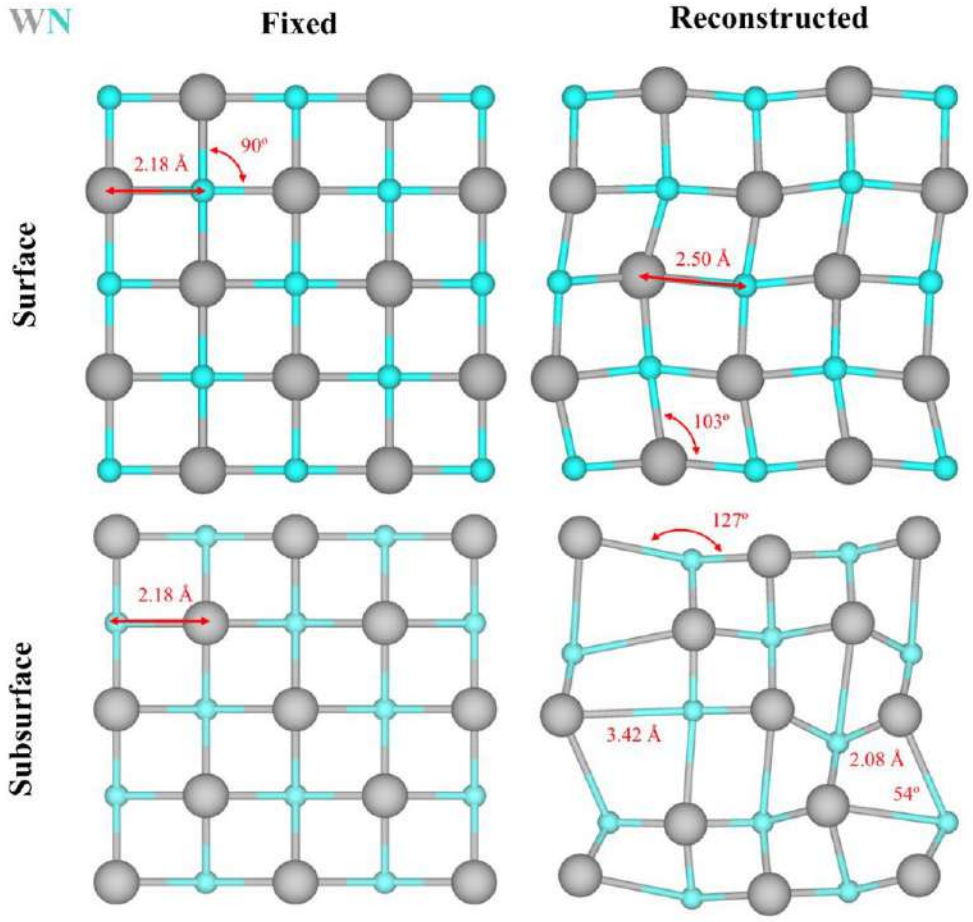

Appendix C

Supporting information to "Supported Molybdenum Carbide Nanoparticles as Hot Hydrogen Reservoirs for Catalytic Applications"

Supported Molybdenum Carbide Nanoparticles as Hot Hydrogen Reservoirs for Catalytic Applications

Marc Figueras[†], Ramón A. Gutiérrez,[‡,§] Francesc Viñes,[*,†] Pedro J. Ramírez,[§,£] Jose Rodriguez,[*,‡] Francesc Illas[†]

[†] *Departament de Ciència de Materials i Química Física & Institut de Química Teòrica i Computacional (IQTCUB), Universitat de Barcelona. c/ Martí i Franquès 1-11, 08028 Barcelona, Spain.*

[‡] *Chemistry Department, Brookhaven National Laboratory, Upton, NY 11973, United States.*

[§] *Facultad de Ciencias, Universidad Central de Venezuela, Caracas 1020-A, Venezuela.*

[£] *Present address: Zoneca-CENEX, R&D Laboratories, Alta Vista, 64770 Monterrey, Mexico.*

[*] **Corresponding authors**: José A. Rodriguez (rodriguez@bnl.gov), Francesc Viñes (francesc.vines@ub.edu)

Experimental Details

For the preparation of the MoC_y/Au(111) systems, we followed a procedure described in previous studies.[1,2] The MoC_y nanoparticles were generated by deposition of Mo metal onto a reactive multilayer of ethylene, which was physisorbed on a Au(111) surface at 100 K. Upon heating to 750 K, part of the ethylene desorbed and the MoC_y nanoparticles were left on the gold substrate. These transformations could be followed by using a combination of X-ray Photoemission Spectroscopy (*XPS*), Temperature Programmed Desorption (*TPD*), and Scanning Tunnelling Microscopy (*STM*).[1,2] In this synthetic approach, it is possible to control the C/Mo ratio in the carbide nanoparticles, and this was varied between 0.6 and 1.1. No signal was observed in the O 1s XPS region indicating that the prepared NPs did not contain oxygen.[3] Images acquired by STM showed that the generated nanoparticles were small (0.8-1.5 nm) and grew over the face-centred cubic (*fcc*) troughs located on either side of the elbows of the reconstructed Au(111) substrate.[1]

The reactivity of the MoC_y/Au(111) surfaces towards H_2 was examined in a system which combines an Ultra-High Vacuum (*UHV*) chamber (base pressure ~$7 \cdot 10^{-10}$ mbar) and a batch reactor.[2] Within this system, the sample could be transferred between the reactor and UHV chamber without exposure to air. The UHV chamber was equipped with instrumentation for XPS, Ultraviolet Photoelectron Spectroscopy (*UPS*), Low-Energy Electron Diffraction (*LEED*), Ion Scattering Spectroscopy (*ISS*), and TPD. In

the tests to study the interactions with hydrogen, MoC_y/Au(111) surfaces were positioned in the batch reactor at ~300 K, then 1 Torr of H_2 was introduced for a period of five minutes. After this exposure, the hydrogen gas was removed from the reactor and, through differentially pumped stages, each sample was transferred back to the UHV chamber for surface characterization with XPS and TPD. The samples were free of oxygen and only contained Mo, C, and H on top of the gold substrate.

Computational Details

The hydrogen reservoir capabilities on MoC_y/Au(111) has been assessed using a stoichiometric $Mo_{12}C_{12}$ cluster supported on a Au(111) surface slab model. Such supported nanoparticle structures was obtained and characterized in a previous work,[3] obtained first by a thorough search of cluster minima in vacuum, using shape templates from similar TiC compound gained by data mining searches combining interatomic potentials and Density Functional Theory (*DFT*) calculations,[4] plus exhaustively sampling the attachment of such clusters on a Au(111) slab model of *p*(6×6) dimensions. The Au(111) slab model is four-layered, where the two upmost layers have been allowed to relax, while the bottommost two layers were kept frozen mimicking the bulk Au environment, *i.e.* 2+2 approach, built and relaxed from a previously optimized Au bulk using the very same computational scheme. Such large dimensions were found to be necessary to properly isolate MoC_y clusters from periodically replicated images, and for the same purpose, a very large vacuum region of 30 Å was added.

The DFT calculations were carried out using the Perdew-Burke-Ernzerhof (*PBE*)[5] exchange-correlation (*xc*) functional, adding a dispersive forces treatment by Grimme D3 correction,[6] already found to be accuracy-wise suited for such systems.[3] Spin-polarization was found to be negligible such past studies,[3] and so presently not accounted for. The effect of core electrons on the valence electron density has been described by the Projector Augmented Wave (*PAW*) method of Blöchl,[7] as implemented in the employed Vienna *Ab-initio* Simulation Package (*VASP*) code,[8] as implemented by Kresse and Joubert.[9] Optimizations were carried out fully relaxing the aforementioned two gold layers, the attached MoC clusters, and the H_x (x = 1,2) species upon. The electronic and atomic optimization criteria were set to 10^{-5} eV and 0.01 eV·Å^{-1}, respectively, that together with a basis set of plane waves with a kinetic energy limit of 415 eV and a 3×3×1 **k**-point mesh ensure results well within the chemical accuracy of 1 kcal·mol^{-1}, *i.e.* below ~0.04 eV. Transition State (*TS*) structures were acquired by means

of the Climbing-Image Nudged-Elastic-Band (*CI-NEB*) method,[10] and adsorption minima and TSs were characterized as so by a frequency analysis carried out by Hessian matrix building and diagonalization, constructed by finite differences of 0.03 Å in length.

Several initial geometries were tested for the MoC_y nanoparticle, and the most stable structure was chosen to study the H_x adsorption, the H_2 dissociation, and the H diffusion. The optimization procedure used to gain the minimum energy structure of the nanoparticles was also used to optimize the geometry of the different species adsorbed on the supported nanoparticles. Note that, due to the large number of possible topologically distinct sites a considerable number of geometry optimization runs was necessary.

Figure S1. Amounts of CH_x species generated on $MoC_{1.1}$/Au(111) and $MoC_{0.6}$/Au(111) after several cycles of hydrogen adsorption (1 Torr of H_2, 300 K, 5 minutes) and desorption (heating at 500 K).

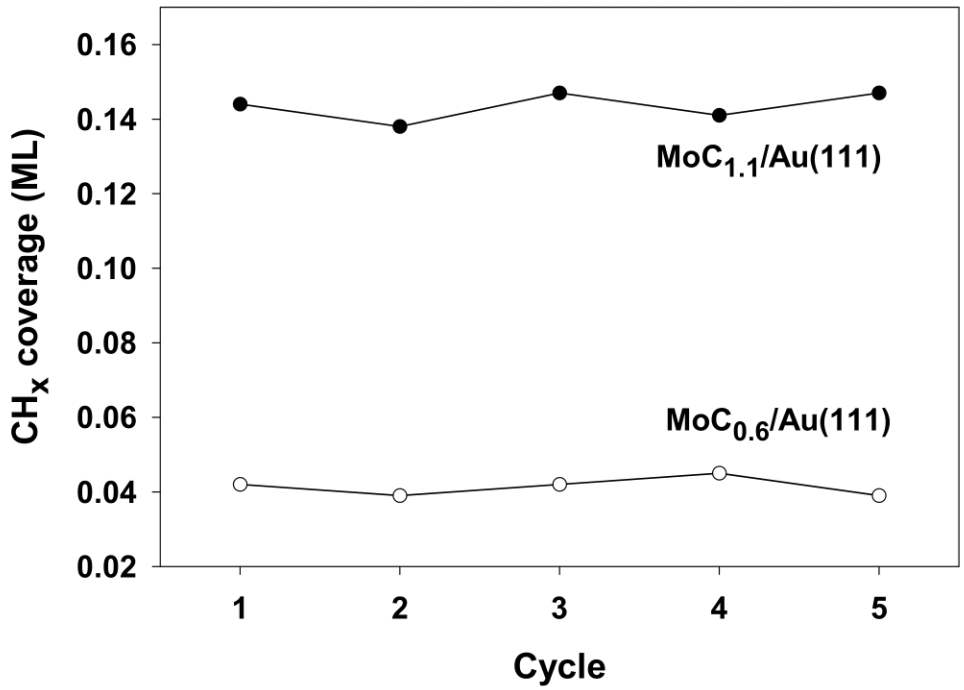

References

(1) Horn, J. M.; Song, Z.; Potapenko, D. V.; Hrbek, J.; White, M. G. Characterization of Molybdenum Carbide Nanoparticles Formed on Au(111) Using Reactive-Layer Assisted Deposition. *J. Phys. Chem. B* **2005**, *109*, 44–47.

(2) Posada-Pérez, S.; Ramírez, P. J.; Evans, J.; Viñes, F.; Liu, P.; Illas, F.; Rodriguez, J. A. Highly Active Au/δ-MoC and Cu/δ-MoC Catalysts for the Conversion of CO_2: The Metal/C Ratio as a Key Factor Defining Activity, Selectivity, and Stability. *J. Am. Chem. Soc.* **2016**, *138*, 8269–8278.

(3) Figueras, M.; Gutiérrez, R. A.; Prats, H.; Viñes, F.; Ramírez, P. J.; Illas, F.; Rodriguez, J. A. Boosting the Activity of Transition Metal Carbides Towards Methane Activation by Nanostructuring. *Phys. Chem. Chem. Phys.* **2020**, *22*, 7110–7118.

(4) Lamiel, O.; Bromley, S. T.; Illas, F. Low-energy Nanoscale Clusters of $(TiC)_n$ n = 6, 12: A Structural and Energetic Comparison with MgO. Theor. Chem. Acc. **2013**, *132*, 1312.

(5) Perdew, J. P.; Burke, K.; Ernzerhof, M. Generalized Gradient Approximation Made Simple. *Phys. Rev. Lett.* **1996**, *77*, 3865–3868.

(6) Grimme, S.; Antony, J.; Ehrlich, S.; Krieg, S. A. A Consistent and Accurate *Ab Initio* Parametrization of Density Functional Dispersion Correction (DFT-D) for the 94 Elements H-Pu. *J. Chem. Phys.* **2010**, *132*, 154104.

(7) Blöchl, P. E. Projector Augmented-Wave Method. *Phys. Rev. B* **1994**, *50*, 17953–17979.

(8) Kresse, G.; Furthmüller, J. *Phys. Rev. B: Condens. Matter Mater. Phys.* **1996**, *54*, 11169–11186.

(9) Kresse, G.; Joubert, D. From Ultrasoft Pseudopotentials to the Projector Augmented-Wave Method. *Phys. Rev. B* **1999**, *59*, 1758–1775.

(10) Henkelman, G.; Uberuaga, B. P.; Jónsson, H. A. A Climbing Image Nudged Elastic Band Method for Finding Saddle Points and Minimum Energy Paths. *Phys. Rev. B: Condens. Matter Mater. Phys.* **2000**, *113*, 9901–9904.

Appendix D

Supporting information to "Supported Molybdenum Carbide Nanoparticles as Excellent Catalyst for CO_2 Hydrogenation"

Supported Molybdenum Carbide Nanoparticles as Excellent Catalyst for CO_2 Hydrogenation

Marc Figueras[†], Ramón A. Gutiérrez, [§, ‡] Francesc Viñes,[†] Pedro J. Ramírez,[§,£] Jose Rodriguez,[*,‡] Francesc Illas[*,†]

[†] *Departament de Ciència de Materials i Química Física & Institut de Química Teòrica i Computacional (IQTCUB), Universitat de Barcelona. c/ Martí i Franquès 1-11, 08028 Barcelona, Spain.*

[‡] *Chemistry Department, Brookhaven National Laboratory, Upton, NY 11973, United States.*

[§] *Facultad de Ciencias, Universidad Central de Venezuela, Caracas 1020-A, Venezuela.*

[£] *Present address: Zoneca-CENEX, R&D Laboratories, Alta Vista, 64770 Monterrey, Mexico.*

[*] **Corresponding authors**: José A. Rodriguez (rodriguez@bnl.gov), Francesc Illas (francesc.illas@ub.edu)

S1. Cartesian coordinates of the supported nanoparticle structure without support, free nanoparticle, and the free nanoparticle at high hydrogen coverage.

Supported nanoparticle structure without support

24

Lattice="17.56453244467384 0.0 0.0 0.0 15.211331302683535 0.0 0.0 0.0 37.17069034333515" Properties=species:S:1:pos:R:3 pbc="T T T"

C	9.67149381	3.27456388	26.10612069
C	6.97454708	6.44933655	26.34904908
C	5.60656655	8.13801850	24.24793909
C	8.39112786	4.79466022	24.12257495
C	7.38992134	9.43613054	26.29448332
C	8.79700341	7.80271276	24.06621709
C	10.05718999	6.16736004	26.91189072
C	11.46276674	4.39022177	24.13714822
C	12.93102169	5.76137315	26.14951479
C	11.95712477	7.49101619	24.02272279
C	10.44837918	9.17608156	26.24147675
C	9.03310291	10.68774637	24.20998497
Mo	5.94382448	8.08930800	26.13899670

Mo	8.47707170	5.02384417	26.16571376
Mo	7.17333223	6.53651208	24.21375700
Mo	9.75398058	3.34667671	24.20165783
Mo	7.39782751	9.29310147	24.09624158
Mo	8.81531456	7.70580784	26.17296085
Mo	10.11382783	6.13870517	24.23177785
Mo	11.22588019	4.65484805	26.27684515
Mo	9.02814710	10.52041504	26.08313054
Mo	10.44762592	8.93738752	24.12690819
Mo	11.55019850	7.37768179	26.13018033
Mo	12.91974384	5.76123028	24.22910870

Free nanoparticle

24

Lattice="19.0 0.0 0.0 0.0 18.0 0.0 0.0 0.0 20.0" Properties=species:S:1:pos:R:3 pbc="T T T"

C	10.57052567	6.26490593	7.82094864
C	10.17848879	10.40946551	8.17250604
C	12.14991044	12.32337563	8.77750730
C	12.58876710	8.21486542	8.21727210
C	9.69629096	12.39122115	10.54417780
C	12.62660237	10.04353807	10.67272991
C	9.50785713	8.05399981	10.00035824
C	12.43922239	5.70612141	10.12622823
C	9.98810457	5.77253444	11.89516007
C	11.95889935	7.68842263	12.49950076
C	9.54620167	9.88194060	12.45591371
C	11.56326631	11.83363985	12.85145893
Mo	10.25964824	12.30634845	8.63046538
Mo	10.43833107	8.31473638	8.22518137
Mo	12.24758428	10.22376283	8.70740139
Mo	12.42849500	6.27002933	8.20162295
Mo	11.91148652	11.95026330	10.80970117
Mo	10.01036148	10.21450151	10.32712994

Mo	12.12558668	7.88253767	10.34537960
Mo	10.22440152	6.14750252	9.86339695
Mo	9.70531620	11.82713479	12.46930147
Mo	11.69646009	9.78287257	12.44761066
Mo	9.88854816	7.87293273	11.96546522
Mo	11.87785523	5.79138306	12.04132389

High hydrogen coverage

43

Lattice="17.56453244467384 0.0 0.0 0.0 15.211331302683535 0.0 0.0 0.0 37.17069034333515" Properties=species:S:1:pos:R:3 pbc="T T T"

C	9.60952017	3.24083303	27.65791087
C	7.25499771	6.91788757	27.04309257
C	5.94498627	7.70393486	24.60457576
C	8.10384784	4.28845907	25.32884900
C	7.17150373	10.39916846	25.22485971
C	8.65269782	6.90791012	23.73561954
C	10.39594987	6.39900738	27.46905008
C	11.09598015	3.58420833	24.78754712
C	13.18134630	5.30403145	26.38036235
C	11.65813376	6.35489732	23.87744201
C	10.86389155	8.97101469	25.64219918
C	9.31538201	9.69225609	23.21486706
Mo	6.33963790	8.66849191	26.19625103
Mo	8.61066543	5.17620156	27.13689353
Mo	7.22556906	6.14364267	25.02174282
Mo	9.45188187	2.91612662	25.63343997
Mo	7.62821778	8.66420761	23.83061321
Mo	9.09647272	7.75919599	26.07196681
Mo	9.89315722	5.45464602	24.57298459
Mo	11.24381402	4.51020343	26.84018367
Mo	9.39094830	10.38799325	24.98937905
Mo	10.36949027	8.04048180	23.70950038
Mo	11.79962473	7.01113028	25.84876212

Mo	12.61048869	4.74824998	24.46503182
H	5.22352725	9.90122982	26.69678475
H	4.84410333	8.11704573	26.85592149
H	7.58350564	4.45795528	28.35254524
H	10.56581801	3.53467048	28.30822401
H	11.65366713	8.77791164	26.53926887
H	7.67908796	10.82557181	26.15736054
H	6.16478048	7.20973473	27.44137660
H	10.56672927	6.81090197	28.47323712
H	14.09028424	4.87292687	26.83951801
H	9.12582634	2.57752684	28.39026440
H	11.19377918	10.11997163	25.58041339
H	6.58409976	11.22861475	24.80610093
H	9.23918128	12.10339585	25.27871171
H	10.71003376	11.36951575	24.49195443
H	9.20574539	8.62404800	27.55786330
H	13.34486769	6.42237184	26.78829775
H	13.23491944	7.88025107	25.36805633
H	7.58041306	6.47765693	28.09489945
H	11.97077013	4.63904315	28.41979418

Appendix E

Supporting information to "Size and Stoichiometry Effects on the Reactivity of MoC_y Nanoparticles Toward Ethylene"

Size and Stoichiometry Effects on the Reactivity of MoC_y Nanoparticles Towards Ethylene

Carlos Jimenez-Orozco,*[a] Marc Figueras,[b] Elizabeth Florez,[a] Francesc Viñes,[b] José A. Rodriguez,[c] Francesc Illas*[b]

[a] *Universidad de Medellín, Facultad de Ciencias Básicas, Grupo de Materiales con Impacto (Mat&mpac), Carrera 87 No 30-65, Medellín, Colombia*

[b] *Universitat de Barcelona, Departament de Ciència de Materials i Química Física & Institut de Química Teòrica i Computacional (IQTCUB), c/ Martí i Franquès 1-11, 08028 Barcelona, Spain.*

[c] *Brookhaven National Laboratory, Chemistry Department, Upton, New York 11973, United States of America*

* Corresponding authors: cjimenez@udem.edu.co, francesc.illas@ub.edu

Contents:

Table S1. Total energy difference, ΔE, between the lowest and second lowest structures for each explored stoichiometry. All values are given in eV.

Cluster	ΔE
Mo_4C_6	0.31
Mo_5C_6	0.03
Mo_6C_4	0.05
Mo_6C_5	0.16
Mo_6C_6	0.30
$Mo_{10}C_{12}$	0.62
$Mo_{12}C_6$	0.22
$Mo_{12}C_8$	0.27
$Mo_{12}C_{10}$	0.28
$Mo_{12}C_{12}$	0.05

Table S2. Formation energies, E_{form}, for each stoichiometric NP —*i.e.* with a Mo/C ratio of 1—, per MoC units N; taking as atomic references bulk Mo and graphite. Band gap energy, E_{gap}, band energies for the valence and conduction bands, B_{val} and B_{con}, respectively, are displayed. All values are given in eV.

NP	E_{form}	(E_{form} / N)	B_{val}	B_{con}	E_{gap}
Mo_6C_6	22.26	3.71	-0.03	0.11	0.14
$Mo_{12}C_{12}$	34.07	2.84	-0.1	0.05	0.15
$Mo_{24}C_{24}$	51.69	2.15	-0.05	0.10	0.15
$Mo_{32}C_{32}$ (Wulff)	59.03	1.84	-0.11	0.04	0.15

Table S3. Band gap energy, E_{gap}, for the non-stoichiometric MoC_y NPs. All values are given in eV. The band energies for the valence and conduction bands, B_{val} and B_{con}, respectively, are displayed.

NP	B_{val}	B_{cond}	E_{gap}	Mo/C
Mo_4C_6	-0.07	0.08	0.15	0.67
Mo_5C_6	-0.13	0.01	0.14	0.83
Mo_6C_4	-0.12	0.02	0.14	1.50
Mo_6C_5	-0.04	0.10	0.14	1.20
Mo_8C_{12} (MetCar)	-0.02	0.13	0.15	0.67
$Mo_{10}C_{12}$	-0.04	0.10	0.14	0.83
$Mo_{12}C_6$	-0.10	0.04	0.14	2.00
$Mo_{12}C_8$	-0.14	0.00	0.14	1.50
$Mo_{12}C_{10}$	-0.04	0.11	0.15	1.20
$Mo_{14}C_{13}$ (Nanocube)	-0.12	0.03	0.15	1.08

The E_{gap} was also calculated using the HSE06 funcional for Mo_6C_6 and the MetCar, which are representative systems of stoichiometric and non-stoichiometric NPs, respectively. In both cases, the E_{gap} values were 0.158 eV, being ~0.01 eV different from those obtained using the PBE functional; 0.145 eV and 0.147 eV, respectively.

Table S4. Adsorption of C_2H_4 on MoCy NPS. Details for the most stable structure in every case is shown, as in Table 1 of the manuscript.

Nanoparticle	Inputs	Different outputs	Site	E_{ads} / eV	%ZPE contribution	*d*(CC) / Å	CC bond elongation / Å [a]
Stoichiometric NPs							
Mo_6C_6	20	8	π-M	-1.76	4.11	1.43	0.10
$Mo_{12}C_{12}$	65	19	π-M	-1.65	3.79	1.42	0.09
$Mo_{24}C_{24}$	5	5	π-M	-1.84	3.53	1.42	0.09
$Mo_{32}C_{32}$ (Wulff)	3	3	di-σ-CM	-1.54	4.28	1.55	0.22
Non-stoichiometric NPs							
Mo_4C_6	11	7	π-M	-1.98	1.11	1.44	0.11
Mo_5C_6	15	8	di-σ-CC	-1.97	2.05	1.56	0.23
Mo_6C_4	18	9	σ-M, μ-M	-2.88	3.51	1.51	0.18
Mo_6C_5	12	7	σ-M, μ-M	-1.99	4.53	1.51	0.18
Mo_8C_{12} (MetCar)	19	12	π-M	-1.80	3.71	1.43	0.10
$Mo_{10}C_{12}$	52	20	di-σ-CM	-1.78	4.33	1.58	0.25
$Mo_{12}C_6$	89	42	σ-M, μ-M	-2.08	4.55	1.48	0.15
$Mo_{12}C_8$	113	45	σ-M, μ-M	-1.86	5.01	1.49	0.16
$Mo_{12}C_{10}$	51	25	σ-M, μ-M	-1.76	5.18	1.50	0.17
$Mo_{14}C_{13}$ (Nanocube)	17	11	π-M	-1.85	4.48	1.44	0.11
Total different geometries	490	221	--	--	--	--	--
δ-MoC(001) (surface) [b]	19	14	π-M	-0.44eV	5.1	1.36	0.03
β-Mo_2C(100)-C (surface) [b]	18	11	C C-top, C Mo-h1	-1.49	5.3	1.51	0.18
β-Mo_2C(100)-Mo (surface) [b]	16	7	Mo-top, C-h2	-2.50	6.6	1.48	0.15

[a] Elongation relative to gas phase (1.33 Å for the C=C double bond).

[b] The references are the same shown in Table 1 of the manuscript.

Table S5. Adsorption energies for the two most stable structures of ethylene on every carbide nanoparticle; ΔE is the difference between these values. Adsorption modes are specified.

Nanoparticle	**Most stable**	**2nd most stable**	**Most stable**	**2nd most stable**	**Delta**
	Binding mode		**E_{ads} (eV)**		**ΔE (eV)**
Mo_5C_6	di-σ-CC	π-M	-1.97	-1.83	0.14
Mo_6C_4	σ-M, μ-M	π-M	-2.88	-1.95	0.93
Mo_6C_5	σ-M, μ-M	π-M	-1.99	-1.75	0.24
Mo_6C_6	π-M	di-σ-CM	-1.76	-1.32	0.44
Mo_8C_{12} (metcar)	π-M (vertex)	π-M (vertex, rot)	-1.80	-1.73	0.07 [a]
$Mo_{10}C_{12}$	di-σ-CM	π-C, α-C	-1.78	-1.52	0.26
$Mo_{12}C_6$	σ-M, μ-M	di-σ-MM	-2.08	-1.81	0.27
$Mo_{12}C_8$	σ-M, μ-M	di-σ-CM	-1.77	-1.67	0.10
$Mo_{12}C_{10}$	σ-M, μ-M	π-M	-1.76	-1.59	0.17
$Mo_{12}C_{12}$	π-M (vertex bottom)	π-M (vertex side)	-1.65	-1.44	0.21
$Mo_{14}C_{13}$ (nanocube)	π-M (vertex)	π-M (central)	-1.85	-1.01	0.84
$Mo_{24}C_{24}$	π-M (vertex)	π-M (facet)	-1.84	-1.17	0.67
$Mo_{32}C_{32}$ (Wulff)	di-σ-CM	π-M (vertex)	-1.54	-1.40	0.14

[a] The E_{ads} for the 3rd most stable structure is -1.62 eV in a π-M (vertex, rot) binding mode. While the E_{ads} for the 4th most stable structure is -1.43 eV in a di-σ-CM mode.

Table S6. Energy contributions to the C_2H_4 adsorption energy, E_{ads}, on the different studied MoC_y NPs, including C_2H_4 distortion, E_{dis}, NP deformation, E_{def}, and attachment energy, E_{att}. All values are given in eV. The δ-MoC(001) surface is included for comparison.

NP	E_{ads}	E_{def}	E_{dis}	E_{att}
Mo_4C_6	-1.98	0.19	0.52	-2.69
Mo_5C_6	-1.97	0.84	3.68	-6.49
Mo_6C_4	-2.88	0.07	1.50	-4.45
Mo_6C_5	-1.99	0.16	3.64	-5.79
Mo_6C_6	-1.76	0.31	0.38	-2.45
Mo_8C_{12} (Metcar)	-1.80	0.13	0.40	-2.33
$Mo_{10}C_{12}$	-1.78	0.29	2.25	-4.32
$Mo_{12}C_6$	-2.08	0.22	1.15	-3.45
$Mo_{12}C_8$	-1.86	0.32	1.25	-3.43
$Mo_{12}C_{10}$	-1.76	0.26	1.33	-3.35
$Mo_{12}C_{12}$	-1.65	0.24	0.30	-2.19
$Mo_{14}C_{13}$ (Nanocube)	-1.85	0.21	0.52	-2.58
$Mo_{24}C_{24}$	-1.84	0.00	0.31	-2.15
$Mo_{32}C_{32}$ (Wulff) [a]	-1.54	0.53	2.17	-4.24
Surface	-0.44	0.27	-0.03	-0.68

[a] For the second most stable structure (adsorption *via* π-M mode) the E_{ads}, E_{def}, E_{dis}, and E_{att} are -1.40, 0.13, 0.24, and -1.77 eV, respectively.

Table S7. Cohesive energies, E_{coh}, in eV, per N, which is the number of MoC units in the studied stoichiometric MoC NPs.

NP	E_{coh} / eV	$N^{-1/3}$
Mo_6C_6	-11.07	0.55
$Mo_{12}C_{12}$	-11.95	0.44
$Mo_{24}C_{24}$	-12.63	0.35
$Mo_{32}C_{32}$	-12.94	0.31

Figure S1. Formation energies per MoC unit for each of the studied stoichiometric MoC NPs as a function of the MoC units, *N*.

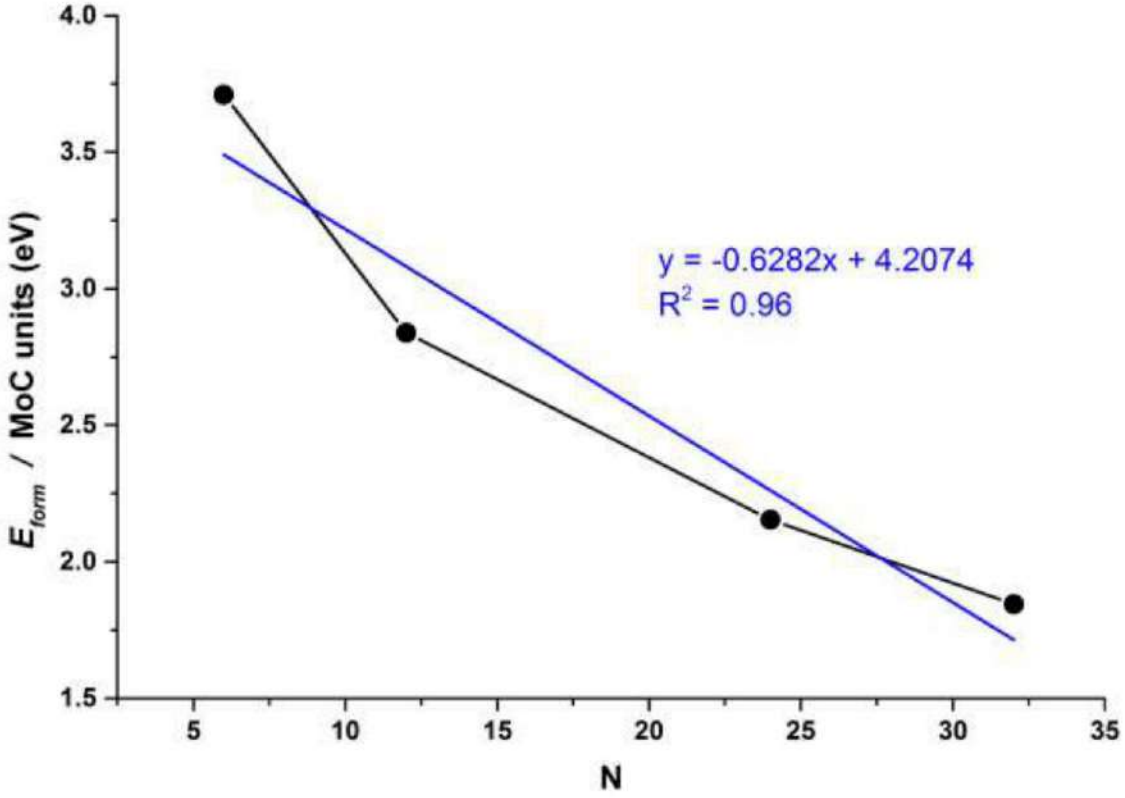

Figure S2. CDD (top panels) and ELF (bottom panels) for the C_2H_4 binding on $Mo_{32}C_{32}$ NP *via* π-M mode (left) and di-σ-CM mode (right). For the CDD, red and green colors represent isovalue regions —0.05 $e/Å^3$— where charge was lost or earned, respectively.

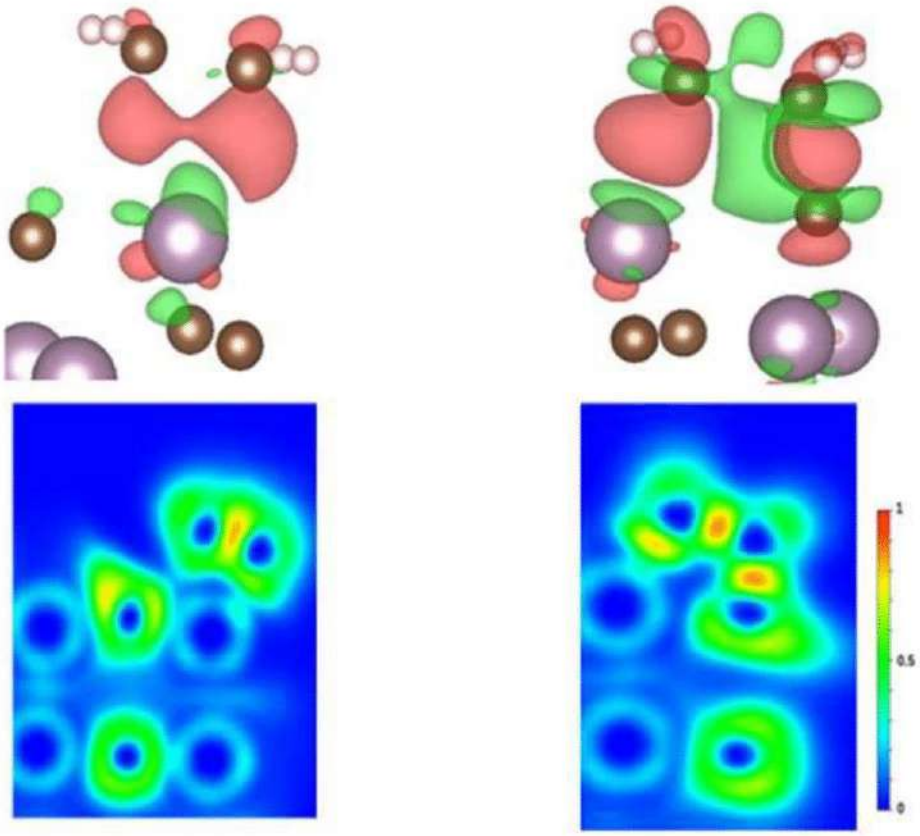

Figure S3. Geometry changes in the Mo_5C_6 NP upon C_2H_4 adsorption. Atoms are numbered for clarity. The distance between atoms is represented by *d*, while angles represented by α.

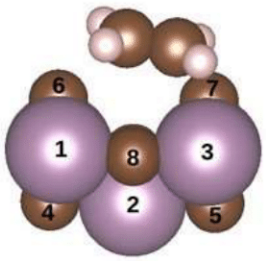

a) Before adsorption

α(816) = 100.3 °
α(123) = 89.8 °
α(687) = 83.0 °
d(67) = 3.90 Å
d(16) = 1.88 Å

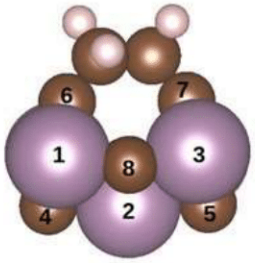

b) After adsorption

α(816) = 95.2 °
α(123) = 88.1 °
α(687) = 64.8 °
d(67) = 3.18 Å
d(16) = 1.99 Å

Figure S4 Geometry changes in the Mo_4C_6 NP upon C_2H_4 adsorption. Atoms are numbered for clarity. Particularly, the C_X atom was moved, forming a C_XC_2 bond.

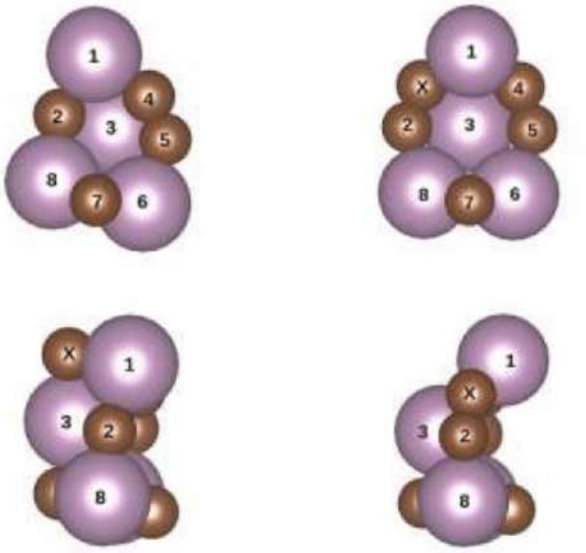

a) Before adsorption b) After adsorption

Figure S5. NP deformation energy, E_{def}, and C_2H_4 distortion energy, E_{dis}, on non-stoichiometric NPs sorted relative to the amount of Mo in the explored NPs.

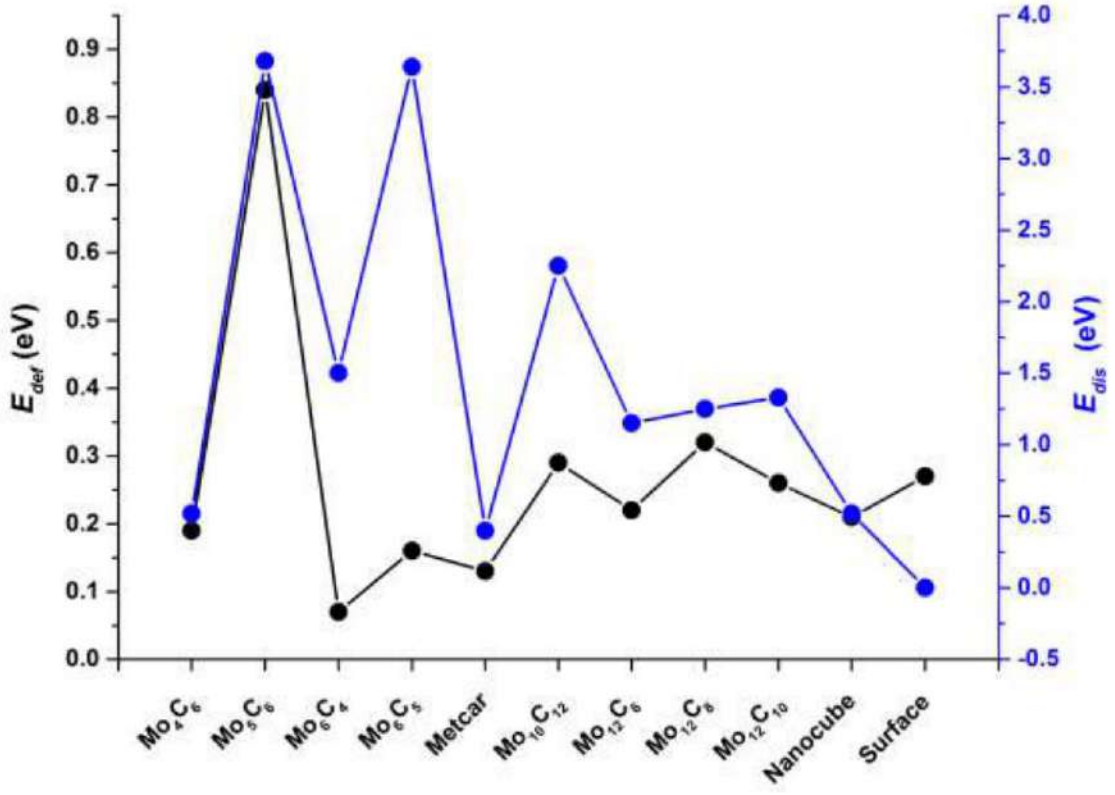

Figure S6. Effect of Mo/C ratio of $Mo_{12}C_x$ NPs in *Top*: adsorption energy, E_{ads}, and size, seized by $N^{-1/3}$; *middle:* NP deformation energy, E_{def}, and C_2H_4 distortion energy, E_{dis}; *bottom:* Bader charge in adsorbed C_2H_4, and attachment energy, E_{att}.

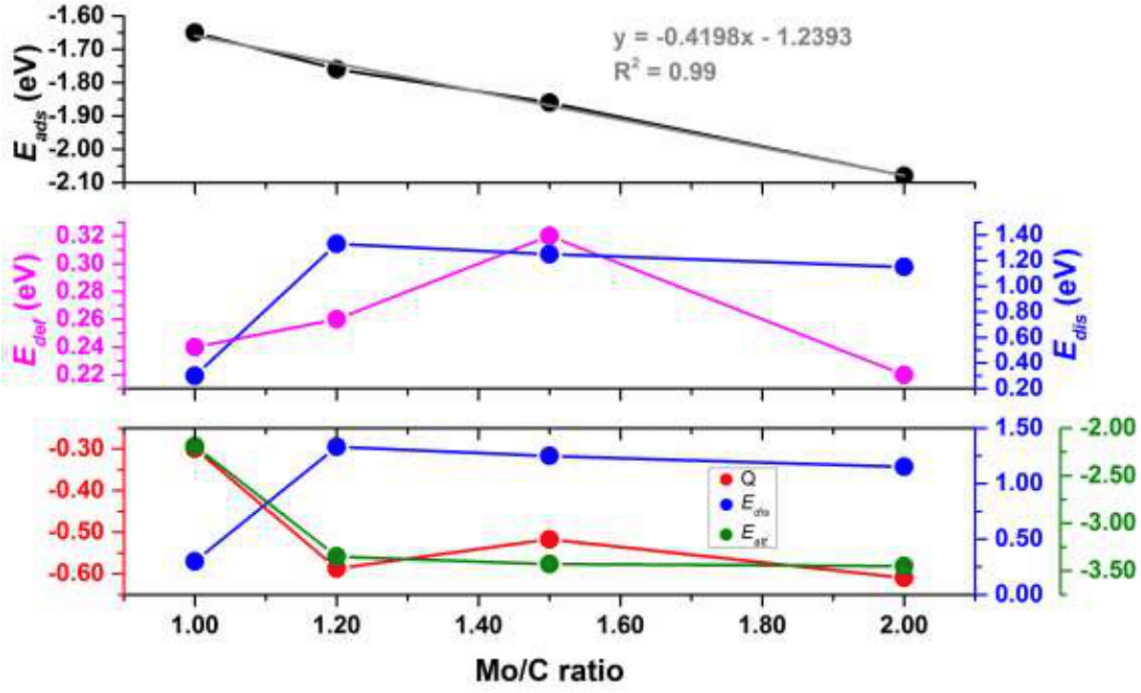

Figure S7. CDD (top panels) and ELF (bottom panels) for the C_2H_4 binding through di-σ-CC on Mo_5C_6 NP (left panels) and through di-σ-CM on $Mo_{10}C_{12}$ NP (right panels). Color coding as in Figure S7.

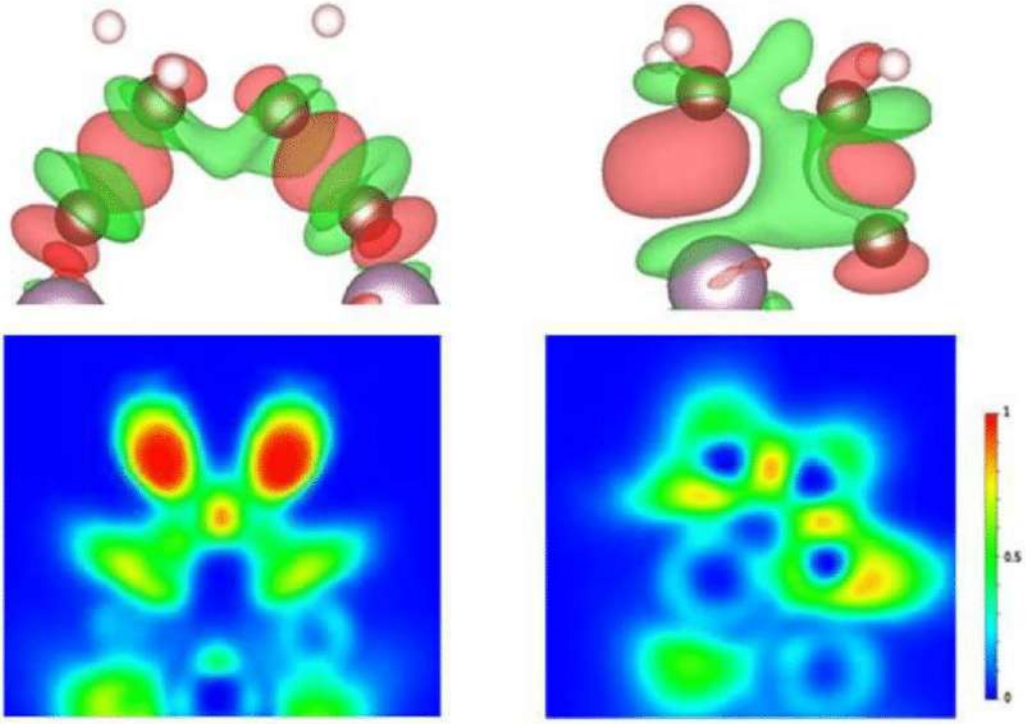

Figure S8. ELF plots for C_2H_4 *via* π-M mode on the $Mo_{12}C_{12}$ NP (left) and on the δ-MoC(001) surface (right).

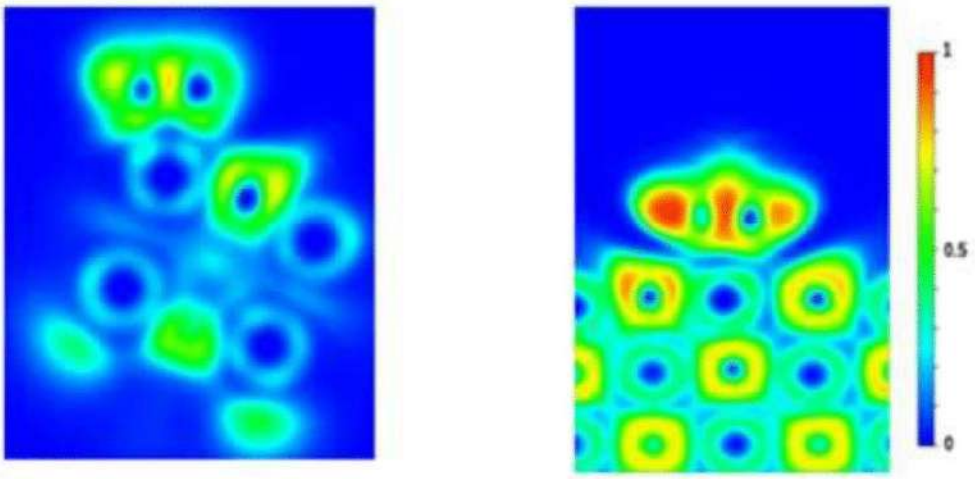

Geometry coordinates of bare NPs and C_2H_4 adsorbed on them

The coordinates are shown in four subsections:

- Bare nanoparticles – stoichiometric
- Bare nanoparticles – non-stoichiometric
- C_2H_4 adsorption on NPs – stoichiometric
- C_2H_4 adsorption on NPs – non-stoichiometric

Bare nanoparticles – stoichiometric

Mo_6C_6

C Mo
6 6

0.4742657457187457 0.4496823074066315 0.3818976031066794
0.6053657186150783 0.4775499828183796 0.4255829796172116
0.5067571153093141 0.4111367694342336 0.5363694126949003
0.4932428846906859 0.5888622305657618 0.4636305873050997
0.3946342813849217 0.5224500171816203 0.5744170203827884
0.5257342542812542 0.5503176925933684 0.6181023968933207
0.5321998251038716 0.5340806964950889 0.3816554730740616
0.5425985606014440 0.3975843486992125 0.4375255168043919
0.4405367873337955 0.4873521649837379 0.4801888803694792
0.5594632126662045 0.5126478350162621 0.5198111196305210
0.4678001748961282 0.4659193035049110 0.6183435269259339
0.4574014393985560 0.6024156513007874 0.5624744831956081

$Mo_{12}C_{12}$

C Mo
12 12

0.4720774235430554 0.3537594721947031 0.3676166547061968
0.4524029237567291 0.5721012292585144 0.3888473113448185
0.5556957887345888 0.6728308261736089 0.4177457221736276
0.5794087218370123 0.4573702426273982 0.3856697809652374
0.4281031503785115 0.6757717986829235 0.5132123175227576
0.5820352171088956 0.5522474566085265 0.5160260496326430
0.4183297918267570 0.4476749784885641 0.4842790890852697
0.5721906337102780 0.3241148110900980 0.4871255794592102
0.4445881044979814 0.3270859924064311 0.5825381240131975
0.5479327113502990 0.4277929841466346 0.6114758503015736
0.4209897192696914 0.5425404628071675 0.6146744714777270
0.5283221467682324 0.6461231468685682 0.6326859263858253
0.4561807995141436 0.6723139056151979 0.4123557288098141
0.4659670175819883 0.4611399589862017 0.3895920831181812
0.5615904881635672 0.5619226520787137 0.4131564979913875
0.5702679928614600 0.3549580805552210 0.3858333827497802
0.5448502987235813 0.6526378021729329 0.5250840569790327
0.4446963564749211 0.5612405744906113 0.5010043011033076
0.5556360473325697 0.4386636772480301 0.4993124668386812
0.4554728893991609 0.3472642681281997 0.4751941736579468
0.4301231110601904 0.6449556442435025 0.6145074259257512
0.5344143737542737 0.5387638688453578 0.6107217083530472
0.4387469861296367 0.4379993421108637 0.5871594373802793
0.5441003062224823 0.3275818241720501 0.5879728600246850

$Mo_{24}C_{24}$

C	Mo		
24	24		
0.4663724361960696	0.5010279140507450	0.6468219782538901
0.6822469470838356	0.5010279140507450	0.6466636434351892
0.3644324588557654	0.3986682671921494	0.6358447193997634
0.3644324588557654	0.6033875604093385	0.6358447193997634
0.5731384443391185	0.3920693869838939	0.6442116388528790
0.5731384443391185	0.6099864406175943	0.6442116388528790
0.3452737178876288	0.5010279140507450	0.5347976839016760
0.5685923401340388	0.5010279140507450	0.5260550497670453
0.4655193202509921	0.3823306942046802	0.5337940751682591
0.4655193202509921	0.6197251333968082	0.5337940751682591
0.6816258857973603	0.3910660799551910	0.5348325509778844
0.6816258857973603	0.6109897476462972	0.5348325509778844
0.4660447107564544	0.5010279140507450	0.4226139380341827
0.6850904077475477	0.5010279140507450	0.4294051236805745
0.3555287857621656	0.3916194618405674	0.4266594077939481
0.3555287857621656	0.6104363657609205	0.4266594077939481
0.5717891467021212	0.3865247676724696	0.4267019693133127
0.5717891467021212	0.6155310599290194	0.4267019693133127
0.3580465299145674	0.5010279140507450	0.3200959600643256
0.5724375535543135	0.5010279140507450	0.3002749955452457
0.4641960259080268	0.3913274359578477	0.3174617139866028
0.4641960259080268	0.6107283916436406	0.3174617139866028
0.6743981617135462	0.3981281698120275	0.3271972458530992
0.6743981617135462	0.6039276577894607	0.3271972458530992
0.4691248681727413	0.3994536628946535	0.6319774147528414
0.4691248681727413	0.6026021647068345	0.6319774147528414
0.6705304739146590	0.4037570589768281	0.6324133275911172
0.6705304739146590	0.5982987686246601	0.6324133275911172
0.3656594866982092	0.5010279140507450	0.6346380116810965
0.5722269561901152	0.5010279140507450	0.6318537860368880
0.4601968947643985	0.5010279140507450	0.5352178051931819
0.6706499081501952	0.5010279140507450	0.5328505337433282
0.3663835807947160	0.4008989647748166	0.5318313142910814
0.3663835807947160	0.6011568628266712	0.5318313142910814
0.5703970993613813	0.3984486376565514	0.5339180241138647
0.5703970993613813	0.6036071899449367	0.5339180241138647
0.4664809656881920	0.3977101187907905	0.4303100793733572
0.4664809656881920	0.6043457088106975	0.4303100793733572
0.6705638074474638	0.4001251488536446	0.4298976612601065
0.6705638074474638	0.6019306787478437	0.4298976612601065
0.3638890322516695	0.5010279140507450	0.4298022442993970
0.5726839207951435	0.5010279140507450	0.4209091615059004
0.4695946311820594	0.5010279140507450	0.3218881544549246
0.6705689172169566	0.5010279140507450	0.3266969339672762
0.3674792052175038	0.4022387807814999	0.3299812974951310
0.3674792052175038	0.5998170468199882	0.3299812974951310
0.5695974299370835	0.4018957782033397	0.3265978640444649

0.5695974299370835 0.6001600493981485 0.3265978640444649

$Mo_{32}C_{32}$ (Wulff)

C Mo

32 32

0.4434599344242056 0.5604298554223793 0.6661624695520699
0.6603217516785518 0.5590568802975912 0.6608478191019245
0.3343870757474314 0.4545396998331121 0.6622351011556382
0.3421425215179706 0.6613265022905743 0.6517973972203577
0.5512330621425831 0.4530824359265215 0.6669566918796417
0.5489382078362632 0.6698807907619652 0.6596963754361379
0.3286180400643378 0.5591907401461038 0.5516936647373943
0.5514938659636639 0.5604754524507215 0.5521815112406759
0.4426598769777168 0.4510932472353430 0.5533468625564587
0.4429901145815141 0.6738661149834767 0.5503388891932548
0.6654245235921822 0.4521524950151406 0.5525490779220739
0.6598291970440794 0.6689429364745328 0.5485473949938656
0.4426450024882960 0.5587101268073025 0.4436225907448588
0.6651964337714259 0.5585781041298113 0.4439428322827227
0.3286789775651734 0.4507469350030292 0.4454256689269317
0.3334470822667687 0.6676370856448710 0.4447584108530319
0.5514704077067639 0.4502306317550485 0.4442684415373770
0.5502607911764144 0.6730126327561666 0.4428192700014129
0.3336117556215173 0.5554584604092957 0.3349102878972551
0.5504103467267499 0.5573536189172097 0.3293384653594939
0.4432798120005287 0.4498082577546249 0.3305474500230642
0.4443831787662172 0.6667121899799371 0.3335721033875034
0.6601168554626996 0.4518379906966090 0.3357006874849687
0.6513791382720253 0.6587479036993353 0.3418434894220538
0.6526047685236331 0.3520809458896917 0.6547422328622029
0.6606464520516733 0.3417258995496347 0.4478706364091211
0.5513776766844982 0.3375989271334321 0.5538842202361343
0.5493078999597693 0.3406131308290424 0.3369900732995444
0.4456791066696253 0.3434923569783542 0.6633570676225472
0.4437317518850432 0.3361480615758154 0.4465026249967030
0.3345303895206801 0.3423809139068370 0.5522991149788966
0.3424402062697236 0.3485966203115164 0.3453504438411198
0.4452893050946488 0.4545407632223141 0.6551133013195680
0.4460917962909257 0.6601764091473968 0.6503760358867945
0.6510785803439731 0.4561444209006153 0.6523980083411185
0.6463680208428324 0.6562705270352397 0.6461176474374277
0.3435465877193732 0.5572576962735323 0.6515811071327717
0.5492598430290205 0.5588771321829292 0.6539803717094929
0.4402994939863084 0.5622929480659073 0.5544294277373950
0.6532559623212032 0.5580180532187875 0.5497505277500692
0.3408400539844986 0.4534185976101287 0.5511189546039529
0.3431150220568817 0.6590562648488288 0.5475618310622777

0.5541241457943099 0.4489340787043035 0.5557168211557257
0.5488137588615862 0.6621939425154787 0.5487140776343260
0.4405649952025866 0.4480166719298455 0.4424437879873076
0.4445286351523869 0.6606649525582970 0.4446963694540952
0.6532766261425818 0.4528156548009613 0.4466458616315773
0.6501865457206732 0.6584585799227964 0.4457775520533242
0.3407204625942188 0.5564789375624858 0.4459270286445510
0.5534234470350811 0.5613312634043203 0.4410285490824913
0.4446692138190095 0.5556296117603500 0.3417029209452010
0.6503007490746825 0.5546943801813398 0.3441002572073590
0.3434060842273472 0.4527904761817907 0.3454911123283302
0.3470018100249413 0.6530430726090977 0.3474716926651186
0.5490167639382236 0.4516957157839289 0.3424275113337956
0.5471547099140753 0.6573617324970416 0.3430635488101486
0.6512224192269733 0.3522058817057196 0.5505393969985949
0.6467215470332042 0.3545175195962255 0.3503707157463107
0.5483980615879130 0.3530634956064986 0.6535852834610058
0.5494413803835920 0.3484547372174644 0.4478536771055052
0.4454443171282711 0.3492958122899565 0.5521013007025869
0.4464233359701332 0.3500763835640299 0.3464597316915833
0.3482552433915973 0.3569808676667238 0.6495736294322717
0.3438147881473610 0.3509291413705171 0.4493211472915632

Bare nanoparticles – non-stoichiometric

Mo_4C_6

C Mo
6 4

0.4926980893103352 0.5801285194268621 0.5456145746782193
0.5262563219185940 0.4449467198762009 0.4127868602489291
0.5098209771806878 0.4348252767259186 0.6234417973360740
0.5203460558897535 0.5917722697097046 0.4819335476415897
0.4998589546022337 0.4014812722794411 0.4614596247171501
0.3833791558807906 0.4555236844418903 0.5688066977769045
0.5626326950329833 0.5412406324947674 0.4021209699180901
0.4520268111507634 0.4995802710308679 0.4811350073166224
0.4552410312303036 0.3859614405570356 0.5569124920694979
0.4501405372206166 0.5135048834000817 0.6170093463605169

Mo_5C_6

C Mo
6 5

0.4767884106998963 0.4495078921134947 0.3807358224963053
0.6022773986760654 0.4801046040380541 0.4321288696387029
0.5021884767614893 0.4170350067876214 0.5321980016828363
0.4896501577936903 0.5812309503732394 0.4650842118169578
0.3957792326057827 0.5234011378679639 0.5768105714133540
0.5282311942390052 0.5476163797847136 0.6113510863775176
0.5337906673354382 0.5338991918298248 0.3852244002305341
0.5439769719851384 0.4005743942170952 0.4397376034069325
0.4360741899784202 0.4864159141447502 0.4787026645587815
0.4709876006786047 0.4671211101223349 0.6163591973611275
0.4608184393590307 0.6004590105426999 0.5618644512440483

Mo_6C_4

C Mo
4 6

0.4748262281643924 0.4581166305866459 0.3796472098662593
0.6027555404606234 0.4850332443262508 0.4220317613605004
0.3960455398227434 0.5318092297556397 0.5710742272139712
0.5240480319587968 0.5584234962967989 0.6134438825031041
0.5202255943130597 0.5443200703449902 0.4107208974473707
0.5514873336139818 0.4029194215872184 0.4061473991952447
0.4484509676239687 0.4581141333132248 0.4949043586755917
0.5558357620759636 0.4804689007991496 0.5304684401174178
0.4561814823498811 0.4917619120190077 0.6374515433161621
0.4699662538945945 0.5913880372125242 0.5331574514159412

Mo_6C_5

C Mo
5 6

0.4762681742370063 0.4510370096266172 0.3845149100142109
0.5000956662448743 0.4099268703387935 0.5355246542072152
0.4864657081686019 0.5883097843282883 0.4626755417079522
0.3954554204853622 0.5233308893564512 0.5767088927407400
0.5283052638322090 0.5483103653327177 0.6130272969201371
0.5359248077761976 0.5355271184448114 0.3886155361242061
0.5461274442318143 0.4020398711206354 0.4431356368710624
0.4366910028303082 0.4864398578766682 0.4786297164924420
0.5631448513523409 0.5100171757910275 0.5127388583759185
0.4683357595469531 0.4651706997381524 0.6174598072494959
0.4578620169276348 0.6022523403020443 0.5614733971474095

Mo_8C_{12} (MetCar)

C Mo
12 8

0.5876408053667256 0.5568793183278536 0.6078688522882081
0.6184892801099607 0.4974514491563299 0.6215204166499435
0.4635777748847257 0.3751101638323388 0.6289411123629342
0.5333599835100781 0.3722393753794500 0.6344997934493752
0.3921085835636817 0.5068298670620305 0.6036407639225001
0.4294413226857339 0.5634503596514002 0.5953401175002926
0.3959517175097229 0.3921099640898163 0.4938983805764433
0.4349996627102826 0.3992297489585092 0.4382721253235060
0.5193288316074733 0.5744221881571442 0.4732603742961572
0.5210104531060404 0.5238272880323370 0.4248282924550534
0.6223803040800914 0.3826800623718046 0.5117704876094338
0.5932106495928908 0.3926305320691871 0.4507888841736515
0.4444944253485328 0.4941915658304639 0.5038089163434525
0.5814964719700645 0.4885017232828531 0.5146269003350773
0.5133804220530496 0.6043699840421929 0.5637487388480948
0.5072699255465002 0.3818001602892181 0.5240342209919067
0.6211390503247626 0.3997384002349008 0.6088510940159760
0.3834310233878562 0.4095791749730153 0.5900917630634661
0.5039087927528543 0.4811648623933591 0.6190691458792241
0.5192204410389789 0.4319337488158174 0.3988496416153139

$Mo_{10}C_{12}$

C Mo
12 10

0.4755291773980019	0.3566224953168060	0.3593651561939879
0.4578683050203054	0.5667439949451563	0.3881964842767829
0.5544474561050876	0.6725775291340312	0.4097982738865085
0.5710323990156567	0.4613948182144298	0.3893706022979515
0.4326121489522663	0.6646951345994410	0.5124064580351302
0.5760134476443284	0.5506596329785509	0.5163407023965760
0.4241266020827013	0.4491024804754886	0.4839268911875862
0.5675258929014646	0.3350441049708195	0.4878470350165287
0.4458190526226176	0.3272047314591333	0.5906394475220154
0.5423832850473289	0.4330707212305214	0.6120604227406616
0.4291944607338962	0.5383971811663812	0.6109294759676658
0.5247149708893133	0.6432006050448820	0.6408052157589310
0.4587198303138891	0.6682648809885166	0.4121532904815908
0.4604428962602967	0.4572871375459826	0.3883816766253574
0.5650078226836257	0.5674210212190687	0.4158250705658375
0.5674455600974113	0.3571757558574973	0.3865740468306527
0.4509617734884515	0.5545270551030512	0.5007658360075382
0.5492303632566333	0.4452283530893553	0.4994972906688773
0.4327889789755872	0.6426235571143692	0.6136959092062142
0.5397841901673175	0.5425008204115187	0.6118834091525756
0.4352179925378366	0.4323553941015135	0.5844843717208548
0.5415321817997309	0.3315432434477330	0.5881488805176360

$Mo_{12}C_{6}$

C Mo
6 12

0.3785131353812542	0.4579095786474384	0.3985811428710538
0.4787394522924581	0.5845678425419251	0.3614180884116400
0.5227792746894222	0.4296634037412259	0.3692558616943665
0.5834850748740542	0.6120125945263766	0.4808935995141833
0.4438094289619137	0.6581597053764506	0.4916943831236057
0.4060511300475547	0.3892065055121601	0.5492074691407495
0.4667154336627619	0.4889238607803408	0.5546908734517321
0.5834001255332064	0.5133010465580170	0.6321573629299180
0.4112761492321958	0.5611540685679811	0.4545130192098262
0.3415530449530579	0.4456272422931311	0.4920432746844966
0.4504768174480929	0.4885452344002977	0.3317659163705270
0.5380376658401668	0.5163290417052047	0.4394355522754425
0.5839596534758758	0.4249586160249200	0.5353917377076044
0.6472852942183936	0.5528084869430672	0.5421290679070613
0.5101195953167683	0.6117324971155862	0.5589599787759298
0.5145036757088600	0.6604150512860526	0.4174748723722054
0.4648617008063903	0.3904662143851561	0.4493772887626001
0.4923136843174222	0.3399594609802719	0.5674691430389571

$Mo_{12}C_8$

C Mo
8 12

0.5241301250278312 0.4178625668815670 0.6370922155321139
0.3773645208697474 0.4562292252895404 0.4003675970890868
0.4753860529357254 0.5828113212625752 0.3618261454297098
0.5241475146987256 0.4375073260015014 0.3631504619078996
0.6265179800126646 0.5388016538661873 0.5965864952783164
0.5981388104823964 0.6257740059752024 0.4629197871006667
0.4513765717917337 0.6445535617091380 0.5000300254293393
0.3975234653323625 0.3789036756233912 0.5412663780637317
0.4454138456818129 0.4749361369232687 0.5795622661183586
0.5518645642478859 0.5154339334281985 0.6643917684758733
0.4221809215722487 0.5470834603842931 0.4604890352164048
0.3342576485478475 0.4440042074746984 0.4920645065382274
0.4457184069743221 0.4889093100213557 0.3298545942797375
0.5567941123302589 0.5232105243382748 0.4223636039554322
0.5759851602016255 0.4520202997495772 0.5426740901313991
0.6645101894221739 0.5592999765389024 0.5027748516143618
0.5306647747036166 0.5860628085677604 0.5495094119297548
0.5099253521495370 0.6603187174187468 0.4211474142631744
0.4698995921154463 0.4111190087827552 0.4554764509937215
0.4896241471252623 0.3429979510479626 0.5720142120554783

$Mo_{12}C_{10}$

C Mo
10 12

0.5282566624420113 0.4186717973291039 0.6375632988553619
0.3536508044297406 0.5190685505902479 0.5403097485858197
0.3722718705321810 0.4581064009212454 0.3981951027690727
0.4766170159883956 0.5843543089690257 0.3597985129379637
0.5225865615237097 0.4403843073591247 0.3610570116797973
0.6242993478419265 0.5411792989072950 0.5996505709463236
0.5992357114660436 0.6233392542984291 0.4643929906854893
0.4546954316846907 0.6487387917446696 0.4978217778080207
0.4001187737814078 0.3751635105936941 0.5418207228639105
0.5476004514852590 0.3523292382798076 0.5038600829694957
0.4446598877549874 0.4756737550673691 0.5794213623960189
0.5506850484841621 0.5149461363072234 0.6655397833552144
0.4196146282474160 0.5507993562873850 0.4593477559587882
0.3326532531043469 0.4349540673675065 0.4903466126402236
0.4420905100276755 0.4911027393623115 0.3300822670083861
0.5552989553949956 0.5244462263445584 0.4207496087293165
0.5806532314864654 0.4513060986878656 0.5390127442739399
0.6643144859036312 0.5560525077460454 0.5067429763905551
0.5288085275279570 0.5850035351274059 0.5485758051216720
0.5135117346640072 0.6607347840753945 0.4197672200795637
0.4701736472538087 0.4131696241813358 0.4528267954409557
0.4892165937412685 0.3402494259076008 0.5822796632148481

$Mo_{14}C_{13}$ (nanocube)

C Mo
13 14

0.5137418617601126	0.6217502342616281	0.3878941668990735
0.6263840945890849	0.5004832907586723	0.3957990427569398
0.3934414567984996	0.5090076980460031	0.3707248203421939
0.5061714837554957	0.3876472941148705	0.3786952338136318
0.3770393904913793	0.3877163396073333	0.4826468403663494
0.6099627517075576	0.3793738373882663	0.5076357993424013
0.6176109614650115	0.6134724898363560	0.5168189316832403
0.4973015496984821	0.5005801357954344	0.4997393447632121
0.3846561165020080	0.6218091810386366	0.4918385444351463
0.4883857325351370	0.6134897077710816	0.6207820366479534
0.6011613979448853	0.4922208880777866	0.6287490812614628
0.3682724104857505	0.5006188862719489	0.6036385863893723
0.4809491711680974	0.3793817053318367	0.6115940552085459
0.6139656777985304	0.6032474089646405	0.4125378478855239
0.4094966918464474	0.6106944583123894	0.3905692271759386
0.5087369265092251	0.5043280198306929	0.3942081891753952
0.6073001813965690	0.3977564635560449	0.4044416974448783
0.4028596072268275	0.4052179285030291	0.3825277049630466
0.5007538297731448	0.6066485337296514	0.5038949016250915
0.4938769896154585	0.3945064308749108	0.4955743541014399
0.3917851714562744	0.5043848227015278	0.4883740621842816
0.6028291818364562	0.4967913261647620	0.5110845637295851
0.5917248984912954	0.5959926678452361	0.6169301918551986
0.3872799644175683	0.6033690383628718	0.5950203084828924
0.4858899773059633	0.4968235477121307	0.6052694624467192
0.5851743212469149	0.3905147081522184	0.6089132332086429
0.3807166232304318	0.3978534833058234	0.5869330349697439

C_2H_4 adsorption on NPs – stoichiometric

Mo_6C_6

C	Mo	H		
8	6	4		
0.4417787585373599			0.4701621347629018	0.3953967754603466
0.5751563470626785			0.4489045787410614	0.4215667869403023
0.4743715216193061			0.4130085531663222	0.5442325143865248
0.5159252063289828			0.5903776623825687	0.4769586055112625
0.4144078967148708			0.5522678825053760	0.5998888549895497
0.5485528263339413			0.5309482073525676	0.6261070205539155
0.4397181497636716			0.4432309990609556	0.7480688143390142
0.4355097533818992			0.3802467560774933	0.7072625203284733
0.5238417077558423			0.5313186243705096	0.3884910195239004
0.4917499980057862			0.3931722031915300	0.4398481591661973
0.4353313721874782			0.5100720855483798	0.4995214978050322
0.5543813565514070			0.4911075001147671	0.5229070857638385
0.4654152131640828			0.4700759528662823	0.6364028341547814
0.4982393546338426			0.6075133021466085	0.5811029659199908
0.4856069154059375			0.4531958912503913	0.7813889473809696
0.3918703213247171			0.4707473219244299	0.7644434330265770
0.4776182171039269			0.3410713249059922	0.7094686125539990
0.3843655310972112			0.3589753307729471	0.6915716578204851

$Mo_{12}C_{12}$

19.0000000000000000 0.0000000000000000 0.0000000000000000
0.0000000000000000 19.0000000000000000 0.0000000000000000
0.0000000000000000 0.0000000000000000 19.0000000000000000

C Mo H
14 12 4

0.4469004325911687	0.3892586166942011	0.3429551899029598
0.4248673975013960	0.5996355861077101	0.4040095736976613
0.5287432643546139	0.7007266055717161	0.4407813746048844
0.5477931794170251	0.4936869341493004	0.3672165678014016
0.4177275996547367	0.6733779010264962	0.5524762180300882
0.5806882912147909	0.5675074007911699	0.5076235837922550
0.4098861089701120	0.4567977540317490	0.4803878997157145
0.5663525856257202	0.3512870851508663	0.4380102213720218
0.4628623609460868	0.3214278955108505	0.5487522625376247
0.5676495641039981	0.4236751016539353	0.5844576491760596
0.4417901676406030	0.5276852002893071	0.6222490609642577
0.5411367854107118	0.6336967216032861	0.6463791456491512
0.5963426751352821	0.3453996409296957	0.2447753800205872
0.6278775889883145	0.3104238757066746	0.3025834803802098
0.4295857067383790	0.6914698096364946	0.4497709827267560
0.4389747116325520	0.4923958278940503	0.3848478681306041
0.5364360339375354	0.5940147261038414	0.4129350337088211
0.5471474649976233	0.3923839631838432	0.3415216811776400
0.5394521670722890	0.6591547176358863	0.5405308546863654
0.4400065300654941	0.5649761366460073	0.5152257089432682
0.5508245953648804	0.4602354309934907	0.4743755704582422
0.4499023417603789	0.3627681670147653	0.4477217934759177
0.4419878776749934	0.6282167220109960	0.6435601810377699
0.5509550090111258	0.5294541097055830	0.6040842305758201
0.4544331436560285	0.4282987429235724	0.5734633599600100
0.5614731432669975	0.3312797692393907	0.5396413970684691
0.5559430403172593	0.3193599347365605	0.2131906196046289
0.6246991611486185	0.3879169783408301	0.2180007759941074
0.6112385145389353	0.2576233221343509	0.3178558162968274
0.6797659941193235	0.3259859307390942	0.3218406477676394

$Mo_{24}C_{24}$

C	Mo	C	H
24	24	2	4

0.4678276837059378	0.5005168732796020	0.6474228729198167
0.6846309432281277	0.4957113707104069	0.6472361612692940
0.3653672904116286	0.3990773072131441	0.6325476934046635
0.3679913808322615	0.6054621943845215	0.6363576640605523
0.5724143520273117	0.3877110593445318	0.6414166961910222
0.5744186372496052	0.6077149094581138	0.6462356003031569
0.3392903220930836	0.5052702574750252	0.5319422434797751
0.5662821022811342	0.5008140774870466	0.5274284850750226
0.4642066626075756	0.3812096611731212	0.5299636278654746
0.4664957516590921	0.6110147413048795	0.5350332303878267
0.6819064256910874	0.3893152378190576	0.5332114893659591
0.6832281092269008	0.6092954263305964	0.5386983516823785
0.4649900242842256	0.4970570148906046	0.4251796041345806
0.6870673501595050	0.5037854989255629	0.4305211782720951
0.3571499820059748	0.3979587931945386	0.4222174027303605
0.3566835880346992	0.6209957718074635	0.4274909190394247
0.5718048342889769	0.3833422075082356	0.4236137514572061
0.5733132936179189	0.6128813860928466	0.4295428399929425
0.3608196120324184	0.5126918114828891	0.3197390719063952
0.5733591558668695	0.5087203249444974	0.3004207076435883
0.4651149949085114	0.3995275445753343	0.3156465457777385
0.4670348752770015	0.6226171181968448	0.3184311954654196
0.6753194068889027	0.4037859014696746	0.3263505183406374
0.6759756995000265	0.6100892100258487	0.3322693713320117
0.4664712781069806	0.3998261078129594	0.6291864547071464
0.4704258666621238	0.6005180432992202	0.6340828947786733
0.6697801233436604	0.3991418106436618	0.6306333521714688
0.6717825840603660	0.5932726974353170	0.6357125923108704
0.3650990034054883	0.5032029584218677	0.6302107708370868
0.5720636304237265	0.4973183732307713	0.6315303118037731
0.4610689510087156	0.5010854657577852	0.5337253839386480
0.6702264209727529	0.4988636677475735	0.5344942864901177
0.3654362864988084	0.4061423858064088	0.5281631595771332
0.3661571592758698	0.6035671959274539	0.5307187464219575
0.5715520639319549	0.3977171381676258	0.5313453535026974
0.5735032538663490	0.6022745464974800	0.5364296288549026
0.4705143229107733	0.3965062326493100	0.4289930695747264
0.4638515088283295	0.6059266111166873	0.4253539237147527
0.6707254365528349	0.4028977908907642	0.4274842849720267
0.6723460836296778	0.6036493737277160	0.4343972052844609
0.3642950167256868	0.5087817476892915	0.4287563686480623
0.5737043734616429	0.5028042607949926	0.4223235733151061
0.4698249475481610	0.5102709104313763	0.3246472682210159
0.6712765272894416	0.5077244915649362	0.3275968389605295
0.3683421853811824	0.4095485812301257	0.3258455856861555
0.3695657944007366	0.6110270892153843	0.3299832848973751
0.5707096807977364	0.4092544031866357	0.3251124423977399

0.5702863205388317 0.6065146210414857 0.3289544597708579
0.2982706989115080 0.3590500211124168 0.2548658344467660
0.3329913680071752 0.3065392684933110 0.2875985719176899
0.3117657309208510 0.3736842491744715 0.2038790586098949
0.2470594112864932 0.3717262736323605 0.2694760136754145
0.3745684057516584 0.2811905085462761 0.2630025571572954
0.3096691029033052 0.2792034934291150 0.3286601100799954

$Mo_{32}C_{32}$ (Wulff)

C Mo H
34 32 4

0.4505271589753300 0.5587794074093707 0.6675909672960240
0.6666830906650794 0.5436773069572141 0.6628382593848157
0.3347002532402609 0.4603583472975593 0.6634017471054445
0.3568957364463358 0.6669013369400716 0.6531671135690279
0.5508926332867046 0.4446190384508872 0.6685109031038530
0.5634868732301552 0.6612091496293910 0.6611491890604623
0.3359808822376155 0.5662368689192877 0.5532999884462219
0.5587372294318984 0.5528105075711061 0.5551618553962717
0.4436736435636277 0.4504142490813379 0.5518833887407429
0.4588073981982096 0.6723129608167977 0.5514682806258308
0.6649699927005794 0.4367901453685032 0.5547768373169406
0.6745966800126307 0.6528569748230726 0.5518670223410944
0.4505352128144298 0.5574332455676083 0.4448593081809709
0.6732284452684700 0.5433754289465267 0.4473815788600184
0.3284007373467994 0.4590587478665297 0.4462299386728164
0.3502778737155746 0.6750498672121499 0.4462571118103330
0.5511711145859699 0.4432756637424076 0.4455140679298649
0.5679651634809600 0.6658832613315602 0.4426978567165908
0.3444152448209738 0.5644680405695834 0.3365325650536831
0.5622507968224216 0.5549284923783973 0.3309130399356082
0.4473576187617640 0.4527562144855261 0.3275145213286548
0.4601579275175249 0.6698371881807565 0.3347357306948285
0.6638816310844351 0.4399445799921683 0.3384604305160600
0.6834243627921580 0.6458238026628927 0.3438864253287674
0.6457855250494017 0.3375157800492973 0.6558414705024498
0.6554164928410907 0.3289792971076543 0.4486519651157929
0.5449801435651106 0.3299620684075744 0.5545665666671431
0.5458705908563053 0.3368629865002152 0.3373942949163434
0.4379718993326077 0.3429706794608443 0.6632284433727585
0.4385954869175723 0.3344020651253214 0.4466034887213766
0.3287505755228481 0.3491953539159166 0.5516706625936844
0.3398104490941484 0.3578364359558355 0.3448321880604636
0.6175874813866322 0.7215889634825302 0.2783439793907501
0.6907882519554585 0.7012513239731297 0.2930628338597671
0.4452964609583668 0.4530014864506408 0.6540340934565760
0.4596556791583726 0.6580873984174511 0.6517881764528642
0.6506787500514039 0.4411444585950711 0.6546705123677454
0.6596160195542039 0.6418308299650880 0.6492366407342659
0.3506666410964669 0.5620026934088886 0.6528483334272938
0.5556614214553354 0.5503211754886247 0.6563770711975637
0.4476912654764767 0.5614798696412436 0.5555395613002209
0.6602567640020861 0.5435847033340961 0.5525378051168992
0.3420571147618226 0.4597844200518034 0.5511210156331895
0.3577245837340395 0.6644599328189187 0.5491516755158034
0.5545482380053549 0.4407382745508813 0.5570911761080400
0.5632765147507769 0.6541432003051474 0.5504113032397180
0.4438570165001078 0.4501386707442472 0.4445171858856864

0.4596987509287771	0.6591223129784993	0.4458842259294493
0.6530639429003728	0.4390454556730508	0.4479223273377791
0.6667823783349822	0.6434443606310551	0.4497511678791152
0.3486164096644550	0.5623966707318068	0.4475358809859261
0.5634683930532587	0.5549481580022464	0.4423120071362123
0.4545931900061824	0.5567517118276981	0.3429577954896473
0.6613990717152693	0.5422759523644245	0.3479676245534029
0.3478273126332142	0.4607176764397978	0.3464294724842709
0.3625001075209487	0.6606245221146306	0.3489857575873910
0.5515457165528526	0.4477740726147869	0.3433750080465353
0.5584425635256131	0.6556053113248526	0.3422619008865817
0.6452863455860031	0.3379348611382099	0.5517428374676708
0.6432128081795115	0.3433521224740430	0.3507884772196463
0.5414257566332447	0.3450872121488991	0.6544268203942752
0.5438194148308306	0.3417969956641195	0.4483096795056288
0.4403708577703302	0.3482405488577668	0.5510355310797271
0.4432534580290913	0.3532836030473634	0.3468554274928841
0.3417791408108373	0.3621942424928788	0.6488755686977601
0.3402791069455710	0.3585048624231295	0.4485751589781501
0.6032956600244755	0.7132469481408922	0.2257759581002075
0.6070595737143367	0.7742346607786471	0.2906521832346127
0.7168605604048880	0.6841319855557417	0.2474544907390189
0.7202117515065078	0.7437515966088297	0.3126054428063792

C_2H_4 adsorption on NPs – non-stoichiometric

Mo_4C_6

C Mo H
8 4 4

0.4869109789338764 0.5821112704873923 0.5423658497121838
0.5224590882733543 0.4484630307451806 0.4129305334170624
0.5146910284863522 0.4366427881010583 0.6197495558428432
0.5164196882342531 0.5893727054132559 0.4789816169655390
0.4940216284850987 0.4023932943182817 0.4578407170787179
0.3853931532302882 0.4545297065868695 0.5712418989330352
0.6885471444468554 0.5320030433914144 0.4265084552218169
0.6736665709293216 0.5636249557016052 0.3590931957305010
0.5757293321844315 0.5363901710757560 0.4132163989255819
0.4466388200661215 0.4994714566464457 0.4810317036171420
0.4575503209299995 0.3860001140777554 0.5568861025829007
0.4525865905932892 0.5135904324907720 0.6169765409885811
0.7075337824125002 0.4776330331856518 0.4295307591784104
0.7062110254535137 0.5646540211141782 0.4706640549571464
0.6814379960117930 0.5332029211408992 0.3107460535978192
0.6801469436322621 0.6204784748574127 0.3519998586006493

Mo_5C_6

C Mo H
8 5 4

0.4654903221644421 0.4415827931158816 0.3825111753197368
0.5960779629321309 0.4763885686292093 0.4410585363535101
0.4866433886514142 0.4099150960069304 0.5373952550668402
0.4861182297597721 0.5820321776069318 0.4475615422998975
0.4020694270595207 0.5356787096967717 0.5748734992301263
0.5486168648979570 0.5392166183847944 0.5889199774400822
0.6223113334080188 0.5157377099583769 0.5704603449338718
0.6431599679798812 0.5161027192870231 0.4913110381829675
0.5270999853895029 0.5215592914879280 0.3767480845383233
0.5309289331610987 0.3953395382420947 0.4464162819283072
0.4335134025555141 0.4885859739387738 0.4786452826285604
0.4712962192463838 0.4738549616370546 0.6150134560118105
0.4759426509636199 0.6011873308722598 0.5474393362541933
0.6599612069796398 0.5505039738794900 0.5981486401840729
0.6312205955901270 0.4621528755729029 0.5914162796715596
0.6476316644331745 0.5714619030193568 0.4738359749266414
0.6967578242488531 0.4935398275063210 0.4877253101347723

Mo_6C_4

C Mo H
6 6 4

0.4686845060473592 0.4792738734469624 0.3829375402406115
0.5957222256348081 0.5087962463929671 0.4246695885482378
0.3944960583888170 0.5077255745381423 0.5870725000395357
0.5221460453988707 0.5376427010804931 0.6290652098279527
0.4687945557648737 0.6692286716721744 0.4735375417273728
0.4392710435906632 0.6916108877686352 0.5440711773252312
0.5070102612844011 0.5604334960091892 0.4335561549950090
0.5502100656062364 0.4270803982736939 0.3963562069534788
0.4490496458943944 0.4519487251223454 0.4974457867570600
0.5560841069442126 0.4769725002527945 0.5326722027693125
0.4625001350391609 0.4606244304837059 0.6395346013083042
0.4597377429215872 0.5829502670652492 0.5608924215210465
0.5188172980426367 0.6957702422740722 0.4601795735906889
0.4308843673525002 0.6752232957094251 0.4297841055206461
0.4715504944121134 0.7286113121590293 0.5743895996166848
0.3834898828216344 0.7064950810564524 0.5443733763151483

Mo_6C_5

C Mo H
7 6 4

0.4394912513536527 0.4363516195808323 0.4042228147782032
0.4209793595206923 0.4472087406635755 0.5589938958860053
0.5347392633627936 0.5588892983134075 0.4497461686806956
0.4205307737970112 0.6036946581971678 0.5502575562218908
0.5344639864034882 0.5508076854790402 0.6106154940528881
0.5037098441210449 0.2830595941005466 0.5320819660386832
0.5534729219430468 0.3417776615449726 0.5514820074661192
0.5339938162865085 0.4675741408122608 0.4002057114503719
0.4575444451338649 0.3774840142498459 0.4913577574315096
0.4276351096076521 0.5207333231289097 0.4759295523415478
0.5372125153006763 0.4694252396655395 0.5339044052157473
0.4344823354073291 0.5315576889731972 0.6197178721759687
0.5204715137498324 0.6169381599347654 0.5321345889898589
0.5239182152728501 0.2450436809976291 0.4936002600775045
0.4772482908802930 0.2569178992113316 0.5762208277923113
0.6058935613942017 0.3385030089371068 0.5274838722290740
0.5566628644124306 0.3510835198414711 0.6086352842242635

Mo_8C_{12} (MetCar)

C Mo H
14 8 4

0.5226863810395980	0.5747925986543000	0.6118534845198650
0.5809570371905771	0.5411024653710262	0.6190085310785746
0.5158767849056153	0.3483866587896146	0.6309770239714571
0.5765392862932849	0.3809773304563733	0.6324363341040075
0.3900379964923699	0.4314821410819836	0.6134608002487472
0.3903477807694594	0.5003734777311064	0.6071207958967115
0.4323489667599284	0.3398392265387423	0.4978747056598888
0.4552408614279596	0.3690501562105148	0.4401493730928140
0.4394797023886378	0.5661099415661492	0.4806810584308153
0.4615684562541257	0.5286138806930798	0.4280131689533767
0.6240433152340251	0.4482786174411206	0.5052361381832301
0.5859222112389628	0.4455498056431657	0.4456525230221468
0.4097250387121126	0.6806317223730772	0.6299211154089420
0.3589992518436274	0.6710884136859022	0.5805026601106574
0.4256165871573604	0.4551046756230232	0.5076735191733549
0.5376855359862244	0.5216151587371278	0.5138197298366958
0.4286908640865115	0.5840854381394999	0.5774945154802182
0.5325687769507002	0.3835167905829425	0.5249001748226206
0.6299176527986016	0.4565540181305873	0.5998389279564287
0.4251878831290263	0.3432492066648500	0.5957411493802837
0.4982497005248432	0.4631977651492712	0.6223262043449733
0.5034440910874632	0.4444713984762567	0.3985774732288362
0.3993392309685966	0.6703655196604594	0.6826531923034733
0.4502258136700588	0.7163585149302144	0.6217291227345959
0.3092676582809992	0.6536939705058995	0.5952214766670647
0.3600030520093359	0.6996610672137413	0.5339667581402412

$Mo_{10}C_{12}$

C Mo H

14 10 4

0.4787213941141216	0.3216366432312590	0.3821044298538792
0.4479356471978280	0.5343815411765008	0.3816572839424672
0.5581145864758076	0.6439284248334530	0.3716659190467743
0.5729003629407050	0.4336677384966896	0.3972430004704695
0.4339310866120968	0.6496617445129803	0.4865051897816929
0.5637954894385466	0.5433983288183820	0.5077926198561415
0.4356548650661698	0.4271126026919864	0.4955388902296401
0.5714302195694139	0.3225593052024617	0.5112623117744393
0.4482433549492530	0.3277945206391524	0.6146199566971282
0.5447788491053940	0.4348225320145090	0.6213556139819627
0.4268767691580156	0.5438632844933217	0.6057067366419666
0.5268474140976533	0.6496315882590208	0.6187099046706177
0.5475067829162391	0.7126509434725776	0.3300588567854311
0.4671322832473165	0.7267729552101569	0.3146237957413884
0.4565521235002485	0.6386348525825273	0.3852255143188874
0.4637117773474081	0.4271383445355038	0.3973324687438531
0.5570151542557060	0.5429074738229842	0.4053145204374616
0.5708423869838468	0.3296822729860094	0.4068611248525800
0.4461286699520224	0.5407924257682916	0.4947860965145251
0.5520250442198151	0.4304327661526359	0.5089007050372939
0.4343203256388390	0.6466815270947045	0.5912284299474125
0.5367099527799671	0.5458321854723773	0.6058862449518244
0.4390600572248943	0.4321232976804017	0.5970160717360983
0.5441156881233993	0.3308275048665547	0.6119621528542124
0.5757005084664412	0.7066200294083279	0.2796239835763235
0.5717536406723918	0.7564929140637682	0.3593374383583442
0.4539085911032086	0.7191352868644938	0.2589587019321931
0.4485616410563393	0.7780844049464958	0.3333501867784411

$Mo_{12}C_6$

C Mo H
8 12 4

0.3632656678263685	0.4595192483535683	0.4276719697413826
0.4503407437256094	0.5726494309500958	0.3423333729079386
0.4938336395168343	0.4137901315548231	0.3676802211606600
0.5823081577960304	0.6109773579336489	0.4241481394378271
0.4528542610751251	0.6675472958731263	0.4621447898574542
0.4277570287679680	0.4133839371200526	0.5762652399683642
0.7213795375419573	0.5816437128407478	0.5879537617953992
0.7606706982243286	0.5889440063980912	0.5208751967600407
0.4861829086115880	0.5101617825311664	0.5437941076761706
0.6184517180815784	0.5093105206838325	0.5898786433037768
0.4091963376482792	0.5695855011702020	0.4525998563081766
0.3519795769888917	0.4639828574595296	0.5282599333165577
0.4165168549465347	0.4728381871995114	0.3407481302918665
0.5264961653391940	0.5139965304772391	0.4136570602914074
0.6011864248088205	0.4293130349009414	0.4980690321295714
0.6576143842869141	0.5621587066001837	0.4864201972486656
0.5326985591244391	0.6283378598294511	0.5188885952673287
0.5018688935322237	0.6535926445443201	0.3730325847868819
0.4585413728151966	0.3949487416896449	0.4651256277420258
0.5197210237733370	0.3713447608423510	0.5806500563572429
0.7126252676912919	0.6295886923100309	0.6187843561468289
0.7411102560194434	0.5383454082709066	0.6217188077004818
0.7755056261100414	0.6425846571227546	0.5052755500470679
0.8019625077564231	0.5500715668438204	0.5100009389176421

$Mo_{12}C_8$

C	Mo	H
10	12	4

0.5012096752696369	0.4237211867270113	0.6462210007942929
0.3791962183708265	0.4527800254090200	0.3977900877418009
0.4828474046587560	0.5777822389287401	0.3583171645468097
0.5276484482200671	0.4295953703937341	0.3723815797431922
0.6023789641615956	0.5487627525808019	0.6165229814549885
0.5975354702516168	0.6161162191420777	0.4714531239007985
0.4486028836240324	0.6486828228413325	0.4893490730637249
0.3855909717195563	0.3826457636915304	0.5417570858470119
0.6969964094997846	0.4372381852371104	0.5354707050171306
0.7544047149840379	0.4906313269899352	0.5412798158139969
0.4299434259032276	0.4810935113199005	0.5802526853348918
0.5204334632183915	0.5235568408221226	0.6734771178217048
0.4188678875665820	0.5473823906909480	0.4546861533138536
0.3275152162874871	0.4473282311721419	0.4861543190358007
0.4538392853712993	0.4811114680965058	0.3320249290953600
0.5535924135649777	0.5195873055701135	0.4329755410532165
0.5688639517385352	0.4564467252967978	0.5570396861306119
0.6596179522262380	0.5506227178611356	0.5298394467267303
0.5159324260760910	0.5899962084110990	0.5525849613397769
0.5163865727886809	0.6549506300115541	0.4174564984798349
0.4668976637531277	0.4115470402233724	0.4634377272530845
0.4736438926761099	0.3468628497589987	0.5824589378667646
0.6890849495490231	0.4061134059241330	0.5840904279056643
0.6969952504561158	0.4033570595488833	0.4888401135754465
0.7835310718043109	0.4933522591289310	0.5909811249527281
0.7893410714952788	0.4942190068183527	0.4953191528186137

$Mo_{12}C_{10}$

```
   19.0000000000000000    0.0000000000000000    0.0000000000000000
    0.0000000000000000   19.0000000000000000    0.0000000000000000
    0.0000000000000000    0.0000000000000000   19.0000000000000000
  C    Mo   H
   12   12    4
Direct
  0.5007078713750596  0.4256797925267060  0.6494642940425083
  0.3426288204675026  0.5223879086867771  0.5275575305390472
  0.3812371924178836  0.4540315864231136  0.3945509158291898
  0.4903503392946914  0.5752975857204409  0.3618906381475108
  0.5328848623305523  0.4300264299538281  0.3775294953834969
  0.6071991615622988  0.5465983569983526  0.6206708616977314
  0.6042900510578260  0.6141036063249410  0.4779170996658205
  0.4555727906885622  0.6487984517993931  0.4903542715537306
  0.3862644751730859  0.3776016635105262  0.5434211366506378
  0.5380537452630202  0.3500924849454909  0.5267283646993376
  0.7014516085948348  0.4314965504039971  0.5446069999386495
  0.7577764837873928  0.4862912909766241  0.5524636380656667
  0.4277649837656793  0.4811634328658603  0.5797723411380408
  0.5246639875206172  0.5225538692652767  0.6755670158652689
  0.4202810365634419  0.5507801259286346  0.4550270593379268
  0.3275738793233999  0.4356080869677370  0.4807663299330455
  0.4590495187120965  0.4809442108064542  0.3332084793396407
  0.5571497821665725  0.5180291656053775  0.4367624755779144
  0.5742975840468264  0.4495438782861909  0.5598059617906453
  0.6633785645093692  0.5458269076689986  0.5359652302344613
  0.5210468857075409  0.5862820366598773  0.5548223970400283
  0.5259447596422812  0.6532933354539324  0.4213731733277181
  0.4685291673104920  0.4108458096390021  0.4644752225570187
  0.4687099949007953  0.3437435832970578  0.5963041643601457
  0.7038613898459430  0.3976745133973086  0.4980301529937435
  0.6931482943628454  0.4000294983620733  0.5928191757350114
  0.7937744339809784  0.4904914999280409  0.5073098438118595
  0.7859314409168652  0.4881928469844168  0.6027072213496334
```

$Mo_{14}C_{13}$ (nanocube)

C Mo H
15 14 4

0.5518297787576846	0.5883032311967937	0.3561937208311731
0.6327466412704286	0.4464415644066438	0.3882452701705011
0.4074610665872531	0.5069158689719635	0.3581872340768527
0.4898394504012401	0.3640339101192446	0.3893743242672160
0.3680844811719349	0.4159162423631785	0.4909970014261257
0.5942847499655678	0.3552805639222183	0.5202047389865804
0.6550577417466168	0.5796609401798433	0.4855017480932146
0.5120772571383133	0.4984443196188766	0.4880390120033650
0.4340017887580412	0.6361746027761906	0.4573734843592336
0.5330286854516574	0.6278684289855951	0.5818524368877326
0.6154429979919765	0.4895221986269667	0.6188272065788708
0.3918967977251841	0.5432874091590111	0.5870117102246403
0.4715279123602720	0.4073086364486895	0.6206293977329956
0.3577054895618949	0.7074565325144594	0.6266931095717665
0.4050421088066266	0.7536378546904713	0.5893155010854372
0.6455758541285134	0.5514072825858071	0.3850450114013061
0.4477801808737656	0.6028105414162962	0.3580706355514464
0.5197699587398352	0.4775179733330577	0.3844455011652175
0.5905191867734495	0.3543684820062780	0.4157599889477286
0.3941620071523311	0.4079914971410499	0.3893695255729211
0.5411005120959533	0.5993420273377222	0.4715478542691164
0.4840573368900524	0.3966497151957238	0.5035074915004576
0.4099669489667619	0.5238817655408371	0.4751265647302276
0.6131242150811544	0.4697302952476728	0.5014190442345927
0.6306622955119473	0.5875039447041611	0.5873758928529560
0.4302639242287226	0.6433223276420739	0.5629066245796410
0.5033670994201643	0.5160211655814519	0.5922497244518556
0.5756760310529152	0.3928177644166441	0.6168237492734695
0.3767776838334609	0.4408222797326144	0.5920715607527419
0.3648985775909880	0.6982461422829024	0.6830977695479361
0.3029974623207420	0.7020607982288466	0.6094551461721047
0.4481214330395681	0.7794075040123745	0.6174931762692500
0.3861375243266045	0.7831101870114026	0.5436093826427085

References

(1) Lausche, A. C.; Schaidle, J. A.; Schweitzer, N.; Thompson, L. T. (2013). Nanoscale Carbide and Nitride Catalysts. In Reedijk, J. and Poeppelmeier K. (Eds.), *Comprehensive Inorganic Chemistry II-Second Edition* (pp 371-404). Amsterdam, Elsevier.

(2) Levy, R. B.; Boudart, M. *Science* **1973**, *181*, 547-549.

(3) King, T. E. Carbide and Nitride Supported Water-Gas Shift Catalysts. Ph.D. Thesis, University of Michigan, Ann Arbor, MI, 2007.

(4) Toth, L. (1971). *Transition Metal Carbides and Nitrides-Volumen 7*. New York, Academic Press.

(5) Hagg, G. Z. *Phys. Chem.* **1931**, *12*.

(6) Oyama, S.T. (1996). *Chemistry of Transition Metal Carbides and Nitrides.* Glasgow, Blackie Academic & Professional.

(7) Oyama, S. T. J. *Solid State Chem.* **1992**, *96*, 442-445.

(8) Politi, J. R. S.; Viñes, F.; Rodriguez, J. A.; Illas, F. *Phys. Chem. Chem. Phys.* **2013**, *15*, 12617-16625.

(9) Jiang, C.; Jiang, W. *P. S. S. B* **2013**, *251*, 3, 533-536.

(10) Korzhavyi, P. A.; Pourovskii, L. V.; Hugosson, H. W.; Ruban, A. V.; Johansson, B. *Phys. Rev. Lett.* **2001**, *88*, 015505.

(11) Kurlov, A. S.; Gusev, A. I. *Inorg. Mater.* **2006**, *42*, 121-127.

(12) Lu, J.; Hugosson, H.; Eriksson, O.; Nordström, L.; Jansson, U. *Thin Solid Films* **2000**, *370*, 203-212.

(13) Das, T.; Deb, S.; Mookerje, A. *Physica B* **2005**, *367*, 6.

(14) Sahnoun, M.; Daul, C.; Driz, M.; Parlebas, J. C.; Demangeat, C. *Comput. Mater. Sci.* **2005**, *33*, 175.

(15) Johansson, L. I. *Surf. Sci. Rep.* **1995**, *21*, 177.

(16) Chen, J. G.; Eng, J. Jr.; Kelty, S. P. *Catal. Today* **1998**, *43*, 147.

(17) Stefan, P. M.; Shek, M. L.; Lindau, I.; Spicer, W. E.; Johansson, L. I.; Herman, F.; Kasowski, R. V.; Brogen. G. *Phys. Rev. B* **1984**, *29*, 5423.

(18) Johansson, L. I.; Hagström, B. E.; Jacobsson, J. B.; Hagström, S. B. M. *J. Electron Spectrosc. Relat. Phenom.* **1997**, *10*, 259.

(19) Viñes, F.; Sousa, C.; Liu, P.; Rodriguez, J. A.; Illas, F. *J. Chem. Phys.* **2005**, *122*, 174709.

(20) Ahmad, S., Ashraf, I.; Mansoor, M. A.; Rizwan, S.; Iqbal, M. *Nanomaterials* **2021**, *11*, 776.

(21) Holt, J. B.; Munir, Z. A. *J. Mat. Sci*. **1986**, *21*, 251.

(22) Merzhanov, A. G.; Borovinskaya, I. P. *Dokl. Akad. Nauk. SSR* **1972**, *204*, 429.

(23) Jin, S.; Shen, P.; Lin, Q.; Zhan, L.; Jiang, Q. C. *Cryst.Growth Des.* **2010**, *10*, 4, 1590-1597.

(24) Naguib, M.; Kurtoglu, M.; Presser, V.; Lu, J.; Niu, J.; Heon, M.; Hultman, L.; Gogotsi, Y.; Barsoum, M. W. *Adv. Mater.* **2011**, *23*, 4228-4253.

(25) Zhang, T.; Pan, L.; Tang, H.; Du, F.; Guo, Y.; Qiu, T.; Yang, T. *J. Alloy Compd.* **2017**, *695*, 818-826.

(26) Wei, C.; Tao, Y.; An, Y.; Tian, Y.; Zhang, Y.; Feng, J.; Qian, Y. *Adv. Funct. Mater.* **2020**, *30*, 2004613.

(27) Aslam, M. K.; Xu, M. *Nanoscale* **2020**, *12*, 15993-16007.

(28) Hu, H.; Onyebueke, L.; Abatan, A. *J. Miner. Mater. Char. Eng.* **2010**, *9*, 275.

(29) Zhu, Y.; Zhang, Y.; Whang, K.; Li, D.; Ding, F.; Meng, D.; Wang, X.; Zhang, Z. *Mater. Res, Bull.* **2017**, *95*, 79-85.

(30) Lee, G. H.; Moon, S. H.; Kim, M. C.; Kim, S. J.; Choi, S.; Kim, E. S.; Han, S. B.; Park, K. W. *Ceram. Int.* **2018**, *44*, 7972-7977.

(31) Tomás-García, A. L.; Jensen, J. O.; Bjerrum, N. J.; Li, Q. *Electrochim Acta* **2014**, *137*, 639-646.

(32) Chen, Z.Y.; Shi, M. Q.; Ma, C. A.; Chu, Y. Q.; Zhu, A. *J. Powder Thecnol.* **2013**, *235*, 467-474.

(33) Wang, L.; Li, Q.; Zhu, Y.; Qian, Y. *Int. J. Refract. Met. Hard Mater.* **2012**, *31*, 288-292.

(34) Liu, M. C.; Hu, Y. M.; An, W. Y.; Kong, L.B.; Kang, L. *J. Energy Chem.* **2017**, *26*, 750-756.

(35) Giordano, C.; Antonietti, M. *Nano Today* **2011**, *6*, 366-380.

(36) Morishita, T.; Soneda, Y.; Hatori, H.; Inagaki, M. *Electrochim. Acta* **2007**, *52*, 2478-2484.

(37) Horn, J. M.; Song, Z.; Potapenko, D. V.; Hrbek, J.; White, M. G. *J.Phys. Chem. B* **2005**, *109*, 1, 44-47.

(38) Amendola, V.; Riello, P.; Meneghetti, M. *J. Phys. Chem. C* **2010**, *115*, 5140-5146.

(39) Kelly, J. P.; Kanakala, R.; Graeve, O. A. *J. Am. Ceram. Soc.* **2010**, *93*, 3035-3038.

(40) Wang, L.; Li, Q.; Mei, T.; Shi, L.; Zhu, Y.; Qian, Y. *Mater. Chem. Phys.* **2012**, *137*, 1-4.

(41) Rasaki, S. A.; Zhang, B.; Anbalgam, K.; Thomas, T.; Yang, M. *Prog. Solid State Chem.* **2018**, *50*, 1-15.

(42) Choi, J. G. *J. Catal*. **1999**, *182*, 104-116.

(43) Ledoux, M. J.; DelGallo, P.; PhamHuu, C.; York, A. P. E. *Catal. Today* **1996**, *27*, 145-150.

(44) Furimsky, E. *Appl. Catal. A* **2003**, *240*, 1-28.

(45) Chen, X. W., Zhang, T.; Zheng, M. Y.; Xia, L. G.; Li, T.; Wu, W. C.; Wang, X. D.; Li, C. *Ind. Eng. Chem. Res.* **2004**, *43*, 6040-6047.

(46) Pang, J.; Sun, J.; Zheng, M.; Li, H.; Wang, Y.; Zhang, T. *Appl. Catal. B* **2019**, *254*, 510-522.

(47) Palacio, J. C. E.; Orozco, D. J. R.; Lora, E. S.; Venturini, O. J.; Barros, R. M. (2015). Procesos biológicos de conversión. In Martínez, J. M. R.; Lora, E. E. S. (Eds.), *Bioenergía: Fuentes, conversión y sustentabilidad* (pp 123-164). Cyted.

(48) Saha, B. C.; *J. Ind. Microbiol. Biotechnol*. **2003**, *30*, 279-291.

(49) Ji, N.; Zhang, T.; Zheng, M.; Wang, A.; Wang, H.; Wang, X.; Chen, J. G. *Angew. Chem. Int. Ed.* **2008**, *47*, 8510-8513.

(50) Li, C.; Zheng, M.; Wang, A.; Zhang, T. *Energy Environ. Sci.* **2012**, *5*, 6383-6390.

(51) Ma, R.; Hao, W.; Ma, X.; Tian, Y.; Li, Y. *Angew. Chem. Int. Ed.* **2014**, *53*, 7310-7315.

(52) Karim, A. N.; Kamarudin, K. S. (2021). Introduction to direct alcohol fuel cells (DAFCs). In Akay, R. G.; Yurtcan, A. B. (Eds.), *Direct Liquid Fuel Cells Fundamentals, Advances and Future* (pp 49-70). Academic Press.

(53) Stottlemyer, A. L.; Kelly, T. G.; Meng, Q.; Chen, J. G. *Surf. Sci. Rep.* **2012**, *67*, 201-232.

(54) Markovic, N. M.; Gasteiger, H. A.; Ross Jr, P. N.; Jiang, X.; Villegas, I.; Weaver, M. J. *Electrochimica Acta* **1995**, *40*, 91-98.

(55) Ingham, B.; Gaston, N.; Fahy, K.; Chin, X. Y.; Dotzler, C. J.; Rees, E.; Haslam, G.; Barber, Z. H.; Burstein, G. T.; Ryan, M. P. *J. P. C. C* **2012**, *116*, 6159-6165.

(56) Esposito, D. V.; Hunt, S. T.; Kimmel, Y. C.; Chen, J. G. *J. A. C. S.* **2012**, *134*, 3025-3033.

(57) Hwu, H. H.; Chen, J. G.; Kourtakis, K.; Lavin, J. G. *J. P. C. B* **2001**, *105*, 10037-10044.

(58) Wiegert, E. C.; Stottlemyer, A. L.; Zellner, M. B.; Chen. J. G. *J. P. C. C* **2007**, *111*, 14617-14620.

(59) Sottlemeyer, A. L.; Liu, P.; Chen, J. G. *J. Chem. Phys.* **2010**, *133*, 104702.

(60) Weidman, M. C.; Esposito, D. V.; Hsu, I. J.; Chen, J. G. *J. Electrochem. Soc.* **2010**, *157*, F179-F188.

(61) Chi-Jen, Y. *Energy Policy* **2009**, *37*,1805-1808.

(62) Esposito, D. V.; Hunt, S. T.; Stottlemyer, A. L.; Dobson, K. D.; McCandless, B. E.; Birkmire, R. W.; Chen, J. G. *Angew. Chem. Int. Ed.* **2010**, *49*, 9859-9862.

(63) Liu, Y.; Fu, Q.; Flytzani-Stephanopoulos, M. *Catal. Today* **2004**, *93-95*, 241.

(64) Suh, D. J.; Kwak, C.; Kim, J. H.; Kwon, S. M.; Park, T. J. *J. Power Sources* **2005**, *142*, 70.

(65) Rhodes, C.; Hutchings, G. J.; Ward, A. M. *Catal. Today* **1995**, *23*, 43.

(66) Bohlbro, H.; Jorgensen, M. H. *Chem. Eng. World* **1970**, *5*, 46.

(67) Idakiev, V.; Tabakova, T.; Yuan, Z. Y.; Su, B. L. *Appl. Catal. A. Gen.* **2004**, *270*, 135.

(68) Wang, X.; Rodríguez, J. A.; Hanson, J. C.; Gamarra, D.; Martinez- Arias, A.; Fernández- Garcia, M. *J. Phys. Chem. B* **2005**, *109*, 19595.

(69) Sakurai, H.; Akita, T.; Tsubota, S.; Kiuchi, M.; Haruta, M. *Appl. Catal. A Gen.* **2005**, *291*, 197.

(70) Wang, X.; Rodríguez, J. A.; Hanson, J. C.; Perez, M.; Evans, J. *J. Chem. Phys.* **2005**, *123*, 221101.

(71) Liu, P.; Rodriguez, J. A. *J. Chem. Phys.* **2007**, *126*, 164705.

(72) Rodriguez, J. A.; Liu, P.; Hrbek, J.; Evans, J.; Perez, M. *Angew. Chem. Int. Ed.* **2007**, *46*, 1329.

(73) Kim, C. H.; Thompson, L. T. *J. Catal.* **2005**, *230*, 66.

(74) Liu, X. S.; Ruettinger, W.; Xu, A. M.; Farrauto, R. *Appl. Catal. B* **2005**, *56*, 69.

(75) Liu, N.; Mao, J.; Yang, Z. *SURF COAT TECH* **2020**, *402*, 125925.

(76) Pritchard, M. L.; McCauley, R. L.; Gallaher, B. N.; Thomson, W. J. *Appl. Catal* **2004**, *275*, 213-220.

(77) Hwu, H. H.; Chen, J. G. *Chem. Rev.* **2005**, *105*, 185-212.

(78) Oyama, S. T. *Catal. Today* **1992**, *15*, 179.

(79) Moon, D. J.; Ryu, J. W. *Catal. Lett.* **2004**, *92*, 17.

(80) Patt, J.; Moon, D. J.; Phillips, C.; Thompson, L. *Catal. Lett.* **2000**, *65*, 193.

(81) Liu, P.; Rodriguez, J. A. *J. Phys. Chem. B* **2006**, *110*, 19418.

(82) Tominaga, H.; Nagai, M. *J. Phys. Chem. B* **2005**, *109*, 20415.

(83) Viñes, F.; Rodriguez, J. A.; Liu, P.; Illas, F. *J. Catal.* **2008**, *260*, 103-112.

(84) Rodriguez, J. A.; Liu, P.; Gomes, J.; Nakamura, K.; Viñes, F.; Sousa, C.; Illas, F. *Phys. Rev. B* **2005**, *72*, 075427.

(85) Zhang, Y. F.; Viñes, F.; Xu, Y. J.; Li, Y.; Li, J. Q.; Illas, F. *J. Phys. Chem. B* **2006**, *110*, 15454.

(86) Viñes, F.; Sousa, C.; Illas, F.; Liu, P.; Rodriguez, J. A. *J. Phys. Chem. C* **2007**, *111*, 16982.

(87) Core Writing Team, Pachuari, R. K.; Reisingerm A. (Eds.), IPCC, 2007: *Climate Change 2007: Synthesis Report. Contribution of Working Groups I, II and III to the Fourth Assessment Report of the Intergovernmental Panel on Climate Change* (pp 104). Geneva, IPCC.

(88) Shindell, T. D.; Faluvegi, G.; Koch, D. M.; Schmidt, G. A.; Unger, N.; Bauer, S. E. *Science* **2009**, *326*, 5953.

(89) Goswami, B. N.; Venugopal, V.; Sangupta, D.; Madhusoodanan, M. S.; Xavier, P. K. *Science* **2006**, *314*, 5804.

(90) Bowman, D. M. J. S.; Balch, J.; Artaxo, P.; Bond, W. J.; Cochrance, M. A.; D'Antonio, C. M.; DeFries, R.; Johnston, F. H.; Keeley, J. E.; Krawchuk, M. A.; Kull, C. A.; Mack, M.; Moritz, M. A.; Pyne, S.; Roos, C. I.; Scott, A. C.; Sodhi, N. S.; Swetman, T. W. *J. Biogeogr.* **2011**, *38*, 12, 2223-2236.

(91) Kresse, G.; Furthmüller, J. *Comput. Mater. Sci.* **1996**, *6*, 15-50.

(92) Kresse, G. *Phys. Rev. B* **1996**, *54*, 11169-11186.

(93) Kresse, G.; Hafner, J. *Phys. Rev. B* **1993**, *47*, 558-561.

(94) Schrödinger, E. *Ann. Phys.* **1926**, *385*, 437-490.

(95) Schrödinger, E. *Ann. Phys.* **1926**, *384*, 361-376.

(96) Schrödinger, E. *Ann. Phys.* **1926**, *384*, 489-527.

(97) Schrödinger, E. *Ann. Phys.* **1926**, *386*, 109-139.

(98) Schrödinger, E. *Ann. Phys.* **1926**, 384, 734-756.

(99) Schrödinger, E. *Naturwissenschaften* **1926**, *16*, 664-666.

(100) Bron, M.; Oppenheimer, R. *Ann. Phys.* **1927**, *84*, 457-484.

(101) Hohenberg, P. C.; Kohn, W. *Phys. Rev.* **1964**, *136*, 864-871.

(102) Perdew, J. P.; Schmidt, K. *AIP conf. Proc.* **2001**, *577*, 1-20.

(103) Perdew, J. P.; Ruzsinszky, A.; Tao, J.; Staroverov, V. N.; Scuseriam G. E.; Csonka G. *J. Chem. Phys.* **2005**, *123*, 062201.

(104) Janthon, P.; Luo, S. A..; Kozlov, S. M.; Viñes, F.; Limtrakul, J.; Truhlar, D. G.; Illas, F. *J. Chem. Theory Comput.* **2014**, *10*, 9, 3832-3839.

(105) Janthon, P.; Kozlov, S. M.; Viñes, F.; Limtrakul, J.; Illas, F. *J. Chem Theory Comput.* **2013**, *9*, 3, 1631-1640.

(106) Vega, L.; Ruvireta, J.; Viñes, F.; Illas, F. *J. Chem. Theory Comput.* **2018**, *14*, 1, 395-403.

(107) Vega, L.; Martínez, B.; Viñes, F.; Illas, F. *Phys. Chem. Chem. Phys.* **2018**, *20*, 20548-20554.

(108) Ceperley, D. M.; Alder, B. *J. Phys. Rev. Lett.* **1980**, *45*, 566-569.

(109) Vosko, S. H.; Wilk, L.; Nusair, M. *Can. J. Phys.* **1980**, *58*, 1200-1211.

(110) Cramer, C. J.; Truhlar, D. G. *Phys. Chem. Chem. Phys.* **2009**, *11*, 10757.

(111) Rappoport, D.; Crawford, N. R. M.; Furche, F.; Burke, K. (2008). Which functional should I choose?. In Solomon, E. I.; King, R. B. and, Scott, R. A. (Eds.), *Computational Inorganic and Bioinorganic Chemistry*. Wiley, Chichester.

(112) Perdew, J. P.; Burke, K.; Ernzerhof, M. *Phys. Rev. Lett.* **1996**, *77*, 3865.

(113) Perdew, J. P. (1991). Unified theory of exchange and correlation beyond the local density approximation. In Ziesche, P. and Eschrig, H. (Eds.), *Electronic Structure of Solids '91* (pp 11-20). Berlin, Akademie Verlag.

(114) Vega, L.; Viñes, F. *J. Comput Chem.* **2020**, *41*, 2598-2603.

(115) Morales-Garcia, A.; Viñes, F.; Gomes, J. R. B.; Illas, F. *WIREs Comput Mol Sci.* **2021**, el530.

(116) Roothaan, C. C. J. *Rev. Mod. Phys.* **1951**, *23*, 161.

(117) Dovesi, R.; Erba, A.; Orlando, R.; Zicovich-Wilson, C. M.; Civalleri, B.; Maschio, L.; Rerat, M.; Casassa, S.; Baima, J.; Salustro, S.; Kirtman, B. *WIREs Comput Mol Sci.* **2018**, *8*, e1360.

(118) https://www.basissetexchange.org/

(119) Schwerdtfeger, P. *Chem. Phys. Chem.* **2011**, *12*, 3143-3155.

(120) Hay, P. J.; Wadt, W. R. *J. Chem. Phys.* **1985**, *82*, 299.

(121) Hay, P. J.; Wadt, W. R. *J. Chem. Phys.* **1985**, *82*, 270.

(122) Huzinaga, S.; Seijo, L.; Barandiarán, Z.; Klobukowsk, M. *J. Chem. Phys.* **1987**, *86*, 2132.

(123) Blöch, P. E. *Physical Review B* **1994**, *50*, 17953-17979.

(124) Bloch, F. *Z. Phys.* **1929**, *57*, 545-555.

(125) Truhlar, D. G.; Garrett, B. C.; Klippenstein, S. J. *J. Phys. Chem.* **1996**, *100*, 31, 12771-12800.

(126) Henkelman, G.; Jónsson, H. *J. Chem. Phys.* **2000**, *113*, 9978-9985.

(127) Zhao, W.; Kozlov, S. M.; Höfert, O.; Gotterbarm, K.; Lorenz, M. P. A.; Viñes, F.; Papp, C.; Görling, A.; Steinrück, H. P. *J. Phys. Chem. Lett.* **2011**, *2*, 7, 759-764.

(128) Kunkel, C.; Viñes, F.; Illas, F. *Energy Environ. Sci.* **2016**, *9*, 141-144.

(129) Viñes, F.; Sousa, C.; Illas, F.; Liu, P.; Rodriguez, J. A. *J. Phys. Chem. C* **2007**, *111*, 3, 1307-1314.

(130) Posada-Pérez, S.; Ramírez, P. J.; Gutiérrez, R. A.; Stacchiola, D. J.; Viñes, F.; Liu, P.; Illas, F.; Rodriguez, J. A. *Catal. Sci. Technol.* **2016**, *6*, 6766-6777.

(131) Posada-Pérez, S.; Viñes, F.; Rodriguez, J: A.; Illas, F. *Topics in Catalysis* **2015**, *58*, 159-173.

(132) Lamiel-Garcia, O.; Bromley, S. T.; Illas, F. *Theor. Chem. Acc.* **2013**, *132*, 1312.

(133) Fajín, J. L. C.; Cordeiro, M. N. D.S.; Gomes, J. R. B.; Illas, F. *J. Chem. Theory Comput.* **2012**, 8, 1737-1743.

(134) Kunkel, C.; Viñes, F.; Illas, F. *ACS Appl. Energy Mater.* **2018**, *1*, 43-47.

(135) González, S.; Viñes, F.; García, J. F.; Erazo, Y.; Illas, F. *Surf. Sci.* **2014**, *625*, 64-68.

(136) Hao, X.; Wang, Q.; Li, D.; Zhang, R.; Wang, B. *RCS Adv.* **2014**, *4*, 43004-43011.

(137) Ihm, Y.; Cooper, V. R.; Gallego, N. C.; Contescu, C. I.; Morris, J. R. *J. Chem. Theory Comput.* **2014**, *10*, 1-4.

(138) Kim, J.; Maiti, A.; Lin, L.-C.; Stolaroff, J. K.; Smit, B.; Aines, R. D. *Nat. Commun.* **2013**, *4*, 1694.

(139) Yang,Q.; Liu, D.; Zhong, C.; Li, J. *Chem. Rev.* **2013**, *113*, 8261-8323.

(140) Brønsted, J. N. *Chem. Rev.* **1928**, *5*, 231-338.

(141) Evans, M. G.; Polanyi, M. *Trans. Faraday Soc.* **1938**, *34*, 11-24.

(142) Chen, J. G. *Chem Rev.* **1996**, *96*, 1477-1498.

(143) Kurlov, A. S.; Gusev, A. I. *Russ. Chem. Rev.* **2006**, *75*, 617-636.

(144) Jehn, H.; Ettmayer, P. *J. Less-Common Met.* **1978**, *58*, 85-98.

(145) Kanoun, M. B.; Goumri-Said, S.; Jaouen, M. *Phys. Rev. B: Condens. Matter Mater. Phys.* **2007**, *76*, 134109.

(146) Qin, J.; Zhang, X.; Xue, Y.; Li, X.; Ma, M.; Liu, R. *Comput. Mater. Sci.* **2013**, *79*, 456-462.

(147) Fernandez-Guillermet, A.; Häglund, J.; Grimvall, G. *Phys. Rev. B; Condens. Matter Mater. Phys.* **1992**, *45*, 11557-11567.

(148) Giacomo Asara, G.; Viñes, F.; Ricart, J. M.; Rodríguez, J. A.; Illas, F. *Surf. Sci.* **2014**, *624*, 32-36.

(149) Ebrahimi, M.; Simonovis, J. P.; Zaera, F. *J. Phys. Chem. Lett.* **2014**, *5*, 2121-2125.

(150) Zhang, L.; Zhou, M.; Wang, A.; Zhang, T. *Chem. Rev.* **2020**, *120*, 683-733.

(151) Koverga, A. A.; Flórez, E.; Dorkis, L.; Rodriguez, J. A. *J. Phys. Chem. C.* **2019**, *123*, 8871-8883.

(152) Silveri, F.; Quesne, M. G.; Roldán, A.; de Leeuw, N. H.; Catlow, C. R. A. *Phys. Chem. Chem. Phys.* **2019**, *21*, 5335-5343.

(153) Schaidle, J. A.; Thompson, J. A. *J. Catal.* **2015**, *329*, 325-334.

(154) Posada-Pérez, S.; Ramírez, P. J.; Evans, J.; Viñes, F.; Liu, P.; Illas, F.; Rodriguez, J. A. *J. Am. Chem. Soc.* **2016**, *138*, 8269-8278.

(155) Piñero, J.; Ramírez, P. A.; Bromley, S. T.; Illas, F.; Viñes, F.; Rodriguez, J. A. *J. Phys. Chem. C* **2018**, *122*, 28013-28020.

(156) Christmann, K.; Ertl, G.; Pignet, T. *Surf. Sci.* **1976**, *54*, 365-392.

(157) Prats, H.; Piñero, J. J.; Viñes, F.; Bromley, S. T.; Sayós, R.; Illas, F. *Chem. Commun.* **2019**, *55*, 12797-12800.

(158) Jimenez-Orozco, C.; Flórez, E.; Moreno, A.; Liu, P.; Rodríguez, J. A. *J. Phys. Chem. C* **2016**, *120*, 13531-13540.

(159) Jimenez-Orozco, C.; Flórez, E.; Viñes, F.; Rodriguez, J. A.; Illas, F. *ACS Catal.* **2020**, *10*, 6213-6222.

(160) Jimenez-Orozco, C.; Flórez, E.; Moreno, A.; Liu, P.; Rodriguez, J. A. *J. Phys. Chem. C* **2017**, *121*, 19786-19795.

(161) Guo, B. C.; Kerns, K. P.; Castleman, A. W.; *Science* **1992**, *255*, 1411.

(162) Pilgrim, J. S.; Duncan, M. A. *J. Am. Chem. Soc.* **1993**, *115*, 9724-9727.

(163) Viñes, F.; Gomes, J. R. B.; Illas, F. *Chem. Soc. Rev.* **2014**, *43*, 4922-4939.

(164) Jimenez-Orozco, C.; Flórez, E.; Montoya, A.; Rodriguez, J. A. *Phys. Chem. Chem. Phys.* **2019**, *21*, 17332-17342.